Department of Engineering Science
University of Oxford

Ultrasound-enhanced antimicrobial therapy for oral biofilm infections



Davide De Grandi

Oxford-Philips Beyond Antibiotics (EPSRC)
St. Edmund Hall, University of Oxford
August 26, 2026

A thesis submitted for the degree of Doctor of Philosophy
Institute of Biomedical Engineering

Academic Supervisors: Prof Eleanor Stride and Prof Dario Carugo
Industry Supervisors: Dr Bart Gottenbos, Dr Monique Stoffels, Dr Matthias Born
College Advisor: Prof Wei Huang

Acknowledgements

The work that went into this thesis wouldn't have been possible without the continuous support I received from numerous people in recent and past times. I will try my best to acknowledge your precious presence in the next few lines.

First I want to thank my supervisors, who directly impacted the content of my DPhil work with their mentoring and insights. Heartfelt appreciation goes to my academic supervisors Eleanor and Dario, who guided me both scientifically and personally throughout my DPhil journey. The same goes for the whole group at Philips, Mathias, Monique, Loes, Amir, Priscilla, Guido, Alessio, and especially Bart who helped me settle down in Eindhoven during my internship and gave precious technical input during the past four years of work.
A due round of appreciation must go to the fantastic BUBBL research group team, every single one of them has been an invaluable companion during the long weeks in the lab. I would like to mention everyone, but we are a rather numerous bunch. I hope no one would take offence if I mention only the first two familiar faces I was fortunate enough to have once I moved to the UK. I'll never forget the two Irishmen I shared my first matchbox-office with at the UCL School of Pharmacy. Who could have imagined we would have all ended up in Oxford? Thank you Colm and Aaron for always being there in the hard first steps into my expat life.

I truly do not know how to start thanking you Jovana. I couldn't have asked for a better friend, colleague, gossip partner, or talented scientist on my side during my time here. You've been my safe port through the hardship of scientific failures and your continuous presence was

a blessing I cannot overstate. I wish you all the best in your future endeavours. To many more years of coffee breaks, as always, whenever we get the chance.

Luca, the most beloved person in the whole research group, I'll just be one of the many thanking you for all the mentoring you dispense, and for the true friendship we developed over the years. You are so used to giving all of yourself to others that you forget what an incredible feat that is. Thank you for all the stimulating discussions we had over the years.

I have to mention Dario again, as a friend this time. You are the most grounded, humane, and positive person I have ever met, and I say this on behalf of anyone who has ever met you. Throughout the time we spent together I always aspired to be a bit more like you: a bit more considerate with others, a bit more devoted to fighting for the right causes, a bit more understanding, and the list goes on. Not many people get to look up to their supervisor the same way I could. Thank you.

Mora, Avery, Miha, you've been my anchors in difficult times throughout my degree. Thank you for your views of the world and for sharing a little of yourselves with me.

Beppe and Lea, you truly turned my life around in Oxford. On this windy island, so far from our beloved Italy, as siblings we supported each other through the good and bad. Uncountable times we drove through the countryside to have a few joyous attempts at topping a random rock; even more times I found myself confiding in you and finding your sweet understanding on the other side. Although we met relatively recently, you'll always be family and I terribly miss

everyday life with you.

Peri, Ceco, Leo, it always amuses me how natural it feels being together, no matter how long I spend away from you or how we drift through life independently. Knowing that I will always be able to come back to you gives me inner peace wherever I end up. You might not hear from me often enough, but you fuel me through many of my days.

Sara, Fabio, Paolo, Elena, singolarmente siete persone stupende e potrei spendere pagine per ognuno di voi. Non tutti sono così fortunati da avere fratelli sempre presenti e pronti ad ascoltare in ogni momento. Vorrei poter essere ancora nelle vostre vite, vedervi ogni giorno e continuare a crescere insieme nella nostra casa. So che anche senza di me state tutti riuscendo nelle vostre vite e spero di riuscire a dimostrarvi quanto tengo a voi anche da qua. Siete la mia forza e la mia motivazione per tutti i traguardi che ho raggiunto.

Mamma, Papà, siete sempre stati una sicurezza per me e tutti noi. Fin dall'inizio ci avete dato tutto senza mai avere aspettative. Siete sempre stati capaci di motivarmi a provare, a fare, a credere che tutto si può aggiustare. Non penso che sarò mai grande abbastanza da non tornare a voi per chiedervi un consiglio, un suggerimento, una soluzione quando tutto sembra chiudersi intorno a me. Ho imparato ogni cosa da voi e continuo tuttora.

Statement of Originality

I hereby declare that this submission is my own work, and to the best of my knowledge, it contains no materials previously published or written by another person or substantial proportions of material that have been accepted for the award of any other degree or diploma at the University of Oxford or any other educational institution, except where due acknowledgement is made in the thesis. Any contribution made to the research by others with whom I have worked at the University of Oxford or elsewhere is explicitly acknowledged in the thesis. I also declare that the intellectual content of this thesis is the product of my own work, except to the extent that assistance from others in the project's design and conception or style, presentation and linguistic expression is acknowledged.



Conferences, Presentations and Posters

1. Les Houches School of Physics Winter school on Therapeutic ultrasound – Presentation - *Oral biofilm and related pathologies*

2. 2023 European Symposium on Ultrasound Contrast Imaging, Rotterdam, The Netherlands – Poster - **D. De Grandi**, G. LuTheryn, M. Stoffels, M. Born, B. Gottenbos, D. Carugo, E. Stride (2023). *Microbubble-Mediated Mechanical Removal Of Oral Biofilms in-vitro – The concept*

3. 8th EuroBiofilm 2024, Copenhagen, Denmark – Poster - **D. De Grandi**, G. LuTheryn, M. Stoffels, M. Born, B. Gottenbos, D. Carugo, E. Stride (2024). *Microbubble-Mediated Mechanical Removal Of Oral Biofilms in-vitro – Results*

4. Botnar Institute Students Symposium (BISS) 2024 - Presentation - *Oral infections, present treatments shortcomings, and future prospects*

5. 2026 European Symposium on Ultrasound Contrast Imaging, Rotterdam, The Netherlands – Short talk - **D. De Grandi**, M. Stoffels, M. Born, B. Gottenbos, D. Carugo, E. Stride (2026). *Bactericidal effect of ultrasound mediated low concentration antimicrobial treatment on a multi-species oral infection model*

List of publications

1. Effects of Ultrasound Mediated Treatments on Dental Biofilm Attachment and Viability, Accepted on May 22/2026 - Ultrasound in Medicine and Biology (UMB), CONTRIBUTORS: Davide De Grandi, Gareth LuTheryn, Monique Stoffels, Matthias Born, Bart Gottenbos, Dario Carugo, Eleanor Stride

2. Effect of human urinary microenvironment and fluid flow on antibiotic and phage therapy efficacy against uropathogenic Escherichia coli, DOI: 10.1101/2025.11.12.688052, Contributors: Ramon Garcia Maset; Aaron Crowther; Victoria Chu; Davide De Grandi; Rizka O.A. Jariah; Jenny Yoon; Dalia Blumgart; Marloes A.E Hodek; Nicholas Yuen; Benjamin O. Murray et al.

3. 3D bone printing via primed differentiation of stem cells with ultrasound (3DBonUS), DOI: 10.1101/2025.11.04.686554, Contributors: Martina Marcotulli; Chiara Patuto; Chiara Scognamiglio; Federico Serpe; Lucia Iafrate; Efsun Senturk; Sara Keller; Davide De Grandi; Biagio Palmisano; Alessandro Corsi et al.

4. MAKING WAVES: ULTRASOUND-STIMULATED ORGANOIDS TO MODEL FROZEN SHOULDER, DOI: 10.1302/1358-992x.2025.9.083, Contributors: Nicole Dvorak; Jessica Ackerman; Davide de Grandi; Dario Carugo; Christopher D Buckley; Stephanie G Dakin

5. Ultrasound-compatible 3D-printed Franz diffusion system for sonophoresis with microbubbles, DOI: 10.1016/j.ijpharm.2024.124749, Contributors: Chen, X.; De Grandi, D.; Zhu, Y.; Lutheryn, G.; Lane, M.E.; Da Silva Sil Dos Santos, B.; Carugo, D.

6. Rapid Production of Nanoscale Liposomes Using a 3D-Printed Reactor-In-A-Centrifuge: Formulation, Characterisation, and Super-Resolution Imaging, DOI: 10.3390/mi14091763, Contrib-

utors: Yongqing He; Davide De Grandi; Stanley Chandradoss; Gareth LuTheryn; Gianluca Cidonio; Ricardo Nunes Bastos; Valerio Pereno; Dario Carugo

7. Facile production of quercetin nanoparticles using 3D printed centrifugal flow reactors, DOI: 10.1039/d2ra02745c, CONTRIBUTORS: Davide De Grandi, Alireza Meghdadi, Gareth LuTheryn and Dario Carugo

Internships

1. Intern at Philips Healthcare - High Tech Campus 5, 5656 AG Eindhoven.

   September 2025 - January 2026

The internship focused on evaluating the effects of the developed therapeutic US treatment on a saliva-derived clinically relevant oral biofilms' model. The work also further developed the understanding of AW antimicrobial activity on oral biofilms and synergistic effects of US combination therapy.

Abstract

AMR is a well-known global health threat and leading cause of infection-associated deaths worldwide. Among all the resistance mechanisms, the innate ability of specific strains to form bacterial biofilms poses significant challenges in the treatment and eradication of up to 80% of chronic and implant-associated infections. The work presented in this thesis, divided into three main sections, places itself as part of a worldwide research effort to tackle the challenge of ever increasing AMR rates in infectious diseases. More specifically, it focuses on evaluating the possibility of harnessing therapeutic US potential as an adjuvant for improving biofilm dispersion and antimicrobial efficacy in fully formed oral biofilm models.

The first chapter focuses on the development of an experimental set-up capable of delivering reproducibly a combination treatment of therapeutic US and CHX on a simple, yet fully formed, Streptococcus *mutans* biofilm model. We examined the effects of 0.5 MHz US exposure at varying pnp (0.75-3.00 MPa) and CHX concentration (0.025-0.1 w/V %). US treatment was effective at removing biofilm, particularly at peak negative pressures exceeding 2.25 MPa and in the presence of lipid-coated MBs as cavitation nuclei. We also demonstrated that under specific conditions, US combination therapy determines a small yet significant improvement in CHX antimicrobial activity against S. *mutans*.

Building on these findings, in the second part of the project we proceeded to evaluate the effects of US combination therapy on a saliva-derived multispecies biofilm model, following a similar protocol to the one described in the previous chapter. We evaluated the synergistic effects of US in the presence of low concentration oxidative antimicrobials (AW) as we expected that faster acting antimicrobials (compared to CHX) would benefit to a greater extent from the transient

alterations determined by the US treatment. We again evaluated the effect of 0.5 MHz US at pnp between 0.75 and 2.25 MPa in combination with increasing concentration of AW. The antimicrobial activity, in this case, proved to be greatly improved by the US combination therapy with similar effects in both G+ and G- strains, as proved by the CFU counts performed on both the surnatant and tooth-mimicking substrate.

In the third and final chapter, we focused on developing a proof-of-concept experimental device capable of generating lipid-shelled bubbles through an electrolytic process in continuous, followed by ultrasound-mediated size reduction of said bubbles, bringing them to an adequate size for use as cavitation nuclei in therapeutic US applications. The device allowed for the MBs to be directly flushed in an ultrasonic set-up capable of delivering therapeutic US to a *S. mutans* oral biofilm model. Although the MBs concentration obtained using the device was consistently and significantly lower than the concentration of similar cavitation nuclei in comparable applications, we demonstrated the possibility of generating lipid shelled MBs in continuous mode for direct use in US therapy, a complete change in paradigm compared to the many batch methods used in this field. Nonetheless, the treatment effects were yet not comparable to the effects determined by US treatments administered in the presence of classical lipid-shelled cavitation nuclei. Future work could improve the device design by reducing its size, improving bubble sizing control, and changing the electrodes material to favour the generation of antimicrobial species during the electrolytic process.

Keywords: Therapeutic Ultrasound, Biofilm, Oral-biofilm, Antimicrobial resistance, Ultrasound-mediated drug delivery

Contents

Acknowledgements iii

Conferences, Presentations, Posters v

List of publications vii

Internships viii

Abstract x

List of Abbreviations xvii

1 Introduction 1

1.1 Motivation 1

1.2 Oral biofilms, related pathologies and treatments 4

1.2.1 Fundamentals of oral cavity anatomy 4

1.2.2 Oral biofilms 7

1.2.3 Oral infections and present treatments 12

1.2.4 Electrochemically activated water and its potential as an antimicrobial formulation 16

1.3 Therapeutic applications of ultrasound 19
1.3.1 Basic concepts in US physics and pressure fields estimation 19
1.3.2 Lipid-shelled US contrast agents: state of the art 22
1.3.3 Therapeutic US applied to drug delivery 25
1.3.4 Biological effects of US on bacteria due to cavitation 27

2 Effects of US Mediated Treatments on Dental Biofilm Attachment and Viability 30
2.1 Abstract 30
2.2 Brief introduction 31
2.2.1 Rationale for the study 32
2.2.2 Preliminary work 34
2.3 Materials and Methods 36
2.3.1 Materials 36
2.3.2 Biofilm growth protocol 36
2.3.3 Design of the US set-up 37
2.3.4 Characterization of the US set-up 40
2.3.5 Passive Cavitation Detection signal analysis 42
2.3.6 MBs manufacturing 43
2.3.7 CHX and US treatments protocols 45
2.3.8 Bacteria dual staining protocol for fluorescence microscopy 46
2.3.9 Image analysis 47
2.3.10 Statistical analysis 49
2.4 Results 50

2.4.1 Sound field characterization 50
2.4.2 Effect of US on biofilm detachment 52
2.4.3 Bactericidal effect of CHX on dental biofilms 58
2.4.4 Synergies between ultrasonic treatment and CHX on dental biofilm viability 60
2.4.5 Study limitations and future works 64
2.4.6 Conclusions 65
2.4.7 Authors contributions 66
2.5 Supplementary material 66
2.5.1 Preliminary simulation of the set-up US field 66
2.5.2 Increased intake of syto9™due to US treatment 70
2.5.3 Calculation of area of removal: method and consideration 71
2.5.4 One-Way-ANOVA supplementary analyses 73

3 Ultrasound mediated enhancement of sub-MIC antimicrobial treatment efficacy on a saliva-derived microcosm oral biofilm model 76
3.1 Abstract 76
3.2 Introduction 77
3.2.1 Rationale for the study 77
3.3 Materials and Methods 79
3.3.1 Materials 79
3.3.2 Passive Cavitation Detection (PCD) 79
3.3.3 Biofilm growth protocol 81

3.3.4 AW production and characterization 83
3.3.5 US and antimicrobial treatment protocols 84
3.3.6 CFU quantification protocol 86
3.3.7 Statistical analysis 87
3.4 Results and discussion 87
3.4.1 AW characterization 87
3.4.2 Overview of the treatments effects 89
3.4.3 Effect of AW treatment on bacterial viability 92
3.4.4 Effect of therapeutic US treatment on bacterial viability 94
3.4.5 Effect of the combination treatment on bacterial viability 96
3.5 Conclusions 104
3.6 Supplementary material 106
3.6.1 Iodometric titration of hypochlorus acid, hydrogen peroxide, and ozone 106
3.6.1.1 Principle of the titration 106
3.6.1.2 Ozone Decomposition 107
3.6.1.3 Procedure 107
3.6.1.4 Calculations 109
3.6.2 Bovine enamel mechanical wear protocol 109
3.6.3 Bovine enamel wear over 1 year of simulated treatments 110

4 Proof-of-concept — In-line production and use of therapeutic ultrasound cavitation nuclei 115

4.1 Materials and Methods 116

4.1.1 Materials . . . 116
4.1.2 Device design . . . 116
4.1.3 Acoustic modelling of the device . . . 118
4.1.4 MBs lipid formulation . . . 119
4.1.5 Quantification of MB size and concentration by optical microscopy . . . 120
4.1.6 Evaluation of cavitation-induced biofilm removal . . . 122
4.1.7 Statistical analysis . . . 122
4.2 Results . . . 123
4.2.1 Device overview and operation parameters . . . 123
4.2.2 Acoustofluidic MBs generator design . . . 124
4.2.3 MBs production and characterization . . . 129
4.2.4 In-line continuous MBs manufacturing and biofilm US treatment . . . 133
4.3 Discussion . . . 138
4.3.1 Device design and bubble generation . . . 138
4.3.2 Acoustofluidic MBs size tuning . . . 139
4.3.3 Cavitation activity and biofilm removal . . . 140
4.3.4 Future work and potential applications . . . 141
4.4 Conclusions . . . 142
4.5 Supplementary . . . 144
4.5.1 Power spectral density plots in presence of different cavitation nuclei . . . 144

5 Conclusions **147**

5.0.1 Synopsis of findings . . . 147

5.0.2 Limitations and future directions 149
5.0.3 Concluding remarks 153

List of Abbreviations

AC Alternating Current 19, 116, 129, 130, 139, 143

AMR Antimicrobial resistance ix, 1, 8

AW Activated water viii–x, xiv, 16, 18, 19, 76–78, 83–85, 87–93, 96–100, 102–106, 142, 148, 150, 151, 153

BHI Brain Heart Infusion 36, 37

CFU Colony Forming Units x, xiv, 34, 64, 77, 86, 87, 89–91, 99, 105, 106, 148

CHX Chlorhexidine ix, xii, xiii, 14, 16, 18, 30, 31, 33, 45, 46, 49, 58–63, 65, 70, 71, 74, 75, 78, 79, 147–151, 153

DC Duty Cycle 46, 83, 84, 116, 129, 130

DI Deionized 39, 45, 49, 81, 122

DPBS Dulbecco's phosphate buffer saline 37, 43–45, 47, 49, 53, 122

DPPC 1,2-dipalmitoyl-sn-glycero-3-phosphocholine 22

DPPE 1,2-dipalmitoyl-sn-glycero-3-phosphoethanolamine 22

DSPC 2-distearoyl-sn-glycero-3-phosphocholine 22, 43, 44, 120

Embs Electrolysis-generated microbubbles 115, 120, 122, 125, 130, 133–137, 140, 142–146, 149, 152, 153

EPS Extracellular polymeric substances 2, 4, 8–12, 14, 18, 27, 34, 70, 150

FWHM Full width half maximum 35, 105

G+ Gram positive x, 28, 87, 90, 151

G- Gram negative x, 28, 87, 91, 92, 100, 101, 105, 106, 148, 151, 153

GLM Generalised Linear Model 49, 53, 62

HA Hydroxyapatite 37, 39, 41, 45, 47, 48, 50–54, 63, 69, 77, 82, 84–86, 89–93, 95, 99, 103, 104, 117, 134

HIB Heart infusion broth 86, 89, 90, 92, 93, 95, 99, 100, 103, 105

HIFU High Intensity Focused Ultrasound 25, 27, 40–42, 68, 69, 79, 84, 117, 134, 143

HRP Horseradish peroxidase 106, 108

HW Hypotonic water solution 89–91, 93–99

MACB Mac Conkey broth 86, 87, 89, 91–93, 95, 99–101, 104–106

MB Microbubble 44, 115

MBs Microbubbles ix, x, xii, xv, 22–26, 29, 32, 33, 43, 44, 46, 49, 52–57, 61, 62, 64, 71, 73–75, 85, 96, 115, 117–124, 129–136, 139, 141–146, 149, 150, 152, 153

MIC Minimum inhibitory concentration 89

MRI Magnetic resonance imaging 24

PBS Phosphate buffer saline 82, 85, 86, 90, 91, 94, 119, 120

PCD Passive Cavitation Detection xiii, 42, 43, 46, 55, 58, 79, 80, 96, 122, 140, 145

PEG-40-S Polyoxyethylene-40-stearate 43, 44, 119

PFB Perfluoro butane 44

pnp Peak negative pressure ix, x, 30, 33, 45, 50–55, 57, 61, 63, 65, 73, 75, 77, 84, 89, 94, 97–100, 106, 110, 112, 113, 122, 134–137, 140, 141, 144, 145, 148

PRF Pulse Repetition Frequency 84, 122

PSD Power Spectral Density 42, 54–56, 80, 97–99, 135, 144–146, 175

QS Quorum sensing 2, 7

RF Radio-frequency 42

ROS Reactive Oxygen Species 15, 17, 18, 28, 78, 79, 83, 105, 117, 142, 144, 150

SPT Supportive periodontal therapy 13

TCZ Total care zero 85, 90–93

THmbs Tissue Homogenizer-generated microbubbles 115, 120, 133–136, 140, 143–146, 149

UN United Nations 1

US Ultrasound viii–x, xii–xiv, 3, 19–22, 24–28, 30–35, 37–42, 45, 46, 49–54, 56, 58–66, 69–75, 77–80, 84–86, 89–91, 94–96, 98–102, 104–106, 109, 111–113, 115, 117, 121, 122, 124, 128, 130, 132–134, 137, 138, 147–154

WHO World Health Organization 1

Chapter 1

Introduction

1.1 Motivation

AMR is a growing global health pandemic, believed to have directly caused more than 1.1 million deaths in 2021 [1]. In the same year, the UN Interagency Coordinating Group on AMR reported that 10 million deaths each year will be associated with drug-resistant infections by 2050, with an annual economic cost of £69 trillion [1]. Although AMR occurs naturally over time through genetic mutation and natural selection of pathogens that are resistant to antimicrobial agents, many factors in modern society accelerate this rate of evolution. The WHO has identified three major drivers of the development of AMR: (1) poor infection disease prevention and diagnosis; (2) misuse of antimicrobial agents in humans, animals, and water treatment; and (3) lack of awareness and enforcement of the law to limit the first two [1].

Regardless of misconduct and poor practices, some bacteria are inherently more resistant to adverse conditions (e.g., nutrient deprivation, scarce oxygen, antimicrobials, and antibiotics) than others, and even the same bacteria can show different resistance depending on their phenotype and current life stage. Most bacteria can live both in sessile (attached) and planktonic

(in suspension) states. Although biofilms can form and survive in floating state, in this work we focused on their sessile state, as it is more relevant to oral infections-related diseases. The adhesion to any surface (biotic or abiotic) triggers phenotypic modifications in the adhering bacteria, allowing them to live in multicellular communities in which they are encased in a self-produced matrix of extracellular polymeric substances EPS such as polysaccharides, proteins, nucleic acids, and lipids.

The physical structure of a biofilm, the ability of bacteria to chemically communicate by quorum sensing QS within it, and hence adapt to survive in adverse conditions, result in significantly increased resistance of biofilm resident bacteria to classical chemotherapy.

It has been estimated that up to 80% of chronic human infections are determined by surface attached biofilms [2]. Of all the infections affecting humans, oral biofilm-related infections are among the most common worldwide. The oral microbiota is comprised both of commensal and pathogenic bacteria, that live attached to teeth and soft tissue surfaces forming complex and long-lasting biofilms. When the homeostasis of the oral microbiota is broken (e.g. due to prolonged exposure to saccharose and low pH), there is a shift in the microbial community composition that can cause plaque formation and ultimately tissue damage.

Plaque is a specific type of biofilm that forms in direct contact with biological structures containing calcium minerals, such as teeth. Dental plaque is formed by lactic acid-producing bacteria that slowly dissolve some of the enamel's and dentine's minerals. The most widespread diseases caused by pathogenic oral biofilms are dental caries and periodontitis. These are usually a direct result of the progressive thickening of plaque on the surface of teeth, gums, and cheeks. Both diseases can be usually avoided by correct daily dental hygiene, i.e. brushing and flossing; however, factors such as genetics, shifts in dietary habits, immunodeficiency, and systemic

infections will also affect the risk of disease. At present, once the pathology is established, we lack the tools to reproducibly achieve complete eradication through pharmaceutical therapy. Often the only available option is surgical removal of the infected region. Despite some promising anti-plaque methods being developed [3], the lack of truly efficacious and widely available therapeutic options to eradicate low to mid grade oral infections constitutes an unmet healthcare challenge.

At present, the gold standard treatments for plaque related pathologies, such as dental caries and periodontitis, are mechanical debridement and planing of the teeth's surface and root. Most treatment cycles include surgical removal of the damaged tissue and mechanical occlusion of the exposed tissue with specialized resins. Although such treatments can effectively limit the impact of dental biofilm-related pathologies, they have several limitations: gum recession, enamel thickness reduction, root and dentine sensitization, difficulty in debriding/scaling/planing of subgingival and interstitial space, modified enamel and dentine surface roughness following treatment, implant-related infections, and dispersion of viable bacteria that can lead to secondary infections.

The exploration of alternative methods for dental plaque removal and control, with the ultimate aim of reducing side effects and increasing the success rate of current treatment, is for this reason a thriving area of research. Among the various lines of research, the use of therapeutic US has been highlighted as a viable and promising option for biofilm treatment. The use of focused US at frequencies well below the ones used in imaging applications (ranging between 0.25 and 1.5 MHz) has been explored in the past decades as a method to achieve spatially controlled release of drugs and improved their uptake. Positive results have been reported in literature both for improved efficacy of chemotherapy in cancer and infectious disease treatment [4–8]. We

believe that the cavitation-induced mechanical disruption of biofilms' EPS structure could lead to significant improvement in their susceptibility to antimicrobial treatment.

1.2 Oral biofilms, related pathologies and treatments

1.2.1 Fundamentals of oral cavity anatomy

The oral cavity, or mouth, is the first portion of the alimentary canal and respiratory system. It can be divided in two regions: the vestibule and the oral cavity proper. The oral vestibule is the most relevant section for this thesis as it comprises the region starting at the front of the teeth and ending at the uvula.

Figure 1.1: Representation of the front section of the oral cavity (vestibule), maxillary and mandibular teeth arches. The teeth arches are connected to the mouth through the periodontal ligament, which binds teeth root to the alveolar bones. The most common sites for the development of oral infections are the subgingival tooth surface, crevices in between teeth, and crevices/pockets in the molars and bicuspids. Image removed due to missing permission of the rights holder [9].

As shown in figure 1.1, the main structures composing the vestibule are the tongue, palate (divided into hard and soft sections), uvula, alveolar bones, teeth, and lips. The oral cavity has various functions, mainly to facilitate eating, speech and respiration [10].

The teeth are connected and supported by the alveolar bones constituting the upper and lower jaws. The main function of the teeth is chewing, although they also play an important role in speech. There are four types of teeth in humans, starting from anterior to posterior (as shown

in figure 1.1): incisors, cuspids (or canines), bicuspids (or premolars), and molars. Although different types of teeth have specialized functions (e.g. incisors are used mainly for cutting, while molars for chewing), their basic anatomy is similar and is represented in figure 1.2.

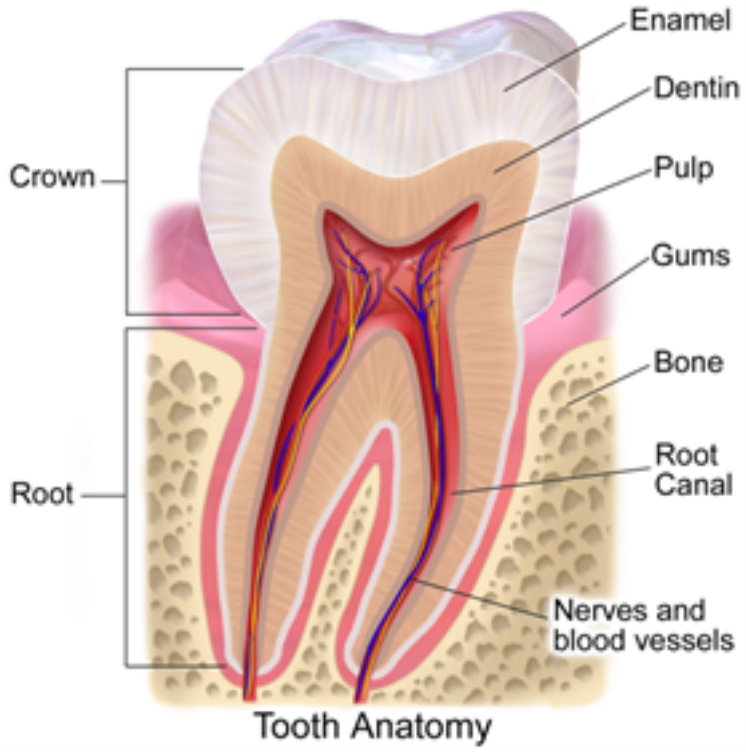


Figure 1.2: The tooth is composed of two sections: the crown (supragingival and exposed region) and the root (subgingival and connected to the alveolar bone through the periodontal ligament). The crown is covered in a thick layer of mineralised tissue, the enamel. Below the enamel there is a vital layer composed of both mineralised tissue and odontoblast, the dentine. The most inner layer is named pulp and is composed of blood vessels, nerves, odontoblast, and connective tissue. The pulp is not mineralised but participates in the remineralisation process of the dentine. Reproduced from Blausen Medical (2014) under CC BY-SA [11].

The tooth can be divided into two main sections, the supragingival exposed section is re-

ferred to as crown, whereas the subgingival section is the root. The outer surface of the crown is composed of enamel: a 1.5 to 3 mm thick layer of minerals, mostly hydroxyapatite. Once fully developed, enamel does not contain cells, vessels, or nerves. The term tooth demineralisation refers to the damage and thinning of enamel, which is usually determined by chronic local exposure to acidic (pH $<$5.5) environment. The central section of the teeth is composed of dentine, which is much softer than enamel (the mineral content is only 44% compared to 96% of enamel) and composes the bulk of the tooth root. The root is connected to the alveolar bone thanks to the periodontal ligament surrounding it. Unlike enamel, dentine contains specialised cells (odontoblasts) devoted to secreting the organic matrix of which it is composed and regulating its mineralization. Dentine contains also nerves endings, unlike enamel, reason for which dentine damage is usually accompanied by increased pain when compared to enamel damage. The external surface of the root is covered in a thin layer of mineralised dentine, called cementum. The main purpose of the cementum is to connect the root to the periodontal ligament. The most inner layer of the tooth is known as the pulp and is composed of connective tissue, blood vessels, nerves, and odontoblasts [10]. The pulp is not mineralised but is involved in the remineralisation process of dentine.

Due to low odontoblast content, and slow rates of remineralization, enamel and dentine damage due to cavities are usually irreversible unless very modest in extension. Chronic enamel and dentine erosion determined by acidic diet or acid-producing bacteria determines pathologies such as dental caries and periodontitis, which often require specialised surgical and occlusion treatment from professionals.

1.2.2 Oral biofilms

Biofilms are complex communities composed of unicellular organisms (e.g. bacteria, yeasts, algae) living together in surface attached or free floating aggregates. These structures are of great relevance in many fields such as bio-fouling, contamination of industrial apparatus, water cleaning systems, agriculture, and human infections. Bacterial biofilm infections are particularly relevant in modern medicine, as they present substantial treatment challenges. Such aggregates can be either surface attached or free floating, although, in most cases relevant to oral infections, the biofilm is attached to biotic (teeth, gums, cheeks) or abiotic (resins for filling, implants, orthodontic inserts) surfaces.

The first studies on sessile bacteria started in the 1930s/40s [12], but the systematic study of their formation, development, and dissemination started only in the 1980s [13]. The most widely accepted theory on the biofilm life cycle is termed the 'five-step biofilm model', although consensus on a comprehensive model is still to be reached [14]. The original five-step model is based on studies carried out on *Pseudomonas aeruginosa* and describes a cyclic process in which bacteria adhere to a surface, proliferate while attached to the surface, and then disseminate from the biofilm. The transition from planktonic to sessile form is a highly regulated process, in which bacterial QS genes are activated.

Figure 1.3: Representation of the 5-step biofilm life cycle model, developed for *Pseudomonas aeruginosa*. The biofilm formation is here described as a closed cycle, which starts with the attachment of bacteria to a host surface, often thanks to dedicated surface-binding proteins. The attachment process is followed by phenotypic changes such as flagella reduction and EPS production. The second phase of the maturation follows when bacteria start replicating and the biofilms act as attachment sites for other planktonic bacteria that join the community, forming layers. Biofilm maturation stages begin with the formation of microcolonies, just a few cells thick (maturation I stage). Subsequently the stratification of bacteria determines a gradient of nutrients and gases through the community, and the formation of thick clusters of fully matured bacteria (maturation II). The final step is termed dispersion or erosion and coincide with the decrease and degradation of matrix components and dispersion of cells in the surrounding media. Dispersed cells often regain their motility and demonstrate increased drug susceptibility compared to adherent biofilm cells. Image removed due to missing permission of the rights holder [14]

As represented in figure 1.3, initial bacterial attachment can result in prolonged development of a surface attached community or in a temporary aggregation that then detaches promptly. After the onset of irreversible attachment, the community undergoes maturation into a biofilm and finally dispersal in the last step of the cycle. In each of these phases, bacteria express characteristic genes and produce specific proteins and chemokines that are strain and community specific. Examples of genes activated by surface adhesion in *P. aeruginosa* are *algC* (involved in lipopolysaccharides and exopolysaccharides production), *sagS* and *brlR* (involved in high antimicrobial tolerance development through expression of hybrid two-component SagS [15, 16]). This example underlines the relevance of surface attachment-induced gene expression in both EPS production and AMR in biofilms [14], although protein expression and tolerance mechanisms are extremely variable and usually strain-specific.

As the biofilm undergoes maturation, bacteria assemble into complex 3D structures that are species and growth-condition dependent. In the initial stages, all bacteria receive nutrients

thanks to the development of small hydrophilic channels forming in between aggregates. As the biofilm gets progressively thicker, the deepest layers start to receive progressively fewer nutrients and gases, driving variation in their viability and phenotype. It has been shown, for example, that bacteria residing at the base of the biofilm express genes linked to oxygen deprivation, nutrient stress, and slow growth [17–19]. These conditions facilitate the development of dormant bacteria, also called persister cells [20, 21]. The development of these metabolically inactive, starved, cells is a key factor in the high recurrence rate of biofilm-related infections. The last stage in the biofilm life cycle is the dispersion of bacteria. In this actively regulated process, bacteria leave the EPS and the biofilm gets slowly eroded. Metabolically inactive cells are then exposed to oxygen and nutrients again and can either repopulate the biofilm or act as attachment sites for floating bacteria.

Although this model of the biofilm cycle has been adopted rapidly by the scientific community, its simplicity impairs its relevance, as more complex inter- and intra-species differences in biofilm development exist. As an example, dental biofilms are known to be often composed of tens of species, that stratify in different relative abundance for each layer. Their relative abundance is dictated by varying environmental conditions such as availability of nutrients, pH levels, and neighbouring species. Such complexity cannot be represented in a simple single-species model, or with few and un-calcified layers. Although expanded conceptual models have been developed [14] to account for the formation of floating aggregates and non-continuously attached biofilms, the reality is that a comprehensive model capable of representing the diversity of biofilms is still missing, and probably is not achievable due to the intrinsic variability of these structures.

The dental plaque is the most common example of oral cavity biofilm. It is a poly-microbial

aggregation of bacteria that can develop over months or even years, causing pathologies such as dental cavities and periodontitis when bacterial growth is not controlled. As reported in [22], *Streptococci* spp. are the most abundant organism in both early stage and mature plaques. As the plaque matures, other gram-negative anaerobic organisms (i.e. Fusobacteria, Vellionella and Treponema) attach to the existing bacterial layer and become embedded in the EPS, increasing rapidly in number. Plaque adhesion and maturation begins supragingivally but usually progresses below the gum line leading to tissue damage over time. One of the most abundant bacteria in oral plaque is *Streptococcus mutans*. It is considered an early colonizer implicated in the onset of an acidic pH environment, favourable to cariogenic bacteria. Due to its importance and prevalence, it is often used in research as a simple mono-species biofilm model.

S. mutans is a facultatively anaerobic, gram-positive coccus. It is generally a commensal bacterium of the oral cavity but when the homeostasis of the microbiome is disrupted, it can express pathogenicity determinants and induce damage to surrounding tissues. At least 25 species of Streptococcus are normally present in the oral cavity and *S. mutans* is strongly associated with caries development, accounting for up to $\sim 40\%$ of the total streptococci in the oral microbiome in individuals showing active caries.

At pH close to 7, the overgrowth of *S. mutans* is controlled by the release of oxygen peroxide and other antimicrobials by the commensal microbiome. In the presence of sucrose, *S. mutans* can synthesize glucose polymers (glucans or mutacines) thanks to the expression of three types of glycosyl transferase (Gtf-B/C/D). These polymers allow more bacteria to adhere to the dental biofilm, which is usually composed of commensal bacteria such as *S. gordonii*, *S. mitis*, *Actinomyces* spp. The attachment of new species to the dental biofilm can trigger a cascade in the *S. mutans* population, driving the catabolization of sucrose to produce large amounts of insoluble

and soluble glucans, which contribute to the build-up of a robust EPS in a self-sustaining cycle. Interestingly, *S. mutans* produces its EPS from sucrose only [23], other sugars (such as glucose, fructose, and galactose) are still metabolized by *S. mutans* but via catabolic metabolism and generate lactic acid as a by-product which lowers the biofilm pH [24]. Low pH and anaerobic conditions favour *S. mutans* growth, reducing the metabolism of other commensal species that then stop producing antimicrobials (e.g. *S. gordonii*'s hydrogen peroxide production is highly impaired when co-cultured with *S. mutans* [25]). Once *S. mutans* becomes prevalent in the biofilm, it starts producing mutacines, killing competing bacteria and establishing itself permanently. The lower pH is also responsible for the initiation of enamel demineralization, the first step in the development of dental caries, root damage, and related inflammatory diseases.

It has been demonstrated that the pathogenicity of *S. mutans* is usually favoured by co-colonization of other microorganisms, such as *C. albicans*. The symbiotic relationship between these two microorganisms has been studied in detail, as it is strongly correlated with increased EPS production and dental caries in children [26].

Susceptibility to oral infections varies between individuals and immunological mechanisms have been proposed to confer protection or susceptibility. These mechanisms have yet to be fully elucidated, but it seems that immunological tolerance to *S. mutans* at the mucosal surface may make individuals more prone to colonization with *S. mutans* and therefore increase susceptibility to dental caries and periodontitis [27].

1.2.3 Oral infections and present treatments

Periodontitis is a common multifactorial dental disease that leads to gradual loss of periodontium (alveolar bone and periodontal ligament). The most common cause of periodontitis in both adults and children is the development of subgingival dental biofilm and consequent organic acids accumulation in the extracellular matrix. Organic acids, lipopolysaccharides, and strain specific toxins produced by bacteria elicit a chronic immune response due to decalcification of bone tissue, leading to irreversible damage. Periodontitis symptoms include gingival inflammation, alveolar bone loss, tooth mobility, and bleeding [28].

Periodontitis is a very common disease, with an estimated prevalence of around 60% in high income countries. Both the prevalence and severity (stage I to IV) of periodontitis increase sharply with age [29]. The first line treatment for early stage periodontitis is patient education in home-care practices. Scaling and root planing are also useful in controlling periodontitis progression. Complete pathogenic biofilm removal however remains mostly unachievable, due to the inaccessibility of small crevices and dissemination of live bacteria in the oral cavity following treatment. Systemic and topical antibiotics can be prescribed, but their effectiveness is impaired by reduced delivery to the target bacterial cells due to the thick EPS layer and poor tissue blood supply.

Dental caries constitute a multifactorial disease determined by the pathological cycle of demineralization and remineralization of dental tissue. Dental demineralization in caries is usually determined by the presence of pathogenic biofilm on the tooth surface. As described above, once pathogenic bacteria attach to the tooth they start metabolising carbohydrates, reducing the local pH and causing bone demineralization. Although most organic acids can initiate dem-

ineralization, dental caries are primarily driven by lactic acid production, as this is the main by-product of bacteria in plaques. As the pH gets lower, the enamel/biofilm matrix interface becomes undersaturated and some of the minerals composing the enamel and dentine (such as calcium phosphates) become solubilised [30]. The widespread use of fluoride compounds (NaF, SnF_2 and acidulated fluorophosphates) has been credited with significant reduction in the incidence of dental caries in the last four decades. The mechanism of action of fluorides has been described in [31] and includes bacteriostatic action, increased rate of remineralization, decreased rate of demineralization thanks to greater resistance to acids of hydroxyapatite-containing fluoride in its crystalline structure, and the inhibition of bacterial enzymes necessary for carbohydrates metabolism.

At present, standard oral hygiene is based upon daily self-care (brushing with toothpaste, flossing, and mouthwash) and one to two mechanical, non-surgical debridement procedures each year. These methods are mostly preventative , as upon the onset of an oral infection it is usually necessary to administer antibiotics and intervene surgically to remove the damaged tissues. Significant efforts have been made to develop more effective localised antimicrobial treatments and regenerative procedures, but at present there is no consensus on a standard practice to eradicate periodontal diseases and avoid relapse [32–34].

One consequence of periodontal therapy is the loss of root cementum, which is believed to help protecting against dentine caries. When root surfaces are exposed, individuals become more susceptible to developing root caries. Antimicrobials can be delivered through various systems, including dentifrices, oral rinse solutions, or local flushing during periodontal pockets treatment. However, there are limited long-term studies that demonstrate the effectiveness of these antimicrobials in supportive periodontal therapy (SPT) programs [35].

Subgingival debridement, which includes procedures such as scaling and root planing, aims to remove plaque and calculus from below the gumline [36]. However, the mechanical action of debridement can cause trauma to the gingival tissues and periodontal ligament, sometimes leading to inflammation and subsequent attachment loss. Moreover, during debridement the root surfaces are exposed, making them more susceptible to bacterial colonization and biofilm formation. The removal of plaque and calculus can also trigger an inflammatory response; if not properly managed, this can result in the breakdown of connective tissue and loss of attachment. Finally, excessive removal of cementum during debridement can damage the attachment fibres and lead to gingival recession [36, 37].

The gold standard antimicrobial for oral infection treatment is chlorhexadine (CHX), due to its broad spectrum of action (on both Gram-positive (G+) and -negative (G-) bacteria) and its relatively low toxicity to human cells [38]. When used in concentrations ranging between 0.1% and 0.2% w/v, CHX mouthwashes have demonstrated efficacy against plaque formation (both in the presence and absence of mechanical cleaning) [38–40].

CHX is a cationic bisbiguanide that primarily acts through electrostatic interaction with the negatively charged bacterial cell membrane. At bacteriostatic concentrations, CHX disrupts membrane integrity and causes leakage of intracellular components; at bactericidal concentrations, it induces complete cytoplasmic coagulation and cell death [38]. CHX is also known to adsorb onto oral surfaces including mucosa, pellicle, and the EPS matrix, from which it is gradually released over a period of several hours, providing sustained antimicrobial activity following a single application [38]. However, this sustained release also means that bactericidal concentrations at the target site are not immediately achieved, and the slow onset of action may limit its effectiveness. Prolonged use of CHX is also associated with side effects including tooth

and restoration staining, altered taste perception, and increased calculus formation [40].

Reactive oxygen species (ROS), including hydrogen peroxide (H_2O_2), ozone (O_3), and sodium hypochlorite ($NaOCl$), represent an alternative class of antimicrobials with potent and broad-spectrum activity. Their mechanism of action is primarily oxidative, as after interacting with biological tissue these agents generate free radicals (mostly $\cdot OH$) that non-selectively damage bacterial lipids, proteins, and nucleic acids [41, 42].

Hydrogen peroxide is commonly used at concentrations between 1% and 3% v/v in oral applications. Its chemical structure and small size favour fast penetration of the bacterial cell membranes, where it acts by oxidizing intracellular components, leading to cell death. Ozone, delivered as aqueous solution, is a highly reactive oxidant with demonstrated efficacy against a broad range of oral pathogens, including species resistant to conventional antibiotics [43]. Its mechanism of action involves direct oxidation of bacterial membrane lipids and proteins, causing rapid cell lysis [43]. Similarly to hydrogen peroxide, ozone acts rapidly and leaves no persistent residues, making it suitable for repeated clinical application. Sodium hypochlorite, most commonly employed in endodontic irrigation at concentrations of 0.5%–5.25% w/v, once dissolved in water determines the formation of hypochlorous acid ($HOCl$), which disrupts membrane functions through oxidative stress [44, 45]. In addition to its antimicrobial properties, $NaOCl$ possesses proteolytic activity, enabling partial dissolution of organic components of the biofilm matrix. However, at clinically effective concentrations, $NaOCl$ is cytotoxic to periodontal and pulpal tissues, limiting its repeated use and making it more suitable to specialized applications such as root canal system cleaning [44].

Another approach to oral microbiome management is the use of essential oils with antimicrobial effects. A popular example of such formulation is Listerine Zero, an alcohol-free mouthwash.

Its active antimicrobial constituents are thymol (0.064%), eucalyptol (0.092%), methyl salicylate (0.060%), and menthol (0.042%). These compounds act synergistically to disrupt bacterial cell wall integrity [46, 47]. Specifically, thymol and eucalyptol intercalate into the lipid bilayer of the bacterial membrane, increasing its permeability and causing leakage of cytoplasmic contents. Menthol acts in a similar fashion, increasing the permeability of the cell membrane and favoring the penetration of other compounds. Methyl salicylate, in addition to inducing membrane destabilising effects, contributes to the mouthwash efficacy with anti-inflammatory activity [48–50]. Unlike CHX, the antimicrobial effect of essential oil formulations is largely confined to the period of active rinsing and shortly thereafter. Listerine Zero has been shown to be effective in reducing supragingival plaque and gingivitis as an adjunct to mechanical oral hygiene, with a comparable efficacy profile to the alcohol-containing formulation and a more favourable side-effect profile for long-term use [49].

1.2.4 Electrochemically activated water and its potential as an antimicrobial formulation

Electrochemically activated water, or activated water (AW), refers to aqueous solutions altered through the application of an electrical current [51]. When a diluted aqueous solution, typically containing a mixture of dissolved salts, is subjected to a controlled direct current, electrochemical reactions at both the anode and cathode drive the production of various reactive species that would not be hardly achievable through conventional chemical mixing [52]. The result is a metastable solution containing a mixture of redox compounds. By convention, two distinct product streams are recognised: the anolytes, produced at the anode, which is acidic (pH $<$

5) and carries a strongly positive redox potential, and the catholytes, produced at the cathode, which is alkaline (pH $>$ 9) and carries a negative redox potential [51, 52]. The chemical species produced during electrochemical activation depend on both the composition of the electrolyte solution and the employed electrodes material, as these determine which oxidation and reduction reactions take place at the electrodes surface [53].

At the anode, oxidative reactions dominate. In the presence of chloride ions, the primary anodic reaction is the oxidation of $Cl-$ to molecular chlorine (Cl_2), which, in water, rapidly yields hypochlorous acid ($HOCl$) and hypochlorite ($ClO-$). At near-neutral to mildly acidic pH (~ 6.2 pH), the predominant species is $HOCl$, which carries the highest biocidal activity of the active chlorine species [52, 53].

Additional oxidative species produced at the anode include hypochlorite radicals ($ClO\cdot$), and molecular ozone (O_3) under certain conditions. Concurrently, water oxidation at the anode surface produces hydroxyl radicals ($\cdot\, OH$). The electrodes material determines if the radicals are released as is in solution, or if they become intermediate in the production of hydrogen peroxide (H_2O_2) or molecular oxygen (O_2) [54].

Electrode materials are broadly classified as ”active” or ”non-active” with respect to their interaction with $\cdot\, OH$. Active anodes adsorb the radicals on their surface. This phenomena reduces the release of free $\cdot\, OH$ in solution and promotes the oxidation of electrolytes present in solution. These electrodes tend to produce active chlorine species efficiently when chloride is present, but generate comparatively lower concentrations of ROS in the bulk solution [55]. A few examples of active electrodes would be platinum, graphite, iridium oxides.

Non-active anodes weakly bind $\cdot\, OH$, which favours the release of free radicals into the bulk solution [55]. In chloride-containing electrolytes, non-active anodes produce both active chlo-

rine species and $\cdot OH$ radicals simultaneously, leading to a more diverse oxidative mixture compared to active anodes [55]. The evolution of $\cdot OH$, especially in non-active electrodes, can follow two main pathways: two-electron oxidation or four-electron oxidation. The first determines water oxidation with abundant production of H_2O_2, whereas the second generates water and molecular oxygen. The selectivity between two-electron pathway and four-electron pathway is governed by the binding energy of $\cdot OH$ on the electrode surface [56].

Noble metals, such as gold, interact only weakly with hydroxyl intermediates as it is relatively chemically inert and does not form stable surface oxide species under mild oxidative conditions [57]. Gold's weak $\cdot OH$ adsorption means that water oxidation produces predominantly H_2O_2 via the two-electron pathway [56, 57]. Furthermore, gold does not catalyse the complete four-electron reduction of oxygen as efficiently as platinum. Contrary to many oxides-based electrodes, gold does not leach metallic ions under normal operating potentials, giving it great biocompatibility.

The antimicrobial efficacy of AW is a direct consequence of the oxidative species it contains, which act through the same mechanisms described in Section 1.2.3 for ROS-based antimicrobials. The combination of species produced in AW is gaining interests as it is believed to show antibiofilm activity. The oxidative mixture disrupts the EPS matrix, degrading the polysaccharide scaffold that otherwise limits diffusion of antimicrobial agents into the biofilm interior [51]. This is a significant practical advantage over conventional antimicrobials such as CHX, whose penetration into mature biofilms is constrained by EPS binding.

A particularly attractive feature of AW from a clinical perspective is the possibility of generating the activated solution *in situ*, at the point of use, from simple salt solutions. This eliminates the handling, storage, and stability limitations associated with pre-mixed chemical disinfectants,

since the reactive species in AW are inherently short-lived and their concentration begins to decay as soon as electrolysis ceases [51, 52]. Generation of the antimicrobial solution on demand also means that the concentration of oxidants could be easily tailored to different applications.

1.3 Therapeutic applications of ultrasound

1.3.1 Basic concepts in US physics and pressure fields estimation

US describes mechanical (pressure) waves with frequencies above 20 kHz. Their application in medicine has been broadly explored in both diagnostics and therapy, since the second half of the 20th century. Ultrasonic devices used in medical applications are commonly composed of a piezoelectric element that mechanically vibrates when supplied with an alternating electric current (AC), a housing, and a matching layer that allows the propagation of pressure waves from the transducer's face into the surrounding media. Although an exhaustive description of US physics is beyond the scope of this document, below are a few key concepts relevant to US propagation, pressure fields, and their modeling.

When an US source (i.e. a piezoelectric transducer) oscillates, it transfers energy to the surroundings, determining cycles of compression and rarefaction in the media. The vibration of "particles" (*i.e.* voxels, small portions of media) is transferred to neighbouring particles. The propagation is wave-like as it occurs without appreciable net mass transfer. The ultrasonic source can be represented as a simple oscillating piston, cycling through compression and expansion. Generally, the transducers used in imaging and therapeutic applications of US vibrate longitudinally to the direction of propagation, although specialized transducers can be used

to produce waves propagating perpendicularly to the front face of the transducer (transverse waves).

In its simplest form (linear propagation) an US wave can be described as a sinusoid defined by its frequency and amplitude [58].

$$x = A\cos(\omega 0t + \phi) \quad \text{or} \quad x = Ae^{j\omega 0t} \tag{1.1}$$

Where A is the amplitude of the wave, $\omega 0$ is the angular frequency, and ϕ is the phase shift. For small amplitude and propagation in a homogeneous lossless fluid, the US pressure field can be estimated from the linear wave equation:

$$\nabla^2 p = \frac{1}{c^2}\frac{\partial^2 p}{\partial t^2} \tag{1.2}$$

Where $\nabla \cdot \nabla = \nabla^2$ is the three-dimensional Laplacian, p is the instantaneous pressure and c is the thermodynamic speed of sound in the chosen media, defined as the square root of the bulk modulus B over the equilibrium density $\rho 0$.

The wave equation in equation (1.2) can be simplified for time-harmonic problems by assuming a sinusoidal steady-state solution of the form $p(\mathbf{r}, t) = \text{Re}\,[\hat{p}(\mathbf{r})\, e^{j\omega t}]$, where $\hat{p}(\mathbf{r})$ is the complex pressure. Substituting this into equation (1.2) yields the Helmholtz equation:

$$\nabla^2 \hat{p} + k^2 \hat{p} = 0 \tag{1.3}$$

where $k = \omega/c$ is the wavenumber. The frequency-domain formulation separates the spatial and temporal dependencies of the pressure field, reducing the problem to a solely spatial one.

This is particularly advantageous for modelling continuous-wave or narrowband US sources, as it substantially reduces computational cost compared to full time-domain approaches.

Real media attenuate US energy as it propagates, primarily through viscous losses and relaxation mechanisms. For this reason, to model lossy media the wavenumber is usually represented as a complex value:

$$k = \frac{\omega}{c} - j\alpha \tag{1.4}$$

where α is the pressure attenuation coefficient in $\frac{Np}{m}$. The imaginary component of k introduces an exponential pressure decay along the propagation direction. In real applications, sounds rarely travels through a completely homogeneous medium. It is much more common for it to travel through media exhibiting varying acoustic properties. In these cases α is treated as a spatially varying field, $\alpha(\mathbf{r})$, allowing media specific attenuation in the computational domain.

Media heterogeneity also determines spatial variations both in density and compressibility along the US propagation path. Accounting for this requires a generalised form of the Helmholtz equation [58]:

$$\nabla \cdot \left(\frac{1}{\rho(\mathbf{r})} \nabla \hat{p} \right) + \frac{\omega^2}{\rho(\mathbf{r})\, c(\mathbf{r})^2}\, \hat{p} = 0 \tag{1.5}$$

In this formulation, $\rho(\mathbf{r})$ and $c(\mathbf{r})$ are spatially dependent density and speed of sound fields, respectively, and allow to represent structures with differing acoustic impedances $Z = \rho c$. The acoustic impedance of a medium, similarly to the electrical impedance in a circuit, represents a characteristic property of the medium relating the particle velocity in the bulk of the material with the acoustic pressure applied to it. At interfaces between media of differing impedance, differences in density and particle velocity determine partial reflection and transmission of the pressure wave reducing energy transfer efficiency. The magnitude of this phenomenon is gov-

erned by the acoustic reflection and transmission coefficients:

$$R = \frac{Z_2 - Z_1}{Z_2 + Z_1}, \qquad T = \frac{2Z_2}{Z_2 + Z_1} \tag{1.6}$$

where Z_1 and Z_2 are the acoustic impedances of the incident and transmitting media, respectively.

Together, these extensions to the linear wave equation provide a physically complete description of US propagation in realistic environments, forming the basis for numerical pressure field estimation in heterogeneous, lossy media.

1.3.2 Lipid-shelled US contrast agents: state of the art

The development of US contrast agents has driven the advancement of diagnostic imaging, with gas-filled MBs being the most widespread platform. These agents typically consist of a high-molecular-weight gas core (such as perfluorocarbon or sulphur hexafluoride) encapsulated by a stabilising shell. Over the year, lipid-shelled formulations emerged as the predominant design due to their favourable biocompatibility, echogenicity, and ease of fabrication [59–62]. The lipid shell's main component is typically phospholipids such as DSPC, DPPC, or DPPE. These are often mixed with pegylated lipids and cholesterol, to improve shell packing structure and reduce immunoresponse [63, 64]. The lipids naturally self-assemble as a monolayer at the gas-liquid interface, providing mechanical stability whilst maintaining sufficient flexibility to oscillate under acoustic interrogation [59, 60].

The acoustic behaviour of lipid-shelled MBs underlies their efficacy as contrast agents. When insonified at diagnostic frequencies (typically 2 to 10 MHz), these compressible gas bodies

undergo volumetric oscillations that generate backscattered signals containing harmonic components, enabling nonlinear imaging techniques such as amplitude modulation, pulse inversion, and Doppler shifts to discriminate between bubble and tissue echoes. The oscillation dynamics are governed by the interplay of shell properties, bubble-bubble interactions, bubble-tissue interactions, and acoustic driving parameters. Unlike uncoated gas bubbles, lipid-shelled formulations exhibit highly nonlinear behaviour characterised by small amplitude oscillation, buckling, and rupture at elevated acoustic pressures [62, 65, 66]. These phenomena arise from the viscoelastic nature of the lipid monolayer, which resists expansion while offering minimal resistance to compression, resulting in asymmetric oscillations that enhance harmonic generation.

Table 1.1: Commercially available contrast agent for ultrasonic imaging

Trade name	**Shell material**	**Gas core**
Definity (Luminity)	Lipid	Octafluoropropane
Optison	Sonicated albumin	Octafluoropropane
Lumason (SonoVue)	Lipid	Sulfur hexafluoride
Sonazoid	Sucrose	Perfluorobutane

Commercial lipid-shelled MBs formulations have achieved widespread clinical adoption and continue to evolve. Table 1.1 reports the most extensively used agents, each with distinct shell composition, size distribution, and gas core composition. These agents have demonstrated utility across numerous clinical indications, including echocardiography for left ventricular opacification, characterisation of focal liver lesions, and assessment of microvascular perfusion in transplant organs. More recent regulatory approvals have expanded their use to

paediatric populations and novel applications such as vesicoureteral reflux detection, reflecting ongoing refinement of safety profiles and dosing protocols [67, 68].

Beyond conventional imaging, lipid-shelled MBs have emerged as versatile theranostic platforms. Molecular imaging strategies exploit surface conjugation ligands to achieve selective binding to disease specific markers [69–71]. This approach would enable non-invasive visualisation of conditions such as localised inflammation, angiogenesis, and thrombosis at molecular resolution, with several targeted formulations advancing towards clinical translation [72, 73]. The lipid shell also facilitates drug and gene delivery applications: therapeutic payloads can be incorporated within the shell, adsorbed onto the surface, or encapsulated in attached nanoparticles, with US triggered release achieving spatiotemporally controlled deposition at target sites [74, 75].

Lipid-shelled MBs are typically generated through mechanical agitation, sonication, or microfluidic techniques, each yielding distinct size distributions and shell characteristics [60, 61]. The choice of gaseous core profoundly influences stability: perfluorocarbons, due to their low solubility and diffusivity, substantially improve stability compared to air-filled bubbles, with circulation half-lives extending to several minutes [76, 77]. Cryogenic preservation and lyophilisation strategies have been developed to extend shelf-life, with many commercial products supplied as lyophilised powders requiring reconstitution before use.

Recent advances have focused on engineering next-generation lipid-shelled MBs with enhanced functionality. Multimodal contrast agents incorporating magnetic nanoparticles or fluorophores enable hybrid imaging with MRI or fluorescence modalities, facilitating preoperative planning and intraoperative guidance [78–80]. Acoustically sensitive droplets, or phase shifting contrast agents, represent an emerging platform, exploiting the vaporisation of low boiling perfluorocar-

bon nanodroplets to generate MBs *in situ* [81].

1.3.3 Therapeutic US applied to drug delivery

US is best known for its use in diagnostic medical imaging; however, in the past few decades, it has been increasingly proposed for therapeutic purposes, although at lower frequencies (ranging between 0.25 and 1.5 MHz). For example, high intensity focused US (HIFU) can be used to ablate small volumes of biological material (e.g., confined solid cancer or kidney stones) mechanically and/or thermally [82–85]. Typical parameters for these applications would range between 5 and 25 MPa peak pressure, with duty cycles exceeding 50% for thermal ablation while lower peak negative pressures and lower duty cycles (about 1 to 5 %) in hystotripsy applications.

At lower intensities, usually peak negative pressure below 5 MPa and relatively low duty cycle (0.1 to 5%), US can be used to promote permeabilization of the endothelium and improve the extravasation of drugs to desired tissue targets. One of the first applications in this direction was demonstrated by Fellinger and Schmid in 1954, who successfully demonstrated improved treatment for polyarthritis by using focused US to drive hydrocortisone ointment into inflamed tissues [86, 87]. There has also been substantial investigation on the use of US in cancer therapy, to achieve temporally and spatially targeted delivery of chemotherapy drugs into solid tumours [5, 88–90].

Another area of interest for therapeutic US is its use as an adjuvant for antimicrobial treatments. Several studies have reported a synergistic effect between low frequency US (20 to 120 kHz) and antimicrobial chemotherapy [91–93]. More recently, similar effects have been demonstrated

with low MHz-range US on planktonic bacterial cultures [94]. Notably, the "sonobactericidal" potential of US has also been recently demonstrated on *Staphylococcus aureus* biofilms [95–100], one of the most prevalent strains in wound and pulmonary infections.

As for US imaging, the effectiveness of therapeutic US can be enhanced with the addition of MBs or other cavitation nuclei, i.e. small particles that promote the formation of gas bubbles thanks to their physico-chemical propeties (*e.g.* perfluorocarbon nanodroplets, or talc microparticles) [59]. Regardless of the way gas bubbles are introduced in the sound field, when they are exposed to the oscillating pressure field, they contract and expand cyclically. Their behaviour is determined by many US parameters such as pressure amplitude, frequency, duty cycle, burst length [59]. Depending on their shell properties, bubbles show non-linear wall oscillation and buckling once exposed to US [65, 101]. Once a low enough pressure is reached during the rarefaction phase, the bubble shell becomes too unstable and the surface tension can no longer counterbalance the internal gas pressure causing the surrounding liquid to rush in and collapsing the bubble inertially. This generates a shock wave and - when in the vicinity of a hard boundary - a high-speed liquid jet [62, 102]. In this instance, the minimum pressure needed to determine the inertial collapse of a bubble is often defined as Blake threshold [103], although more refined models, accepting less restricting assumptions, have been suggested since the first definition of Blake threshold [104].

Whilst the effects of cavitation on mammalian cells have been extensively characterised [102, 105–108], the study of the biomechanical effects of cavitation on bacterial cells and biofilms is much less developed. It has been demonstrated that cavitation can disrupt the structural integrity of biofilms through a combination of physical effects, and that cavitation-induced mechanical forces can determine detachment of the biofilm from surfaces, making them more susceptible

to antibiotic treatment. Cavitation can also damage the protective EPS layer of the biofilm, favouring exposure of bacteria to antimicrobial agents [7, 8, 92, 109–111].

Although US is routinely used in dentistry practice [112, 113] for procedures such as plaque scaling, root planing, and irrigation, most instruments operate in the 20 to 70 kHz range and rely on the mechanical scraping of tooth surface and the cavitation of media in the immediate vicinity of the instrument's tip to achieve biofilm removal [34, 114–117]. Although it has been demonstrated that part of the cleaning effects of such procedures is due to cavitation, only in recent years researchers started exploring the possibility of utilising a focused US field to achieve spatially controlled biofilm/plaque debridement. To the best of our knowledge, the combination of HIFU treatment for dental procedure with exogenous cavitation nuclei has been virtually unexplored so far.

1.3.4 Biological effects of US on bacteria due to cavitation

Acoustic cavitation is known to affect microorganisms through mechanical, thermal and chemical effects. When bubbles form and then collapse during US rarefaction phases, the rapid acceleration of the bubble wall determines different phenomena such as inertial collapse (with shockwave front formation), liquid micro-jets (especially when in proximity of a hard boundary), and high shear forces determined both by the wall motion and by the acoustic streaming of the surrounding fluid [102, 118–122]. All of these mechanical effects have been reported to physically damage, weaken or tear the outer layer of cells and microorganisms [119, 123–128]. Moreover, during bubble collapse, the sudden reduction in gas core volume produces a dramatic temperature increase. The hot-spot temperature has been estimated through both theoret-

ical models and experimental measurements and is often reported to be in the 5000 to 20000 K range [66, 129, 130]. This phenomenon not only determines high level of thermal ablation *in situ* but, when sustained, also increases the bulk temperature of the surrounding media. At higher frequencies and duty cycles, US propagation dictates a significant bulk temperature increase also due to its viscous attenuation determined by the media.

The incredibly high temperatures and pressure at the centre point of a collapsing bubble, sometimes referred to as hot-spot, are also known to induce the generation of ROS, free radicals (*e.g.* $H\cdot$, $\cdot OH$, $N\cdot$) and subsequent oxidative species [123, 130–132]. It has been demonstrated that radicals generation is weakly correlated with the US frequency, with higher radicals concentrations reached at lower operating frequencies ($<$ 100 kHz) [123, 124, 131].

As thoroughly reviewed by M. Zupanc *et al.* [119], the combination of mechanical, thermal and chemical effects of ultrasonic cavitation have been demonstrated to affect the growth and viability of both G+ and G- bacteria. The effect is both bacterial strain and ultrasound parameters dependent. In general, the consensus seems to be that for the range of 20 to 500 kHz, higher frequencies (above 250 kHz) determine greater bacterial inactivation [133]. Mechanisms of bacterial inactivation are still largely under debate, although some published work [133, 134] has reported that after US treatment some of the dead bacteria presented cell wall damage, suggesting this as the main mechanism of action. In support of this theory, other works [127, 135–138] reported that G+ bacteria are generally more resistant to US therapy, probably due to their thicker and more rigid cell walls. Differences in sensitivity of strains within the same gram-staining group have been previously ascribed to variations in cross-linking level of the outer layer of the cell wall [126, 134]. The hydrophobicity of the bacterial outer layer also plays an important role on the effects of cavitating bubbles, as proximity is a crucial parameter

determining the biological effects of cavitation. Unlike unshelled bubbles, lipid-shelled bubbles are generally hydrophilic and for this reason tend to loosely attach to hydrophilic regions on bacterial and biofilm's surfaces (*e.g.* polysaccharides matrix) [119]. For the same reason, the use of positively charged MBs has been demonstrated to improve the cavitation effects on bacteria and biofilms having a negatively charged outer surface [110].

Chapter 2

Effects of US Mediated Treatments on Dental Biofilm Attachment and Viability

2.1 Abstract

Objective: Dental biofilms are responsible for the majority of oral cavity diseases (e.g. cavities, periodontitis, gingivitis). In this work we explore the effects of therapeutic US on a *Streptococcus mutans* biofilm model. This is the first work in a larger project aimed at evaluating if therapeutic US could be implemented in the standard practice for the prevention and treatment of oral infections.

Methods: *Streptococcus mutans* biofilms were grown on a tooth-mimicking substrate and subsequently exposed to CHX (CHX) and therapeutic US treatments. We examined the effects of low duty cycle (1 %) 0.5 MHz US treatment at varying pnps (0.75-3.00 MPa) and CHX concentrations (0.025, 0.050, and 0.100 % w/V).

Results: US treatment was effective at removing biofilm, particularly at pnps exceeding 2.25 MPa and in the presence of lipid-coated microbubbles as cavitation nuclei. US also improved

the bactericidal action of low-concentration CHX (0.050 % w/V).

Conclusions: We demonstrated that low duty cycle therapeutic US treatment can be used for the mechanical removal of a fully formed and mechanically sound *Streptococcus* biofilm model. Although the US treatment in itself did not reduce the viability of the bacteria, its combination with low concentrations of CHX marginally improved the antimicrobial treatment outcomes.

Keywords: Biofilms, Therapeutic US, Dental Hygiene, Antimicrobial Treatment, *Streptococcus mutans*, AMR, Biofilm removal, Microbubbles, Cavitation

2.2 Brief introduction

Biofilms are complex communities composed of microorganisms (e.g. bacteria, yeasts, algae) living together in aggregates. These structures are of great relevance in many fields such as biofouling, contamination of industrial apparatus, water cleaning systems, agriculture, and human infections. It has been estimated that 65% of human infections are characterised by biofilms rather than bacteria in planktonic form [2]. Biofilm aggregates can be either surface attached or free floating. The physical characteristics of biofilms and their survival mechanisms, such as phenotypic adaptability and genetic resistance, render them highly resistant to antibiotic treatments. As a result, biofilm infections present significant challenges in both medicine and dentistry, contributing to many chronic conditions. Some of the most prevalent biofilm-associated pathologies include native valve endocarditis, otitis media, caries, secondary infections in cystic fibrosis, and periodontitis [2].

2.2.1 Rationale for the study

The use of therapeutic US to improve antimicrobial treatment efficacy in biofilm-related infections has recently received increased attention. Although the mechanisms underlying the synergy between antimicrobial and ultrasonic treatments are still not completely clear, it has been demonstrated that US can enhance the effectiveness of antimicrobial drugs in wound, pulmonary and urinary tract infection models [6, 91, 92, 139, 140]. Ultrasonic scalers (20 to 70 kHz, unfocused field) are the gold standard for removing calcified biofilm (also known as tartar) in dentistry [141]. Similarly, low frequency ultrasonic cleaning is an industry standard for food and equipment surface cleaning [131, 142]. In contrast, data on the use of focused therapeutic US for oral biofilm removal are scarce. Previous research has been carried out to evaluate whether the US wave frequency impacts on the efficacy of US and gentamicin combined, against *Pseudomonas aeruginosa* biofilms grown on a polyethylene substrate [143]. The US frequencies evaluated were 70 kHz, 500 kHz, 2.25 MHz, and 10 MHz. It was found that the antimicrobial effects of gentamicin were significantly enhanced in the presence of US, with lower-frequency US being more effective than higher-frequency. The biofilm employed and the acoustic characteristics of the substrate, however, do not recapitulate those of a dental biofilm. Rux and co-authors demonstrated that low-frequency US (35 kHz) is effective at removing bacteria from biofilms established on bovine enamel slabs [144]. They however did not evaluate higher US frequencies nor their combination with US-responsive agents. Zhu et al. instead utilised higher-frequency US (1 MHz) in combination with plasma-loaded MBs and evaluated its effects on *Enterococcus faecalis* biofilms grown on human tooth disks [145]. Although their approach achieved significant antibacterial and antibiofilm effects, the generation of plasma-

loaded MBs may present translational challenges in dental applications.

It should also be noted that these earlier studies did not provide a quantitative correlation between antibiofilm/antimicrobial effects of US and the magnitude of US-induced cavitation at the site of a dental biofilm. Establishing such a correlation would contribute towards further optimisation and standardisation of US-based treatments against dental biofilms in the future. Building upon these previous observations, the aim of this study was to define if and under which conditions focused US treatment could be used to promote biofilm detachment from a substrate, as ultrasonic cavitation at higher frequencies (i.e., 500 kHz) has been previously reported to interact with biological tissues and biofilms in other settings [115]. Notably, increasing the frequency of the US field and focusing it spatially, may result in improved spatial resolution of treatment when compared to low-frequency US. However, it would also determine an increase in the pnp needed to activate endogenous cavitation nuclei. For this reason, we also evaluated whether the addition of lipid-shell gas MBs (acting as exogenous cavitation nuclei) would improve the anti-biofilm performance of the treatment. US induced cavitation at the treatment site was also quantified throughout this study, to evaluate whether cavitation dose impacts on antibiofilm treatment outcomes. Moreover, lipid-shelled gas MBs were employed as a more clinically applicable formulation compared to other custom-developed cavitation nuclei. In summary, we assessed the effect of higher frequency focused US (in the presence and absence of MBs) combined with an established antimicrobial compound (CHX), on an in-vitro oral biofilm model.

2.2.2 Preliminary work

Prior to the main experiments, a series of preliminary studies was carried out to optimise the biofilm growth protocol, define the experimental parameters, and develop a reproducible US treatment configuration.

The first stage focused on establishing the appropriate growth time for the *S. mutans* biofilm. Initial experiments employed a standard 24 hour growth period, however, given the sucrose enriched media *S. mutans* formed very quickly an EPS enchased structure, determining bacterial death in the deeper layers of the biofilm. This resulted in a high baseline PI fluorescence signal, reducing the dynamic range available to detect treatment induced antimicrobial effects. To minimise bacterial death in control groups, the biofilm growth duration was progressively reduced. The earliest end point when the biofilm showed full coverage of the substrate and thick EPS deposition, while maintaining low PI signal was at the 18 hours mark. For this reason it was selected as growth period for the whole work.

Optimisation of bacterial adhesion to the hydroxyapatite substrates was also required. Preliminary experiments demonstrated inconsistent attachment of *S. mutans* to untreated discs, leading to high variability in the amount of biofilm formed. Although not recommended by the substrate manufacturer, the substrates were briefly treated with a rat tail type I collagen solution, to coat their surface and improve bacterial adhesion, since one of the main adhesion molecular cues for *S. mutans* is collagen. The collagen coating resulted in reproducible and homogeneous substrate coverage and was therefore incorporated into the final growth protocol.

Colony forming unit (CFU) count was initially considered as bacterial viability assay but reliable recovery of bacteria from the hydroxyapatite discs proved challenging. Mechanical scrap-

ing and pipetting failed to detach and disaggregate the remaining biofilm completely. Sufficient dispersion was achievable only through prolonged exposure to a 20 kHz ultrasonic bath. Since ultrasound itself was the experimental variable under investigation, this additional ultrasonic exposure would have introduced a significant confounding factor by potentially altering bacterial viability before plating. For this reason, although not generally accepted as the gold standard technique, quantitative fluorescence staining using the LIVE/DEAD™ biofilm viability assay was selected as the sole method for assessing biofilm viability throughout this work.

The experimental US system was also developed during the preliminary phase with the objective of maximising repeatability while minimising manual labour during the experiments. The sample holder, coupling cone, and positioning inserts were designed so that individual samples could be exchanged rapidly without requiring realignment of the transducer or changes to the acoustic configuration. This approach ensured consistent sample positioning at the acoustic focus throughout the study without the need for repeated manual realignment. The location of the ultrasound focus within the complete set-up was determined experimentally using hydrophone measurements prior to the experiments and was subsequently considered fixed, as the set-up contained no moving parts.

The operating frequency of the focused US transducer was selected following consideration of both the acoustic field geometry and the dimensions of the hydroxyapatite substrate. A frequency of 500 kHz generated a focal region with a FWHM diameter comparable to the 12 mm disc diameter, allowing most of the biofilm surface to be exposed to therapeutically relevant acoustic pressures. At the same time, the rectangular cut-out geometry of the transducer produced peripheral lower-intensity regions within the acoustic field. This characteristic pressure field shape consistently left a proportion of the biofilm attached to the substrate after treatment,

enabling quantitative assessment of both biofilm removal and bacterial viability across a wide range of treatment conditions.

2.3 Materials and Methods

2.3.1 Materials

All the 3D printed parts were manufactured using either a Formlab Form2 stereolithography (SLA) printer with Formlab grey resin (Formlabs, GmbH, 12459 Berlin, Germany) or an Ultimaker S5 FDM printer with Ultimaker tough polylactic acid (PLA) (Ultimaker B.V., 4191 PN Geldermalsen, Netherlands). Computer aided design (CAD) models were produced using Autodesk Inventor Professional 2024™ (Autodesk, San Francisco, CA 94105, USA). Data processing was performed either in MATLAB 2023b (The MathWorks Inc., Natick, Massachusetts, USA) or Python (version 3.9.13). The complete scripts are provided in the Supplementary Material section.

2.3.2 Biofilm growth protocol

S. mutans from carious dentine isolate was acquired from ATCC (ATC-25175, strain NCTC 10449 [IFO 13955], LGC Standards – UK Office, Middlesex, TW11 0LY, UK). The bacteria were suspended in bovine brain heart infusion (BHI) medium (Bacto™ Brain Heart Infusion, Gibco™ , Appleton Woods Limited, Birmingham, UK) and conserved at -70 °C. To start the culture, 10 μL of the frozen stock were spread over a BHI agar plate and grown for 24 to 48 hrs at 37 °C, 5% CO_2, and 95% humidity. A single colony was then selected from the plate, transferred

to 10 mL of BHI, and grown for 24 hrs in the same conditions. A new culture was freshly started before every experiment. The hydroxyapatite (HA) discs (12 mm in diameter , 2.3 mm thick, HADEL02, Himed, NY 11804, USA) were placed in 24 well-plates (model 83.3922.500, flat bottom for suspension cell, Sarstedt, 51588 Nümbrecht, Germany) and treated with 150 μg/mL rat tail type I collagen solution (Gibco™ , Appleton Woods Limited, Birmingham, UK) for 1 hour, to facilitate bacterial attachment and biofilm formation. The discs were then gently rinsed with Dulbecco's phosphate buffer saline [no Ca_{2+}, no Mg_{2+}] (DPBS). The liquid *S. mutans* suspension was diluted to 0.01 optical density (OD) at 600 nm ($\sim$1:50 dilution) using BHI + 75 mM HEPES + 3% sucrose (Sigma Aldrich, Haverhill, UK). 1 mL of the diluted suspension was then gently pipetted in each well containing the collagen-treated HA discs. The biofilm was allowed to grow for 18 hrs at 37 °C, 5% CO_2, and 95% humidity under static conditions.

2.3.3 Design of the US set-up

An experimental set-up was designed to enable reproducible exposure of the samples to US and/or antimicrobial compounds (figure 2.1 A-D). The US transducer utilised was a Sonic Concepts H107 (0.5 MHz fundamental frequency, 63.2 mm geometrical focus, 64 mm active element diameter, custom rectangular cut out of 22×57 mm, Sonic Concepts Inc., Washington, USA). A custom coupling cone was designed and manufactured in house. The cone could be easily filled with propagation media (deionised degassed water) from its top aperture. The use of a cone mounted on the transducer, as shown in figure 2.1, allows appropriate sound propagation to the sample, without the need to submerge the whole experimental set-up in a water bath. A 3D printed fitting was designed to hold a 35 mm diameter μ-dish (low profile dish,

Ibidi GmbH, 82166 Gräfelfing, Germany) at the appropriate distance from the transducer. A 3D printed sample holder was also designed to fit inside the μ-dish, in order to maintain the sample centred and at a distance of 2 mm from the bottom of the dish; in this way, the sample could be placed exactly at the focus of the US field.

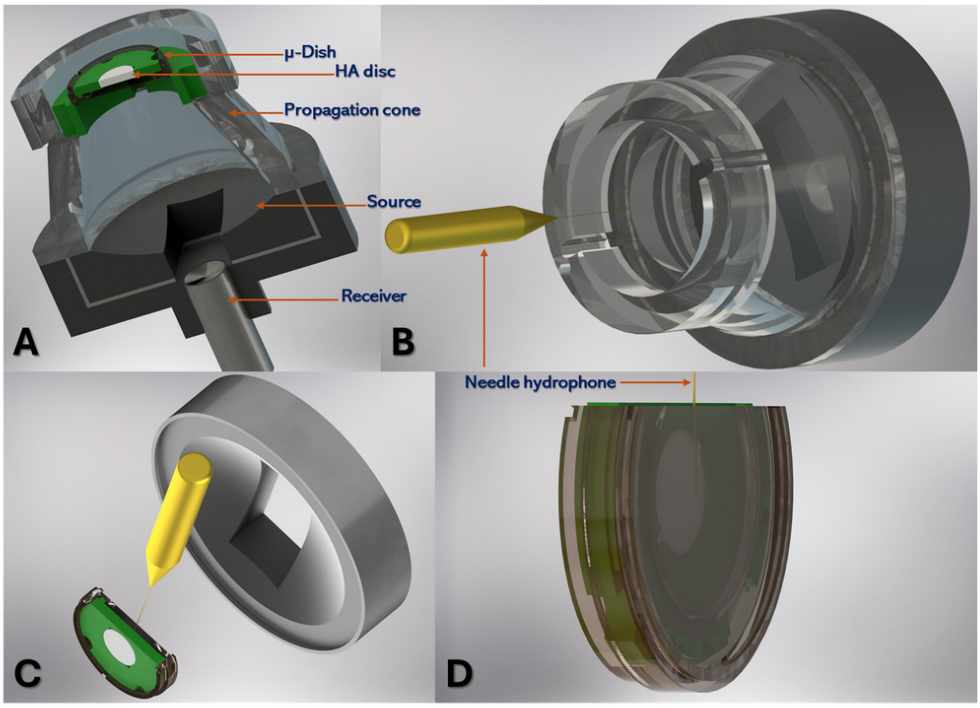


Figure 2.1: Graphical representation of the experimental set-up and of the experimental US field measurement configuration. (A) Components of the set-up. A 0.5 MHz focused transducer was positioned at the bottom of the set-up and kept in place thanks to a tailored plastic holder. The same holder allowed for the insertion of a 12.7 mm immersion transducer, which was used as a passive receiver during experiments. A propagation cone was mounted on top of the plastic holder. The propagation cone served two purposes: 1- it could be filled with the sound propagation media (DI water in these experiments), 2- it fitted a 3D printed plastic holder that allowed for reliable positioning of an Ibidi μ-dish at the focus of the US field. A small 3D printed holder is positioned inside the μ-dish, allowing for reliable positioning of the HA disc specimen at the focus of the US field. (B) Representation of how the free field, focal pressure experimental measurements were taken. In this schematic, the hydrophone is positioned axially to the propagation of the US field. (C) Representation of how the experimental measurements of the US field were obtained inside the μ-dish and with the HA disc at focal distance. (D) A zoomed-in view of panel C, showing how the needle hydrophone was positioned in proximity of the HA disc surface. It should be noted that any exogenous bubble was carefully removed from the system using a pipette filled with degassed water. The system was also positioned in such a way that bubbles tended to float and exit due to their buoyancy.

2.3.4 Characterization of the US set-up

The US field within the designed experimental set-up was subsequently characterized. The acoustic pressure measurements were carried out using a NH0200 needle hydrophone (Precision Acoustics Ltd, Dorset DT2 8QH, United Kingdom). The directivity of the hydrophone at 0.5 MHz was estimated through experimental measurements in underwater free field. The hydrophone was calibrated by running a pressure ramp in the orientation axial to the sound propagation (0° position) and comparing the output to a pre-calibrate secondary hydrophone, used as a standard. The NH0200 hydrophone was then rotated orthogonally to the sound propagation path (90° position) and used to record the same pressure ramp. The effect of directivity on the hydrophone sensitivity was deemed to be within the accuracy limit stated by the manufacturer (9% accuracy at 0.5 MHz) and, for this reason, insignificant. From these measurements, the hydrophone sensitivity was estimated to be 23 mV/MPa. The position of the hydrophone within the tank was controlled robotically by a three-axis Cartesian positioning system (PRO-115, Aerotech, Hampshire, U.K.). A focal pressure calibration was performed in free field (experimental set-up configuration shown in figure 2.1-B) using the needle both in axial and orthogonal orientation in respect to the US propagation path. The HIFU transducer was driven at its fundamental frequency with 15 cycles bursts at increasing voltage amplitudes. The hydrophone's output signal was then denoised, and processed to extract the average peak negative and peak positive amplitudes. The average peak positive and peak negative amplitudes values from the hydrophone were then plotted against the average peak positive and peak negative amplitudes of the driving signal and used to obtain a linear model of the relationship. The linear model R^2 value was > 0.99, confirming that sound propagation non-linearities shouldn't be

expected in the tested pressure range. Once the transducer focal pressure output in free field was established, we characterized the focal pressure generated in the setup when the substrates were positioned at the geometrical focus of the sound field. To evaluate the magnitude of the pressure field in the experimental set-up during treatment, we first ran a first-order k-space pseudospectral method US field simulation, using the MATLAB k-Wave toolbox (Version 1.4). The simulated pressure field in the device was used as a qualitative guide, to inform where the experimental measurements should be taken. Additional details about the simulation parameters and results are reported in section 2.5.1. We then proceeded to experimentally evaluate the US field pressure magnitude in the set-up. The μ-dish was positioned at the focus of the HIFU transducer and a portion of the dish was cut off to allow for the insertion of the needle hydrophone (the set-up configuration is shown in figure 2.1-C,D). The hydrophone was then positioned at the expected focus, and a scan axial to the sound propagation was performed to evaluate the pressure profile between the HA disc surface and the bottom of the μ-dish (see figure 2.3 in the relevant Results section). Having found a pressure maximum in proximity of the HA disc, determined by standing wave interference, we positioned the hydrophone at such maximum and obtained a 2D scan of the US field orthogonal to the sound propagation. We compared this to a corresponding 2D scan in free field, to evaluate potential US field deformation due to misalignment and/or the establishment of standing waves in the set-up (see figure 2.3 and the relevant Results section).

2.3.5 Passive Cavitation Detection signal analysis

PCD is a method that involves recording the sound emitted from a cavitating sample, and processing it to evaluate its magnitude and spectral content. For each US burst emitted from the HIFU (5 Hz burst repetition frequency in all the experiments performed in this work), one radio frequency (RF) dataset was recorded from the PCD receiver (Olympus V320) to capture the sound coming from the sample. The electrical signal generated from the receiver was first filtered using a coaxial high-pass electrical filter (EF509, ThorLabs LTD., Ely, UK), to remove the fundamental frequency reflected from the sample and the third harmonics, since these frequencies have much higher amplitudes than subsequent harmonics in the signal and are irrelevant for spectral analysis. The filtered signal's amplitude was then amplified 125 times using a low noise preamplifier (model SR445A, Stanford Research systems, Sunnyvale, CA, USA), digitised using a digital oscilloscope (Handyscope HS6, TiePie engineering, Sneek, Netherlands) and recorded using TiePie Multichannel software (TiePie engineering, Sneek, Netherlands). The acoustic emissions data were then processed to evaluate their frequency content as well as the total cavitation energy generated during treatment, using a MATLAB script available in the Supplementary Material section. Briefly, the script performs a Welch transform on each RF file. The resulting power spectral density (PSD) plot represents the amplitude of the frequencies composing the electrical signal generated by the receiver. The PSD plots obtained from all the RF signals recorded during one experiment (for a 1-minute-long experiment, at 5 Hz burst repetition frequency, this amounts to 300 PSD plots) are then collected and shown as a colormap, with power spectral density [W / f, 10 kHz frequency resolution] on the ordinate, experiment time on the abscissa, and amplitude of the signal in colour scale. The frequency domain PSD

plots can then be further processed to extrapolate total energy of the signal during the experiments, as well as the portion of the signal energy corresponding to harmonics, ultra-harmonics and broadband. The spectral content of the signal can be used to infer the main cavitation modality: "inertial" collapse of bubbles determines shockwaves and so high broadband in the signal, whereas "stable" cavitation, in which the bubbles oscillate without collapsing, is characterized by high amplitude harmonics and ultra-harmonics. Since for each experiment the PCD set-up was identical, comparison of cavitation activity between different treatments is possible, by comparing directly the signal power and/or energy. It should be noted that the power and derived energy computed in this way are relative to the electrical signal generated by the receiver, and not to the mechanical power exerted by the cavitating bubbles.

2.3.6 MBs manufacturing

The MBs dispersion was manufactured as follows: DSPC and polyethylene-glycol-40-stearate (PEG-40-S) were dissolved in chloroform to a 9:1 molar ratio in a 7 mL glass vial. The chloroform solution was then evaporated using a centrifuge concentrator (Concentrator plus, Eppendorf UK Limited, Stevenage, SG1 2FP, UK), allowing the formation of a dry lipid film at the bottom of the vial. The lipid film was then rehydrated and dispersed in a 8:1:1 (volume ratio) solution of DPBS [no Ca^{2+}, no Mg^{2+}] : propylene-glycol : glycerol (Merck Life Science UK Limited, Dorset, UK), under constant shaking (600 rpm) for 60 minutes at 80 °C using a thermos-mix bath (DLAB HCM100-Pro, DLAB SCIENTIFIC CO. LTD., Beijing 101318, China) to a final lipid concentration of 1 mg/mL. The suspension was then divided in 1 mL aliquots using gas-tight 2 mL glass vials (VIA1120, Scientific Laboratory Supplies Ltd, Not-

tingham, NG11 2AF, UK) and stored at 4 °C for up to two weeks. The lipid shell composition was the same for all experiments (9:1 molar ratio of DSPC and PEG-40-S), as the study did not focus on evaluating specific formulation-dependent MBs/biofilm interactions. Perfluoro-butane (PFB) was chosen for the gas core, as it improves MB stability compared to air [132, 146]. On each day of experiments, 1 vial of lipid suspension was gently rolled for 60 minutes at 4 °C using a STUART SRT6 tube roller mixer (BioCote, Coventry, UK), to ensure homogeneous dispersion following the storage period. The vial was then placed in an ice bath and the air in the head space was removed using a vacuum pump, and replaced with PFB using a 20 mL syringe (Fisher Scientific, Loughborough, UK). This process was repeated 5 times, to ensure complete gas exchange. The vial was then loaded into a tissue homogenizer (Precellys Evolution Touch Homogenizer, Bertin Technologies SAS, 78 180 Montigny-le-Bretonneux, FRANCE), and shaken at 10000 rpm for 45 seconds. The generated MB dispersion was then loaded into a syringe and centrifuged at 300 g for 5 minutes. The subnatant was discarded and the remaining MBs cake was re-dispersed to a final volume of 1 mL in 8:1:1 DPBS:propylene-glycol:glycerol. The MBs were then stored at 4 °C under gentle rolling until use (within 4 hours from manufacturing). Before the start of the experiments, the MBs were sized using a Multisizer 4e (Beckman Coulter, HP11 1JU, UK) and their initial concentration was estimated using a Coulter counter. The MBs had a mean equivalent spherical diameter of 0.85 μm ± 0.08 μm and were diluted to a concentration of 100 million MBs per 1 mL (1e8 MBs /mL), just before use.

2.3.7 CHX and US treatments protocols

A graphical overview of the treatment protocol is presented in figure 2.2. All the biofilm samples were exposed to CHX following the same protocol. A fresh stock of CHX was prepared the day of the experiment and kept in the dark. A stock solution of 20% w/V of CHX was sterilised by passing it through a 0.200 µm syringe filter (Fisher Scientific, Loughborough, UK) and was diluted using sterile DI water to a final concentration of 0.100, 0.050 or 0.025% w/V. The biofilm samples were treated by submerging them in 1 ml of the antimicrobial solution for 4 minutes, within a 24 well plate. For experiments involving US treatment, the samples were exposed to US as described above, in the absence of CHX. Immediately after US treatment, the samples were transferred to a 24 well plate and submerged in the antimicrobial solution (i.e., an interval of ∼30 to 45 seconds occurred between the end of US treatment and the start of antimicrobial treatment). Immediately after exposure to CHX, samples were rinsed with sterile DPBS and were kept submerged in DPBS until staining. The US parameters for this study were selected based on preliminary tests (data not shown). The choice of 0.5 MHz as the driving frequency was mainly due to the relationship between US frequency and focal zone dimensions. Focusing US at 0.5 MHz determines a high intensity region of ∼12 mm diameter (including the side lobes of the field), which was adequate for treating the HA disc selected as biofilm substrate. Focusing the US and increasing the working frequency may improve the spatial resolution of treatment, when compared to classical 20 to 70 kHz scaling treatments, possibly reducing side-effects (e.g. eradication of healthy biofilm population or damage to surrounding tissues). The samples were exposed to US with a pnp between 0.75 and 3.00 MPa (in most experiments 0.75, 2.25 and 3.00 MPa). For all experiments, the burst signal parameters

were fixed at: 1000 cycles burst and 5 Hz PRF (which corresponds to a 1% duty cycle (DC)). The choice of such a low DC was made to prevent heating of the sample during treatment. The treatment time was fixed at 1 minute, which is comparable to daily tooth brushing. During each experiment, acoustic emissions from the sample were recorded passively using a broadband immersion transducer (Olympus V320) with 7.5 MHz fundamental frequency and 12.7 mm active element diameter (Evident Europe GmbH – UK Branch, Stansted, UK). This method is known as passive cavitation detection (PCD) and is described in detail above.

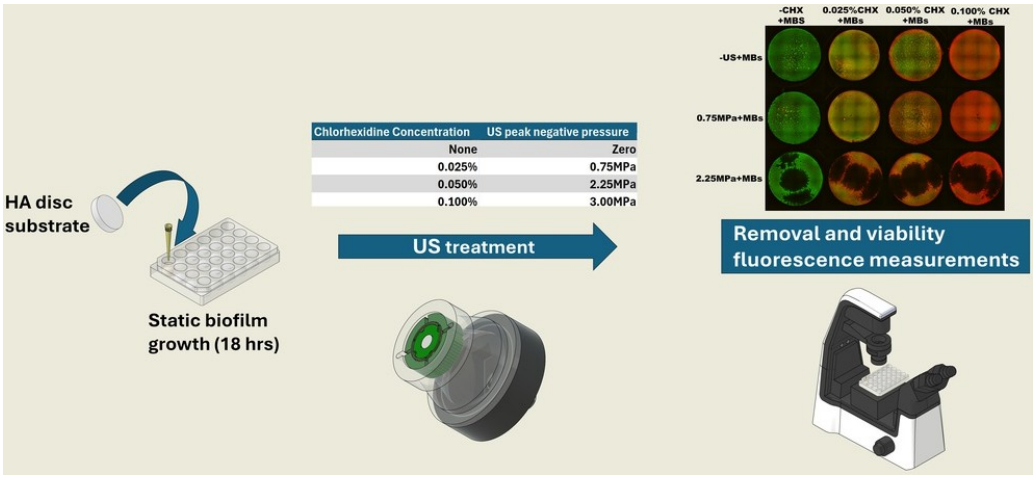


Figure 2.2: The biofilm samples were grown for 18 hours in 24 well-plates. Once biofilms were fully established, samples were transferred in to the US set-up and exposed to either US treatment (with or without MBs), antimicrobial treatment (CHX), or a combination of both. The samples were then stained and analysed using fluorescence microscopy to determine biofilm removal and viability variation caused by the treatment.

2.3.8 Bacteria dual staining protocol for fluorescence microscopy

To assess treatment effectiveness, the biofilm samples were stained using a commercial dual staining kit (Filmtracer™ LIVE/DEAD™ Biofilm Viability Kit, Fisher Scientific - UK Ltd,

Loughborough, United Kingdom) [147]. Syto9™ is a DNA binding molecule that stains both live and dead cells. PI is also a DNA binding molecule, but its molecular structure (strongly ionic) prevents it from crossing the biological barriers of live bacteria. For this reason, PI stains only dead/compromised bacteria. The staining process followed the manufacturer's instructions: 3 μL of each stock dye solution were diluted in 1 mL of sterile DPBS. The HA discs, placed in a 24 well plate, were completely submerged using 500 μL of staining solution. The dyes were allowed to interact with the sample for 20 minutes in the dark. After 20 minutes, the discs were gently rinsed with DPBS and placed in a new 24 well plate, facing downward, for subsequent imaging. Imaging was performed using a Nikon Eclipse Ti2 inverted microscope, coupled with a Nikon D-LEDI light source, a Nikon digital sight 10 camera, and a CFI Plan Fluor 4× objective (Nikon Instruments Inc., Melville, NY, U.S.A.). Each fluorescence image of stained biofilm attached to HA discs had a resolution of 9156×9156 pixels (pixel size: 1.48 μm) and was obtained by acquiring 16 pictures (4×4 layout) that were then stitched together using Nikon's proprietary software (NIS-Elements). The a blend stitching method (Nikon's proprietary algorithm not disclosed) was employed, with 25% overlap. The obtained .TIFF images were then processed as described below.

2.3.9 Image analysis

Dual fluorescent staining (PI and syto9™) was used in this work with two intents: 1- evaluating the area of the disc still covered by biofilm after ultrasonic treatment, and 2- evaluating bacterial death in the biofilm by comparing the fluorescence intensity of PI and syto9™ in the samples (compared to controls). All the images were acquired as described above and then processed

using the Python script shared in the Supplementary Material section. The script runs through the two channels associated with each image, and can be divided into two main sections:

1- Channel binarization:

The script prompts the user to select the area of interest (the HA disc) and proceeds to ignore the outer region of the image. The image is then slightly blurred with a gaussian filter to remove speckle noise, and the contrast is enhanced using the CLAHE algorithm. CLAHE is a well established local contrast enhancing technique that works by dividing the image in tiles and applying histogram equalization to each region independently. Neighbouring tiles are then interpolated to avoid boundary artefacts. The contrast enhanced image is then binarized using an adaptive threshold algorithm (explicitly defined in a local function and available to the reader). The adapting threshold algorithm works by integrating the pixel intensity over a kernel area and comparing it to the local average of neighbouring kernels. The threshold level is tweaked by applying average adjustment proportional to the image maximum intensity. The resulting binary image is used to define the area of the disc not covered by biofilm (defined as area of removal). Further details on area of removal calculation are reported in the Supplementary Material. Syto9™ stains both live and dead bacteria, for this reason the area of removal values reported in this work were computed using the syto9™ fluorescence channel, rather than PI.

2- Channel mean pixel intensity:

Once the binarized image was obtained, as described above, it was used as a mask on the original image. In this way, all the white pixels in the binarized image corresponded to 12-bit grayscale pixels in the masked image, and the remaining pixels were set to zero. Using the masked image, the mean fluorescence intensity (MFI) for the channel is computed as follows: MFI = (sum of the intensity of all pixels in the image)/(number of non-zero pixels). The MFI

was computed in this way to account for the fact that the area covered by biofilm varied greatly at different treatment conditions. Once the mean fluorescence intensity was computed for both channels, the mean fluorescence intensity ratio of PI and syto9™ was computed. This value was employed as a measure of bacterial death in the biofilm.

2.3.10 Statistical analysis

Both biofilm removal and PI/syto9™ ratio data were acquired in separate days to cover all the experimental conditions, due to time restrictions. Given the inevitable biological variability in biofilm growth between experiments carried out on different days, the data were acquired and analysed as follows: on each day and for every condition, three biological replicates were grown for a total of 24 samples. On each day two control groups were grown: DPBS only (true negative) and DI water or MBs (not exposed to US), depending on the treatment conditions used on that day. When CHX+US treatments were performed, a CHX-only treatment at the same concentration was also performed as a positive control. Given the high reproducibility of the analysis methods compared to the biological variability, no technical replicates were performed and each biological replicate contributed a single value to the statistical analysis. The data were then normalised to the same day DPBS control, and significance in the difference between their mean values was evaluated either by performing one-way ANOVA, with the p-value derived from the F-statistic, or using a generalised linear model (GLM). The specific method used is stated in the corresponding discussion section and figure caption. Further information on the GLM is reported in the section 5.0.3, listing 4.

2.4 Results

2.4.1 Sound field characterization

Determining the acoustic field properties of the experimental set-up was essential to define the experimental treatment conditions to which each biofilm sample was exposed. A schematic of the set-up and of the US field characterization approach are presented in figure 2.1 and figure 2.3. The presence of a hard boundary normal to the sound propagation (the HA disc), determines a reflection of the sound wave, with formation of standing waves interference. We first simulated the expected pressure field in k-Wave, as described in section 2.5.1, and used the modelled pressure field as a qualitative guide to inform us where we should expect variations in the pressure field. The experimental results shown in figure 2.3 A, confirm the presence of a high-negative pressure region at $\sim$1 mm from the disc surface. Due to physical impediment, the hydrophone couldn't be positioned closer than $\sim$0.5 mm from the disc surface. A 2D pressure field normal to the direction of sound propagation was recorded at this maximum, and is shown in figure 2.3 B. Following these measurements, it was estimated that the standing wave pattern caused a $\sim$54% increase in pnp magnitude compared to the free field. Constructive interference in standing waves is important in therapeutic US applications, as it can favour cavitation in the vicinity of a target substrate. It should be noted that all pressure values reported in this article refer to the pnp recorded in this high-magnitude region at $\sim$1 mm away from the disc surface.

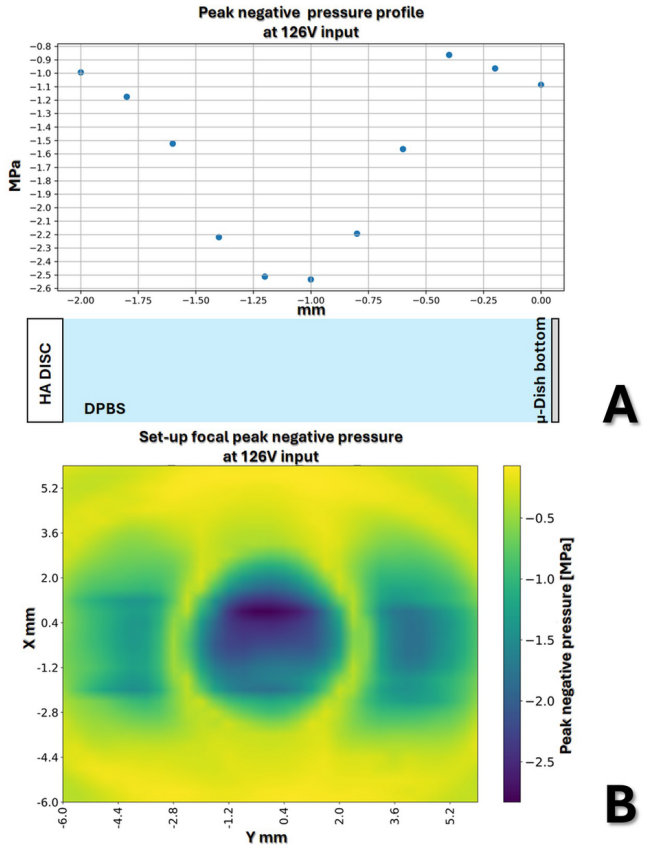


Figure 2.3: (A) Axial pressure profile at constant peak-to-peak input (126 V) inside the μ-dish, as represented in the schematic just below the scatterplot. These measurements were obtained as shown in figure 2.1-C, D. The hydrophone was moved axially to the US propagation direction, from the bottom of the μ-dish (0,00 mm) to the surface of the HA disc (-2.00 mm). As shown in the scatterplot, the sound field was not homogeneous, and there was a clear pnp minimum at $\sim$-1.00 mm. (B) 2D pressure field map, recorded at the -1.00 mm position. Although there was a clear standing wave effect, generating alternating minimum and maximum pnp zones, since the sound wave impacted the specimen orthogonally, there was no appreciable distortion of the sound field distribution compared to the free field measurements.

2.4.2 Effect of US on biofilm detachment

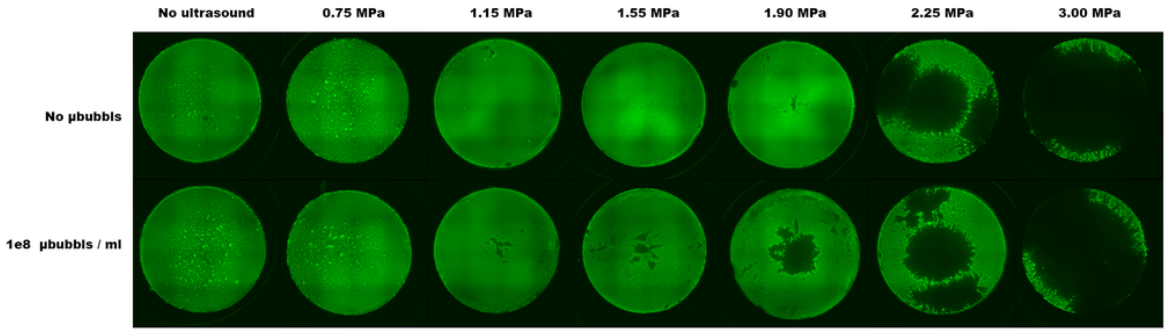


Figure 2.4: Representative images of bacteria still attached to the HA disc surface after ultrasonic treatment. The images show syto9™ stained bacteria (both live and dead bacteria are stained) on a HA disc substrate (12 mm diameter). The top row represents discs treated in the absence of MBs, whereas the bottom row samples were treated in a suspension of MBs (1e8 MBs/mL). As clearly visible, biofilm removal becomes greater as the pnp is increased. Initially, bacteria detach only from the focus of the US field, but as the pressure increases the removal becomes more diffused. [The brightness of these images was enhanced for readability purposes, and the checker-pattern in the images is due to the stitching algorithm].

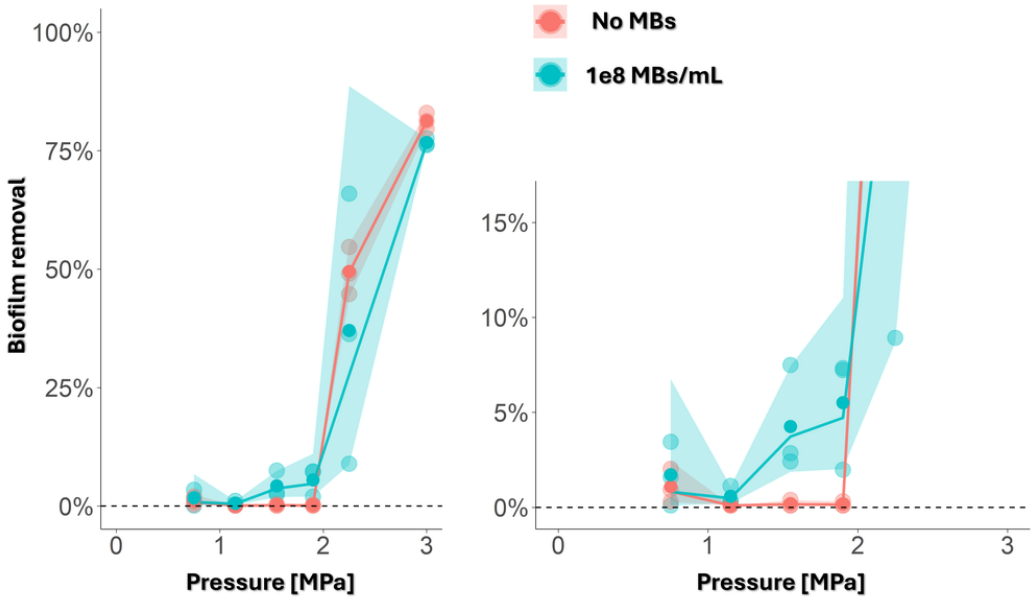


Figure 2.5: Area of removal analysis (portion of disc area cleared from biofilm). The data are fitted to a GLM. The mean GLM values are shown as solid lines, whereas the shadowed regions are the 95% confidence intervals. The rightmost plot is a magnified view of the samples treated at lower pressures for improved readability. Interestingly, a significant difference in biofilm removal can be appreciated at 1.55 and 1.90 MPa pnp. At higher pressures, the biofilm removal does not change with statistical significance when the treatment is delivered in presence of absence of MBs. n=3 (biological) for all groups.

Figure 2.4 shows some representative images of the US treatment's removal effect on the biofilm model and the plot in figure 2.5 shows the corresponding biofilm removal data. In every set of experiments, two control groups were evaluated. One group was completely untreated (neither MBs nor US) and was only moved between dishes containing DPBS. The other control group was exposed to a dispersion of MBs only (without US). As shown in figures 2.4 and 2.5, exposure to MBs alone did not affect the area of the HA disc covered by biofilm compared to the untreated samples. The groups treated with US only, at pnps between 0.75 and 1.90 MPa,

did not show any significant removal of biofilm compared to controls as shown in figure 2.8 and Supplementary figure 2.14. A small dip in biofilm removal is observed at approximately 1.25 MPa pnp; however, this observation is attributed to variability in biofilm growth in control samples and in samples with very little or no biofilm removal. Interestingly, a sharp increase in biofilm removal was observed at $\sim$2.25 MPa pnp. We hypothesize that the rough surfaces of the biofilm and HA disc could favour entrapment of air, and thus act as nucleation sites for cavitation when a sufficient pnp is applied. For this reason, even in the absence of MBs, at pnp focal pressure magnitudes of 2.25 MPa or higher, the cavitation activity in the samples spiked drastically. In the presence of cavitation nuclei (MBs), the biofilm removal increased gradually as the pnp at the focus was increased. For focal pressures of 1.55 MPa pnp or higher, the removal was significantly increased when compared to controls (p-value$<$0.001, figure 2.14). Interestingly, at 1.55 and 1.90 MPa pnp, the biofilm removal was significantly increased in the presence of MBs, when compared to the same samples treated in the absence of cavitation nuclei. Some representative images are shown in figure 2.4, highlighting the removal's pattern at increasing focal pressure levels. Differences in the orientation of biofilm removal patterns in the microscopy images are due to the manual manipulation of the discs; hence, disc positioning on the microscope stage varied across experiments, determining differences in apparent treatment angle. Since the US field is not rotationally symmetric, a spatial reference could be introduced on the samples in the future to achieve consistent spatial positioning during imaging. An estimate of the cavitation energy during each experiment was computed from PSD data. Six representative PSD plots are shown in figure 2.6. At lower pressure (0.75 MPa pnp) and in the absence of cavitation nuclei, there is little to no signal recorded at frequencies between 2 and 12 MHz. In the presence of cavitation nuclei, even at the lowest pressure employed, a weak

broadband signal is still recorded for the first few seconds of treatment and harmonics bands are clearly noticeable. Interestingly the harmonics band signal seems to decay with time, suggesting partial consumption of the cavitation nuclei. As the pressure was increased to 2.25 MPa pnp, the broadband noise increased in magnitude and was sustained throughout the treatment in presence of MBs. Initially, high intensity harmonics band can be appreciated also at this higher focal pressure. In absence of MBs, the broadband signal is showing intermittent pattern probably due to the nucleation of bubbles at the water-substrate interface. The intermittence of the signal might be due to depletion of gas from the suspending media in the vicinity of the substrate, which is then replenished by diffusive processes and acoustic streaming-induced mixing. At 2.25 MPa pnp and in absence of MBs, there are no appreciable high intensity harmonic bands in the PCD trace. At 3.00 MPa pnp the broadband emissions are sustained for the whole treatment both in presence and absence of MBs. The main differences were that in presence of MBs the signal was more intense and showed distinct harmonic bands in the first few seconds of the treatment.

The receiver used to record all the PCD traces has a broadband response but its sensitivity is still frequency dependent, with maximum sensitivity centred around 7 MHz. For this reason, all the PSD plots above show higher intensity signal in correspondence of those frequencies.

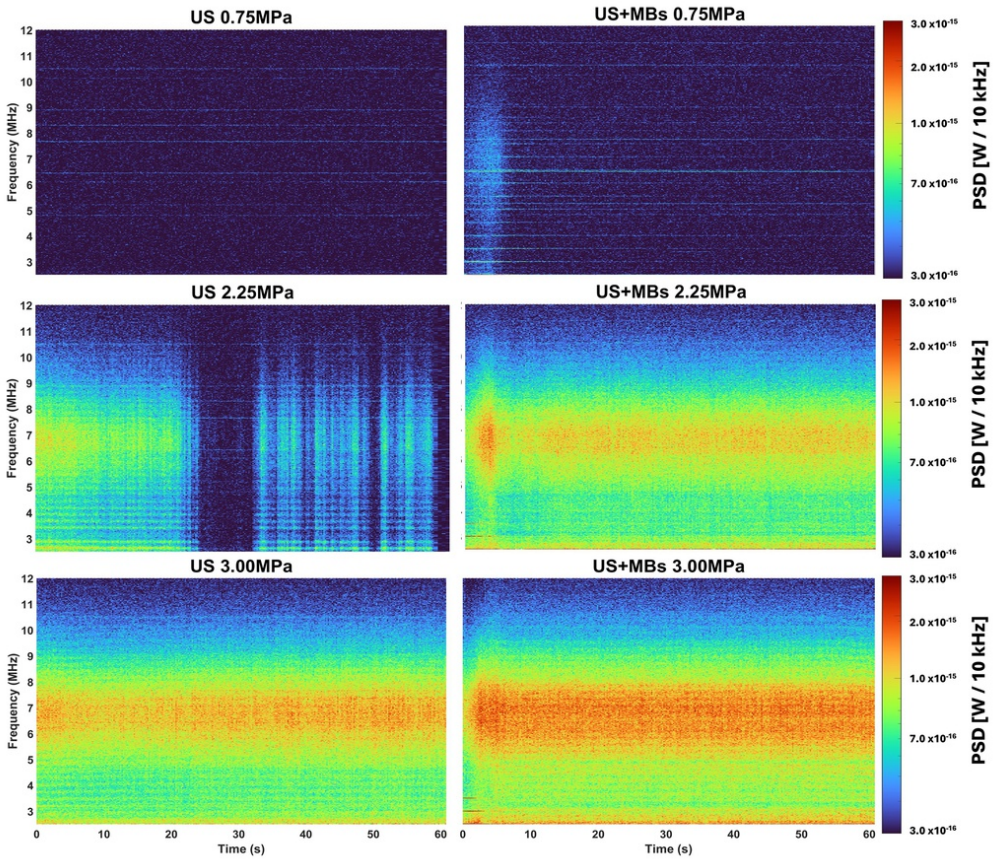


Figure 2.6: Power spectral density (PSD) plots, representing the spectral content of sound passively recorded during US experiments. The left panels are representative tracks recorded in the absence of MBs, whereas the right panels were recorded in the presence of MBs. The abscissa is time (in seconds) elapsed from the beginning of treatment, while the ordinate is the frequency content of the signal in MHz. The magnitude of each frequency (10 kHz resolution) is represented by the colormap. Thin high magnitude bands at the harmonics and ultraharmonics of the driving frequency (0.5 MHz) are expected in the presence of sustained non-inertial cavitation, whereas high magnitude signal spread over a broad range of frequency suggests inertial collapse of MBs at the focus of the US field.

The biofilm removal (calculated as percentage of total disc area) against cavitation energy recorded for each sample, is shown in figure 2.7. A pressure value of 2.25 MPa appears to

be close to the threshold for endogenous cavitation in the experimental system, and thus there is greater variability in the biofilm removal efficacy at this value when compared to greater pressure levels. This can be explained by the stochastic nature of cavitation, which is especially noticeable at peak pressures in the vicinity of the cavitation threshold. As an example, the cavitation energy delivered to the three samples treated at 2.25 MPa pnp, in the presence of MBs (green, north-east pointing triangles in figure 2.7), varies greatly between the three samples. As a result, the biofilm removal also varies greatly between these three samples that were, at least in theory, treated exactly in the same way.

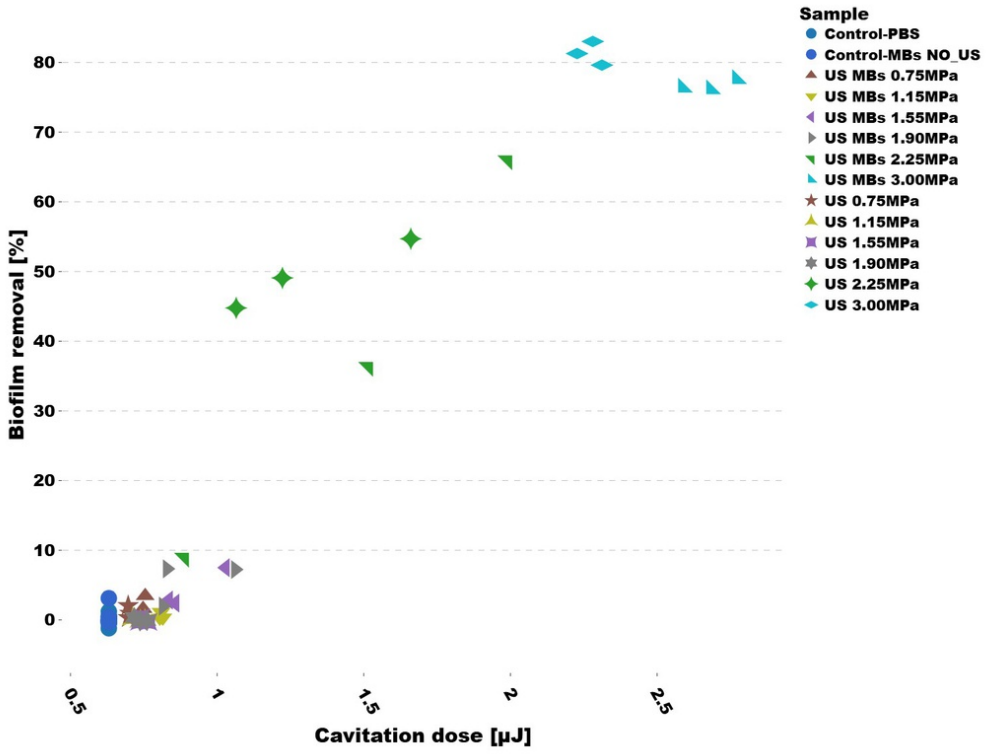


Figure 2.7: Biofilm removal for each sample plotted against the cavitation energy recorded during treatment. The cavitation dose in this graph is the (electrical) energy generated by the PCD receiver when hit by the US radiating from the sample during the treatment. The absolute values presented here do not correlate to the mechanical energy delivered to the sample, but are a good comparison metrics between samples, as they were all recorded in the same way. Biofilm removal correlates with cavitation energy, and variability in biofilm removal is mostly explained by looking at the variability in cavitation energy delivered to the sample.

2.4.3 Bactericidal effect of CHX on dental biofilms

Figure 2.8 represents the ratio between PI and syto9™ mean fluorescence intensities in each sample, normalised to the PI/syto9™ ratio in the control group. Higher values represent greater bacterial death in the biofilm. Treatment efficacy in this work was thus evaluated by comparing

this fluorescence ratio between samples treated at different conditions. Once the effect of US alone on the biofilm model was assessed, we proceeded to evaluate the effect of CHX (gold standard for oral infections) on the model. With these tests, we also evaluated if the imaging and image processing methods were sensitive enough to differentiate effects between treatments. The highest concentration used in this study is 0.100% w/V, which is the lowest concentration of CHX recommended for clinical use[148, 149]. Most of the bacteria in the biofilm that were treated at this CHX concentration took in PI, signifying that they were dead or irreversibly compromised. At a CHX concentration of 0.050% w/V, most bacteria are affected (stained by PI and so dead/irreparably damaged), but the relatively high syto9™ fluorescence intensity suggests that a significant number of bacteria in the biofilm is still viable/uncompromised. At 0.025% CHX concentration, the level of bacterial killing is only slightly higher than in the control group, indicating that such a low concentration of CHX is ineffective at treating the biofilm model.

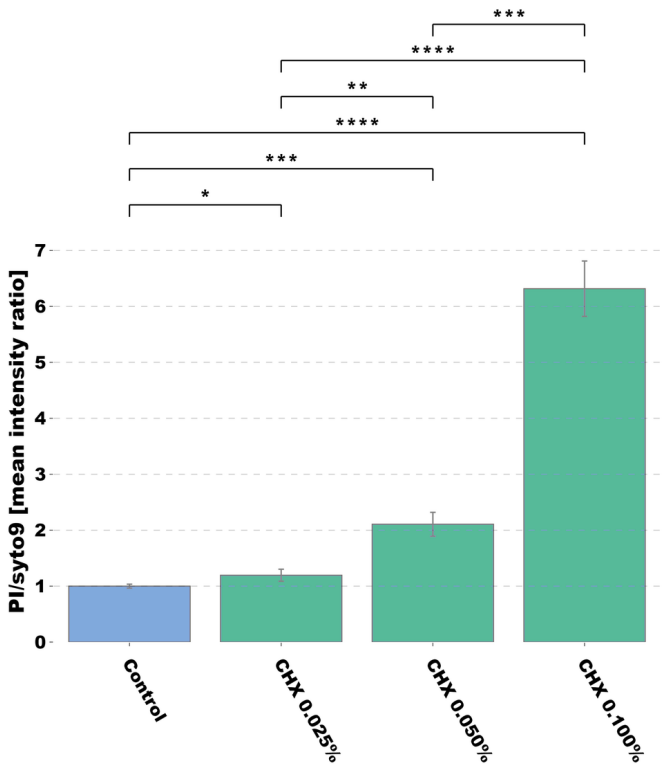


Figure 2.8: Ratio between PI and syto9™ mean fluorescence intensity in samples treated with increasing concentration of CHX. Higher values represent higher intake of PI by the bacteria, corresponding to greater bacterial death in the sample. n=3 (biological) for all groups. *pval<0.05, **pval<0.01, ***pval<0.001, ****pval<0.0001

2.4.4 Synergies between ultrasonic treatment and CHX on dental biofilm viability

Once the effect of CHX alone on the biofilm was evaluated, we treated the biofilms with US and exposed it to CHX right after, as described in the Methods section, to evaluate if exposure to US could improve the efficacy of the antimicrobial on the biofilm. figure 2.9 shows the viability data

(PI/syto9™ mean fluorescence intensity ratio) for samples treated with US+CHX (figure 2.9 B,C) and with US only (figure 2.9A). All values were normalised to the PBS control group. The US treatment in itself did not affect the viability of the biofilm attached to the substrate, as the PI/syto9™ ratio did not increase when compared to the control groups (figure 2.9A). Therefore, whilst US alone – at certain exposure parameters – proved effective at removing biofilms, it did not cause measurable antibacterial effects. In a dentistry setting, US treatment (in the absence of antiseptic) may thus need to be integrated with active removal of the detached biofilm/bacteria (i.e., using an aspiration system), which could then be deactivated at a subsequent stage. When the US treatment in the absence of MBs was combined with antimicrobial treatment, the effect of the antimicrobial was not significantly increased by the US exposure at none of the CHX concentrations and US pnps selected for this study (as shown by the superimposition of GLMs in figure 2.9B and in figure 2.15 in the Supplementary Material). In the presence of MBs, the US treatment at 2.25 MPa pnp significantly improved the antimicrobial activity at every CHX concentration tested (One-Way-ANOVA, p-value$<$0.05). For samples treated at 0.100% CHX, the antimicrobial activity was significantly improved also when the US pnp was 0.75 MPa (One-Way-ANOVA, p-value$<$0.05), as shown in figure 2.9C and figure 2.16 in the Supplementary Material. We hypothesize that the antimicrobial activity improvement was due to two main factors: 1- disruption of the EPS barrier surrounding the bacteria due to the mechanical stress induced by cavitation bubbles. In support to this hypothesis, figure 2.12 in the Supplementary Material reports the same data as in figure 2.9C but with a different scale. From this figure, it can be appreciated how the US treatment determined a significant reduction in PI/syto9™ ratio. This can be explained only with an increased intake of syto9™ when compared to controls. An increased intake of syto9™ , but not of PI, is in accordance with a reduction in the EPS

barrier effect, which favours the interaction of syto9™ with the bacterial wall/membrane and its intracellular penetration. It is also plausible that the US treatment determined transient damage in the bacterial wall/membrane, favouring dye penetration. However, this should have also been likely accompanied by increased intake of PI, particularly since PI is a smaller molecule than syto9™ (668.39 Da molecular weight for PI against 963.58 Da for syto9™). For this reason, we exclude that the US treatment determined extensive membrane damage in the bacteria. A representative set of fluorescence microscopy images used to obtain the data presented in this section is shown in figure 2.10.

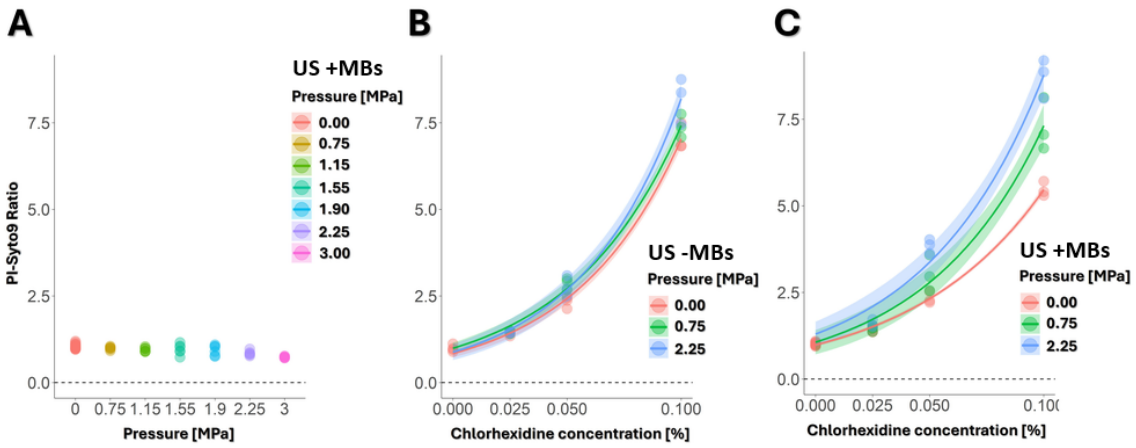


Figure 2.9: (A) PI and syto9™ mean fluorescence intensity ratio in samples exposed to US at increasing focal peak negative pressure. These samples were not exposed to CHX and confirm that the US treatment alone did not reduce bacteria viability. (B) PI and syto9™ mean fluorescence intensity ratio in samples exposed to US (0.75 or 2.25 MPa) in the absence of MBs and treated with increasing concentration of CHX. (C) PI and syto9™ mean fluorescence intensity ratio in samples exposed to US (0.75 or 2.25 MPa) in the presence of MBs (1×10^8 MBs/mL) and treated with increasing concentrations of CHX.
In panels (B) and (C), the data were fitted to a GLM with mean values reported as a solid line, whereas the 95% confidence interval is shown as shadowed area. n=3 (biological) for all groups.

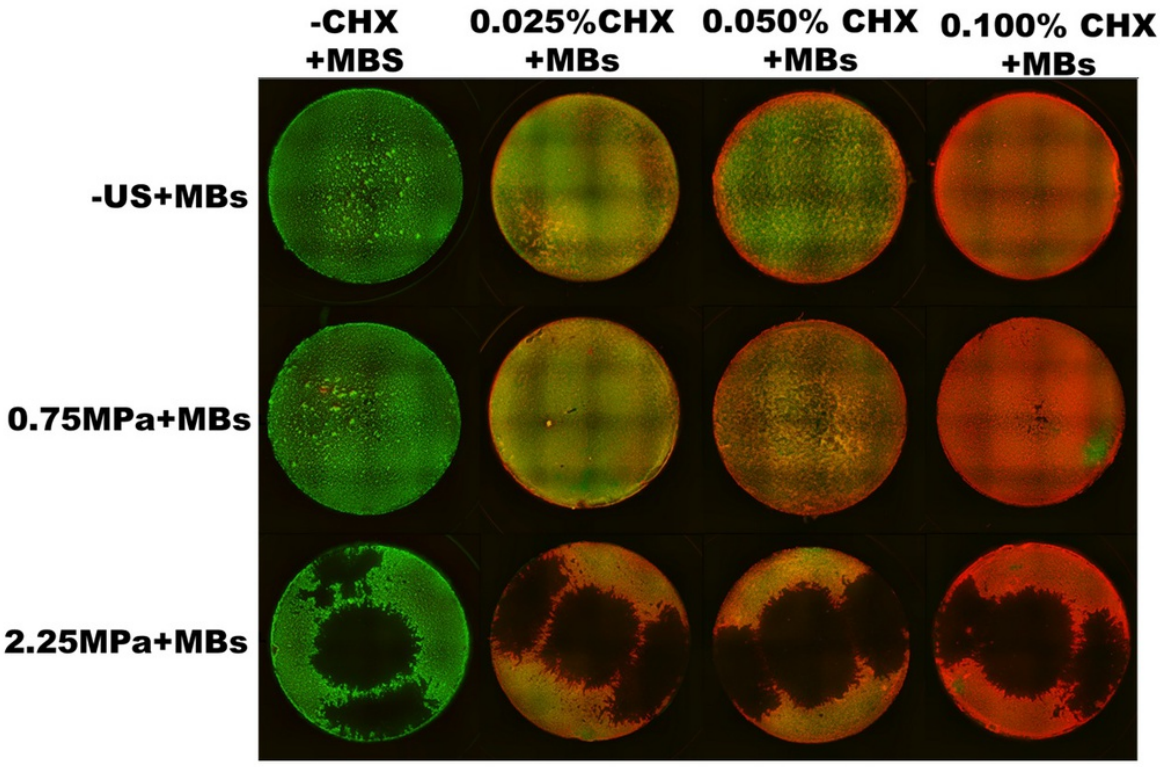


Figure 2.10: Representative microscopy images of dual stained biofilm samples grown on HA disc supports (12 mm diameter), treated with CHX and US at different concentrations and pnps. The images have been generated by overlaying the syto9™ and PI channels for the same microscopy acquisition. As described above, samples containing mostly live bacteria (control and US-only) show high syto9™ fluorescence intensity and low PI fluorescence intensity. As the concentration of CHX is increased, syto9™ fluorescence intensity descreases whereas PI intensity increases. The combination treatment shows the highest PI fluorescence and lowest syto9™ fluorescence. The US+CHX control group is not reported in the figure, as it did not show significant improvement in the bactericidal effect of CHX (and to ensure the figure was of reasonable size for readability purposes). [The brightness of these images was enhanced for readability purposes, and the checker-pattern in the images is due to the stitching algorithm].

2.4.5 Study limitations and future works

An important limitation of this study to highlight is the simplicity of the biofilm model proposed, as it involved only one bacterial species. Interspecies interactions are vital in biofilm evolution, and it will be essential in future work to evaluate how US-mediated treatment impacts on the relative survival of different bacteria. For example, a three species biofilm comprising of *Streptococcus mutans*, *Fusobacterium nucleatum*, and *Porphyromonas gingivalis* would be an interesting evolution of the simple model presented in this work. Assessment of antibiofilm effects in this study has been performed using a microscopy-based fluorescence assay, relying on syto9/PI staining of the biofilm. Previous studies have demonstrated that this is a valid and robust method to evaluate *S. mutans* viability[150, 151]. Future work could extend this analysis to include other techniques for comparison and further validation, such as using methods based on CFU enumeration or metabolic measurements. Such methods were attempted in the present study but proved unreliable, due to the fact that the biofilm was strongly adhered to the substrate, and would thus require further development for implementation. This study also lacked long-term treatments and repeated exposures, due to the selected analysis method. Future work will focus on addressing these limitations and creating conditions more representative of a potential clinical use. Additionally, the scope of our research did not cover the possible mechanical impact of US-induced cavitation on the tooth surface and surrounding soft tissue. This will also be evaluated in future research, as well as a comparison with standard methods used in plaque management. There is evidence from earlier research that US (with/without gas MBs) time exposure parameters comparable to the ones employed in the present study, does not significantly impact on mammalian cell viability in vitro [152, 153]. However, as cell viability is

likely to depend on the cavitation dose (irrespective of the exposure parameters used)[154], further research on treatment safety is required. Moreover, although the acoustic data reported in this study allow accurate comparison of treatments performed at varying pnps in the described set-up, it should be highlighted that the power and energy values shown here refer to the electric signal generated by the piezoelectric receiver, not to the mechanical energy exerted by the cavitating bubbles on the biofilm samples. As such, direct comparison of energy-dependent effects between treatments is possible only when performed on the exact same set-up.

2.4.6 Conclusions

The results of this study demonstrate that focused US with a frequency of 0.5 MHz could be a useful tool in oral biofilm management. They also demonstrate that US could be used to improve the efficacy of conventional oral antimicrobials on oral biofilms. The efficacy of CHX was tested on the portion of biofilm that remained attached to the tooth-mimicking surface after US treatment, to estimate any improvement in oral biofilm management outcomes even in the absence of complete removal. Complete removal of oral biofilm is not only almost unattainable due to the geometry of the crevices formed by the teeth structure, but potentially harmful, as bacteria are a vital part of oral cavity homeostasis. Improvements in bactericidal effects of low-dose CHX could thus be useful in pathological biofilm eradication. To the best of the authors' knowledge, this is the first study evaluating the effect of focused US at 0.5 MHz on an oral cavity-specific infection model . Previous research on oral treatments has focused on the use of lower frequency ($< \sim$120 kHz) unfocused US[32, 34, 112, 117]. Increasing the US frequency and spatially focusing the US beam, significantly improves the spatial resolution

of treatment. Overall, our findings provide valuable insights into the versatility of therapeutic US in biofilm treatment and the possible improvement in current therapies to address the ever-growing challenge of bacterial eradication in biofilm associated infections.

2.4.7 Authors contributions

Conceptualization was carried out by Eleanor Stride, Dario Carugo, Bart Gottenbos, Gareth LuTheryn, Monique Stoffels, Matthias Born, Davide De Grandi. Supervision of the research effort was provided by Gareth LuTheryn, Bart Gottenbos, Eleanor Stride, Dario Carugo. Formal analysis was conducted by Davide De Grandi. The investigation, including data collection, was performed by Davide De Grandi. The original draft of the manuscript was written by Davide De Grandi. Critical review, commentary, and revision of the manuscript were undertaken by Eleanor Stride, Dario Carugo, Gareth LuTheryn, Bart Gottenbos, Monique Stoffels, Matthias Born. Funding acquisition was secured by Eleanor Stride and Dario Carugo. Project administration and day-to-day coordination of the research effort was managed by Eleanor Stride and Dario Carugo.

2.5 Supplementary material

2.5.1 Preliminary simulation of the set-up US field

A two-dimensional first-order k-space pseudospectral simulation was performed using MATLAB k-Wave toolbox (Version 1.4) to model semi-quantitatively the US field in the experimental set-up. The resulting model was used to inform the experimental measurements of

the acoustic field. The k-Wave pseudospectral method is a numerical technique for modelling acoustic wave propagation in heterogeneous, absorbing media. It solves the first-order conservation equations governing acoustic particle velocity and acoustic density perturbation. In the presence of power-law absorption, these equations are expressed as

$$\frac{\partial \mathbf{u}}{\partial t} = -\frac{1}{\rho_0}\nabla p, \tag{2.1}$$

$$\frac{\partial \rho}{\partial t} = -\nabla \cdot (\rho_0 \mathbf{u}), \tag{2.2}$$

$$p = c_0^2 \left[\rho - \tau \frac{\partial}{\partial t}\left(-\nabla^2\right)^{\frac{y}{2}-1} \rho + \eta \left(-\nabla^2\right)^{\frac{y-1}{2}} \rho\right], \tag{2.3}$$

where $\mathbf{u}$ is the particle velocity, ρ is the acoustic density perturbation, p is the acoustic pressure, ρ_0 is the ambient density, c_0 is the speed of sound, and the coefficients τ and η describe frequency-dependent power-law absorption and dispersion. Further details of the numerical method are available in the k-Wave documentation (http://www.k-wave.org/documentation.php). The simulations were performed at a centre frequency of 0.5 MHz on a computational grid of 760×864 points with a spatial resolution of $\Delta x = \Delta y = 100$ μm. The temporal discretisation was determined using a Courant–Friedrichs–Lewy (CFL) number of 0.25, such that

$$\Delta t = \frac{\mathrm{CFL}\,\Delta x}{c_{\max}}, \tag{2.4}$$

where $c_{\max}$ is the maximum sound speed in the computational domain. A perfectly matched layer (PML) of 20 grid points was applied at all domain boundaries to minimise artificial reflections.

A formal mesh independence study was not performed. Instead, the spatial and temporal discretisation parameters were selected conservatively and were deemed sufficiently small for a qualitative model. Numerical stability was verified by ensuring the absence of observable numerical dispersion and spurious boundary reflections throughout the computational domain. The transducer face was placed in water, which acted as propagation medium. Due to the set-up components and the presence of a sample at the geometrical focus, the sound propagation was modelled through various heterogeneous materials. The materials properties and geometry dimensions are clearly defined in table 2.1 and figure 2.11. The materials properties were sourced from literature rather than obtained through experimental measurements, for this reason the results of the model are just a qualitative approximation of the set-up. The acoustic source was modelled as a spherically focused pressure source with a central cut-out, with dimensions equal to the SoniConcepts H107 HIFU transducer. The source was driven at 0.5 MHz with a prescribed pressure amplitude of 1 Pa. The resulting pressure fields were subsequently normalised to facilitate comparison of the spatial pressure distribution.

Table 2.1: Acoustic properties assigned to the materials in the k-Wave simulation.

Material	Speed of sound (m/s)	Density (kg/m^3)	α (dB MHz^{-y} cm^{-1})	y
Air	343	1.225	7.5	2.0
Water	1480	998	0.0022	2.0
Polycarbonate	2270	1200	5.0	1.0
PLA	2230	1240	10.0	1.1
Polyethylene	1950	950	4.0	1.0
Hydroxyapatite	3500	1900	8.7	1.0

The simulations were performed using the CUDA implementation of the k-Wave Toolbox on an NVIDIA Titan Xp GPU with 12 GB of dedicated memory. The colour maps shown

in figure 2.11A,C represent the normalised maximum pressure (p_max) probed in the whole domain. The simulation shows that the presence of the HA disc at the focus of the HIFU transducer results in the formation of a standing-wave interference pattern, characterised by alternating regions of high and low acoustic pressure. The model also predicts the formation of a localised high-pressure region adjacent to the surface of the HA disc, which informed the positioning of the experimental samples during acoustic exposure.

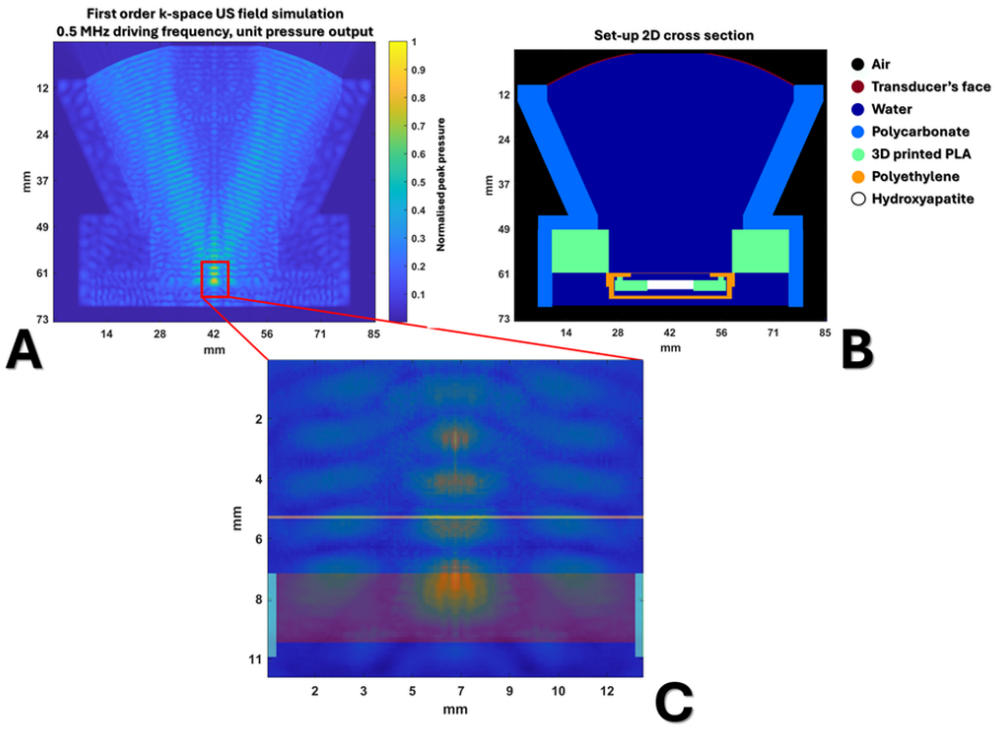


Figure 2.11: (A) A 2D model of the US field in the set-up employed during experiments. The model was computed using MATLAB's k-wave toolbox, utilising a first-order k-space approach. The pressure field is normalised to the peak pressure. (B) The different components of the set-up (2D section) are represented and color-coded. (C) A zoomed-in view of the US field at the HA disc interface.

2.5.2 Increased intake of syto9™due to US treatment

Exposure of the biofilm to US (in the absence of CHX) determined an increased intake of syto9™ when compared to controls. We hypothesize that this could be due to EPS layer disruption. EPS disruption favours the interaction of the dyes (and any molecule present in the solution surrounding the biofilm) with bacterial cells, determining the observed increased uptake of syto9™ , as this molecule can easily cross the bacteria wall/membrane. PI intake was not increased by US treatment, suggesting that the bacteria wall/membrane was not damage by exposure to US and the associated cavitation and streaming.

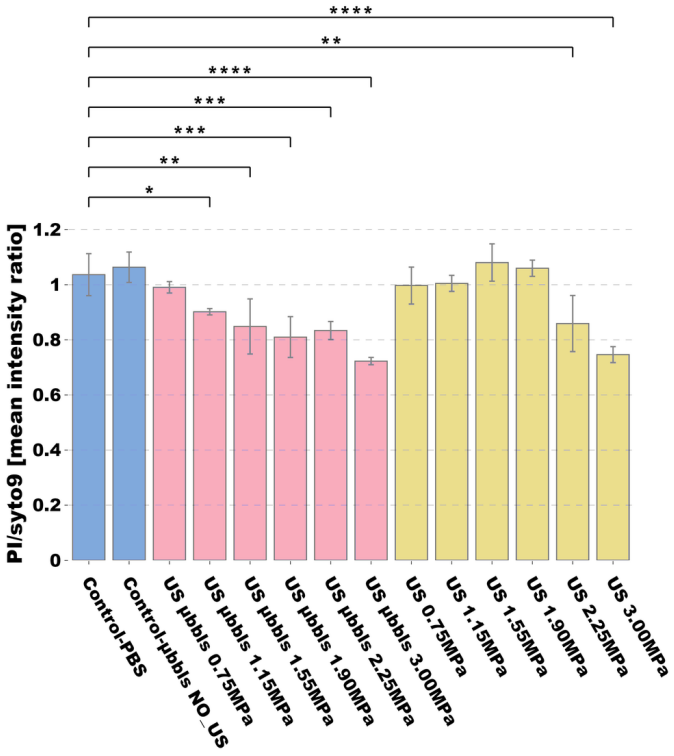


Figure 2.12: PI and syto9™ mean fluorescence intensity ratio in samples exposed to US (0.75 or 2.25 MPa) in the presence and absence of MBs. These samples were not exposed to CHX.

2.5.3 Calculation of area of removal: method and consideration

The fraction of biofilm removed by the US treatment is obtained from the total biofilm-free area after treatment $A_{r,\,meas}$, using the biofilm-free area of untreated samples $A_{r,\,ctr}$ to correct for the residual biofilm-free area in the unexposed region. We approximate the total biofilm-free area

after treatment as the sum of the residual biofilm-free area, assumed to have the same fractional coverage as the controls, and the area removed by the treatment

$$A_{r,meas} = A_{r,US} + (A_{tot} - A_{r,US}) \cdot \frac{A_{r,ctr}}{A_{tot}} \tag{2.5}$$

Where $A_{r,US}$ is the area of biofilm removed by the treatment. The corresponding fraction of biofilm removed by the treatment can be obtained from equation (2.5) as

$$\frac{A_{r,US}}{A_{tot} - A_{r,ctr}} = \frac{A_{r,meas} - A_{r,ctr}}{A_{tot} - A_{r,ctr}} \cdot \frac{A_{tot}}{A_{tot} - A_{r,ctr}} \tag{2.6}$$

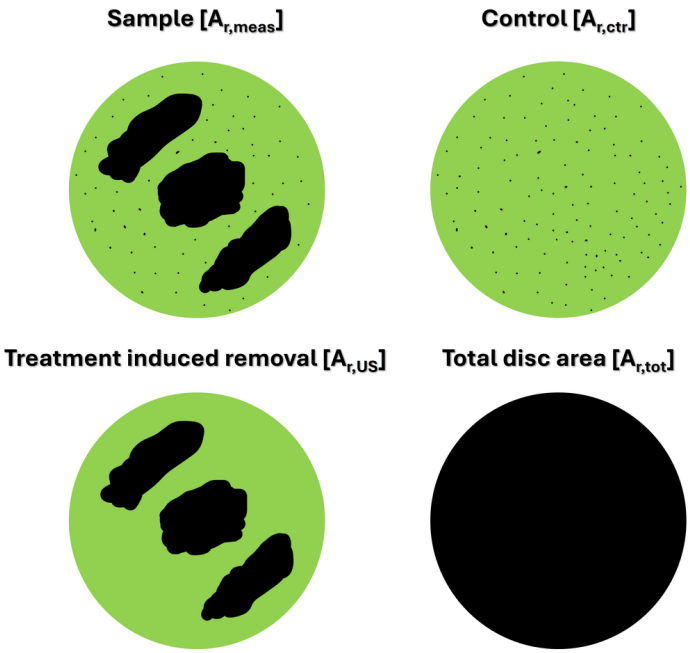


Figure 2.13: Representation of the biofilm areas used in the calculations

2.5.4 One-Way-ANOVA supplementary analyses

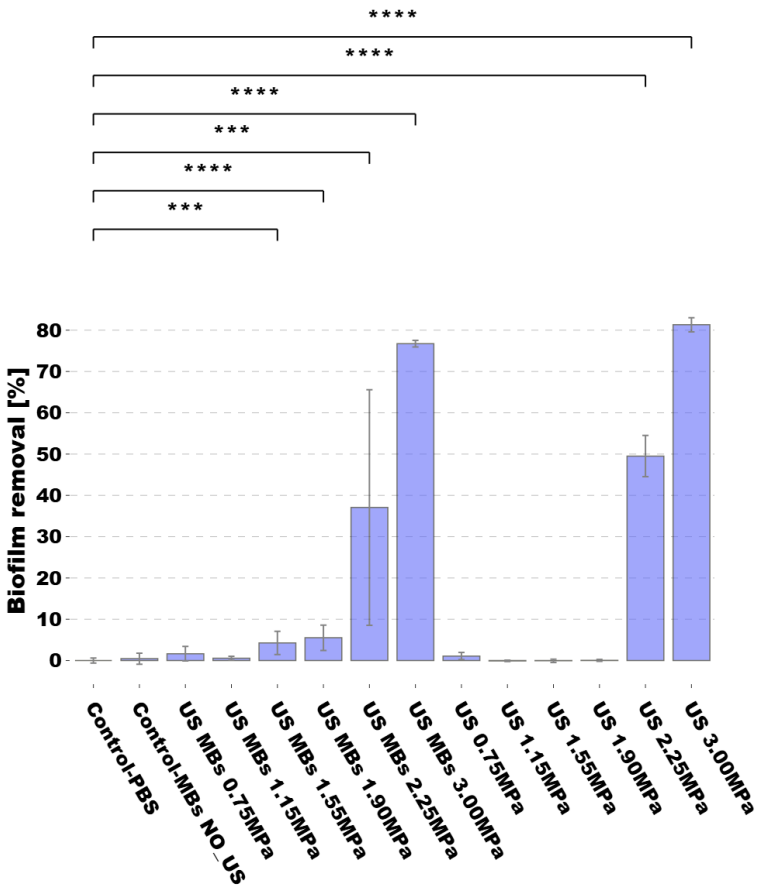


Figure 2.14: The biofilm removal induced by the US treatment is not statistically significant for focal pressures of magnitude lower than 2.25 MPa pnp, in the absence of MBs. On the contrary, statistically significant removal was observed for focal peak pressure magnitude of 1.55 MPa pnp and greater, in the presence of MBs. n=3 (biological) for all groups.
*pval<0.05, **pval<0.01, ***pval<0.001, ****pval<0.0001

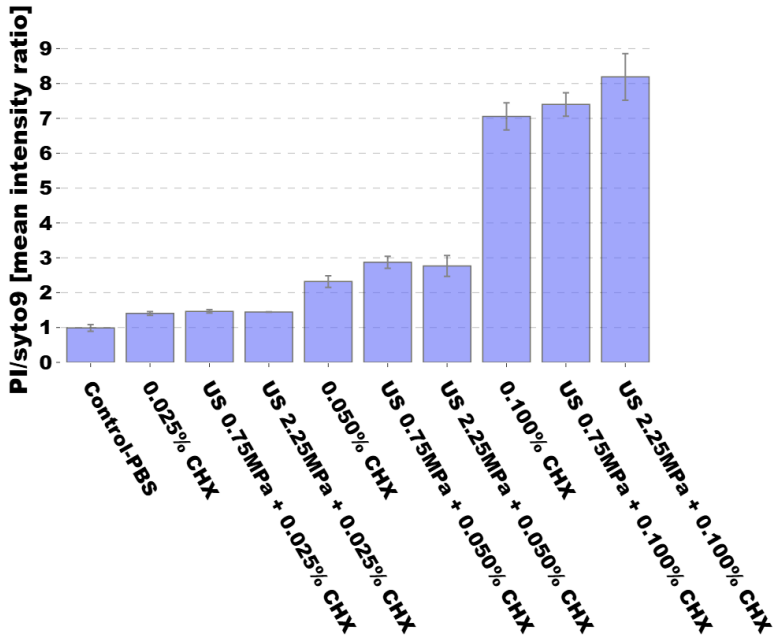


Figure 2.15: In the absence of MBs, the biofilm viability reduction (measured as increased PI/syto9 ratio) induced by the combination of CHX and US treatment did not show any improvement due to the application of US, at any of the focal pressure levels and CHX concentrations tested in this study. n=3 (biological) for all groups.
pval<0.05, **pval<0.01, ***pval<0.001, ****pval<0.0001

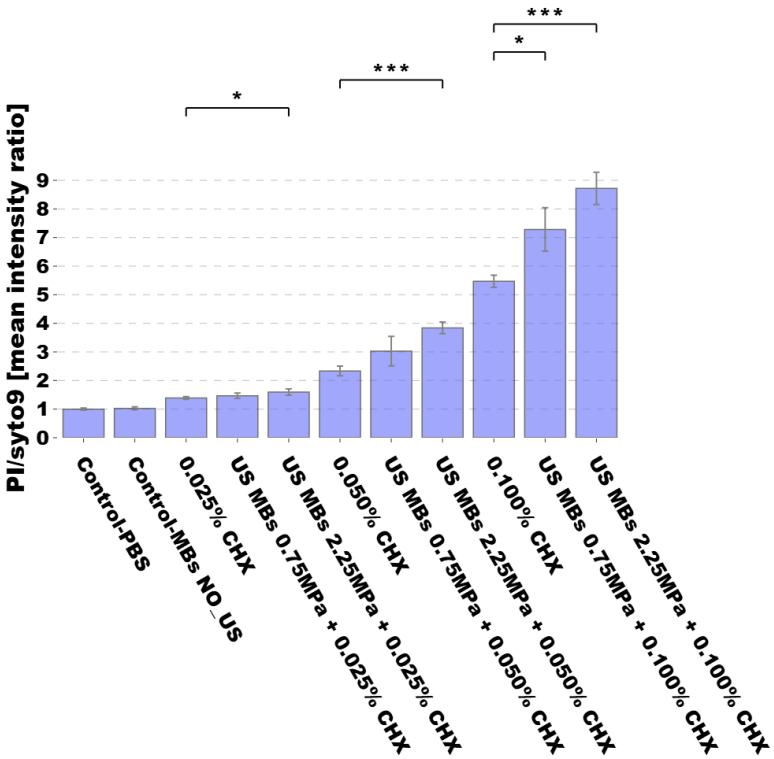


Figure 2.16: In the presence of MBs, the biofilm viability reduction (measured as increased PI/syto9 ratio) induced by the combination of CHX and US treatment showed a statistically significant improvement at all CHX concentrations tested in this study, when the peak focal pressure magnitude was 2.25 MPa pnp. A statistically significant improvement was measured also when the pnp was 0.75 MPa, but only for the highest CHX concentration evaluated. n=3 (biological) for all groups.
pval<0.05, **pval<0.01, ***pval<0.001, ****pval<0.0001

Chapter 3

Ultrasound mediated enhancement of sub-MIC antimicrobial treatment efficacy on a saliva-derived microcosm oral biofilm model

3.1 Abstract

Objective: This study explored the effectiveness of ultrasonic therapy (500 kHz, focused field) as an adjuvant for antimicrobial therapy against a fully formed saliva-derived oral biofilm *in vitro* model.

Methods: Clinical saliva samples were collected, pooled, and utilised to develop a reproducible multi-species oral biofilm model, which was grown in artificial saliva over a tooth-mimicking substrate. The biofilms were subsequently exposed to increasing concentration of an oxidative antimicrobial solution, termed AW. The treatment was then combined with 500 kHz, low duty

cycle (1 %) ultrasonic therapy at varying peak negative pressures (0.75 or 3.00 MPa pnp).

Results: Saliva-derived biofilms models were successfully and reproducibly grown on a HA substrate. The samples were then exposed to antimicrobial treatment in the presence or absence of US and the viability following treatment was assessed by counting CFUs on two different agar media. AW showed concentration dependent efficacy against the multi-species oral biofilm model, which was improved by co-administration of US treatment.

Conclusions: The work demonstrated how AW is a viable antimicrobial compound for the treatment of oral biofilms. In addition, we demonstrated how its antimicrobial effect is improved by co-administration of US treatment. The improvement in antimicrobial activity in the combination therapy could be harnessed for the treatment and prevention of resistant biofilm-infection in the future.

Keywords: Biofilms, Therapeutic Ultrasound, Dental Hygiene, Oral Microbiota, Antimicrobial Treatment, AMR, Biofilm removal, AW, Cavitation

3.2 Introduction

3.2.1 Rationale for the study

Biofilms are the root cause of most oral infections, with incidence reaching up to 45% of the population in first world countries [155], and oral-related infections account for more than 80% of all oral pathologies. Their recurring nature, and the unavoidable need for highly trained professionals to deliver treatments, imposes a significant burden on the healthcare system, com-

parable to pathologies such as cancer, diabetes, and cardiovascular diseases [156, 157].

Therapeutic US has been proposed in recent years as a potential option for improved treatment of biofilm-related infections [6, 7, 110, 158]. Although the effects of therapeutic US on bacteria have been investigated over the past decade [91, 113, 133, 134, 159], there is still no consensus on its efficacy, the mechanisms involved, and whether these are bacterial strain-dependent, especially at frequencies above 125 kHz [92, 140, 160, 161]. It has been demonstrated that US can enhance the effectiveness of antimicrobial drugs in wound, pulmonary and urinary tract infection models [6, 91, 92, 139, 140], but similar work on oral infections is still scarce.

In the previous chapter, a mono-species biofilm model was subjected to a combination of therapeutic US and antimicrobial treatment. Building on these results and addressing some of the study limitations, in this chapter a new set of experiments is described to further investigate combined US + antimicrobial therapy. In particular, it was evaluated whether the synergistic effect of US would be more pronounced if delivered in combination with an antimicrobial with faster-acting kinetics than CHX (*e.g.* ROS or diluted bleach) [162, 163]. A saliva-based biofilm model was also used to assess whether the US effect is in any way influenced by the bacterial strains to which it is applied, as suggested in some previous literature [91, 161].

AW generated by electrolysis of a dilute electrolyte solution, was selected as CHX alternative antimicrobial owing to its practical ease of production and the mechanism of action of the oxidative antimicrobials generates during the electrolysis process. Unlike CHX, which is a relatively large cationic molecule whose antimicrobial activity depends on diffusion through the biofilm matrix and interaction with the bacterial membrane, AW contains a mixture of small ROS and reactive chlorine species that are expected to penetrate the biofilm more readily. ROS act rapidly by inducing oxidative damage to both the bacterial cell membrane and intracellular

components, including proteins, lipids, and nucleic acids, resulting in faster bacterial inactivation than the membrane-targeted action of CHX. The faster diffusion and rapid mode of action of ROS were expected to produce greater synergy with the transient damage to the biofilm structure and the bacterial membrane determined by the ultrasound treatment, compared to CHX.

3.3 Materials and Methods

3.3.1 Materials

All the 3D printed parts were manufactured using either a Formlab Form2 stereolithography (SLA) printer with Formlab grey resin (Formlabs, GmbH, 12459 Berlin, Germany) or an Ultimaker S5 FDM printer with Ultimaker tough polylactic acid (PLA) (Ultimaker B.V., 4191 PN Geldermalsen, Netherlands).

Computer aided design (CAD) models were produced using Autodesk Inventor Professional 2024™ (Autodesk, San Francisco, CA 94105, USA).

Data processing was performed either in MATLAB 2023b (The MathWorks Inc., Natick, Massachusetts, USA) or Python (version 3.9.13). The complete scripts are provided in the Supplementary Material section.

3.3.2 Passive Cavitation Detection (PCD)

PCD is a method that involves recording the sound emitted from a cavitating sample and processing it to evaluate its magnitude and spectral content. For each US burst emitted from the HIFU transducer (5 Hz burst repetition frequency in all experiments performed in this work),

one recording was made using an Olympus V308-SU underwater receiver with broadband response centred on 5 MHz (Evident Europe GmbH, Hamburg, Germany) to capture the sound originating from the sample. The electrical signal generated from the receiver was first filtered using an EF509 coaxial 1.8 MHz high-pass electrical filter (ThorLabs LTD., Ely, UK), to remove the fundamental frequency component that is associated with reflections of the incident US wave from the sample, and up to the third harmonic.

The filtered signal was then amplified 5 times using a low-noise preamplifier (model SR445A, Stanford Research systems, Sunnyvale, CA, USA), digitised using a digital oscilloscope (Handyscope HS6, TiePie engineering, Sneek, Netherlands) and recorded using the TiePie Multichannel software (TiePie engineering, Sneek, Netherlands). The acoustic emissions data were processed to evaluate their frequency content and the total cavitation energy generated during treatment, using a MATLAB script (listing 1). Briefly, the script performs a Welch transform on each recording. The resulting power spectral density (PSD) plots represent the amplitude of the frequencies composing the electrical signal generated by the receiver. The PSD plots obtained from all of the recordings during one experiment (for a 1-minute long experiment, at 5 Hz burst repetition frequency, which amounts to 300 PSD plots) were then collected and plotted as a colormap, with power spectral density [W / f, 10 kHz frequency resolution] on the ordinate, experiment time on the abscissa, and amplitude of the signal in colour scale. The frequency-domain PSD were then used to calculate the total energy of the emissions during the experiments, as well as the proportion of harmonic, ultra-harmonic, and broadband components.

Since for each experiment the PCD set-up was identical, the cavitation activity of different treatments could be directly compared by evaluating the corresponding cavitation signal power

and/or energy. Anyway, since the receiver utilized for this work was different compared to the one used in chapters 2 and 4, direct comparison of cavitation measurements obtained in these sets of experiments is not possible. It should be noted that the power and derived energy computed in this study correspond to the electrical signal generated by the receiver and do not directly represent the acoustic power radiated by the cavitating bubbles.

3.3.3 Biofilm growth protocol

For this work we developed a multispecies biofilm model starting from clinical saliva samples. Participants were asked to refrain from brushing their teeth for 24 hours and to avoid food or beverage ingestion in the 1 hour preceding the sampling. 20 mL of saliva and plaque were collected from each participant (internal ethics board (ICBE) approval number: ICBE-S-000407 (dd 1 Jul 2021)). The samples were then vortexed, pooled, aliquoted, and stored in 20% glycerol (Sigma-Aldrich Chemie, NL) at -80°C until needed. Artificial saliva was prepared as follows: to 800 mL of DI water we added 2.5 g of mucin (M2378, Sigma-Aldrich Chemie, NL), 2.0 g of BactoPeptone (BD 211677, Gibco™), 2.0 g of BBL-Trypticase Peptone (BD 211921, Gibco™), 1.0 g of Bacto Yeast Extract (BD 212750, Gibco™), 0.2 g of sodium chloride (9625, Sigma-Aldrich Chemie, NL), 0.2 g of potassium chloride (3911, Sigma-Aldrich Chemie, NL), 0.2 g calcium chloride (383147, Sigma-Aldrich Chemie, NL), and 50 mM of PIPES (P-6757, Sigma-Aldrich Chemie, NL). After 1 hour of magnetic stirring, 1 mL of hemin stock solution (prepared as discussed below) was added to the mixture and the pH was brought to 7.8 pH using 8M $NaOH$. The volume was then brought to 1 L and the mixture autoclaved at 121 °C for 20 minutes. The Hemin stock solution was prepared in advance by mixing 10 mg of hemin

(H9039, Sigma-Aldrich Chemie, NL) in 10 mL of 0.1% $NaOH$ aqueous solution. Once the artificial saliva equilibrated to room temperature, 200 μL of 0.984 mg/mL solution of vitamin K1 (95271, Sigma-Aldrich Chemie, NL) dissolved in 95% ethanol were added to it under a biological fume-hood.

From the clinical saliva samples, a liquid culture stock was generated as follows: 98 mL of artificial saliva, were inoculated with 2 mL of clinical saliva sample and allowed to grow aerobically at 37°C, 95% humidity, and 5% CO_2. This liquid bacterial stock was then stored with 20% glycerol at -80°C until needed. All the experiments were run using this bacterial culture stock, to reduce the experimental variability.

For each experiment, a biofilm was generated by diluting the liquid culture stock 1:50 with the same artificial saliva described above, but spiked with 1% sucrose. 1 mL of this diluted bacterial seeding dispersion was then placed in a well of a 24 well-plate (Corning Life Sciences B.V, Amsterdam, NL) containing a HA disc (12 mm in diameter , 2.3 mm thick, HADEL02, Himed, NY 11804, USA) that was used as an artificial tooth substrate. Prior to the seeding step, the HA discs were treated for 1 hour with a 0.1% acetic acid solution containing 150 μg/mL rat tail collagen type I (Corning™, UK) to favour bacterial adhesion. The submerged discs were then placed in an aerobic incubator for 20 hours at 37°C, 95% humidity, and 5% CO_2. After incubation the substrates were gently washed with sterile PBS and placed in a clean 24 well-plate containing 1 mL of sterile PBS, before being used in the experiments.

3.3.4 AW production and characterization

In this work, AW is defined as a low concentration salt solution that has been subjected to electrochemical treatment. Depending on the salt species present in the solution, the chemical properties of the electrodes, and the applied voltage, different toxic species (*e.g. ROS, peroxides, chlorides*) can be generated during the electrochemical treatment of the water. A standard water solution was used for the experiments containing 80 mg/L $CaCl_2$, 290 mg/L $MgCl_2$, and 210 mg/L Na_2SO_4. This will be referred to as the "high" concentration electrolyte solution. It was diluted in 1:2 and 1:4 ratios, using deionised water, to generate "medium" and "low" concentration solutions.

The electrochemical "activation" of the electrolyte solutions was performed utilising a commercially available electrode used in an air-disinfecting device (Hydro Air Washer, SOOVON CO., LTD., Incheon, Korea). The manufacturer claims that the electrode can be used to generate toxic species with strong antimicrobial properties [164].

The electrochemical generation of toxic species followed the same protocol for all the samples: 150 mL of electrolyte solution were placed in a 400 mL borosilicate glass beaker. The electrode was then completely submerged in the solution and kept at $\sim$1 cm from the bottom of the container. The electrochemical process was run for 5 minutes with an input voltage of 12 V DC using an ES015-10 power supply (Delta Elektronika, 4301 ND Zierikzee, NL). The maximum current was not limited and varied depending on the electrolytes concentration in the sample. The AW was prepared freshly before each experiment and was utilised within 15 minutes.

Given the electrochemical conditions and the ions present in the solutions, we expected three main toxic species to be produced during the process: hypochlorous acid, hydrogen peroxide,

and ozone. The relative concentration of these three components is determined not only by the reaction conditions but also by the electrode materials, which are not fully disclosed by the manufacturing company. To evaluate the concentration of toxic species generated during the electrolytic process we performed three subsequent iodometric titrations. These measurements allowed to evaluate the concentration of sodium hypochlorite, hydrogen peroxide, and ozone in all samples. The details of this protocol are provided in section 3.6.1.

3.3.5 US and antimicrobial treatment protocols

The antimicrobial treatment consisted of submerging each infected HA disc in 2 mL of AW (low, medium, or high concentration depending on treatment condition) for 4 minutes, in the configuration represented in figure 2.1. In the case of US treated samples, the disc was positioned in a low-profile Ibidi μ-dish (ibidi GmbH, Gräfelfing, Germany) thanks to a 3D printed holder designed in-house. The μ-dish was then placed in the ultrasonic set-up, so that the biofilm was at the focus of a HIFU transducer (H107, 0.5 MHz fundamental frequency, 63.2 mm geometrical focus, 64 mm active element diameter, custom rectangular cut out of 22×57 mm, Sonic Concepts Inc., Washington, USA). The US parameters for this work were: driving frequency of 0.5 MHz, 1000 cycles per burst, pulse repetition frequency (PRF) of 5 Hz, duty cycle (DC) of 1%, and peak negative pressure (pnp) at the sample location of either 0.75 MPa or 3.00 MPa. The ultrasonic set-up utilized for this work was the same illustrated in sections 2.3.4 and 2.4.1. As previously described in the set-up characterization section, the focal peak negative pressure refers to the pressure maximum measured at $\sim$1 mm from the HA substrate. Total ultrasonic treatment time was fixed at 60 seconds. For the samples treated with combination

therapy (US+AW), the μ-dish was filled with the antimicrobial solution and exposed to 60 seconds of US treatment. The total exposure time to the antimicrobial was also constant and equal to 4 minutes. In the negative control, the disc was subjected to the same procedures and manipulations, except for US and/or AW exposure. During the treatment, an unfocused 5 MHz ultrasonic transducer (Olympus V308 – SU, Evident Europe GmbH, Hamburg, Germany) was used to passively record the acoustic emissions generated in the sample. Although lipid-shelled MBs were not introduced into the treatment solution for this set of experiments, the electrolysis process continuously generated a substantial number of small, unshelled gas bubbles during the 5 min AW manufacturing process. Throughout electrolysis, the AW appeared as a milky, opaque dispersion of bubbles, which readily floated to the surface due to buoyancy or dissolved into the solution within seconds after the electrolysis process ended. We hypothesize that, although the bubbles generated during electrolysis were not sufficiently stable to remain in suspension until the AW was used for treatment, the process promoted the dissolution of oxygen and hydrogen into the AW, leaving it saturated or close to saturation with dissolved gases. We expected that the rough surfaces of both the HA substrate and the biofilm would act as nucleation sites for the dissolved gases, promoting bubble formation within and/or on the biofilm surface and increasing cavitation activity compared with an equivalent electrolyte solution that did not undergo the electrolysis process.

A marketed alcohol-free mouthwash (Listerine TCZ) was included in the study as a positive control, whereas PBS and hypotonic electrolyte solutions were used as negative controls.

3.3.6 CFU quantification protocol

CFU counting is widely accepted as the gold standard protocol for evaluating the bactericidal effect of antimicrobials. It was therefore utilised in this study to evaluate the effect of the different treatment conditions. Since during the US treatment, part of the biofilm is expected to detach from the HA substrate (as clearly demonstrated in chapter 2), we performed the CFU counting both on the supernatant and the biofilm still attached to the HA disc separately.

Right after treatment, the supernatant ($\sim$2 mL) was withdrawn and placed in a sterile vial. Then 200 μL were transferred to a second sterile vial and diluted 10 times with sterile PBS. This step was necessary to dilute the antimicrobials still present in the solution. Subsequently, the HA disc was taken from the experimental sample holder and placed in a clean well containing 2 mL of sterile PBS. The biofilm was then detached from the substrate with the following protocol: 1 minute of manual scraping using a pipette tip, followed by 5 minutes of sonication (Ultrasonic Cleaning Bath CPX1800, Branson Ultrasonics™, Fisher Scientific, Landsmeer, NL) to detach the remaining biofilm and break up clumps. A 10x dilution series was then performed on each sample, and each dilution was plated on Heart Infusion agar plates and Mac Conkey (Oxoid, UK) agar plates. The limit of detection for the method, calculated as described in [165], was estimated to be $\sim$ 133 CFU/mL in the original sample.

Plates were allowed to grow at room temperature for 18 hours and then incubated for 6 hours at 37°C, 95% humidity, and 5% CO_2. Both bacterial dispersions (from the supernatant and from the HA substrate) were plated following the same protocol both on HIB and MACB agar plates. HIB agar plates are non-selective and should for this reason allow most of the bacteria present in the sample to grow, although it is expected that at the culturing conditions used in this work

G+ bacteria might be slightly favoured. MACB is a selective media that allows only a selected group of bile salts-resistant G- bacteria to grow.

3.3.7 Statistical analysis

The statistical analysis performed in the present work employed a Linear Mixed Model (LMM) approach to account for the blocked experimental design, where treatments were tested across different experimental days (blocks). Given the intrinsic heteroscedasticity of CFU/mL data, these were log10 transformed before performing the analysis to normalize variance and meet model assumptions. The model considers treatment as fixed effect and experimental day (block) as random intercept, allowing for valid comparisons between treatments tested in different blocks by accounting for day to day variation. After verifying model convergence and examining variance components, pairwise comparisons were performed using Welch's t-tests on the transformed data, with p-values adjusted for multiple comparisons using the Bonferroni method. Statistical significance was set at α = 0.05. The results are presented using barplots showing the modelled groups mean effect $\pm$95% confidence interval. The data points are overlaid on the barplots, using different colours to specify which block each single data point belongs to.

3.4 Results and discussion

3.4.1 AW characterization

We performed an iodometric titration of the oxidants generated during the electrolysis process used to produce AW as described in section 3.6.1. As shown in table 3.1, the process did not

result in ozone generation in significant concentrations in any of the samples. This could be due to factors such as pH, electrode materials, and/or the chemical nature of the electrolytes present in the starting solution [53–55].

The measurements suggest that the electrochemical reaction generates mostly hypochlorous acid (HOCl, which persists in solution in the form of sodium hypochlorite) and, to a lesser extent, hydrogen peroxide (H_2O_2). Interestingly, the ratio of HOCl to H_2O_2 increases exponentially as the electrolytes concentration in the samples decreases.

Table 3.1: Toxic species generated during the electrochemical activation of aqueous electrolyte solutions. Concentrations of sodium hypochlorite and hydrogen peroxide are expressed in mM and are 10 to 100 times more diluted than the gold standard treatment. Although ozone was one of the possible products of the reaction, its generation was not detected in this experiment. n=3 for all samples.

Sample	[H_2O_2]	[HOCl]	[O_3]
AW-High	3.50 $\pm$1.75 mM	17.00 $\pm$2.65 mM	0.00 mM
AW-Medium	0.40 $\pm$0.10 mM	6.00 $\pm$0.50 mM	0.00 mM
AW-Low	0.05 $\pm$0.05 mM	4.90 $\pm$0.20 mM	0.00 mM

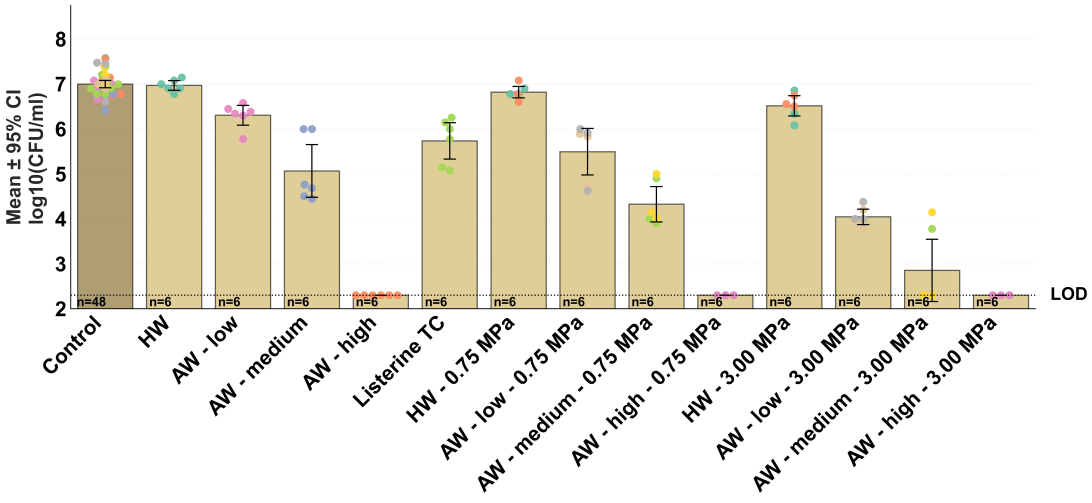
Sodium hypochlorite and hydrogen peroxide are effective antimicrobials used in standard oral health care practice. The usual concentration in mouthwashes and rinsing solutions can vary between 1 to 6 % for sodium hypochlorite and 1 to 3 % for hydrogen peroxide [166–169]. The concentrations of toxic agents obtained in this work is substantially lower than the clinical standard ($\sim$10x dilution for sodium hypochlorite and $\sim$100x dilution for hydrogen peroxide). Although higher concentrations could be obtained by optimizing the electrochemical process, the very low concentration of toxic agents in this study was desirable for two reasons. Firstly,

the objective of this work was to evaluate the synergistic effect of US and antimicrobials; as such, the treatment efficacy of AW had to be below the MIC, allowing for partial survival of the bacterial biofilm. Secondly, it has been suggested that in healthy individuals harsh treatments could have a detrimental effect on oral cavity homeostasis, due to the complete elimination of the host bacterial flora [170]. In these cases, gentler modalities such as AW, could be a better option for long-term management of oral microbiota.

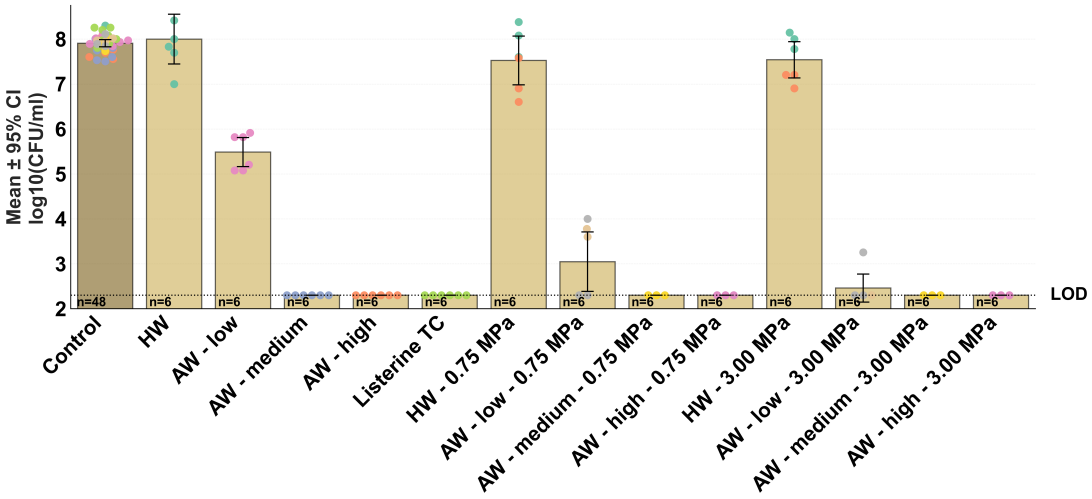
3.4.2 Overview of the treatments effects

In this short section we present the obtained data on biofilm viability following different treatment regimes. In the following figures and sections HW stands for samples treated with a hypotonic electrolyte solution (same as AW before the electrolytic process), while AW stands for samples treated with AW obtained as described above, at various concentrations. Samples treated with US show the value of pnp utilized at the end of the sample name.

Figures 3.1 and 3.2 show how the AW treatment affects both the portion of the biofilm still attached to the HA disc and the portion free floating in the supernatant following the treatment. CFU counting was performed both on HIB and MACB agar substrates.

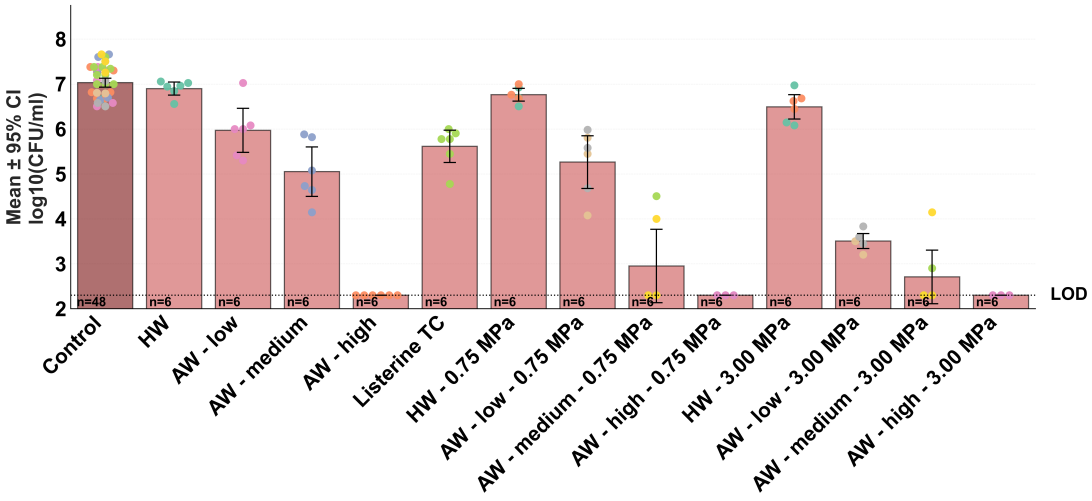


(a) Sessile bacteria collected from the HA substrate, cultured on HIB

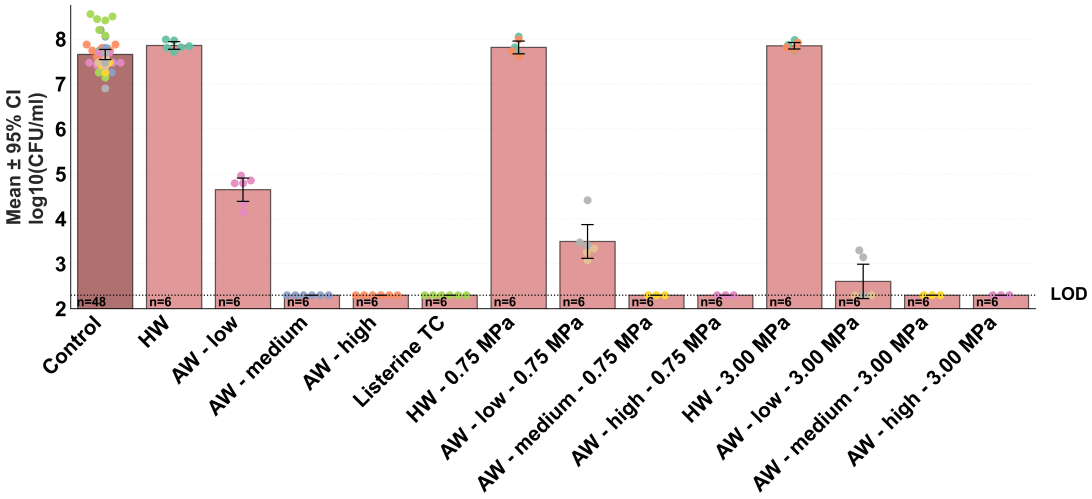


(b) Planktonic bacteria free floating in the supernatant, cultured on HIB

Figure 3.1: Bacterial viability following treatments with AW only, US only, and combination therapy at three concentrations of AW. Listerine TCZ was used as a positive control, PBS and hypotonic electrolyte solution (HW) were used as negative controls. The results presented in this figure derive from CFU counting performed on HIB agar plates, as such they represent the whole bacterial population present in the sample, although it is expected that G+ bacteria would find more favourable growth conditions.



(a) Sessile bacteria collected from the HA substrate, cultured on MACB



(b) Planktonic bacteria free floating in the supernatant, cultured on MACB

Figure 3.2: Bacterial viability following treatments with AW only, US only, and combination therapy at three concentrations of AW. Listerine TCZ was used as a positive control, PBS and hypotonic electrolyte solution (HW) were used as negative controls. The results presented in this figure derive from CFU counting performed on MACB agar plates, as such they represent only a selected group of G- bacteria capable of growing on bile salts containing agar medium.

3.4.3 Effect of AW treatment on bacterial viability

Firstly, we evaluated the response of the biofilm model to AW at three increasing concentrations and to Listerine TCZ without ultrasound exposure.

The results, presented in the first six bars of figures 3.1 and 3.2, show how the bacterial sensitivity to the treatment changes greatly between the planktonic/free floating bacteria found in the supernatant and the sessile ones still attached to the HA substrate. This applied to both total bacteria (HIB plates cultures) and a selected group of G- bacteria (MACB plates cultures). Interestingly, Listerine TCZ mouthwash showed relatively poor bactericidal effect for bacteria in sessile state ($\sim log\ 1.1$ reduction), whereas it completely eradicated the portion of bacteria that were free floating in the supernatant.

The results confirm that electrolysis of water solutions is a viable method of generating an oxidative antimicrobial mixture with efficacy comparable to a commercial alcohol-free mouthwash, at least for the *in vitro* model used in this study. The results also confirm that the medium concentration of AW determines a modest (∼2 log) reduction in sessile bacteria viability. The low concentration seems to determine a slight reduction ($\sim 0.7\ log$ reduction) in sessile bacteria viability when compared to controls. As reported in table 3.2, although AW shows a concentration dependent bactericidal effect, only the AW-high group shows a statistically significant reduction in bacterial viability in the HA substrate samples compared to the control, whereas all treatments show statistically significant reduction in viability compared to the control for the bacteria released in the supernatant.

Published work [171, 172] previously reported the antimicrobial potential of AW on various bacterial strains in planktonic form. The present section not only is agreement with these find-

ings, but confirms AW activity on an oral biofilms model.

Table 3.2: Pairwise comparisons between Control and treatment groups for HA Disc and Supernatant locations, across HIB and MACB culturing media. Adjusted p-values are corrected for multiple comparisons.
ns = not significant, * $p < 0.05$, ** $p < 0.01$, *** $p < 0.001$

Group 1	Group 2	Location	Media	Adjusted p	Significance
Control	HW	Disc	HIB	1	ns
Control	AW - low	Disc	HIB	0.0825	ns
Control	AW - medium	Disc	HIB	0.1086	ns
Control	AW - high	Disc	HIB	7.54×10^{-57}	***
Control	Listerine TCZ	Disc	HIB	0.1291	ns
Control	HW	Supernatant	HIB	1	ns
Control	AW - low	Supernatant	HIB	1.15×10^{-3}	**
Control	AW - medium	Supernatant	HIB	3.38×10^{-61}	***
Control	AW - high	Supernatant	HIB	3.38×10^{-61}	***
Control	Listerine TCZ	Supernatant	HIB	3.38×10^{-61}	***
Control	HW	Disc	MACB	1	ns
Control	AW - low	Disc	MACB	0.6836	ns
Control	AW - medium	Disc	MACB	0.0666	ns
Control	AW - high	Disc	MACB	9.17×10^{-53}	***
Control	Listerine TCZ	Disc	MACB	0.0326	*
Control	HW	Supernatant	MACB	0.7737	ns
Control	AW - low	Supernatant	MACB	1.43×10^{-5}	***
Control	AW - medium	Supernatant	MACB	3.03×10^{-53}	***
Control	AW - high	Supernatant	MACB	3.03×10^{-53}	***
Control	Listerine TCZ	Supernatant	MACB	3.03×10^{-53}	***

3.4.4 Effect of therapeutic US treatment on bacterial viability

To evaluate the effects of therapeutic US treatment on bacterial viability, tests were performed using a tailored ultrasonic system previously described (sections 2.3.3, 2.3.4 and 2.4.1). The only minor change to the set-up reported previously, is the receiver used to record cavitation data, which improved the sensitivity of the method. The new receiver and data acquisition method are described above in section 3.3.2.

The effects of the ultrasonic treatment on bacterial viability are presented in figures 3.1 and 3.2. The samples treated with therapeutic US, named HW-0.75 MPa and HW-3.00 MPa, were compared to PBS and HW controls. As shown in table 3.3, no appreciable changes in bacterial viability were determined by the US treatment at any of the tested conditions, confirming the results obtained in our previous work (presented in chapter 2) and in accordance with other published work using similar US parameters [173]. Although multiple articles in the literature claim that bacterial inactivation is achievable through US treatment alone [91, 134, 174, 175], the frequency, intensity, and treatment times do not compare with those employed in the present work.

These obtained results suggest that the US treatment, when performed at 500 kHz frequency, pnp between 0.75 and 3.00 MPa, and 1% duty cycle; has no effect on bacterial viability on our multispecies oral biofilm model. Therefore, any bactericidal effect improvement that might arise by the combination therapy of US and antimicrobials has to be attributed to synergies between the two rather than a direct effect of the US itself.

Table 3.3: Pairwise comparisons between Control, HW, and US treated HW groups for HA Disc and Supernatant locations, on both HIB and MACB culturing media. Adjusted p-values are corrected for multiple comparisons.
ns = not significant, * $p < 0.05$, ** $p < 0.01$, *** $p < 0.001$

Group 1	Group 2	Location	Media	Adjusted p	Significance
Control	HW	Disc	HIB	1	ns
Control	HW - 0.75 MPa	Disc	HIB	1	ns
Control	HW - 3.00 MPa	Disc	HIB	0.5858	ns
HW	HW - 0.75 MPa	Disc	HIB	1	ns
HW	HW - 3.00 MPa	Disc	HIB	0.7903	ns
Control	HW	Supernatant	HIB	1	ns
Control	HW - 0.75 MPa	Supernatant	HIB	1	ns
Control	HW - 3.00 MPa	Supernatant	HIB	1	ns
HW	HW - 0.75 MPa	Supernatant	HIB	1	ns
HW	HW - 3.00 MPa	Supernatant	HIB	1	ns
Control	HW	Disc	MACB	1	ns
Control	HW - 0.75 MPa	Disc	MACB	1	ns
Control	HW - 3.00 MPa	Disc	MACB	0.8675	ns
HW	HW - 0.75 MPa	Disc	MACB	1	ns
HW	HW - 3.00 MPa	Disc	MACB	1	ns
Control	HW	Supernatant	MACB	0.7737	ns
Control	HW - 0.75 MPa	Supernatant	MACB	1	ns
Control	HW - 3.00 MPa	Supernatant	MACB	0.6619	ns
HW	HW - 0.75 MPa	Supernatant	MACB	1	ns
HW	HW - 3.00 MPa	Supernatant	MACB	1	ns

3.4.5 Effect of the combination treatment on bacterial viability

In a subsequent step of the study, a combination treatment (therapeutic US and AW) was evaluated. Firstly, we evaluated the cavitation activity generated in HW and AW treated samples. As described in section 3.3.5, although lipid-shelled MBs were not introduced into the treatment solution, the electrolysis process continuously generated a substantial volume of gas in the form of small, unshelled bubbles during the 5 min AW manufacturing process. Due to buoyancy and the high solubility of molecular oxygen and hydrogen in water, the bubbles generated during electrolysis were very short lived. We hypothesized that this process could leave the AW solutions saturated with dissolved gases, facilitating gas bubble nucleation at the substrate surface during US treatment compared with HW treated samples.

The total cavitation energy generated during US treatment was estimated from PCD measurements, as described in the Methods section. The results, presented in figure 3.3, confirm that the total acoustic emissions generated from AW treated samples were significantly higher than those from samples treated under the same conditions in the presence of HW. This behaviour indirectly supports our hypothesis that AW may exhibit a lower cavitation threshold than standard HW, due to its higher dissolved gas concentration. No significant differences in cavitation activity were detected among AW samples produced using electrolyte solutions of different concentrations.

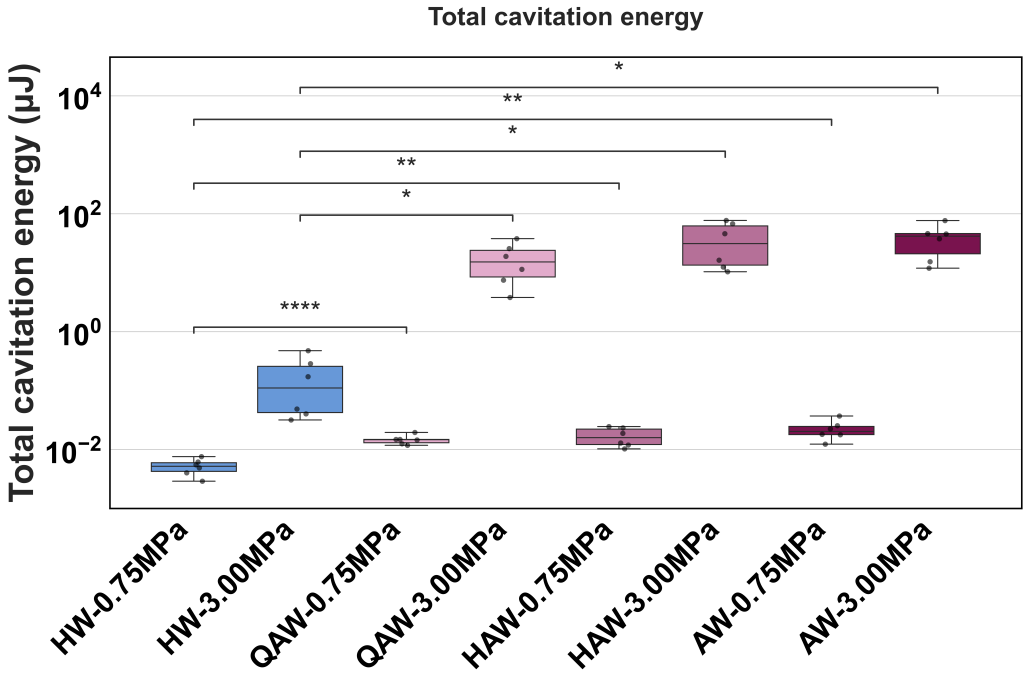


Figure 3.3: Broadband cavitation emission energy measured in the presence of HW or AW at increasing pnp.
$n = 6$ (biological replicates) for all conditions. Groups were compared using one-way ANOVA followed by Bonferroni adjusted t-tests. $*p < 0.05$, $**p < 0.01$, $***p < 0.001$, $****p < 0.0001$.

Figure 3.4 shows representative PSD plots obtained from passive acoustic measurements performed during treatment of samples with either HW or AW. Representative plots are shown only for one AW formulation because all AW samples exhibited virtually identical acoustic behaviour.

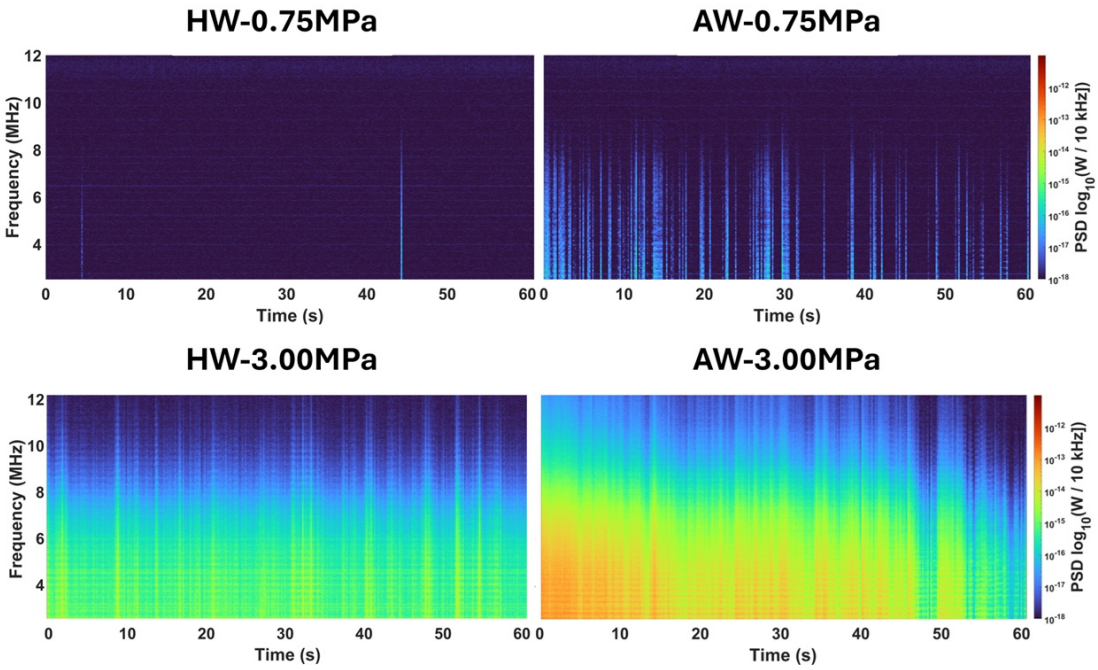


Figure 3.4: Power spectral density (PSD) plots, representing the spectral content of sound passively recorded during US experiments. The left panels are representative tracks recorded for samples treated with HW at either 0.75 or 3.00 MPa pnp, whereas the right panels were recorded for samples treated with AW at the same pnps. The abscissa is time (in seconds) elapsed from the beginning of treatment, while the ordinate is the frequency content of the signal in MHz. The magnitude of each frequency (10 kHz resolution) is represented by the colormap. Thin high magnitude bands at the harmonics and ultraharmonics of the driving frequency (0.5 MHz) are expected in the presence of sustained non-inertial cavitation, whereas high magnitude signal spread over a broad range of frequency suggests inertial collapse of bubbles at the focus of the US field.

At the lower focal pressure value (0.75 MPa pnp), HW produced no appreciable acoustic emissions above the background noise, apart from very brief and isolated bursts of broadband signal. In contrast, samples treated with AW at the same pressure exhibited both quantitatively and qualitatively different behaviour. Throughout the treatment, sparse but recurrent broadband bursts were observed, with their intensity gradually decreasing towards the end of the exposure.

No clear harmonic bands were detected in these traces.

At the higher focal pressure value (3.00 MPa pnp), both HW and AW treated samples exhibited broadband emissions throughout the treatment. However, the emission intensity was substantially higher in AW treated samples. In both groups, distinct harmonic bands were also observed in the PSD traces, particularly during bursts of high broadband emission. The signal intensity in AW treated samples at 3.00 MPa progressively decreased during treatment, suggesting that ultrasonically induced cavitation could be degassing the treatment solution.

The effects of the treatment on bacterial viability are presented in figures 3.1 and 3.2. As already discussed above, the treatment efficacy is AW concentration dependent both for CFU counts performed on HIB and MACB agar plates. This trend is confirmed also in the combination therapy. Similarly to what was already observed for the AW only treatment, the efficacy is also dependent on the state of the bacteria: complete eradication, or close to it, was achieved in virtually all the treated supernatant samples, in which the bacteria are free floating in their planktonic form. In contrast, the bactericidal effect of the combination therapy showed a marked dependency on AW concentration for the samples still attached to the HA disc.

Although not obvious at first glance, the combination of US and AW treatment determined an improved antimicrobial effect when compared to AW alone, with improved effect especially in the bacteria still attached to the HA substrate. As shown in tables 3.4 and 3.5, although no statistical difference in control and AW-low and AW-medium alone was verified, the combination therapy with US at 3.00 MPa pnp shows statistically significant efficacy improvement compared to the control at both concentrations; in particular the treatment with AW alone determined a viability reduction of 0.7 ± 0.1 log and 1.9 ± 0.3 log for AW-low and -medium respectively, whereas the combination therapy determined a viability reduction of 2.9 ± 0.1 log

and 3.2 ± 0.3 log for the two AW concentrations respectively. The same is true for the combination therapy with US at 0.75 MPa pnp at AW-medium concentration, where the viability reduction goes from 0.7 ± 0.1 log and 1.9 ± 0.3 log to 1.5 ± 0.26 log and 2.7 ± 0.2 log respectively.

In addition, statistically significant improvement in antimicrobial effects was verified between AW-low and AW-low+US at 3.00 MPa pnp both for total bacteria cultured on HIB and for a selected group of G- cultured on MACB; the combination with US determined an additional ~ 1.7 log bacterial viability reduction compared to the AW only treatment. For the G- group, a statistically significant reduction in viability was verified also between AW-medium and AW-medium+US at 3.00 MPa pnp treatment, with an US-induced additional reduction in bacterial viability of ~ 2.3 log.

Results of statistical analysis for the supernatant samples are not shown for conciseness since they did not provide any additional insight to what already discussed in the sections above, with the only exception that we verified a statistically significant reduction in bacterial viability between supernatant samples treated with AW-low and AW-low+US at 3.00 MPa pnp (adjusted $p - value \sim 0.001$), confirming the positive effect of the combination therapy on treatment outcomes.

Although previous work pointing at synergy between antimicrobial therapy and US treatment, for different antimicrobial compounds, has been published before [6–8, 92, 173], it is still not completely defined which conditions (*e.g.* US parameters), for which bacterial strains, and for which antimicrobials, US combination therapy could yield meaningful improvement to the treatment outcomes. The results reported in this section not only confirm that the effect of AW is amplified by concurrent delivery of therapeutic US at 500 kHz, but the effect is definitely

peak pressure and cavitation energy-dependent. The combination therapy did not show drastically different effect on a selected group of G- strains growing on MACB agar plates or on total bacteria, partly in disagreement with previous claims [91, 134, 174–177], indicating that the bactericidal effect of US treatment is strictly dependent on the selected parameters, conditions of exposure, and the biofilm mechanical and biological characteristics.

Although the results presented in this work strongly support that US treatment can adjuvate the antimicrobial activity of small molecules, it is necessary to underline that the bacterial community present in the biofilm model was not thoroughly characterized. For this reason, although the viability results are still valid, a precise effect of US mediated treatments on the bacterial population composition cannot be determined from the current dataset. The biofilm model employed in this work was generated from pooled clinical saliva samples to reproduce, as closely as possible, the complexity of the oral microbiota. However, the aerobic conditions selected for the culturing process would already be expected to shift the bacterial composition compared with the original saliva sample. The microbial composition of both the inoculum and the mature biofilms was not assessed beyond conventional culture methods. Therefore, it cannot be established whether the observed reduction in bacterial viability affected all members of the microbial community uniformly or whether specific bacterial groups were preferentially susceptible or resistant to the treatment. Likewise, it is not possible to determine whether the combination therapy induced changes in the bacterial composition that could influence the long-term stability or pathogenicity of the biofilm.

The use of Heart Infusion agar and MacConkey agar provided only a coarse characterization of the bacterial population, allowing the quantification of the total culturable bacteria and of a se-

lected group of Gram-negative microorganisms, respectively. However, culture-based methods cannot reliably identify changes in microbial diversity or detect selective enrichment or depletion of individual bacterial species following treatment.

Future studies should complement viability measurements with molecular characterization of the biofilm community. Sequencing of the 16S rRNA gene would enable taxonomic characterization of the bacterial community before and after treatment, making it possible to evaluate changes in species diversity and relative abundance. Such analyses would clarify whether therapeutic US, either alone or in combination with AW, exerts a selective effect on particular bacterial groups or broadly affects the whole microbial community.

An even more comprehensive characterization could be achieved through shotgun metagenomic sequencing. Metagenomics would simultaneously improve the taxonomic resolution of the analysis and provide information on the functional genetic content of the biofilm. This could enable the identification of genes associated with antimicrobial resistance, biofilm formation, or other biological functions that may influence the response to AW, US, or their combination. Integrating these molecular approaches with the viability assays presented in this work would provide a more complete understanding of the mechanisms underlying the enhanced antimicrobial efficacy observed with the combined US and AW treatment, while also assessing whether the therapy preserves or disrupts the composition of the oral microbial community.

Table 3.4: Pairwise comparisons for the combination treatment conditions for HA Disc location in HIB culturing media. Adjusted p-values are corrected for multiple comparisons.
ns = not significant, * $p < 0.05$, ** $p < 0.01$, *** $p < 0.001$

Group 1	Group 2	Location	Media	Adjusted p	Significance
Control	AW - low	Disc	HIB	0.0825	ns
Control	AW - low - 0.75 MPa	Disc	HIB	0.1908	ns
Control	AW - low - 3.00 MPa	Disc	HIB	4.04×10^{-7}	***
Control	AW - medium	Disc	HIB	0.1086	ns
Control	AW - medium - 0.75 MPa	Disc	HIB	2.38×10^{-3}	**
Control	AW - medium - 3.00 MPa	Disc	HIB	6.25×10^{-3}	**
Control	AW - high	Disc	HIB	7.54×10^{-57}	***
Control	AW - high - 0.75 MPa	Disc	HIB	7.54×10^{-57}	***
Control	AW - high - 3.00 MPa	Disc	HIB	7.54×10^{-57}	***
AW - low	AW - low - 0.75 MPa	Disc	HIB	1	ns
AW - medium	AW - medium - 0.75 MPa	Disc	HIB	1	ns
AW - high	AW - high - 0.75 MPa	Disc	HIB	1	ns
AW - low	AW - low - 3.00 MPa	Disc	HIB	3.71×10^{-6}	***
AW - medium	AW - medium - 3.00 MPa	Disc	HIB	0.0735	ns
AW - high	AW - high - 3.00 MPa	Disc	HIB	1	ns

Table 3.5: Pairwise comparisons for the combination treatment conditions for HA Disc location in MACB culturing media. Adjusted p-values are corrected for multiple comparisons.
ns = not significant, * $p < 0.05$, ** $p < 0.01$, *** $p < 0.001$

Group 1	Group 2	Location	Media	Adjusted p	Significance
Control	AW - low	Disc	MACB	0.6836	ns
Control	AW - low - 0.75 MPa	Disc	MACB	0.1582	ns
Control	AW - low - 3.00 MPa	Disc	MACB	2.88×10^{-9}	***
Control	AW - medium	Disc	MACB	0.0666	ns
Control	AW - medium - 0.75 MPa	Disc	MACB	0.0151	*
Control	AW - medium - 3.00 MPa	Disc	MACB	1.99×10^{-3}	**
Control	AW - high	Disc	MACB	9.17×10^{-53}	***
Control	AW - high - 0.75 MPa	Disc	MACB	9.17×10^{-53}	***
Control	AW - high - 3.00 MPa	Disc	MACB	9.17×10^{-53}	***
AW - low	AW - low - 0.75 MPa	Disc	MACB	1	ns
AW - medium	AW - medium - 0.75 MPa	Disc	MACB	0.2299	ns
AW - high	AW - high - 0.75 MPa	Disc	MACB	1	ns
AW - low	AW - low - 3.00 MPa	Disc	MACB	7.00×10^{-3}	**
AW - medium	AW - medium - 3.00 MPa	Disc	MACB	0.0195	*
AW - high	AW - high - 3.00 MPa	Disc	MACB	1	ns

3.5 Conclusions

The work presented in this chapter evaluated the possibility of improving the bactericidal effect of small and fast acting molecules (sodium hypochlorite and hydrogen peroxide), using therapeutic US as adjuvant. Building on the work presented earlier in the thesis, 500 kHz was

selected as the fundamental frequency of the US treatment as it represents a compromise between spatial resolution of the treatment (focal diameter ∼3 mm and FWHM diameter ∼ 12 mm), relatively low viscous losses (scaling quadratically with frequency), and easier induction of heterogeneous cavitation at the samples surface in the absence of contrast agents. Again, based on the earlier results, chlorhexidine was substituted with AW as the model antimicrobial drug. This change was made for multiple reasons. First, chlorhexidine's mode of action induces a delayed bacterial death compared to ROS and sodium hypochlorite. It is expected that molecules with a faster bactericidal mode of action might benefit the most from the transient mechanical effect determined by the US on the biofilm and bacterial structures. In addition, AW is an interesting option for oral care management as it can be easily generated in a small medical device feeding from tap water. The tunable and relatively mild antimicrobial of activity of AW is therefore a promising option to reduce disruption of the beneficial oral microbiota.

AW proved to be a viable antimicrobial for the treatment of the saliva derived biofilm model we developed for this work, with results comparable to a popular marketed alcohol free mouthwash, if not better at higher AW concentrations. The proposed *in vitro* model also showed complete resilience to the US treatment itself, as no meaningful drop in CFU count was found in the absence of AW exposure.

After exposing the biofilm model to the AW and US treatments separately, and evaluating the effects of the single treatments on bacterial viability, it was found that the combination of US and antimicrobial agents (here AW) yielded consistent and promising results. Throughout this study, the effect of treatment on total bacteria (CFU count performed on HIB agar plates) and on a selected group of G- bacteria (CFU count performed on MACB agar plates), were evaluated separately, as previous published work suggests that G- might be more susceptible to the me-

chanical stress induced by the US treatment. Although the results partly agree with data from literature, as a marginally increase in effect of the combination therapy of AW-medium and US was shown only for the G- bacteria grown on MACB agar plates, the bactericidal effect of the combination therapy was not dramatically different between total bacteria and G-s. Regardless of strain specific effects, the combination treatment determined a reduction in CFU counts compared to the AW treatment alone. This improvement in bactericidal effect of the combination treatment was more pronounced when the focal pressure magnitude of the US was increased to 3.00 MPa pnp. The higher US intensity determined a marked and statistically significant reduction in bacterial viability in the treated samples. The treatment had similar effects on both total bacteria and G- ones. An improvement in bactericidal activity was demonstrated also for free floating bacteria treated at the lowest AW concentration.

3.6 Supplementary material

3.6.1 Iodometric titration of hypochlorus acid, hydrogen peroxide, and ozone

3.6.1.1 Principle of the titration

Three aliquots measured under different conditions: (1) total oxidants immediately, (2) H_2O_2 inactivated by HRP before titration, and (3) after ozone decomposition over time.

$$O_3 + 2I^- + 2H^+ \rightarrow I_2 + O_2 + H_2O \tag{3.1}$$

$$HOCl + 2I^- + H^+ \rightarrow I_2 + Cl^- + H_2O \tag{3.2}$$

$$H_2O_2 + 2I^- + 2H^+ \rightarrow I_2 + 2H_2O \tag{3.3}$$

Equations (3.1) to (3.3) show the oxidation of iodate ions to iodine determined by the three analytes considered in this titration study.

$$I_2 + 2S_2O_3^{2-} \rightarrow 2I^- + S_4O_6^{2-} \qquad \text{(Iodine titration using thiosulfate)}$$

$$2H_2O_2 \xrightarrow[\text{pH 7}]{\text{HRP}} 2H_2O + O_2 \tag{3.4}$$

3.6.1.2 Ozone Decomposition

As described in [178, 179], ozone decomposition at pH $\sim$7 is relatively slow, with half-life of up to 100 minutes. For this reason Na_2HPO_4 is added to the sample, to increase the pH to 8 and reduce ozone half-life to around 10 minutes. The sample is then left in the dark and under agitation for 90 minutes, leading to an expected ozone concentration reduction $>$95%

3.6.1.3 Procedure

Evaluation of total oxidants:

1. To 50.0 mL fresh sample, add $\sim$5 mL acid buffer (citrate-HCl pH 2.7) until pH=3.5
2. Add 1 or 2 mL 10% KI (has to be in excess), stopper, dark, 5 min
3. Titrate with standardized $Na_2S_2O_3$, 1% starch solution to endpoint

4. Towards the end, allow time for the blue particulate to react, it takes up to 1-2 minutes for it to disappear. Not waiting long enough determines overestimation.

5. Record V_1

$$n_{\text{total}} = \frac{C_t \times V_1}{2}$$

Evaluation of oxidant after inactivation of hydrogen peroxide using HRP:

1. To 50.0 mL fresh sample, add 5 mL phosphate buffer pH 6.0

2. Add 0.5 mL of HRP solution, stir 15 min (destroys H_2O_2)

3. Add ∼5 mL of acid buffer (citrate-HCl pH 2.7) until pH=3.5 + 1 or 2 mL 10% KI (you have to be sure it is in excess)

4. Stopper, dark, 5 min, titrate with $Na_2S_2O_3$, 1% starch solution to endpoint

5. Record V_2

$$n_{O_3+Cl_2} = \frac{C_t \times V_2}{2}$$

Evaluation of oxidant after inactivation of ozone in slightly alkaline conditions:

1. To 50.0 mL sample add 2ml of Na_2HPO_4 or until pH=8. Then store in dark at room temperature for 1.5 hours

2. Add ∼5 mL of acid buffer (citrate-HCl pH 2.7) until pH=3.5 + Add 1 or 2 mL 10% KI (you have to be sure it is in excess)

3. Stopper, dark, 5 min, titrate with $Na_2S_2O_3$, 1% starch solution to endpoint

4. Record V_3

$$n_{Cl_2+H_2O_2} = \frac{C_t \times V_3}{2}$$

3.6.1.4 Calculations

$$[H_2O_2] = \frac{n_{\text{total}} - n_{O_3+Cl_2}}{0.050}$$
$$[O_3] = \frac{n_{\text{total}} - n_{H_2O_2+Cl_2}}{0.050}$$
$$[Cl_2] = \frac{n_{\text{total}}}{0.050} - [H_2O_2] - [O_3]$$

3.6.2 Bovine enamel mechanical wear protocol

4x4 mm *ex-vivo* bovine incisors enamel specimens, polished up to 4000 grit silicon carbide sandpaper (Intertek Clinical Research, Brentwood, Essex, UK), were used to evaluate the mechanical wear induced by the ultrasonic treatment. As a control, the samples were also subjected to the standard practice of mechanical brushing using an electric sonic toothbrush (Sonicare diamond clean 9000, Philips, Eindhoven, NL). The objective of this test was to evaluate the wear determined by one year of either therapeutic ultrasound treatment or mechanical brushing with an electric toothbrush available on the market. Data from the literature [180, 181] show that on average an adult spends up to ∼8.5 seconds brushing the same spot each day, with a force of 2.2 N, which amounts to ∼55 minutes of total brushing time in one year when the subject brushes twice daily. For the ultrasonic treatment devised in this study we hypothesised that the standard protocol would entail one treatment daily, corresponding to one minute of continuous US exposure, which amounts to 6 hours of total exposure time over one year.

For the wear study, we only considered the greater pnp magnitude of 3.00 MPa pnp. This value is well above the inertial cavitation threshold in the proposed set-up, probably due to the presence of a rough surface at the focus, acting as nucleation site for the gas dissolved in the media. Cavitation measurements were performed during each experiment, to ensure continuous inertial cavitation throughout the treatment. The cavitating media (undegassed deionised water) was changed every 30 minutes to allow for consistent cavitation throughout the experiment.
The wear determined by one year of simulated mechanical treatment was evaluated by optical profilometry measurements. Each sample was analysed using a VHX-5000 optical profilometer (Keyence International NV/SA, Mechelen, Belgium) before treatment to evaluate sample flatness, and eventual slopes and drifts due to manufacturing inconsistencies. Following the initial pre-treatment evaluation, half of the sample was covered with adhesive tape, to protect it from the wear. The tape-covered section was then used as an internal control during the profilometry measurements performed after the treatment.
For each sample two types of profilometry images were obtained: a series of stitched images at 200x magnification with 1.8 μm vertical pitch resolution, to evaluate the effect at a large but low resolution scale; multiple images in random locations at 1000x magnification with vertical pitch of 0.5 μm, to obtain insights into microscopic damage at higher resolution.

3.6.3 Bovine enamel wear over 1 year of simulated treatments

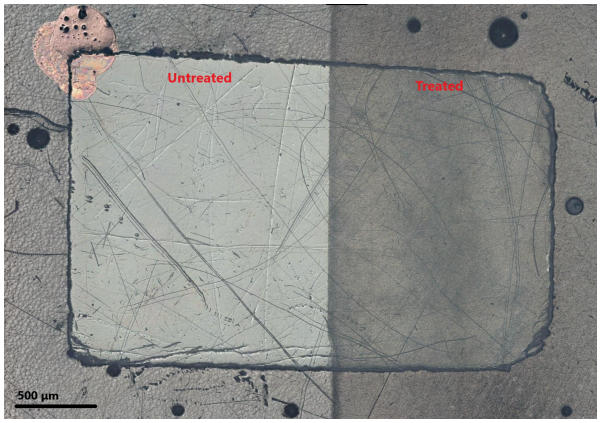
Due to the corruption of the profilometry files obtained and the impossibility to repeat the measurements due to samples disposal, the data reported in this section are incomplete. This is also the reason why this set of data is presented only in the supplementary material rather than the

main text.

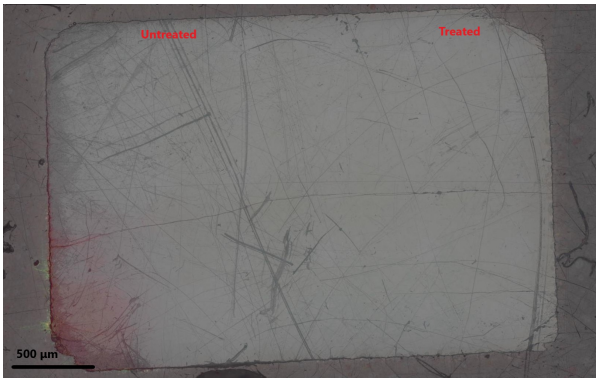
It is well known, and reported in literature, that mechanical brushing, especially when performed with an electric toothbrush, determines enamel wear overtime [182]. The wear is usually minimal for enamel ($< 1\mu$m/year), whereas it can be more significant in the case of exposed dentin (up to 30 μm/year).

Given the complete lack of data in the literature, reporting the possible dental wear due to US treatment in the frequency, duty cycle and pressure range utilised in this work, we decided to run a first preliminary study and report our findings. Although at the moment we still cannot provide quantitative wear estimation, we plan to expand these results in the future and evaluate the effects of US treatment over longer exposure times and in presence of exogenous cavitation nuclei.

At present, we would like to present two representative set of images showing qualitatively the striking difference in effect of 1 year of simulated US treatment and 1 year of brushing with an electric sonic toothbrush.

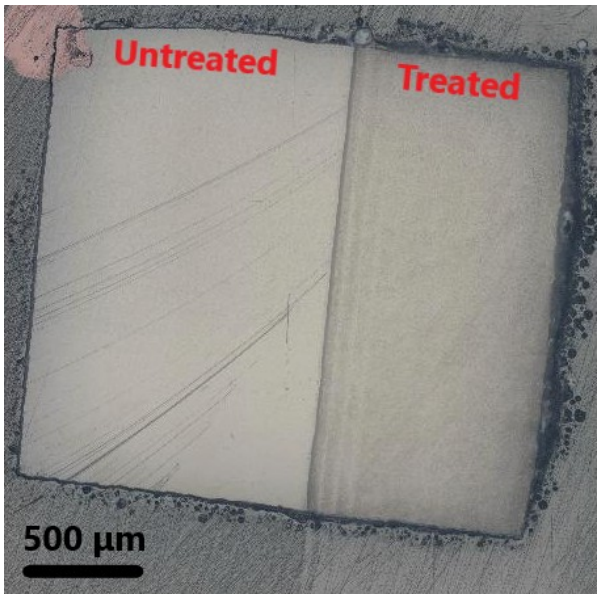


(a) Bovine enamel sample brushed with a sonic brush simulating 1 year of wear

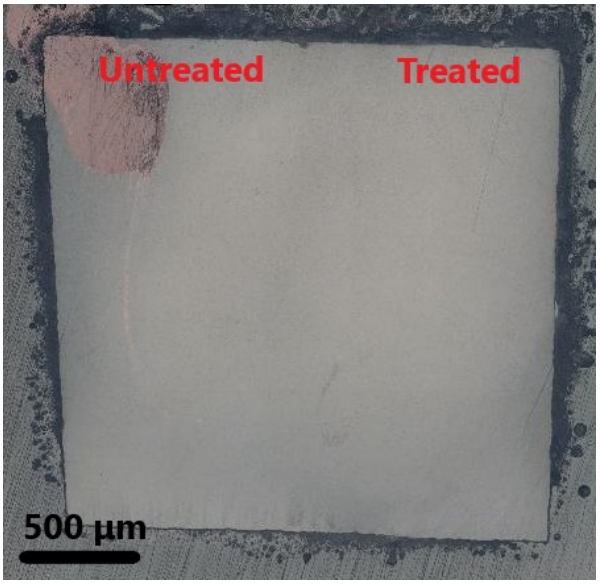


(b) Bovine enamel sample exposed to US treatment at 3.00 MPa pnp simulating 1 year of wear

Figure 3.5: Visual representation of bovine enamel wear induced by 1 year of simulated brushing and US treatment. This images were recorded at 200x magnification. Unfortunately No scale-bars can be included in these images due to corruption of the datasets.



(a) Bovine dentine sample brushed with a sonic brush simulating 1 year of wear



(b) Bovine dentine sample exposed to US treatment at 3.00 MPa pnp simulating 1 year of wear

Figure 3.6: Visual representation of bovine dentine wear induced by 1 year of simulated brushing and US treatment. This images were recorded at 200x magnification. Unfortunately No scale-bars can be included in these images due to corruption of the datasets.

Representative profilometry images of enamel and dentin samples subjected to one year of simulated treatment are shown in figures 3.5 and 3.6. In both enamel and dentin specimens exposed to mechanical brushing, the treated region can be qualitatively distinguished from the protected area (used as internal control) by its darker grey appearance, suggesting surface wear following the brushing protocol. In contrast, no obvious visual difference between the treated and untreated regions could be identified in either enamel or dentin samples exposed to therapeutic US, indicating that the treatment did not produce appreciable surface wear detectable by optical profilometry.

All specimens exhibited scratches across their surfaces. These marks were already present be-

fore treatment and originated from the polishing procedure used during sample preparation, rather than from treatment modality.

Interestingly, the brushed samples appeared to exhibit less pronounced polishing scratches within the treated region, likely due to the progressive removal of the superficial surface layer during the simulated brushing procedure. No comparable change in scratch appearance was observed in the ultrasound-treated specimens.

It should be noted that these observations are purely qualitative. Owing to corruption of the profilometry datasets embedded within the acquired images, quantitative measurements of surface wear could not be recovered. For this reason, no quantitative comparison between the treatment groups can be reported from this preliminary study.

Chapter 4

Proof-of-concept — In-line production and use of therapeutic ultrasound cavitation nuclei

One of the major limitations of using cavitation nuclei in US therapies is that MB agents are supplied in small volume vials and have fixed size distributions optimized for intravenous use only. To address this limitation, a laboratory-scale device capable of generating MBs of tunable size through electrolysis (Embs) was developed. This proof-of-concept device is used to demonstrate the possibility of reproducibly generating MBs as part of an in-line system to perform therapeutic US treatment on a previously described *S. mutans* biofilm model. We compared the treatment efficacy with results previously obtained using SonoVue-like MBs manufactured using a homogenisation batch method (THmbs).

4.1 Materials and Methods

4.1.1 Materials

All of the 3D printed parts were manufactured using either a Formlab Form2 stereolithography (SLA) printer with Formlab grey resin (Formlabs, GmbH, 12459 Berlin, Germany) or an Ultimaker S5 FDM printer with Ultimaker tough polylactic acid (PLA) (Ultimaker B.V., 4191 PN Geldermalsen, Netherlands). Computer aided design (CAD) models were produced using Autodesk Inventor Professional 2024™ (Autodesk, San Francisco, CA 94105, USA). Data processing was performed either in MATLAB 2023b (The MathWorks Inc., Natick, Massachusetts, USA) or Python (version 3.9.13). The complete scripts are provided in the Supplementary Material section.

4.1.2 Device design

The device utilized in this work was composed of four sections, represented in figure 4.1. A syringe pump (NE-1000, New Era Pump systems Inc., NY, USA) was used to force the fluids through the system at flow rates between 1 and 20 mL/min. 60 mL syringes (Fisherbrand, UK) were used as reservoirs. The first stage was an electrolysis chamber equipped with two gold mesh electrodes ($\sim$ 8x15 mm, mesh 100, Fisher Scientific, UK) connected to a programmable power source (Teledyne T3AFG40, Teledyne, CA, USA) providing a variable voltage in AC or DC mode. The bubbles generated by the electrolysis process were then passed through the second stage of the device, composed of a flat 63 kHz bolted ultrasound transducer coupled to a Teflon™ tube using a 3D printed resin block figure 4.2, air gaps were eliminated using a

thin film of castor oil. This acoustofluidic section was designed to maximise the peak positive pressure magnitude in the fluid flowing through the device, inducing buckling and bursting of the bubbles, ultimately reducing their size [183, 184].

The piezoelectric element selected to build the acoustofluidic section of the MBs generator had a resonant frequency of 63.05 kHz. The transducer was designed by the manufacturer to have electric impedance ranging from 100 to 7 Ω in the ∼62 to ∼64 kHz frequency range. For this reason, and following a standard approach already described in the literature [185], we decided to run the piezoelectric element using a frequency sweep, rather than including an impedance matching network in the system. Specifically, the driving signal was swept from 62.3 to 63.7 kHz with 20 ms period.

The last section of the device was a 3D printed sample holder connected directly to the flow system transporting the produced MBs. The holder was designed to position a 12 mm diameter, 2.3 mm thick HA disc (HADEL02, Himed, NY 11804, USA) at the focus of a HIFU US transducer (H107, 0.5 MHz fundamental frequency, 63.2 mm geometrical focus, 64 mm active element diameter, custom rectangular cut out of 22×57 mm, Sonic Concepts Inc., Washington, USA), as shown in figure 4.8. Samples were held facing downwards, favouring interaction between the biofilm and the generated MBs through buoyancy.

The concept of lipid-shelled bubbles size reduction using a small acoustofluidic device was already described in the literature for a different application by Carugo *et. al.* [185]. In the present work, the bubbles are generated through an electrolysis process rather than by flow focusing in a microfluidic device as previously described. The electrolysis process reduces control over the initial bubble size distribution, but allows the generation of chemical species such as ROS, bleach, and ozone; opening new possibilities for the *in situ* generation of antimicro-

bials for biofilms treatment in the future. For the sake of simplicity, we utilised gold electrodes in this particular preliminary study, reducing the generation of metallic oxides products to the minimum. We focused mainly on gas and MBs production rates, rather than trying to optimize antimicrobial activity of the generated suspension.

4.1.3 Acoustic modelling of the device

Numerical simulations were performed using COMSOL Multiphysics (COMSOL inc., MA, USA) in order to predict the acoustic pressure distribution within the acoustofluidic device and to optimize the device geometry for maximum pressure amplitude inside the Teflon™ channel location; the model was implemented in the Pressure Acoustics, Frequency Domain interface. The geometry was constructed in two dimensions to represent the cross-section of the whole device (the fluid domain and the encompassing solid domains). The acoustic pressure field p within the fluid domain was governed by the Helmholtz equation:

$$\nabla \cdot \left(\frac{1}{\rho(\mathbf{r})} \nabla \hat{p} \right) + \frac{\omega^2}{\rho(\mathbf{r})\, c(\mathbf{r})^2}\, \hat{p} = 0 \tag{4.1}$$

where $\omega = 2\pi f$ is the angular frequency, $\rho(r)$ is the density of the fluid, and $c(r)$ is the speed of sound in the fluid, and $\hat{p}$ is the complex pressure amplitude. The model was driven by a harmonic out-of-plane displacement applied to the piezoelectric element face, simulated using a normal displacement boundary condition. The outer boundaries of the device were treated as sound-hard boundaries (wall, impedance = ∞), corresponding to a zero normal acceleration condition.

A frequency-domain study was performed at the device mean operating frequency (63.0 kHz). To identify the optimal configuration, a parametric sweep was conducted over critical device dimensions: the total length of the 3D printed resin propagation block and the location of the fluid domain within it. The fluid domain dimensions were kept constant, as they are constrained by the Teflon™ tube used to build the device. For each iteration in the sweep, the steady-state acoustic pressure field was computed.

Following the parametric analysis, the optimal device dimensions were selected based on the criterion of maximizing the average acoustic pressure intensity and the peak positive pressure in the fluid domain, as bubble buckling is favoured by their compression rather than rarefaction [183, 184].

4.1.4 MBs lipid formulation

Given the relatively high volume of solutions needed to run this proof of concept device, we selected lecithin as the main lipidic component of the formulation due to its low cost compared to purified phospholipids. Lecithin refers to a mix of phospholipids of natural origin, composed mainly of phosphatidylcholine and in lesser part of a mixture of various other phosphatides. For this work, we used lecithin extracted from soy beans with L-αphosphaditilcholine content $>$90% (ThermoFisher Scientific, UK). Following data from our previous study and the literature [186–188], we opted for a formulation containing lecithin, PEG-40-S, and cholesterol in a 9:1:1 molar ratio. The lipid components were first dissolved in 20 mL propylene glycol under magnetic stirring at 37°C for 10 minutes, aiming at 200 mg/mL lecithin concentration. Once the lipids were completely dissolved, they were added drop wise to 180 mL of PBS. During this

process the PBS was kept at 60°C and under vigorous magnetic stirring (∼600 rpm). Once the whole lipidic solution was added to PBS, the milky solution was sonicated using a 20 kHz probe sonicator (Fisherbrand™ 505 Sonicator, UK) at 80% amplitude, in pulsed sonication mode (10 seconds on, followed by 6 seconds off), for a total time of 25 minutes. During the sonication process the temperature of the solution was kept between 60 and 70 °C. After sonication the solution presented itself as translucent, slightly turbid, and with a slight green-blue tint. The obtained liposomes were then characterised using a DLS particle size analyzer (Zetasizer, Malvern Panalytical, UK) and were deemed stable at 4°C for up to two weeks. The final concentration of lecithin in the liposomes was 20 mg/mL. The solution was either used as is or diluted with PBS to a final concentration of lecithin of 10, 5, 2, or 1 mg/mL.

The protocol used to produce THmbs is the same as that described in section 2.3.6. This formulation is also referred to as SonoVue-like in this work because, unlike Embs, THmbs are heavy-gas-core bubbles featuring DSPC in their lipid shell with mean equivalent spherical diameter ~ 1 μm, making them similar to SonoVue, the clinically approved ultrasound contrast agent produced by Bracco.

4.1.5 Quantification of MB size and concentration by optical microscopy

The electrolysis process determines formation of hydrogen and oxygen gases mainly. As thoroughly reported in the literature [189, 190], one of the reasons for reduced air-core bubbles stability is the higher water solubility of gases like O_2 and N_2, which determines an increased concentration gradient between the inside and outside of the MBs and faster bubbles dissolution. Oxygen solubility in water sit at around 40 mg/mL at room temperature and atm, whereas

in the same conditions perfluoro-butane has a solubility of about 1.5 mg/mL [191, 192]. Due to the very low stability of our formulation, the only sizing method we successfully used to estimate size and concentration of the produced MBs was optical measurement using a microscope. To perform such measurements, the set-up was kept as described in section 4.1.2, but the stage normally used for the therapeutic US treatment was swapped with an optical microscope. The bubbles were passed through an optically clear channel (μ-Slide Luer, 400 μm depth, Ibidi GmbH, Gräfelfing, Germany) and the flow was stopped temporarily to capture the images. After each imaging step, the system was completely flushed before producing more bubbles and taking subsequent images.

Bubbles' size and concentration was quantified with an in-house Python script (version 3.9.13) available in the supplementary material. Very briefly, the script automatically finds the centre of each bubble (even when multiple bubbles are in contact with each other), exploiting the light diffraction caused by the lipid shell during imaging, and then proceeds to evaluate the radius of each one by finding the shortest path between each centre and the closest blob edge. Multiple checks are in place to avoid false positives or wrong path selection in edge cases. Data obtained from multiple images were pooled to compute bubbles size distribution for each sample.

To assess size dispersity of the samples, the polydispersity index (PDI) value for each size distribution was computed as follow: $PDI = (\frac{\sigma}{\overline{X}})^2$, where σ is the standard deviation of the particles' size distribution and $\overline{X}$ is the mean particle size, as defined in ISO 22412:2025 [193].

4.1.6 Evaluation of cavitation-induced biofilm removal

Once the MBs manufacturing capabilities of the device were characterised, we ran a preliminary experiment to demonstrate the possibility of continuous generation of MBs and immediate use for US treatment. For this study, we selected the same biofilm infection model described in chapter 2.

To keep continuity with previous treatment protocols, the treatment time was set to 1 minute, during which Embs were continuously generated and flowed at the sample location. The US parameters were kept unchanged compared to previous experiments, specifically the frequency was set at 500 kHz, the pnp ranged between 0.75 and 3.00 MPa, the US bursts were 1000 cycles long with 5 Hz PRF.

The readers are referred to section 2.3 for a description of the protocols used to produce the biofilm infection model, the fluorescence microscopy image acquisition and analysis, and the PCD method.

4.1.7 Statistical analysis

Biofilm removal data were acquired in separate days to cover all the experimental conditions, due to time restrictions. Given the inevitable biological variability in biofilm growth between experiments carried out on different days, the data were acquired and analysed as follows: on each day and for every condition, three biological replicates were grown for a total of 24 samples. On each day, two control groups were grown: DPBS only (true negative) and DI water or MBs (not exposed to US), depending on the treatment conditions used on that day. The data were then normalised to the same day DPBS control, and significance in the difference between

their mean values was evaluated by performing one-way ANOVA, with the p-value derived from the F-statistic accounting for Holm-Bonferroni correction.

4.2 Results

4.2.1 Device overview and operation parameters

In this work, we developed an acoustofluidic device capable of generating MBs with tunable size, starting from an electrolysis process. An overview of the four stages is presented in figure 4.1

The effect of flow rate on bubble production was evaluated in the range 1 to 20 mL/min. At flow rates below 5 mL/min bubbles had the tendency to coalesce and clog the tubing, producing non-homogeneous bubble dispersion. At 5 mL/min and above, the clogging issue was much reduced or non-existent. For this reason, and whilst attempting to minimise bubble dilution, 5 mL/min was selected as the flow rate for all subsequent testing.

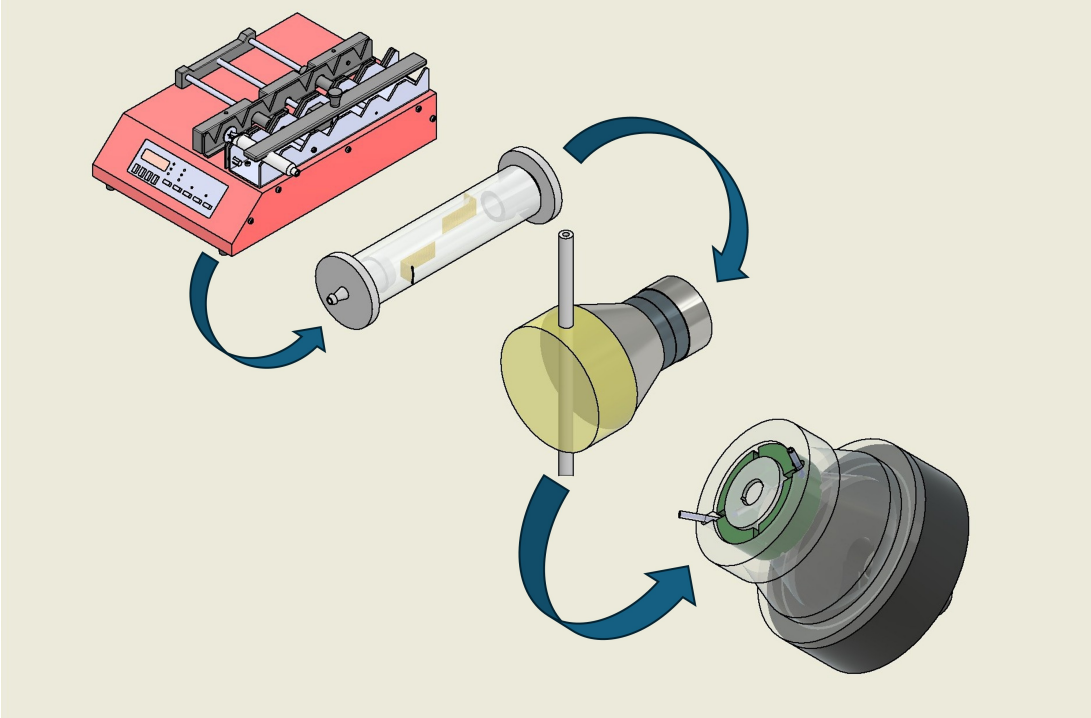


Figure 4.1: Schematic representation of the four components necessary to run the experiment. From left to right, a NE-1000 syringe pump, the electrolysis reactor, the acoustofluidic system utilised to break up the bubbles generated during the electrolysis process, and the therapeutic US set-up in which the biofilm samples received the treatment.

4.2.2 Acoustofluidic MBs generator design

The acoustofluidic stage, shown in figure 4.2 was modelled in COMSOL Multiphysics, to evaluate the appropriate dimensions necessary to obtain a pressure field antinode in the fluid domain, thanks to standing waves interference. Being constrained by both the selected tubing dimensions and the dimensions of the US transducer itself, the modelling focused on evaluating the optimal thickness of the 3D printed resin propagation block and the position of the fluid domain within it.

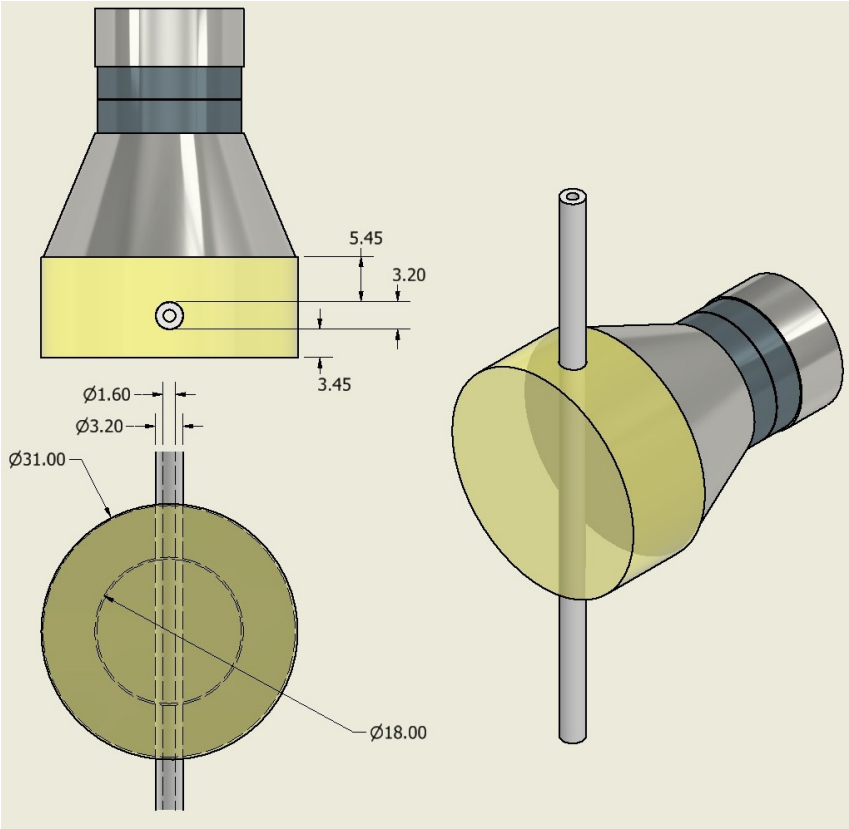


Figure 4.2: Schematic representation of the acoustofluidic device utilised to control the diameter of the manufactured Embs; dimensions are expressed in mm. The device is composed of a bolted piezoelectric element (dark grey), an aluminium propagation block designed by the manufacturer (silver), a 3D printed resin propagation block (translucent yellow), and a 3.2 mm diameter Teflon™ tube through which the bubbles dispersion flows. The device dimensions were optimised through a 2D acoustic model developed in COMSOL Multiphysics.

The results of the optimization process are summarised in figure 4.3 and figure 4.4. The average sound intensity ($\frac{p_{RMS}^2}{\rho c}$) was estimated in the fluid domain, at constant fluid domain dimensions and varying the thickness of propagation media (3D printed resin) frontally and posteriorly (respectively t_Resin_1 and t_Resin_2 in figure 4.3). As clearly visible in figure 4.3,

the average acoustic pressure intensity in the fluid domain presents various relative maximum peaks clusters. These arise when the length of the resin block approaches $\lambda/4$, $\lambda/2$, $3\lambda/4$, and λ considering the whole propagation path and the different bulk sound velocities in the media. The $\sim \lambda/4$ configuration cluster was the one favouring the highest pressure antinode magnitude in the channel, while maintaining the device dimensions relatively contained; for this reason, the local maxima of this cluster was selected as the optimal configuration for the device. In this configuration t_Resin_1 and t_Resin_2 equal 5.5 mm and 3.5 mm respectively, and the expected total acoustic pressure field in the fluid domain is presented in figure 4.4.

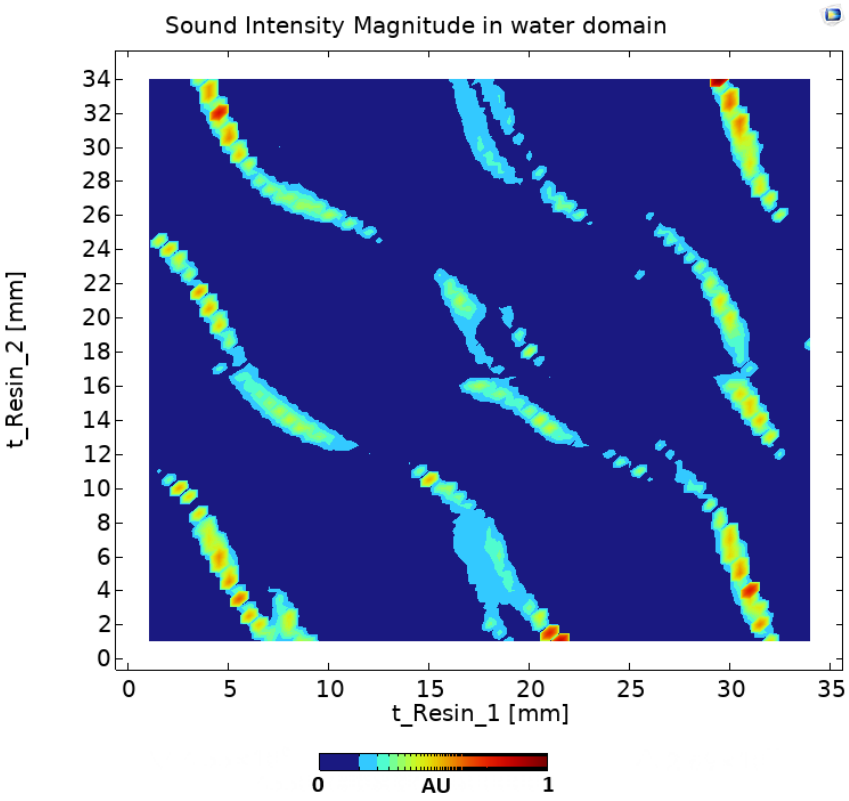


Figure 4.3: Relative rms intensity ($\frac{p_{RMS}^2}{\rho c}$) in the fluid domain estimated through a multiphysics model in COMSOL. We estimated the most advantageous standing wave pattern depending on the resin block dimensions and position of the fluid domain in the propagation block. The sound intensity is represented in arbitrary units (AU) ranging 0 to +1 in log_{10} scale.

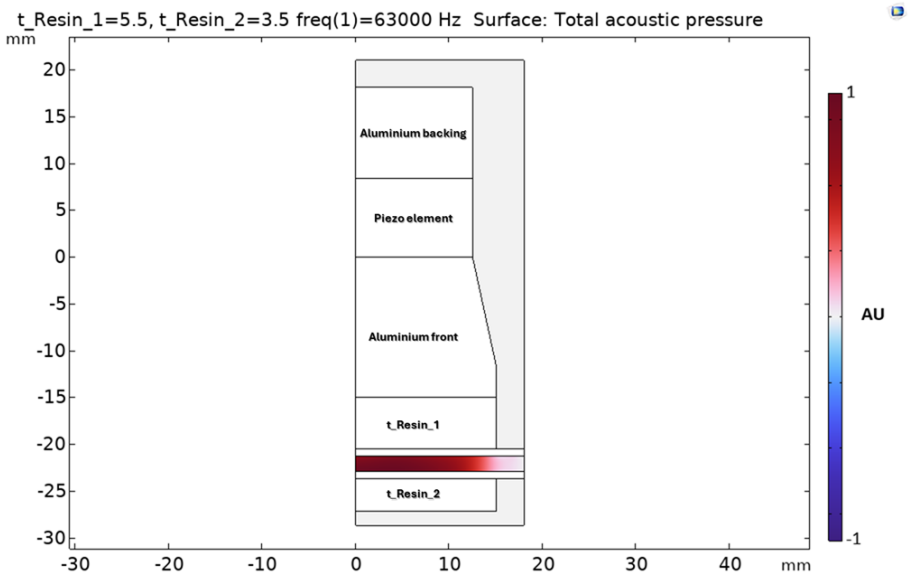


Figure 4.4: Representation of total acoustic pressure field in the fluid domain at the optimized resin block dimensions. The pressure is reported in arbitrary units (AU) ranging -1 to +1 in log_{10} scale.

While an experimental confirmation of the pressure field magnitude would have been ideal, the reduced dimensions of the opening in the propagation block did not allow for the insertion of any hydrophone available to us, capable of reliably measuring the pressure field at 63 kHz. For the scope of this preliminary study, US intensity-dependent bubbles size reduction (presented in section 4.2.3) was accepted as proof that a sufficiently high acoustic intensity was reached in the fluid domain. Further indirect characterization measurements (such as pressure field estimation from transmission measurements through the device backing) will be needed in future optimization of the device.

4.2.3 MBs production and characterization

The first stage encountered by the lipid solution was the electrolysis reactor shown in figure 4.5. Here it would come in contact with two gold meshes electrodes. The electrolysis process was assessed at varying input voltage (1 to 20 V), both in DC and AC mode. The AC frequency was evaluated between 10 and 0.01 Hz. The range was evaluated empirically with preliminary tests on the system.

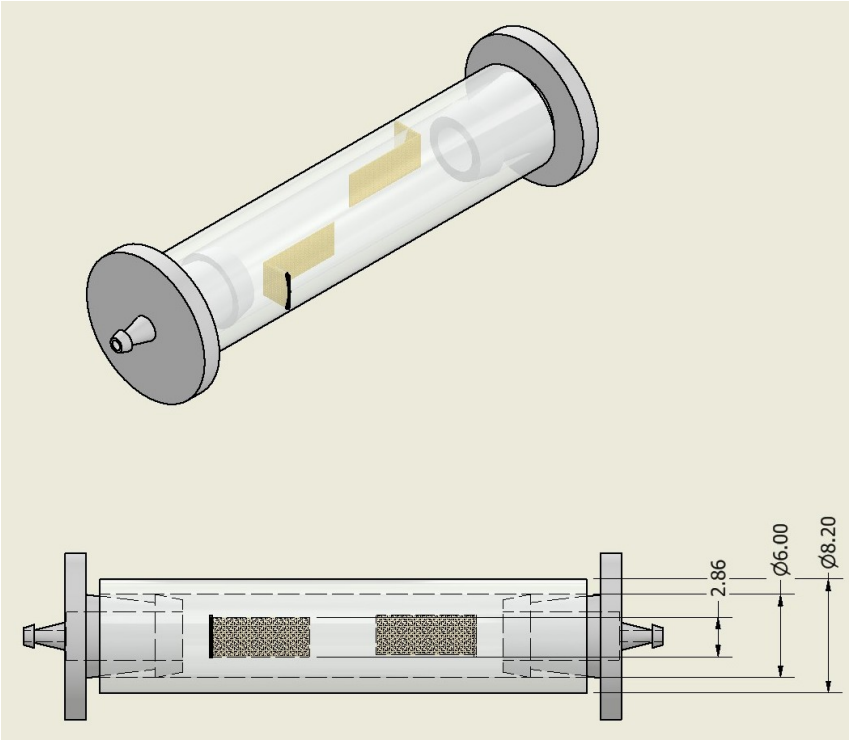


Figure 4.5: Schematic representation of the electrolysis reactor; two straight-through reduction Luer fittings (6.4 mm to 2.4 mm) are placed at the end of a 6 mm inner diameter flexible PVC tube as inlet and outlet. Two gold meshes ($\sim$ 8x15 mm, mesh 100) are positioned in the device through small slits in the tube lining and sealed in place using electrical grade silicon. dimensions are expressed in mm.

The electrolysis of water, when the electrodes' material is pure gold, generates almost exclusively oxygen and hydrogen gases, although redox products of lipid shell components are also inevitable. For this reason, Embs obtained through the method discussed in this work tend to be significantly less stable than the common perfluorocarbon core lipid-shelled MBs used in biomedical imaging applications US. This is mostly due to the high diffusion coefficient of small molecule gases through the lipid shell and redox impurities generated in the process.

In this work, given the relatively large size of the MBs generated through electrolysis and their very low stability, we decided to evaluate their size optically, in a clear optical channel connected in-line with the generator. Although this limited the minimum detectable diameter at $\sim$ 3 μm (calculated as three times the Abbe limit of the optical system used to perform the measurements), it allowed us to avoid time breaks in between generation and measurement of the samples.

Building on previous published work [101, 186, 188, 194] and prior experience, 5 mg/mL was selected as the starting concentration of lecithin for bubble manufacturing. Initially, the effect of increasing voltage was tested. Using DC, depending on the voltage magnitude applied to the system, the reactor either generated a very low number of bubbles or a continuous stream that quickly clogged the tube. For this reason, after testing the 5 to 20 V range for DC, bubble production using AC was investigated instead.

The cyclical potential inversion determined by AC improved bubble detachment from the electrode meshes, reducing drastically foam formation in the tube. After testing AC in a frequency range between 0.1 and 10 Hz (data not shown), we selected 20 V pkpk, 0.2 Hz AC as a good compromise between bubble production rate and reduced clogging/foaming.

Having established a reliable protocol for bubbles generation, the effect of lipid concentration

on bubble formation, size, and stability was investigated. Four concentrations of lecithin were tested: 1, 2, 5, 10 mg/mL, maintaining fixed the molar ratio of the other lipid shell components. At 1 and 2 mg/mL lecithin concentrations, bubbles either did not form or were so unstable that it was not possible to confidently measure their size and concentration with the proposed optical method. At lecithin concentrations of 5 and 10 mg/mL, it was possible to reproducibly obtain bubbles and estimate both their size distribution and concentration, as shown in figures 4.6 and 4.7 (”000V pkpk (no_US)” traces).

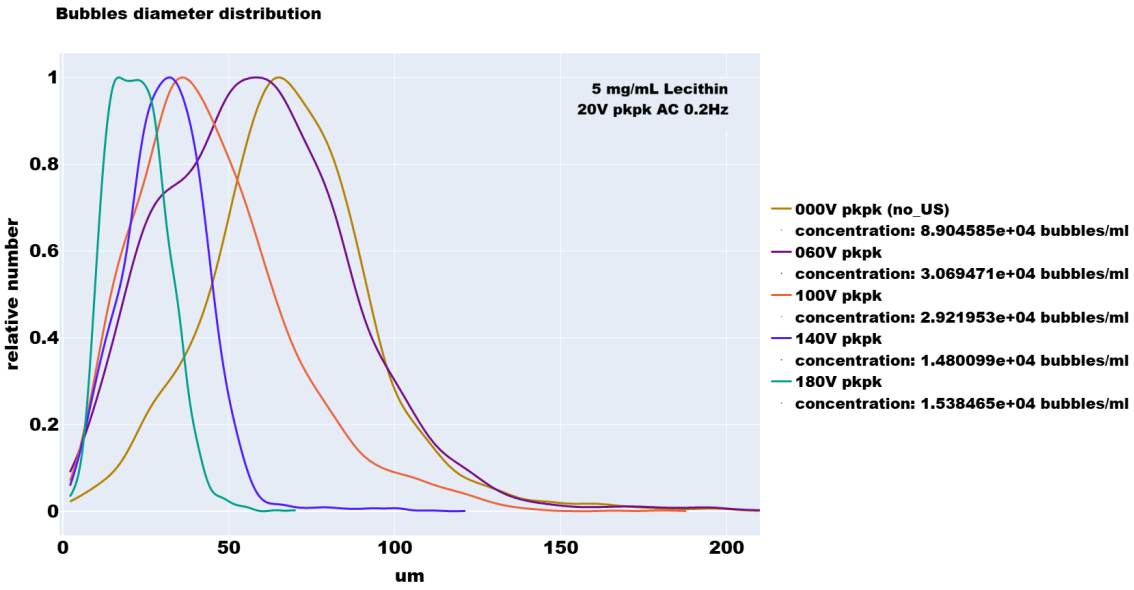


Figure 4.6: MBs equivalent spherical diameter size distribution at increasing acoustofluidic-stage ultrasound field intensities. The transducer peak-to-peak driving voltage is indicated in the rightmost legend. The lecithin concentration (fixed at 5 mg/mL) and the electrolysis driving voltage (20 V pkpk at 0.2 Hz) are shown in the upper-right corner of the plot.

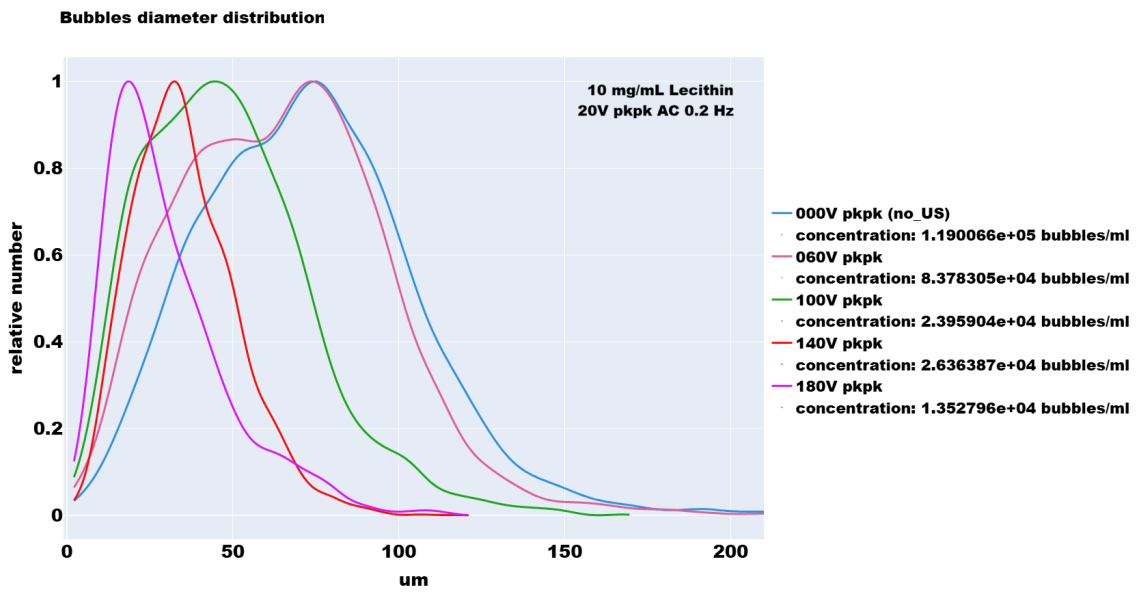


Figure 4.7: MBs equivalent spherical diameter size distribution at increasing acoustofluidic-stage ultrasound field intensities. The transducer peak-to-peak driving voltage is indicated in the rightmost legend. The lecithin concentration (fixed at 10 mg/mL) and the electrolysis driving voltage (20 V pkpk at 0.2 Hz) are shown in the upper-right corner of the plot.

Once it was established that the system was capable of reliably generating lipid-shelled MBs during the electrolysis process, the feasibility of bubble size reduction by exposure to a continuous low frequency US field, was investigated (section 4.2.2). The US transducer's driving voltage amplitude was gradually increased from 60 V pkpk to 180 V pkpk. Increasing US intensity produced a decrease in both size distribution and concentration of the MBs, with mean size going from $\sim$69 μm to $\sim$23 μm and concentration dropping from 9e4 MBs/mL to 1.5e4 MBs/mL. At all stages the PDI was < 0.3, except for the sample containing 10 mg/mL of lecithin treated at 180V pkpk, for which the PDI was 0.38 (see figures 4.6 and 4.7 and table 4.1). The formulation containing 5 mg/mL of lecithin seemed to consistently favour formation of

Table 4.1: Mean diameter, Standard Deviation, and PDI for MBs formulations exposed to increasing US intensity

Mean	Std	PDI	Driving voltage	Lecithin concentration
68.97	27.24	0.15	000V pkpk (no_US)	5 mg/mL
58.88	28.95	0.24	060V pkpk	5 mg/mL
45.98	24.36	0.28	100V pkpk	5 mg/mL
31.27	13.38	0.18	140V pkpk	5 mg/mL
22.62	8.92	0.15	180V pkpk	5 mg/mL
73.31	33.71	0.21	000V pkpk (no_US)	10 mg/mL
65.25	30.88	0.22	060V pkpk	10 mg/mL
48.68	25.55	0.27	100V pkpk	10 mg/mL
35.64	16.01	0.20	140V pkpk	10 mg/mL
30.65	19.10	0.38	180V pkpk	10 mg/mL

slightly smaller MBs size and with lower PDI at all tested conditions. In addition to this, as shown in figure 4.7, at 10 mg/mL lecithin concentration even at the highest US intensity settings the size distributions show the presence of larger MBs tails. For this reason, the 5 mg/mL formulation was used for subsequent experiments.

4.2.4 In-line continuous MBs manufacturing and biofilm US treatment

Once the MBs production protocol was characterised, the selected Embs formulation (5 mg/mL lecithin, 5 mL/min flow rate, 180 V pkpk transducer driving voltage) was tested against SonoVue-like MBs (THmbs) produced following the tissue homogenizer protocol described in section 2.3.6. Biofilm removal was evaluated using the same *S. mutans* biofilm model presented in chapter 2. The treatment in the presence of THmbs was delivered as described in section 2.4.2, whereas the treatment in the presence of Embs was performed in continuous mode as described in sec-

tion 4.1.6. Both treatment protocols were delivered using the set-up shown in figure 4.8.

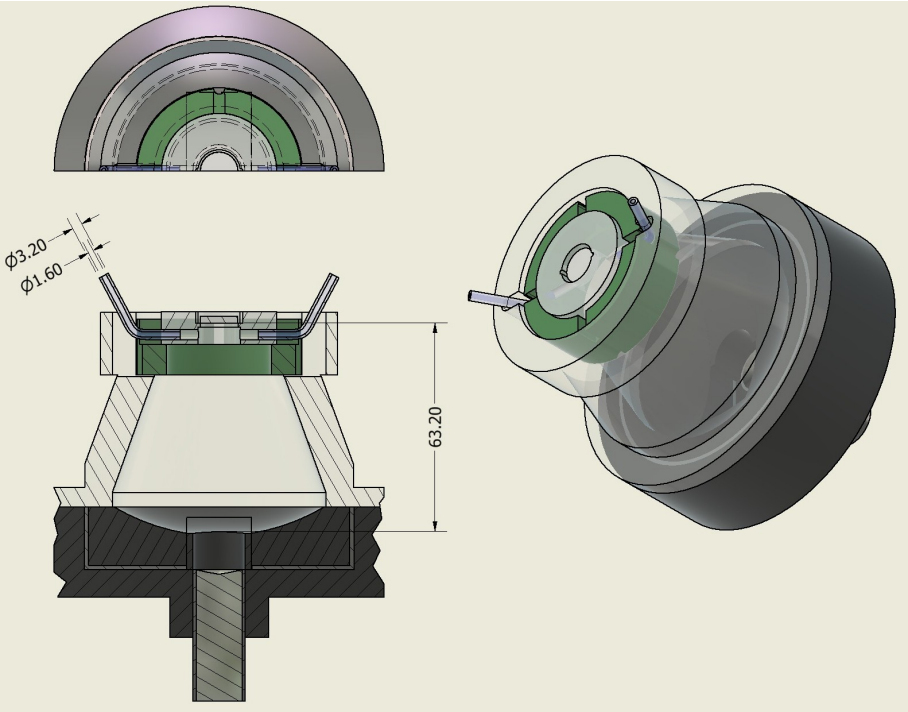


Figure 4.8: Schematic representation of the US system utilised to treat biofilm samples in presence of the MBs dispersion. The HA disc substrate is positioned at the centre of a 3D printed holder (transparent) and held at the focus of the HIFU transducer focus. The treatment media can be flowed through the system thanks to inlet and outlet openings positioned right below the HA substrate. Dimensions are expressed in mm.

Figure 4.9 shows the broadband emission energy recorded during 1 minute treatments in the presence of the two MBs formulations and in the absence of exogenous cavitation nuclei. Both types of bubble generated significantly higher broadband emissions at all tested pnp conditions compared with the suspending liquid alone. Interestingly, THmbs outperformed the broadband emission energy of Embs at 0.75 MPa and 3.00 MPa, but not at the intermediate 1.90 MPa pres-

sure. Whereas at 1.90 MPa we recorded BB emission energy of about 8.8±0.5 μJ, at 0.75 MPa the THmbs generated about 0.7±0.1 μJ higher emission than Embs and at 3.00 MPa the difference in energy emission between the two formulations increased to 2±0.3 μJ. This behaviour is better understood by examining the PSD plots shown in the supplementary materials section figures 4.12 to 4.14. Although the MBs were supplied continuously in the Embs group, the broadband emissions were detected in isolated bursts. This phenomena might be explained by acoustic shielding determined by different factors such as the increased mean bubble size, the presence of a few very large bubbles, and possible foam formation during ultrasound exposure. The hypothesis of the shielding is corroborated by the Embs PSD plot presented in figure 4.14. At this pnp magnitude, even in the absence of cavitation nuclei we recorded continuous broadband emissions from the samples whereas the ”burst” pattern in emission is still present for the Embs group. Interestingly, although the total broadband emission energy for Embs is lower than the THmbs group, the peak broadband emission energy in all samples was higher for the Embs group. This is in all likeliness due to the bigger size of the Embs.

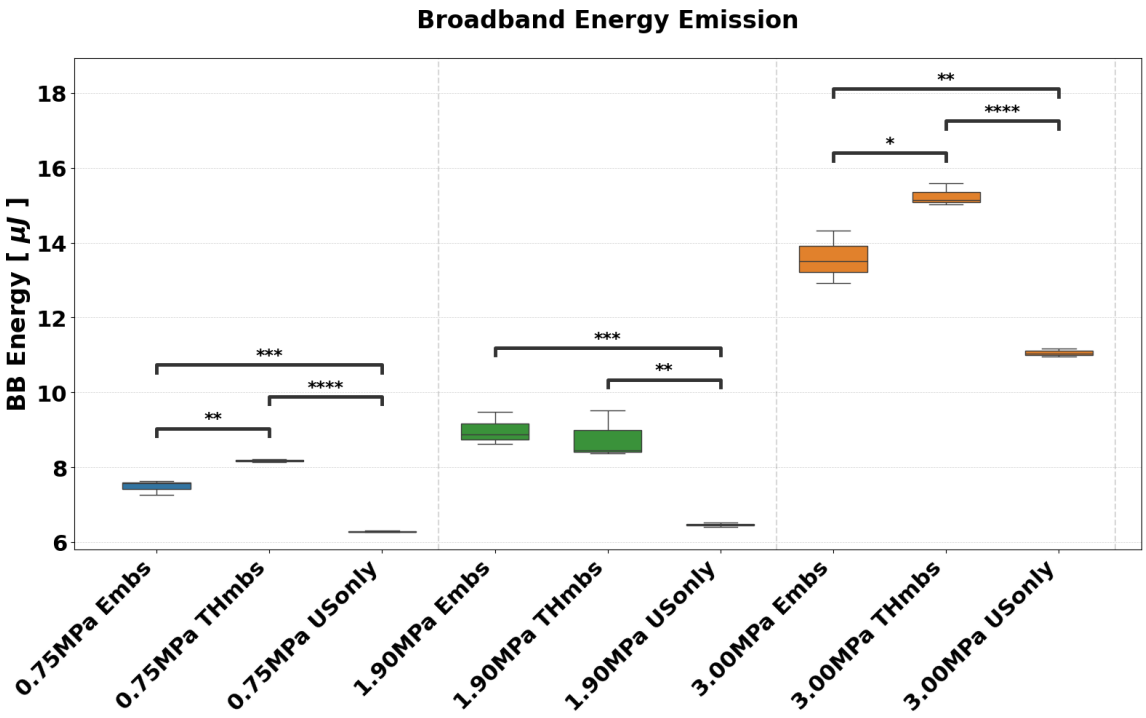


Figure 4.9: Broadband emission energy in the presence of THmbs, Embs, and in the absence of MBs at increasing pnp magnitude.
n=3 (biological) for all conditions, *pval<0.05, **pval<0.01, ***pval<0.001, ****pval<0.0001

The biofilm removal determined by the different treatment groups followed a similar pattern to that described in chapter 2. More specifically, the samples treated in the presence of THmbs showed a marginally, yet significant, higher removal degree at 1.90 and 3.00 MPa compared to the samples treated in the absence of MBs. At both pnps values the removal improved by $\sim$7% in presence of MBs. The samples treated in the presence of Embs showed a different behaviour. At 1.90 MPa pnp biofilm removal was in between that of no MBs and THmbs, although no statistically significant improvement in biofilm removal, when compared to the samples treated in absence of cavitation nuclei, was achieved. At 3.00 MPa pnp biofilm removal in the presence

of Embs was significantly lower than in both the other groups, whereas the broadband emission was still significantly higher than in the group treated in the absence of cavitation nuclei. Our hypothesis is that, at least at higher pnp magnitude, the bigger bubbles present in the Embs suspension determine significant shielding and/or foam formation.

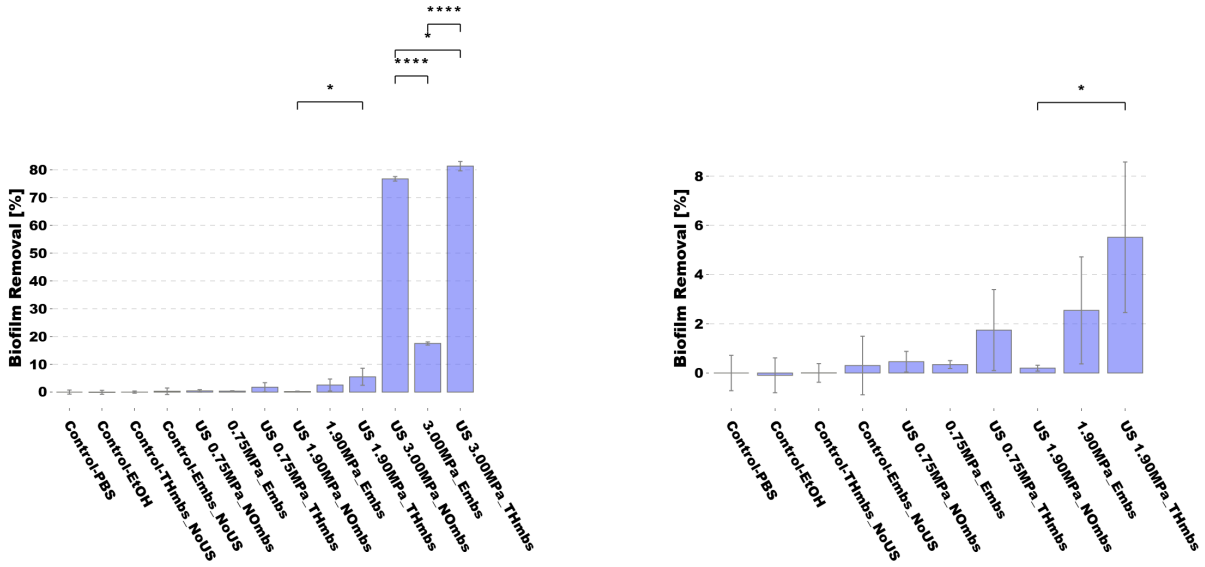


Figure 4.10: Biofilm removal (A_{US}) determined by the US treatment at increasing pnp magnitude and in the presence of different cavitation nuclei. (a) Shows all data points, (b) shows the same data points but omitting the 3.00 MPa pnp for improved graphical overview of the removal during milder treatment conditions.
n=3 (biological) for all conditions, *pval<0.05, **pval<0.01, ***pval<0.001, ****pval<0.0001

Consistent with the data presented in chapter 2, the US treatment in the absence of antimicrobial compounds did not produce any appreciable reduction in bacterial viability when compared to the controls, c.f. figure 4.11.

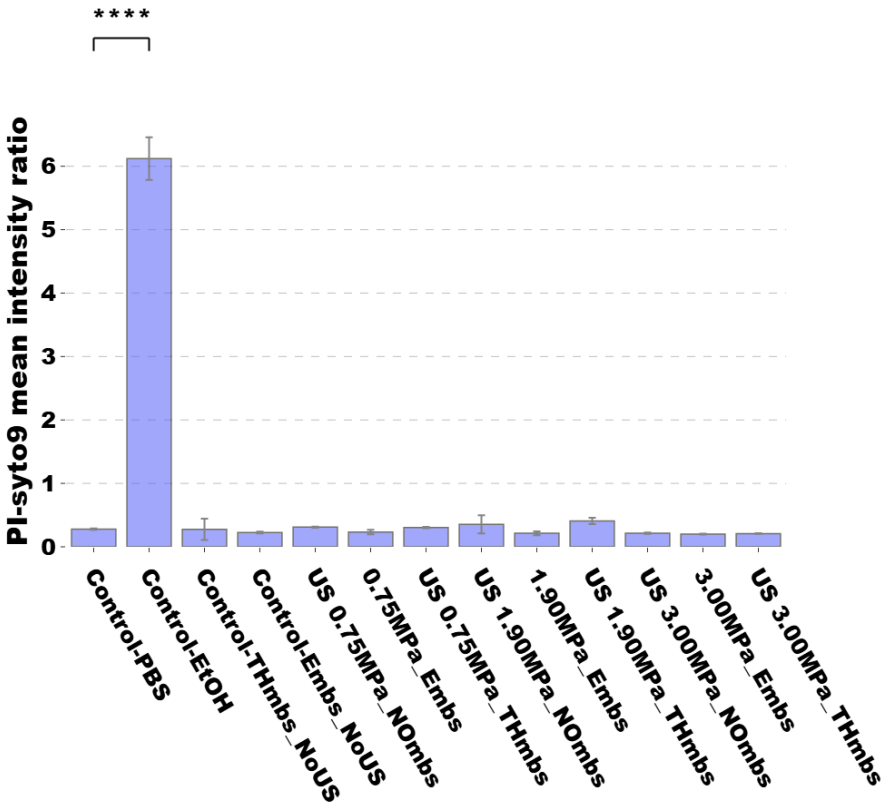


Figure 4.11: PI-syto9 mean intensity ratio for US treatment (ethanol as negative control). The error bars show the standard deviation for each group.
n=3 (biological) for all conditions, *pval<0.05, **pval<0.01, ***pval<0.001, ****pval<0.0001

4.3 Discussion

4.3.1 Device design and bubble generation

The selection of 5 mL/min as the operating flow rate avoided the coalescence and clogging observed at lower flow rates. This behaviour, consistent with gas bubbles' tendency to coalesce

under low shear stress [195, 196], underlines the importance of hydrodynamic parameters in the operation of continuous-flow microfluidic systems for microbubble production or processing. The cyclical potential inversion determined by AC was also deemed beneficial for the system, as it promotes periodic detachment of gas nuclei from the electrode surface, preventing the accumulation of gas on the electrodes which would lead to coalescence and foam formation [197]. The selected parameters of 20 V pkpk at 0.2 Hz represent an empirically optimised condition, though a more systematic characterisation could further refine MBs production rates.

The failure to produce measurable bubbles at 1 and 2 mg/mL lecithin concentration, suggests that at low concentration the phospholipids were not able to efficiently stabilize the small bubbles, leading to their quick dissolution. The differences in performance between the formulation containing 5 and 10 mg/mL of lecithin are to be ascribed to differences in shell's packing density and/or the lipid composition of the shell [189, 198].

4.3.2 Acoustofluidic MBs size tuning

The COMSOL guided optimisation of the resin propagation block geometry allowed to estimate the maximum pressure antinode intensity within the fluid domain. Although no confirmation of the pressure magnitude obtained in the fluid domain was possible, we selected the $\sim \lambda/4$ configuration as the optimal geometry, balancing pressure magnitude estimation and device form-factor. The observed decrease in both mean bubble diameter and concentration with increasing transducer driving voltage provides indirect, yet convincing, evidence that an acoustic pressure field of sufficient magnitude was established in the fluid domain. The reduction in mean diameter from approximately 69 μm to 23 μm at 5 mg/mL lecithin across the tested transducer's

driving voltage range represents a meaningful control over Embs size, although the resulting Embs remain considerably larger than clinically approved perfluorocarbon-core agents such as SonoVue. Such difference might not be considered an issue, when considering the different application suggested.

Although, for the proposed application, greater bubble size and higher PDI do not pose health risk concerns, the increased size dispersity of the formulation in addition to the gas core chemistry are believed to be the primary drivers for the observed differences in cavitation activity between Embs and THmbs.

4.3.3 Cavitation activity and biofilm removal

The PCD data confirm that both Embs and THmbs are effective cavitation nuclei, generating significantly greater inertial cavitation activity than the media alone across all tested pnp values. The intermittent nature of the broadband emissions recorded for Embs, in contrast to the more continuous signal observed for THmbs, points towards a complex interplay between bubble size distribution, acoustic shielding, and possible foam formation during sonication. The larger mean diameter of Embs, and the increased size dispersity, increase the likelihood of acoustic shielding by a population of large, strongly scattering bubbles. This interpretation is supported by the burst pattern of emission even at 3.00 MPa pnp, where continuous broadband emissions were recorded even in the absence of exogenous nuclei, suggesting that the Embs population itself was disrupting uniform acoustic propagation to the target.

The fact that Embs produced significantly lower biofilm removal than both THmbs and the control group (without exogenous cavitation nuclei) at 3.00 MPa, despite generating comparable

or higher peak broadband emission energies, strongly suggests that acoustic shielding and/or foam formation at the sample surface were limiting the effective delivery of cavitation energy to the biofilm. At lower pnp conditions the differences between groups were less pronounced, suggesting that shielding effects became increasingly significant as driving pressure, and hence bubble activity, increased.

Consistent with the findings reported in chapter 2, ultrasound treatment alone did not produce a measurable reduction in bacterial viability, confirming that the mechanical disruption of the biofilm matrix does not imply inactivation of the dispersed bacteria.

4.3.4 Future work and potential applications

Although the present work demonstrates the feasibility of continuous electrolysis-driven MBs production and acoustofluidic size tuning, more investigations are needed before this technology can have meaningful impact in healthcare applications. First, future developments should focus on the miniaturisation of the device and the optimisation of its power consumption. Reducing the overall footprint and improving energy efficiency would facilitate the translation of the technology into portable or handheld systems suitable for dentistry or home-care applications, while also improving the scalability of continuous MBs production.

A second area where major improvement might be achieved is the formulation of the MBs shell. The phospholipid formulation employed in this work was adapted from conventional mechanically generated ultrasound contrast agents and was not specifically designed for electrolysis-driven bubble generation. Future studies should investigate different phospholipid and auxiliary shell components tailored to the unique physicochemical conditions associated with electroly-

sis, with the aim of improving bubble stability, reducing size dispersity, and increasing production efficiency.

The choice of electrode material also represents a central point for the device optimisation. Different electrode materials would influence not only the efficiency of gas generation but also the electrochemical products generated during electrolysis. In particular, the possibility of simultaneously producing Embs and AW containing ROS or other antimicrobial compounds could provide a synergistic therapeutic effect. Such approach may prove a successful and economical way for point-of-care generation of cavitation agents and antimicrobials while preserving the current continuous-flow nature of the platform.

The proposed technology has potential applications across a broad range of biofilm related challenges. In dentistry, Embs could be integrated with ultrasonic scalers or irrigation systems to improve the removal of dental plaque and biofilms from inaccessible anatomical sites. More broadly, the technology could be applied to the treatment of other easily accessible, yet difficult to treat, biofilm induced infection, such as chronic wound biofilms or diabetic foot, where enhanced cavitation activity may improve biofilm disruption and increase the penetration of topical antimicrobials. Additional applications may include the decontamination of medical devices and implants, as well as other clinical and industrial settings where biofilm removal remains a significant challenge.

4.4 Conclusions

In this work, we successfully developed and characterised a novel acoustofluidic platform for the continuous, tunable generation of lipid-shelled MBs via electrolysis, and validated its po-

tential for *in vitro* biofilm HIFU treatment. Unlike conventional microfluidic flow-focusing methods, our approach leveraged electrolysis to produce gas bubbles that were subsequently broken down into smaller MBs using a low-frequency acoustofluidic stage. Optimisation of the electrolysis parameters revealed that 0.2 Hz AC at 20 V pkpk, combined with a lipid concentration of 5 mg/mL lecithin, provided a stable and reproducible MBs dispersion with minimal clogging or foaming. The acoustofluidic stage, successfully reduced MBs mean diameter from approximately 69 μm to 23 μm as the driving voltage increased from 0 to 180 V pkpk, while maintaining a relatively narrow size distribution (PDI $\sim$0.15). Higher lecithin concentrations (10 mg/mL) led to larger MBs and greater size variability, confirming 5 mg/mL as the optimal formulation.

Preliminary biofilm removal experiments using a *S. mutans* model demonstrated that the generated Embs are capable of inducing cavitation activity, although they produced a more erratic burst pattern of noise than THmbs. Broadband emission energy was significantly higher in the presence of both MBs formulations compared to conditions where no cavitation nuclei were employed; however, at higher acoustic pressures (3.00 MPa), Embs treated samples exhibited substantially lower biofilm removal compared to THmbs and no MBs controls, likely due to acoustic shielding by larger bubbles and transient foam formation. At lower pressures (1.90 MPa), Embs showed intermediate removal efficacy, though variability was high. Importantly, no significant reduction in bacterial viability was observed under any treatment condition without antimicrobial agents, confirming our previous findings.

This study establishes a proof-of-concept for the continuous electrolytic and acoustofluidic manufacturing of MBs and their direct integration into biofilm HIFU treatment. The proposed system offers a scalable alternative to conventional MBs batch production, with the added po-

tential for *in situ* generation of reactive species. Future work should focus on: (i) experimental validation of the acoustic pressure field within the microchannel using indirect acoustic measurements. (ii) Improving MBs formulation and production rates, favouring smaller mean diameter, higher concentration, and reduced size dispersity following the acoustofluidic stage-induced size reduction. (iii) Leveraging the electrolytic generation of ROS and other antimicrobial species to achieve combined sonodynamic and chemical biofilm eradication. With these refinements, the proposed acoustofluidic technology holds promise for real time, continuous MBs production in therapeutic settings.

4.5 Supplementary

4.5.1 Power spectral density plots in presence of different cavitation nuclei

Nine representative PSD plots are shown in figures 4.12 to 4.14. At the lowest focal pressure (0.75 MPa pnp), the control samples showed negligible acoustic emissions between 2 and 12 MHz, with no appreciable harmonic content. In contrast, both MBs formulations generated harmonic bands, although these were substantially more pronounced for THmbs than for Embs. The harmonic emissions remained visible throughout most of the treatment for THmbs, whereas they were considerably weaker for Embs.

At 1.90 MPa pnp, harmonic emissions remained absent in the control group. Embs generated intermittent high intensity broadband bursts, with no appreciable harmonic bands. THmbs produced an initial burst of broadband emissions immediately after the start of treatment, followed

by weak harmonic bands that progressively decreased in intensity over time.

At the highest pressure investigated (3.00 MPa pnp), broadband emissions were sustained throughout the treatment even in the control samples, indicating cavitation activity in the absence of exogenous nuclei. Embs produced intermittent broadband bursts, featuring the highest peak emission energy than any group, while harmonic bands remained undetectable. In contrast, THmbs generated continuous broadband emissions with greater overall intensity than the control but lower peak amplitudes than the transient bursts observed for Embs.

The receiver used to acquire all PCD traces had a broadband frequency response, although its sensitivity was frequency dependent, with a maximum centred at approximately 7 MHz. Consequently, all PSD plots exhibit increased signal intensity around this frequency, independently of the cavitation activity generated during treatment.

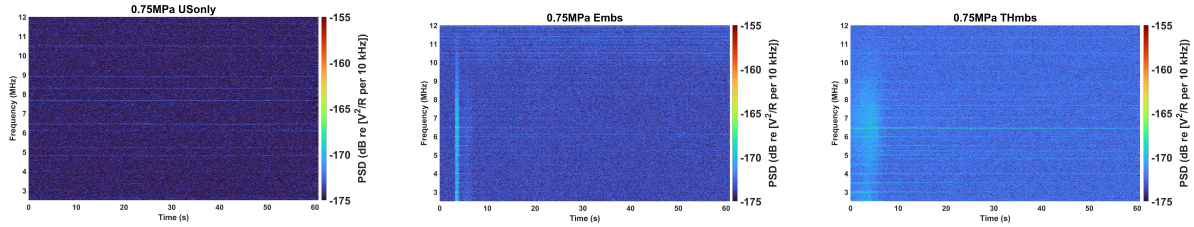


Figure 4.12: Representative PSD plots at 0.75 MPa pnp. From left to right: No MBs, Embs, and THmbs

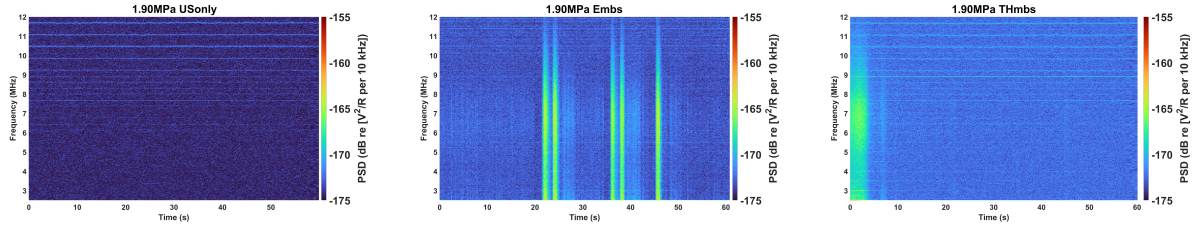


Figure 4.13: Representative PSD plots at 1.90 MPa pnp. From left to right: No MBs, Embs, and THmbs

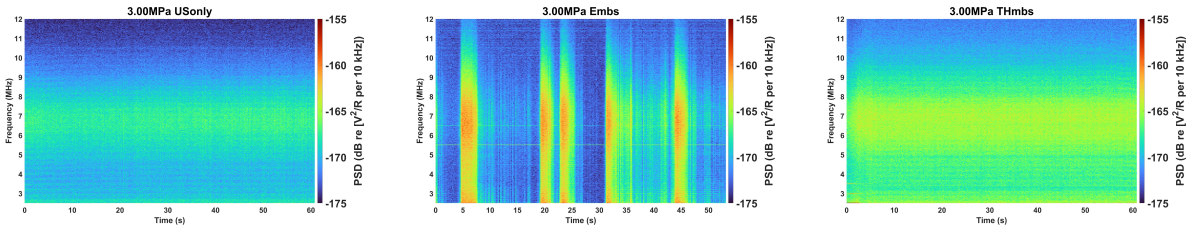


Figure 4.14: Representative PSD plots at 3.00 MPa pnp. From left to right: No MBs, Embs, and THmbs

Chapter 5

Conclusions

The investigation pursued in this thesis evaluated the potential of therapeutic US as an adjunctive tool for oral biofilm infection management, bringing insights into US synergy with antimicrobial treatment and proposing a proof-of-concept acoustofluidic platform capable of generating cavitation nuclei in continuous format for immediate use in US treatment. This work aims at providing a useful foundation for understanding how US parameters, antimicrobial selection, and cavitation nuclei can be optimised to address the clinical challenge of biofilm associated infections.

5.0.1 Synopsis of findings

The first study (chapter 2) established that focused US at 0.5 MHz can significantly enhance the bactericidal efficacy of CHX on a single species, fully developed oral biofilm model. The results demonstrated that US treatment not only can promote biofilm detachment, but could also potentiate antimicrobial activity against the biofilm fraction that remains adherent to the surface. To the best of the author's knowledge, this was the first evaluation of focused US at 0.5 MHz on an oral cavity specific infection model, as the majority of the existing research in

this field reports on the effects of lower frequency (<120 kHz) unfocused US. By increasing the frequency and spatially focusing the US beam, we significantly improved the spatial resolution of treatment, reducing the risk of off target effects.

The second study (chapter 3), built upon the previous findings, focused on evaluating the synergistic effects of US in combination with AW. AW, with its fast onset, tunable, and mild antimicrobial activity, was identified as a promising alternative to CHX for long term oral care management. This study tested the effects of AW at three increasing concentrations and compared it with a marketed alcohol-free mouthwash; proving that AW antimicrobial activity is similar, if not higher, than currently marketed products.

Another critical outcome of this study was the demonstration that the clinical, multispecies oral biofilm model exhibited complete resilience to US treatment alone, with no meaningful reduction in CFU observed in the absence of AW. This finding partly contradicts previously published work and underscores that the bactericidal effects of US are strongly dependent on the selected parameters, exposure conditions, and the mechanical and biological characteristics of the biofilm. The combination therapy of US (particularly at 3.00 MPa pnp) with AW yielded marked and statistically significant reductions in bacterial viability compared to the control and the AW alone groups, affecting both total bacterial count and a selected group of bile salts resistant G- species count similarly. These results confirmed that US mediated enhancement of antimicrobial activity is not tied to CHX specifically. On the contrary, the improvement in treatment efficacy was even more pronounced in the case of faster acting oxidative stress inducing antimicrobials.

The third study (chapter 4) advanced the translational potential of this work by developing a novel acoustofluidic platform for the continuous, tunable generation of lipid-shelled MBs via electrolysis. The proposed approach moves from the standard batch approach for MBs production and enables tunable continuous MBs generation, which could be directly integrated into therapeutic settings. Preliminary biofilm removal experiments on fully formed *S. mutans* biofilms demonstrated that Embs are capable of inducing cavitation activity, although their performance was more variable than that of pre-formed MBs. We believe that, at least partly, the reduced biofilm removal efficiency in Embs-mediated treatments, compared to treatments delivered in the presence of THmbs, is due to the bigger mean bubble diameter and higher PDI which lead to coalescence, foaming, and ultimately scattering of the incoming ultrasonic wave. Importantly, no significant reduction in bacterial viability was observed without antimicrobial agents across any treatment condition, confirming our previous findings and reinforcing the conclusion that US alone, inside the tested treatment parameter space, does not inherently kill bacteria.

5.0.2 Limitations and future directions

Despite the positive results presented in this thesis, this study still suffers from several limitations which should be acknowledged. Although having different oral biofilm models and antimicrobial compounds throughout this work allowed to cover a greater experimental space, it also hindered direct comparisons between the effect of different drugs on oral biofilms and their interaction with US therapy. For example, the effect of CHX on *S. mutans* biofilms was significantly, yet only marginally, improved by co-administration with US therapy. We hypothesize

that this might be due to CHX's slower kinetics of action compared to other antimicrobial compounds (such as ROS), but realistically it could also be due to the mechanical structure of the biofilm model utilized, as *S. mutans* biofilms grow at a faster pace than saliva-derived biofilms and generate greater amounts of EPS, granting bacteria a thicker protective layer against antimicrobial treatment. On the contrary, the antimicrobial effect of AW was greatly improved by its combination with US. This could well be due to the different mechanism of action of the compounds present in AW, but the thinner saliva-derived biofilm might have also played a role in improving the magnitude of the effect.

The *in vitro* nature of all three studies, while essential for controlled mechanistic investigation, does not fully replicate the complex environment of the oral cavity, including salivary flow, continuous microbial recolonisation, calcification, and host immune factors. The biofilm models, although clinically derived, were grown for a relatively short period of time and under static flow conditions, which may not capture the full spatial and metabolic heterogeneity of *in vivo* biofilms. Furthermore, the relatively low number of experimental repeats in some comparisons limited statistical power, and the variability in MBs performance indicates that further refinement of the acoustofluidic platform is required before further translation.

Based on the findings of this thesis, the following priorities for future research are proposed:

1. **Explore the effects of CHX and AW on different *in vitro* models:** Testing the effects of CHX on the saliva-derived model and of AW on the *S. mutans* model would allow to compare directly the results obtained in chapter 2 and chapter 3. In particular, it would be of great interest to understand if the greater impact of US combination therapy shown

in chapter 3 should be attributed to the different biofilm model or to the different mode of action of AW compared to CHX.

2. **Evaluate strain specific response to US stimulation:** Although in chapter 3 we presented the effects of the treatment on both total bacteria and G-, future work should focus on strain specific differences, evaluating what characteristics make a bacterial strain sensitive or resistant to US exposure. The mechanism through which US improves the efficacy of antimicrobial treatment is still debated, although a good amount of research has been published on the matter. In particular, Runyan *et. al.* [199] demonstrated how low frequency US can increase the membrane permeability of *P. aeruginosa*. Similar results have been confirmed in multiple occasions [200, 201], but definitive proofs that US treatment performed at at higher frequency (*e.g.* 0.25 to 1.5 MHz) determines similar effects on the bacterial membrane are not available. On the contrary, the effects of US (at frequencies between 0.25 and 1.5 MHz) on mammalian cells and their membrane permeability have been extensively reported [202]. An in-depth mechanistic effect of therapeutic US on both G+ and G- bacteria would be a necessary next step in improving our understanding of US-mediated antimicrobial therapies.

3. **Evaluation of long term effects of US mediated oral microbiome management:** Although promising result were obtained *in vitro* across all three chapters, the longevity and location of oral biofilms makes some of our claims hard to confirm in a clinical setting. As such, it would be of great interest to test the developed treatment protocol on an oral infectious disease *in vivo* model [203]. Similar work as been previously pursued by Hong *et. al.* [204], where they demonstrated both *in vitro* and *in vivo* the beneficial effects

of plasma-mediated antimicrobial treatment for oral biofilms. Since we could not find any report regarding an equivalent study on US-mediated therapies for oral biofilms, we believe this would be a valuable extension of the work presented in this thesis.

4. **Refinement of Embs formulation:** Future work should focus on perfecting both the lipid shell formulation and the manufacturing parameters, with the intent of producing Embs with smaller mean diameter, higher concentration, and improved size dispersity. This would improve cavitation activity and reduce the acoustic shielding effects observed at higher pressures. Although lecithin is not the most commonly used surfactant in MBs manufacturing, Waqar *et. al.* recently demonstrated the possibility of obtaining a monodisperse suspension of lecithin-cholesterol MBs using a probe sonication manufacturing protocol [194, 205]. Although the protocol described in previous literature differs from the one described in this work, we believe that further exploration of the formulation space (e.g. variation of the components' molar ratio, variation in the fluid viscosity) could allow the production of a monodisperse MBs suspension using the electro-acoustofluidic system described in chapter 4.

5. **Clinical device development:** The continuous, scalable nature of the electro-acoustofluidic platform described in chapter 4 makes it suitable for integration into a handheld device. Future engineering efforts should focus on miniaturisation, power efficiency, and regulatory compliance.

5.0.3 Concluding remarks

The results presented in this study suggest that US has beneficial synergistic effect when paired with antimicrobials for the treatment of oral biofilm infections. Although the specific mechanism underlying the beneficial effects of US-mediated therapies in bacterial infections are still debated, the results presented in chapters 2 and 3 demonstrated that focused US at 0.5 MHz significantly enhances the bactericidal efficacy of CHX against fully developed oral biofilms, marking the first evaluation of this frequency, and its combination with lipid-shell MBs, on an oral infection model. This set of studies not only proves the efficacy of US as a mechanical adjuvant to antimicrobial chemotherapy, but correlates the beneficial effects of ultrasound exposure to the broadband energy emissions recorded from the sample, which are an indicator of cavitation activity at the sample site.

The combination of US with AW proved highly effective against a clinically derived multi-species oral biofilm model. While US alone did not reduce bacterial viability, its synergy with AW yielded marked reductions in both total and G- bacterial counts. These findings confirm that US-mediated antimicrobial enhancement is not specific to CHX and can be even more pronounced with oxidative stress-inducing agents.

The final section of the work demonstrated the feasibility of continuous generation of lipid-shelled MBs via electrolysis and their immediate use for US treatment. Preliminary experiments confirmed that Embs can induce cavitation activity and subsequent biofilm removal, although improvement to the production rate and size dispersity of the formulation are needed to allow for effective and reproducible treatment delivery. Collectively, the results of this study clarify how US parameters, antimicrobial selection, and cavitation nuclei can be optimised to obtain

CHAPTER 5.

US-mediated improved management of biofilm associated oral infections.

Bibliography

[1] Mohsen Naghavi et al. “Global burden of bacterial antimicrobial resistance 1990–2021: a systematic analysis with forecasts to 2050”. English. In: *The Lancet* 404.10459 (Sept. 2024), pp. 1199–1226. ISSN: 0140-6736, 1474-547X. DOI: 10.1016/S0140-6736(24)01867-1. URL: https://www.thelancet.com/journals/lancet/article/PIIS0140-6736(24)01867-1/fulltext (visited on 09/03/2025).

[2] Muhsin Jamal et al. “Bacterial biofilm and associated infections”. eng. In: *Journal of the Chinese Medical Association: JCMA* 81.1 (Jan. 2018), pp. 7–11. ISSN: 1728-7731. DOI: 10.1016/j.jcma.2017.07.012.

[3] Daniela Berger et al. “Oral Biofilms: Development, Control, and Analysis”. en. In: *High-Throughput* 7.3 (Sept. 2018). DOI: 10.3390/ht7030024. URL: https://www.ncbi.nlm.nih.gov/pmc/articles/PMC6163956/ (visited on 09/18/2024).

[4] Guilian Shi et al. “Low-frequency HIFU induced cancer immunotherapy: tempting challenges and potential opportunities”. en. In: *Cancer Biology & Medicine* 16.4 (Nov. 2019), p. 714. DOI: 10.20892/j.issn.2095-3941.2019.0232. URL: https://pmc.ncbi.nlm.nih.gov/articles/PMC6936245/ (visited on 10/28/2024).

[5] Farshad Moradi Kashkooli et al. “Integrating Therapeutic Ultrasound With Nanosized Drug Delivery Systems in the Battle Against Cancer”. en. In: *Technology in Cancer Research & Treatment* 22 (Jan. 2023), p. 15330338231211472. ISSN: 1533-0346. DOI: 10.1177/15330338231211472. URL: https://doi.org/10.1177/15330338231211472 (visited on 12/21/2024).

[6] Gareth LuTheryn et al. “Bactericidal and anti-biofilm effects of uncharged and cationic ultrasound-responsive nitric oxide microbubbles on Pseudomonas aeruginosa biofilms”. English. In: *Frontiers in Cellular and Infection Microbiology* 12 (Aug. 2022). ISSN: 2235-2988. DOI: 10.3389/fcimb.2022.956808. URL: https://www.frontiersin.org/journals/cellular-and-infection-microbiology/articles/10.3389/fcimb.2022.956808/full (visited on 01/11/2025).

[7] Jamie D. Liu et al. “Ultrasound-Mediated Antibiotic Delivery to In Vivo Biofilm Infections: A Review”. en. In: *ChemBioChem* 25.20 (2024), e202400181. ISSN: 1439-7633. DOI: 10.1002/cbic.202400181. URL: https://onlinelibrary.wiley.com/doi/abs/10.1002/cbic.202400181 (visited on 06/02/2026).

[8] Gareth LuTheryn et al. “Ultrasound-mediated therapies for the treatment of biofilms in chronic wounds: a review of present knowledge”. en. In: *Microbial Biotechnology* 13.3 (Aug. 2019), p. 613. DOI: 10.1111/1751-7915.13471. URL: https://pmc.ncbi.nlm.nih.gov/articles/PMC7111087/ (visited on 10/28/2024).

[9] Barney Breazeale. *Oral Vestibule - Dental Anatomy*. en. Aug. 2023. URL: http://www.globehealth.net/dental-anatomy/oral-vestibule.html (visited on 08/29/2023).

[10] Rickne C. Scheid. *Woelfel’s Dental Anatomy*. en. Google-Books-ID: UNtzFQszCuQC. Lippincott Williams & Wilkins, 2012. ISBN: 978-1-60831-746-2.

[11] Blausen.com staff and Blausen com staff. “Medical gallery of Blausen Medical 2014”. In: *[[WikiJournal of Medicine—WikiJournal of Medicine]]* 1.2 (Aug. 2014). ISSN: 2002-4436. DOI: 10.15347/WJM/2014.010. URL: https://upload.wikimedia.org/wikiversity/en/8/82/Medical_gallery_of_Blausen_Medical_2014.pdf.

[12] Claude E. Zobell. “The Effect of Solid Surfaces upon Bacterial Activity1”. In: *Journal of Bacteriology* 46.1 (July 1943), pp. 39–56. ISSN: 0021-9193. URL: https://www.ncbi.nlm.nih.gov/pmc/articles/PMC373789/ (visited on 07/03/2023).

[13] J. W. Costerton et al. “Bacterial biofilms in nature and disease”. eng. In: *Annual Review of Microbiology* 41 (1987), pp. 435–464. ISSN: 0066-4227. DOI: 10.1146/annurev.mi.41.100187.002251.

[14] Karin Sauer et al. “The biofilm life cycle: expanding the conceptual model of biofilm formation”. en. In: *Nature Reviews Microbiology* 20.10 (Oct. 2022). Number: 10, pp. 608–620. ISSN: 1740-1534. DOI: 10.1038/s41579-022-00767-0. URL: https://www.nature.com/articles/s41579-022-00767-0 (visited on 08/22/2023).

[15] Kajal Gupta et al. “Antimicrobial Tolerance of Pseudomonas aeruginosa Biofilms Is Activated during an Early Developmental Stage and Requires the Two-Component Hybrid SagS”. In: *Journal of Bacteriology* 195.21 (Nov. 2013), pp. 4975–4987. ISSN: 0021-9193. DOI: 10.1128/JB.00732-13. URL: https://www.ncbi.nlm.nih.gov/pmc/articles/PMC3807491/ (visited on 08/22/2023).

[16] Jye-Lin Hsu et al. “Characterization of the Histidine-containing Phosphotransfer Protein B-mediated Multistep Phosphorelay System in Pseudomonas aeruginosa PAO1”. en. In: *Journal of Biological Chemistry* 283.15 (Apr. 2008), pp. 9933–9944. ISSN: 00219258. DOI: 10.1074/jbc.M708836200. URL: https://linkinghub.elsevier.com/retrieve/pii/S0021925820570671 (visited on 08/22/2023).

[17] Philip S. Stewart and Michael J. Franklin. “Physiological heterogeneity in biofilms”. en. In: *Nature Reviews Microbiology* 6.3 (Mar. 2008), pp. 199–210. ISSN: 1740-1526, 1740-1534. DOI: 10.1038/nrmicro1838. URL: https://www.nature.com/articles/nrmicro1838 (visited on 06/06/2023).

[18] Kerry S. Williamson et al. “Heterogeneity in Pseudomonas aeruginosa Biofilms Includes Expression of Ribosome Hibernation Factors in the Antibiotic-Tolerant Subpopulation and Hypoxia-Induced Stress Response in the Metabolically Active Population”. en. In: *Journal of Bacteriology* 194.8 (Apr. 2012), pp. 2062–2073. ISSN: 0021-9193, 1098-5530. DOI: 10.1128/JB.00022-12. URL: https://journals.asm.org/doi/10.1128/JB.00022-12 (visited on 06/06/2023).

[19] Diego O. Serra and Regine Hengge. “Stress responses go three dimensional – the spatial order of physiological differentiation in bacterial macrocolony biofilms”. en. In: *Environmental Microbiology* 16.6 (June 2014), pp. 1455–1471. ISSN: 1462-2912, 1462-2920. DOI: 10.1111/1462-2920.12483. URL: https://onlinelibrary.wiley.com/doi/10.1111/1462-2920.12483 (visited on 06/06/2023).

[20] Kotaro Chihara et al. “Mathematical modeling of dormant cell formation in growing biofilm”. English. In: *Frontiers in Microbiology* 6 (May 2015). ISSN: 1664-302X. DOI: 10.3389/fmicb.2015.00534. URL: https://www.frontiersin.org/journals/microbiology/articles/10.3389/fmicb.2015.00534/full (visited on 02/19/2026).

[21] Jing Yan and Bonnie L. Bassler. “Surviving as a Community: Antibiotic Tolerance and Persistence in Bacterial Biofilms”. In: *Cell Host & Microbe* 26.1 (July 2019), pp. 15–21. ISSN: 1931-3128. DOI: 10.1016/j.chom.2019.06.002. URL: https://www.sciencedirect.com/science/article/pii/S1931312819302914 (visited on 02/19/2026).

[22] H. L. Ritz. “Microbial population shifts in developing human dental plaque”. eng. In: *Archives of Oral Biology* 12.12 (Dec. 1967), pp. 1561–1568. ISSN: 0003-9969. DOI: 10.1016/0003-9969(67)90190-2.

[23] Qizhao Ma et al. “Acetylation of glucosyltransferases regulates Streptococcus mutans biofilm formation and virulence”. en. In: *PLOS Pathogens* 17.12 (2021), e1010134. ISSN: 1553-7374. DOI: 10.1371/journal.ppat.1010134. URL: https://journals.plos.org/plospathogens/article?id=10.1371/journal.ppat.1010134 (visited on 07/04/2023).

[24] Walter J. Loesche. “Microbiology of Dental Decay and Periodontal Disease”. eng. In: *Medical Microbiology*. Ed. by Samuel Baron. 4th. Galveston (TX): University of Texas Medical Branch at Galveston, 1996. ISBN: 978-0-9631172-1-2. URL: http://www.ncbi.nlm.nih.gov/books/NBK8259/ (visited on 07/04/2023).

[25] Lanyan Zheng et al. “Environmental Influences on Competitive Hydrogen Peroxide Production in Streptococcus gordonii ∇”. In: *Applied and Environmental Microbiology* 77.13 (July 2011), pp. 4318–4328. ISSN: 0099-2240. DOI: 10.1128/AEM.00309-11. URL: https://www.ncbi.nlm.nih.gov/pmc/articles/PMC3127700/ (visited on 08/22/2023).

[26] Megan L. Falsetta et al. “Symbiotic Relationship between Streptococcus mutans and Candida albicans Synergizes Virulence of Plaque Biofilms In Vivo”. In: *Infection and Immunity* 82.5 (May 2014), pp. 1968–1981. ISSN: 0019-9567. DOI: 10.1128/IAI.00087-14. URL: https://www.ncbi.nlm.nih.gov/pmc/articles/PMC3993459/ (visited on 07/04/2023).

[27] J.P. Butcher et al. “Effects of Streptococcus mutans on Dendritic Cell Activation and Function”. EN. In: *Journal of Dental Research* 90.10 (Oct. 2011), pp. 1221–1227. ISSN: 0022-0345. DOI: 10.1177/0022034511412970. URL: https://doi.org/10.1177/0022034511412970 (visited on 09/04/2025).

[28] TaeHyun Kwon, Ira B. Lamster, and Liran Levin. “Current Concepts in the Management of Periodontitis”. In: *International Dental Journal* 71.6 (Feb. 2021), pp. 462–476. ISSN: 0020-6539. DOI: 10.1111/idj.12630. URL: https://www.ncbi.nlm.nih.gov/pmc/articles/PMC9275292/ (visited on 07/04/2023).

[29] Meliha Germen et al. “Periodontitis Prevalence, Severity, and Risk Factors: A Comparison of the AAP/CDC Case Definition and the EFP/AAP Classification”. In: *International Journal of Environmental Research and Public Health* 18.7 (Mar. 2021), p. 3459. ISSN: 1661-7827. DOI: 10.3390/ijerph18073459. URL: https://www.ncbi.nlm.nih.gov/pmc/articles/PMC8037399/ (visited on 07/04/2023).

[30] Nigel B. Pitts et al. “Dental caries”. en. In: *Nature Reviews Disease Primers* 3.1 (May 2017). Number: 1, pp. 1–16. ISSN: 2056-676X. DOI: 10.1038/nrdp.2017.30. URL: https://www.nature.com/articles/nrdp201730 (visited on 07/04/2023).

[31] Rizwan Ullah and Muhammad Sohail Zafar. “ORAL AND DENTAL DELIVERY OF FLUORIDE: A REVIEW”. en. In: *Fluoride 48(3) 195-204* (2015).

[32] Stefan Renvert and G. Rutger Persson. “Supportive periodontal therapy”. en. In: *Periodontology 2000* 36.1 (2004). _eprint: https://onlinelibrary.wiley.com/doi/pdf/10.1111/j.1600-0757.2004.03680.x, pp. 179–195. ISSN: 1600-0757. DOI: 10.1111/j.1600-0757.2004.03680.x. URL: https://onlinelibrary.wiley.com/doi/abs/10.1111/j.1600-0757.2004.03680.x (visited on 09/18/2024).

[33] Luc van der Sluis et al. “Disinfection of the Root Canal System by Sonic, Ultrasonic, and Laser Activated Irrigation”. en. In: *Disinfection of Root Canal Systems*. Section: 11 _eprint: https://onlinelibrary.wiley.com/doi/pdf/10.1002/9781118914014.ch11. John Wiley & Sons, Ltd, 2014, pp. 217–238. ISBN: 978-1-118-91401-4. DOI: 10.1002/9781118914014.ch11. URL: https://onlinelibrary.wiley.com/doi/abs/10.1002/9781118914014.ch11 (visited on 01/30/2025).

[34] B. Verhaagen et al. “Acoustic streaming induced by an ultrasonically oscillating endodontic file”. In: *The Journal of the Acoustical Society of America* 135.4 (Apr. 2014), pp. 1717–1730. ISSN: 0001-4966. DOI: 10.1121/1.4868397. URL: https://doi.org/10.1121/1.4868397 (visited on 01/30/2025).

[35] J. M. McIntyre, J. D. Featherstone, and J. Fu. “Studies of dental root surface caries. 2: The role of cementum in root surface caries”. eng. In: *Australian Dental Journal* 45.2 (June 2000), pp. 97–102. ISSN: 0045-0421. DOI: 10.1111/j.1834-7819.2000.tb00248.x.

[36] GA (Fridus) Van der Weijden, Gijs J. Dekkers, and Dagmar E. Slot. “Success of non-surgical periodontal therapy in adult periodontitis patients: A retrospective analysis”. en. In: *International Journal of Dental Hygiene* 17.4 (May 2019), p. 309. DOI: 10.1111/idh.12399. URL: https://pmc.ncbi.nlm.nih.gov/articles/PMC6852011/ (visited on 10/24/2024).

[37] Yue Yan et al. “Clinical evaluation of ultrasonic subgingival debridement versus ultrasonic subgingival scaling combined with manual root planing in the treatment of periodontitis: study protocol for a randomized controlled trial”. In: *Trials* 21.1 (Jan. 2020), p. 113. ISSN: 1745-6215. DOI: 10.1186/s13063-019-4031-y. URL: https://doi.org/10.1186/s13063-019-4031-y (visited on 10/24/2024).

[38] Patrice James et al. “Chlorhexidine mouthrinse as an adjunctive treatment for gingival health”. en. In: *Cochrane Database of Systematic Reviews* 3 (2017). ISSN: 1465-1858. DOI: 10.1002/14651858.CD008676.pub2. URL: https://www.cochranelibrary.com/cdsr/doi/10.1002/14651858.CD008676.pub2/full (visited on 10/17/2024).

[39] Rachel Mei Ling Chye et al. “Effectiveness of Different Commercial Chlorhexidine-Based Mouthwashes After Periodontal and Implant Surgery: A Systematic Review”. en-US. In: *Implant Dentistry* 28.1 (Feb. 2019), p. 74. ISSN: 1056-6163. DOI: 10.1097/ID.0000000000000854. URL: https://journals.lww.com/implantdent/fulltext/2019/02000/effectiveness_of_different_commercial.12.aspx (visited on 10/17/2024).

[40] Alex Solderer et al. “Efficacy of chlorhexidine rinses after periodontal or implant surgery: a systematic review”. eng. In: *Clinical Oral Investigations* 23.1 (Jan. 2019), pp. 21–32. ISSN: 1436-3771. DOI: 10.1007/s00784-018-2761-y.

[41] E L Thomas et al. “Antibacterial activity of hydrogen peroxide and the lactoperoxidase-hydrogen peroxide-thiocyanate system against oral streptococci.” In: *Infection and Immunity* 62.2 (Feb. 1994), pp. 529–535. ISSN: 0019-9567. DOI: 10.1128/iai.62.2.529-535.1994. URL: https://pmc.ncbi.nlm.nih.gov/articles/PMC186138/ (visited on 05/19/2026).

[42] M. Finnegan et al. “Mode of action of hydrogen peroxide and other oxidizing agents: differences between liquid and gas forms”. en. In: *Journal of Antimicrobial Chemotherapy* 65.10 (Oct. 2010), pp. 2108–2115. ISSN: 0305-7453, 1460-2091. DOI: 10.1093/jac/dkq308. URL: https://academic.oup.com/jac/article-lookup/doi/10.1093/jac/dkq308 (visited on 05/19/2026).

[43] Federica Veneri et al. “Ozone therapy in dentistry: An overview of the biological mechanisms involved (Review)”. In: *Biomedical Reports* 21.2 (June 2024), p. 115. ISSN: 2049-9434. DOI: 10.3892/br.2024.1803. URL: https://pmc.ncbi.nlm.nih.gov/articles/PMC11190636/ (visited on 05/19/2026).

[44] José F. Siqueira et al. “Efficacy of Instrumentation Techniques and Irrigation Regimens in Reducing the Bacterial Population within Root Canals”. In: *Journal of Endodontics* 28.3 (Mar. 2002), pp. 181–184. ISSN: 0099-2399. DOI: 10.1097/00004770-200203000-00009. URL: https://www.sciencedirect.com/science/article/pii/S0099239905606085 (visited on 05/19/2026).

[45] Cheng-Feng Tsai et al. “In vitro cytotoxicity and antibacterial activity of hypochlorous acid antimicrobial agent”. In: *Journal of Dental Sciences* 19.1 (Jan. 2024), pp. 345–356. ISSN: 1991-7902. DOI: 10.1016/j.jds.2023.07.007. URL: https://www.sciencedirect.com/science/article/pii/S199179022300212X (visited on 05/19/2026).

[46] D. H. Fine et al. “Effect of an essential oilcontaining antiseptic mouthrinse on plaque and salivary Streptococcus mutans levels”. en. In: *Journal of Clinical Periodontology* 27.3 (2000). _eprint: https://onlinelibrary.wiley.com/doi/pdf/10.1034/j.1600-051x.2000.027003157.x, pp. 157–161. ISSN: 1600-051X. DOI: 10.1034/j.1600-051x.2000.027003157.x. URL: https://onlinelibrary.wiley.com/doi/abs/10.1034/j.1600-051x.2000.027003157.x (visited on 05/19/2026).

[47] Domenico Trombetta et al. “Mechanisms of Antibacterial Action of Three Monoterpenes”. In: *Antimicrobial Agents and Chemotherapy* 49.6 (June 2005), pp. 2474–2478. ISSN: 0066-4804. DOI: 10.1128/AAC.49.6.2474-2478.2005. URL: https://pmc.ncbi.nlm.nih.gov/articles/PMC1140516/ (visited on 05/19/2026).

[48] P. Pan et al. “Determination of the in situ bactericidal activity of an essential oil mouthrinse using a vital stain method”. en. In: *Journal of Clinical Periodontology* 27.4 (2000). _eprint: https://onlinelibrary.wiley.com/doi/pdf/10.1034/j.1600-051x.2000.027004256.x, pp. 256–261. ISSN: 1600-051X. DOI: 10.1034/j.1600-051x.2000.027004256.x. URL: https://onlinelibrary.wiley.com/doi/abs/10.1034/j.1600-051x.2000.027004256.x (visited on 05/19/2026).

[49] Alex Nogueira Haas et al. “Essential oils-containing mouthwashes for gingivitis and plaque: Meta-analyses and meta-regression”. en. In: *Journal of Dentistry* 55 (Dec. 2016), pp. 7–15. ISSN: 03005712. DOI: 10.1016/j.jdent.2016.09.001. URL: https://linkinghub.elsevier.com/retrieve/pii/S0300571216301683 (visited on 05/19/2026).

[50] Christopher T. D Price, Ian R Lee, and John E Gustafson. “The effects of salicylate on bacteria”. In: *The International Journal of Biochemistry & Cell Biology* 32.10 (Oct. 2000), pp. 1029–1043. ISSN: 1357-2725. DOI: 10.1016/S1357-2725(00)00042-X. URL: https://www.sciencedirect.com/science/article/pii/S135727250000042X (visited on 05/19/2026).

[51] R. M. S. Thorn et al. “Electrochemically activated solutions: evidence for antimicrobial efficacy and applications in healthcare environments”. en. In: *European Journal of Clinical Microbiology & Infectious Diseases* 31.5 (May 2012), pp. 641–653. ISSN: 1435-4373. DOI: 10.1007/s10096-011-1369-9. URL: https://doi.org/10.1007/s10096-011-1369-9 (visited on 05/19/2026).

[52] Institute of Information and Communication Technologies Bulgarian Academy of Sciences, Bulgaria et al. “Electrochemically Activited Water: Biophysical and Biological Effects of Anolyte and Catholyte Types of Water”. In: *European Journal of Molecular Biotechnology* 7.1 (Mar. 2015), pp. 12–26. ISSN: 23106255, 24091332. DOI: 10.13187/ejmb.2014.7.12. URL: https://www.semanticscholar.org/paper/Electrochemically-Activited-Water.-Biophysical-and-Gluhchev-Ignatov/ccb95eedab7c3158417a7c1d122051702a2f53eb (visited on 05/19/2026).

[53] Marco Panizza and Giacomo Cerisola. “Direct And Mediated Anodic Oxidation of Organic Pollutants”. In: *Chemical Reviews* 109.12 (Dec. 2009), pp. 6541–6569. ISSN: 0009-2665. DOI: 10.1021/cr9001319. URL: https://doi.org/10.1021/cr9001319 (visited on 05/19/2026).

[54] Mohammadreza Mahmoodi and Esmail Pishbin. “Ozone-based advanced oxidation processes in water treatment: recent advances, challenges, and perspective”. en. In: *Environmental Science and Pollution Research* 32.7 (Feb. 2025), pp. 3531–3570. ISSN: 1614-7499. DOI: 10.1007/s11356-024-35835-w. URL: https://doi.org/10.1007/s11356-024-35835-w (visited on 05/19/2026).

[55] Enric Brillas and Carlos A. Martínez-Huitle. “Decontamination of wastewaters containing synthetic organic dyes by electrochemical methods. An updated review”. en. In: *Applied Catalysis B: Environmental* 166-167 (May 2015), pp. 603–643. ISSN: 09263373. DOI: 10.1016/j.apcatb.2014.11.016. URL: https://linkinghub.elsevier.com/retrieve/pii/S0926337314007176 (visited on 05/19/2026).

[56] Samira Siahrostami et al. “One- or Two-Electron Water Oxidation, Hydroxyl Radical, or H2O2 Evolution”. In: *The Journal of Physical Chemistry Letters* 8.6 (Mar. 2017), pp. 1157–1160. DOI: 10.1021/acs.jpclett.6b02924. URL: https://doi.org/10.1021/acs.jpclett.6b02924 (visited on 05/19/2026).

[57] Lei Hou et al. “An electrochemical study of the dissolution behavior of gold in a novel glycine-thiosulfate system”. en. In: *Minerals Engineering* 202 (Nov. 2023), p. 108273. ISSN: 08926875. DOI: 10.1016/j.mineng.2023.108273. URL: https://linkinghub.elsevier.com/retrieve/pii/S089268752300287X (visited on 05/19/2026).

[58] L. Kinsler. *Fundamentals of Acoustics*. Wiley, 2000.

[59] Klazina Kooiman et al. “Ultrasound-Responsive Cavitation Nuclei for Therapy and Drug Delivery”. eng. In: *Ultrasound in Medicine & Biology* 46.6 (June 2020), pp. 1296–1325. ISSN: 1879-291X. DOI: 10.1016/j.ultrasmedbio.2020.01.002.

[60] E Stride and N Saffari. “Microbubble ultrasound contrast agents: A review”. en. In: *Proceedings of the Institution of Mechanical Engineers, Part H: Journal of Engineering in Medicine* 217.6 (June 2003), pp. 429–447. ISSN: 0954-4119, 2041-3033. DOI: 10.1243/0954411036072907 2. URL: http://journals.sagepub.com/doi/10.1243/09544110360729072 (visited on 07/06/2023).

[61] Awaneesh Upadhyay and Sameer V. Dalvi. “Microbubble Formulations: Synthesis, Stability, Modeling and Biomedical Applications”. eng. In: *Ultrasound in Medicine & Biology* 45.2 (Feb. 2019), pp. 301–343. ISSN: 1879-291X. DOI: 10.1016/j.ultrasmedbio.2018.09.022.

[62] Dui Qin et al. “Cavitation Dynamics and Inertial Cavitation Threshold of Lipid Coated Microbubbles in Viscoelastic Media with Bubble–Bubble Interactions”. en. In: *Micromachines* 12.9 (Sept. 2021). ISSN: 2072-666X. DOI: 10.3390/mi12091125. URL: https://www.mdpi.com/2072-666X/12/9/1125 (visited on 02/20/2026).

[63] J. Angel Navarro-Becerra, Jair I. Castillo, and Mark A. Borden. “The Effect of Poly(ethylene glycol) Configuration on Microbubble Pharmacokinetics”. In: *ACS biomaterials science & engineering* 10.5 (May 2024), pp. 3331–3342. ISSN: 2373-9878. DOI: 10.1021/acsbiomaterials.3c01764. URL: https://pmc.ncbi.nlm.nih.gov/articles/PMC12380076/ (visited on 02/20/2026).

[64] *Lateral Phase Separation in Lipid-Coated Microbubbles — Langmuir*. URL: https://pubs.acs.org/doi/10.1021/la052841v (visited on 02/20/2026).

[65] Philippe Marmottant et al. “A model for large amplitude oscillations of coated bubbles accounting for buckling and rupture”. In: *Journal of The Acoustical Society of America - J ACOUST SOC AMER* 118 (Dec. 2005), pp. 3499–3505. DOI: 10.1121/1.2109427.

[66] Slimane Merouani et al. “Theoretical estimation of the temperature and pressure within collapsing acoustical bubbles”. In: *Ultrasonics Sonochemistry* 21.1 (Jan. 2014), pp. 53–59. ISSN: 1350-4177. DOI: 10.1016/j.ultsonch.2013.05.008. URL: https://www.sciencedirect.com/science/article/pii/S1350417713001168 (visited on 02/20/2026).

[67] Daniel Staub et al. “Novel applications of contrast-enhanced ultrasound imaging in vascular medicine”. eng. In: *VASA. Zeitschrift fur Gefasskrankheiten* 42.1 (Jan. 2013), pp. 17–31. ISSN: 0301-1526. DOI: 10.1024/0301-1526/a000244.

[68] Emmett Kennady et al. “Novel use of contrast enhanced ultrasonography with urodynamics in children: A comparison study to fluoroscopy”. eng. In: *Neurourology and Urodynamics* 43.3 (Mar. 2024), pp. 711–718. ISSN: 1520-6777. DOI: 10.1002/nau.25422.

[69] Ziyao Wang et al. “Recent progress in theranostic microbubbles”. In: *Chinese Chemical Letters* 34.9 (Sept. 2023), p. 108137. ISSN: 1001-8417. DOI: 10.1016/j.cclet.2023.108137. URL: https://www.sciencedirect.com/science/article/pii/S1001841723000098 (visited on 02/20/2026).

[70] Alexander L. Klibanov. "Ligand-Carrying Gas-Filled Microbubbles:′ Ultrasound Contrast Agents for Targeted Molecular Imaging". In: *Bioconjugate Chemistry* 16.1 (Jan. 2005), pp. 9–17. ISSN: 1043-1802. DOI: 10.1021/bc049898y. URL: https://doi.org/10.1021/bc049898y (visited on 02/20/2026).

[71] Amol M Takalkar et al. "Binding and detachment dynamics of microbubbles targeted to P-selectin under controlled shear flow". In: *Journal of Controlled Release* 96.3 (May 2004), pp. 473–482. ISSN: 0168-3659. DOI: 10.1016/j.jconrel.2004.03.002. URL: https://www.sciencedirect.com/science/article/pii/S0168365904001208 (visited on 02/20/2026).

[72] N. Deshpande, A. Needles, and J. K. Willmann. "Molecular ultrasound imaging: current status and future directions". English. In: *Clinical Radiology* 65.7 (July 2010), pp. 567–581. ISSN: 0009-9260, 1365-229X. DOI: 10.1016/j.crad.2010.02.013. URL: https://www.clinicalradiologyonline.net/article/S0009-9260(10)00125-X/abstract (visited on 02/20/2026).

[73] *Ultrasound Molecular Imaging With BR55 in Patients With Breast and Ovarian Lesions: First-in-Human Results — Journal of Clinical Oncology*. URL: https://ascopubs.org/doi/10.1200/JCO.2016.70.8594 (visited on 02/20/2026).

[74] Ine Lentacker, Stefaan C. De Smedt, and Niek N. Sanders. "Drug loaded microbubble design for ultrasound triggered delivery". en. In: *Soft Matter* 5.11 (May 2009), pp. 2161–2170. ISSN: 1744-6848. DOI: 10.1039/B823051J. URL: https://pubs.rsc.org/en/content/articlelanding/2009/sm/b823051j (visited on 02/20/2026).

[75] Qian Gong et al. "Drug-Loaded Microbubbles Combined with Ultrasound for Thrombolysis and Malignant Tumor Therapy". In: *BioMed Research International* 2019 (Oct. 2019), p. 6792465. ISSN: 2314-6133. DOI: 10.1155/2019/6792465. URL: https://pmc.ncbi.nlm.nih.gov/articles/PMC6791276/ (visited on 02/20/2026).

[76] Romain Melich et al. "Preparation and characterization of perfluorocarbon microbubbles using Shirasu Porous Glass (SPG) membranes". In: *Colloids and Surfaces A: Physicochemical and Engineering Aspects* 560 (Jan. 2019), pp. 233–243. ISSN: 0927-7757. DOI: 10.1016/j.colsurfa.2018.09.058. URL: https://www.sciencedirect.com/science/article/pii/S0927775718311658 (visited on 02/20/2026).

[77] Csongor Szíjjártó et al. "Effects of perfluorocarbon gases on the size and stability characteristics of phospholipid-coated microbubbles: osmotic effect versus interfacial film stabilization". eng. In: *Langmuir: the ACS journal of surfaces and colloids* 28.2 (Jan. 2012), pp. 1182–1189. ISSN: 1520-5827. DOI: 10.1021/la2043944.

[78] Jerry S. Cheung et al. "Microbubbles as a novel contrast agent for brain MRI". In: *NeuroImage* 46.3 (July 2009), pp. 658–664. ISSN: 1053-8119. DOI: 10.1016/j.neuroimage.2009.02.037. URL: https://www.sciencedirect.com/science/article/pii/S1053811909002018 (visited on 02/20/2026).

[79] Åsa Barrefelt et al. "Fluorescence labeled microbubbles for multimodal imaging". In: *Biochemical and Biophysical Research Communications* 464.3 (Aug. 2015), pp. 737–742. ISSN: 0006-291X. DOI: 10.1016/j.bbrc.2015.07.017. URL: https://www.sciencedirect.com/science/article/pii/S0006291X15302485 (visited on 02/20/2026).

[80] Joshua Owen et al. "Magnetic targeting of microbubbles against physiologically relevant flow conditions". In: *Interface Focus* 5.5 (Oct. 2015), p. 20150001. ISSN: 2042-8898. DOI: 10.1098/rsfs.2015.0001. URL: https://pmc.ncbi.nlm.nih.gov/articles/PMC4549839/ (visited on 02/20/2026).

[81] Phoebe J. Welch et al. "Perfluorocarbon nanodroplet size, acoustic vaporization, and inertial cavitation affected by lipid shell composition in vitro". eng. In: *The Journal of the Acoustical Society of America* 152.4 (Oct. 2022), p. 2493. ISSN: 1520-8524. DOI: 10.1121/10.0014934.

[82] Zhen Xu et al. "Histotripsy: A Method for Mechanical Tissue Ablation with Ultrasound". eng. In: *Annual review of biomedical engineering* 26.1 (July 2024), pp. 141–167. ISSN: 1545-4274. DOI: 10.1146/annurev-bioeng-073123-022334. URL: https://doi.org/10.1146/annurev-bioeng-073123-022334 (visited on 10/28/2024).

[83] Shengchen Su et al. "High-intensity focused ultrasound ablation to increase tumor-specific lymphocytes in prostate cancer". In: *Translational Oncology* 53 (Mar. 2025), p. 102293. ISSN: 1936-5233. DOI: 10.1016/j.tranon.2025.102293. URL: https://www.sciencedirect.com/science/article/pii/S1936523325000245 (visited on 02/19/2026).

[84] Che-Hsueh Yang et al. "High-Intensity Focus Ultrasound Ablation in Prostate Cancer: A Systematic Review". eng. In: *Journal of Personalized Medicine* 14.12 (Dec. 2024), p. 1163. ISSN: 2075-4426. DOI: 10.3390/jpm14121163.

[85] Nitin Abrol and Nitin S. Kekre. "Focused ultrasound guided relocation of kidney stones". In: *Indian Journal of Urology : IJU : Journal of the Urological Society of India* 31.1 (2015), pp. 28–32. ISSN: 0970-1591. DOI: 10.4103/0970-1591.139577. URL: https://pmc.ncbi.nlm.nih.gov/articles/PMC4300567/ (visited on 02/19/2026).

[86] J. Kost. "Ultrasound for controlled delivery of therapeutics". In: *Clinical Materials* 13.1 (Jan. 1993), pp. 155–161. ISSN: 0267-6605. DOI: 10.1016/0267-6605(93)90103-E. URL: https://www.sciencedirect.com/science/article/pii/026766059390103E (visited on 09/08/2025).

[87] Baris E. Polat et al. "Ultrasound-Mediated Transdermal Drug Delivery: Mechanisms, Scope, and Emerging Trends". In: *Journal of controlled release : official journal of the Controlled Release Society* 152.3 (June 2011), pp. 330–348. ISSN: 0168-3659. DOI: 10.1016/j.jconrel.2011.01.006. URL: https://pmc.ncbi.nlm.nih.gov/articles/PMC3436072/ (visited on 02/19/2026).

[88] Sayan Mullick Chowdhury, Taehwa Lee, and Jürgen K. Willmann. "Ultrasound-guided drug delivery in cancer". English. In: *Ultrasonography* 36.3 (May 2017), pp. 171–184. ISSN: 2288-5919, 2288-5943. DOI: 10.14366/usg.17021. URL: //www.e-ultrasonography.org/journal/view.php?doi=10.14366%2Fusg.17021&utm_source=chatgpt.com (visited on 12/21/2024).

[89] Filip Ivanovski et al. "Ultrasound-mediated spatial and temporal control of engineered cells in vivo". en. In: *Nature Communications* 15.1 (Aug. 2024), p. 7369. ISSN: 2041-1723. DOI: 10.1038/s41467-024-51620-2. URL: https://www.nature.com/articles/s41467-024-51620-2 (visited on 12/21/2024).

[90] Deepa Sharma, Kai Xuan Leong, and Gregory J. Czarnota. "Application of Ultrasound Combined with Microbubbles for Cancer Therapy". en. In: *International Journal of Molecular Sciences* 23.8 (Jan. 2022). Number: 8, p. 4393. ISSN: 1422-0067. DOI: 10.3390/ijms23084393. URL: https://www.mdpi.com/1422-0067/23/8/4393 (visited on 12/21/2024).

[91] Yun Cai et al. "A Review of the Combination Therapy of Low Frequency Ultrasound with Antibiotics". In: *BioMed Research International* 2017 (2017), p. 2317846. ISSN: 2314-6133. DOI: 10.1155/2017/2317846. URL: https://pmc.ncbi.nlm.nih.gov/articles/PMC5662814/ (visited on 02/04/2026).

[92] Kirby R. Lattwein et al. "Sonobactericide: An emerging treatment strategy for bacterial infections". In: *Ultrasound in medicine & biology* 46.2 (Feb. 2020), pp. 193–215. ISSN: 0301-5629. DOI: 10.1016/j.ultrasmedbio.2019.09.011. URL: https://www.ncbi.nlm.nih.gov/pmc/articles/PMC9278652/ (visited on 01/11/2025).

[93] Shengpu Gao et al. "Inactivation of bacteria and yeast using high-frequency ultrasound treatment". In: *Water Research* 60 (Sept. 2014), pp. 93–104. ISSN: 0043-1354. DOI: 10.1016/j.watres.2014.04.038. URL: https://www.sciencedirect.com/science/article/pii/S0043135414003236 (visited on 09/12/2025).

[94] İrfan Ayan et al. "The effect of low-intensity pulsed sound waves delivered by the Exogen device on Staphylococcus aureus morphology and genetics". en. In: *Acta Orthopaedica et Traumatologica Turcica* 42.4 (Dec. 2008). Number: 4, pp. 272–277. ISSN: 1017-995X, 1017-995X. URL: https://dergipark.org.tr/en/pub/aott/issue/18196/192119 (visited on 10/28/2024).

[95] Huajun Zhou et al. "Effect of low frequency ultrasound plus fluorescent composite carrier in the diagnosis and treatment of methicillin-resistant staphylococcus aureus biofilm infection of bone joint implant". en. In: *Int J Clin Exp Med 2018;11(2):799-805* (). ISSN: ISSN:1940-5901/IJCEM0070101.

[96] Kirby R. Lattwein et al. "An in vitro proof-of-principle study of sonobactericide". en. In: *Scientific Reports* 8.1 (Feb. 2018), p. 3411. ISSN: 2045-2322. DOI: 10.1038/s41598-018-21648-8. URL: https://www.nature.com/articles/s41598-018-21648-8 (visited on 10/28/2024).

[97] Hao Guo et al. "Stimulated phase-shift acoustic nanodroplets enhance vancomycin efficacy against methicillin-resistant Staphylococcus aureus biofilms". In: *International Journal of Nanomedicine* 12 (June 2017). _eprint: https://www.tandfonline.com/doi/pdf/10.2147/IJN.S134525, pp. 4679–4690. ISSN: 1176-9114. DOI: 10.2147/IJN.S134525. URL: https://www.tandfonline.com/doi/abs/10.2147/IJN.S134525 (visited on 10/28/2024).

[98] Flemming Forsberg et al. "Ultrasound Triggered Microbubble Destruction for Disrupting Biofilms in Synovial Fluid". In: *2020 IEEE International Ultrasonics Symposium (IUS)*. Sept. 2020, pp. 1–4. DOI: 10.1109/IUS46767.2020.9251545. URL: https://ieeexplore.ieee.org/abstract/document/9251545 (visited on 10/28/2024).

[99] Phillip G. Durham et al. "Harnessing ultrasound-stimulated phase change contrast agents to improve antibiotic efficacy against methicillin-resistant *Staphylococcus aureus* biofilms". In: *Biofilm* 3 (Dec. 2021), p. 100049. ISSN: 2590-2075. DOI: 10.1016/j.bioflm.2021.100049. URL: https://www.sciencedirect.com/science/article/pii/S2590207521000071 (visited on 10/28/2024).

[100] Joop J. P. Kouijzer et al. "Vancomycin-decorated microbubbles as a theranostic agent for *Staphylococcus aureus* biofilms". In: *International Journal of Pharmaceutics* 609 (Nov. 2021), p. 121154. ISSN: 0378-5173. DOI: 10.1016/j.ijpharm.2021.121154. URL: https://www.sciencedirect.com/science/article/pii/S0378517321009601 (visited on 10/28/2024).

[101] Marlies Overvelde et al. "Nonlinear shell behavior of phospholipid-coated microbubbles". eng. In: *Ultrasound in Medicine & Biology* 36.12 (Dec. 2010), pp. 2080–2092. ISSN: 1879-291X. DOI: 10.1016/j.ultrasmedbio.2010.08.015.

[102] Marco Cattaneo et al. "Cyclic jetting enables microbubble-mediated drug delivery". en. In: *Nature Physics* 21.4 (Apr. 2025), pp. 590–598. ISSN: 1745-2481. DOI: 10.1038/s41567-025-02785-0. URL: https://www.nature.com/articles/s41567-025-02785-0 (visited on 02/20/2026).

[103] E. A. Neppiras and B. E. Noltingk. "Cavitation Produced by Ultrasonics: Theoretical Conditions for the Onset of Cavitation". en. In: *Proceedings of the Physical Society. Section B* 64.12 (Dec. 1951), p. 1032. ISSN: 0370-1301. DOI: 10.1088/0370-1301/64/12/302. URL: https://doi.org/10.1088/0370-1301/64/12/302 (visited on 05/27/2026).

[104] Pierre Coulombel and Fabian Denner. *Prediction of the critical tension required for cavitation onset in transient pressure fields*. Aug. 2025. DOI: 10.5281/ZENODO.15839418. URL: https://zenodo.org/doi/10.5281/zenodo.15839418 (visited on 05/27/2026).

[105] Madhumithra Subramanian Karthikesh and Xinmai Yang. "The effect of ultrasound cavitation on endothelial cells". en. In: *Experimental Biology and Medicine* 246.7 (Jan. 2021), p. 758. DOI: 10.1177/1535370220982301. URL: https://pmc.ncbi.nlm.nih.gov/articles/PMC8719027/ (visited on 10/29/2024).

[106] Qianxi Wang, Kawa Manmi, and Kuo-Kang Liu. "Cell mechanics in biomedical cavitation". en. In: *Interface Focus* 5.5 (Oct. 2015), p. 20150018. DOI: 10.1098/rsfs.2015.0018. URL: https://pmc.ncbi.nlm.nih.gov/articles/PMC4549844/ (visited on 10/29/2024).

[107] Lauren Mancia et al. “Modeling tissue-selective cavitation damage”. en. In: *Physics in medicine and biology* 64.22 (Nov. 2019), p. 225001. DOI: 10.1088/1361-6560/ab5010. URL: https://pmc.ncbi.nlm.nih.gov/articles/PMC6925591/ (visited on 10/29/2024).

[108] Zahra Izadifar, Paul Babyn, and Dean Chapman. “Mechanical and Biological Effects of Ultrasound: A Review of Present Knowledge”. English. In: *Ultrasound in Medicine and Biology* 43.6 (June 2017), pp. 1085–1104. ISSN: 0301-5629, 1879-291X. DOI: 10.1016/j.ultrasmedbio.2017.01.023. URL: https://www.umbjournal.org/article/S0301-5629(17)30052-2/fulltext (visited on 09/12/2025).

[109] Sara B. Keller et al. “Quantitative evaluation of anti-biofilm cavitation activity seeded from microbubbles or protein cavitation nuclei by passive acoustic mapping”. en. In: *Physics in Medicine & Biology* 69.21 (Oct. 2024), p. 215008. ISSN: 0031-9155. DOI: 10.1088/1361-6560/ad7f1a. URL: https://dx.doi.org/10.1088/1361-6560/ad7f1a (visited on 10/29/2024).

[110] Gareth LuTheryn et al. “Cationic Microbubbles for Non-Selective Binding of Cavitation Nuclei to Bacterial Biofilms”. eng. In: *Pharmaceutics* 15.5 (May 2023), p. 1495. ISSN: 1999-4923. DOI: 10.3390/pharmaceutics15051495.

[111] Nina Vyas et al. “Which Parameters Affect Biofilm Removal with Acoustic Cavitation? A Review”. In: *Ultrasound in Medicine & Biology* 45.5 (May 2019), pp. 1044–1055. ISSN: 0301-5629. DOI: 10.1016/j.ultrasmedbio.2019.01.002. URL: https://www.sciencedirect.com/science/article/pii/S0301562919300067 (visited on 10/29/2024).

[112] Sandra Mozo, Carmen Llena, and Leopoldo Forner. “Review of ultrasonic irrigation in endodontics: increasing action of irrigating solutions”. en. In: *Medicina Oral, Patología Oral y Cirugía Bucal* 17.3 (Dec. 2011), e512. DOI: 10.4317/medoral.17621. URL: https://pmc.ncbi.nlm.nih.gov/articles/PMC3476090/ (visited on 10/30/2024).

[113] Yen-Liang Chen et al. “Application and development of ultrasonics in dentistry”. In: *Journal of the Formosan Medical Association* 112.11 (Nov. 2013), pp. 659–665. ISSN: 0929-6646. DOI: 10.1016/j.jfma.2013.05.007. URL: https://www.sciencedirect.com/science/article/pii/S0929664613001745 (visited on 10/30/2024).

[114] Ryeol Park et al. “Root canal irrigation system using remotely generated high-power ultrasound”. In: *Ultrasonics Sonochemistry* 90 (Nov. 2022), p. 106168. ISSN: 1350-4177. DOI: 10.1016/j.ultsonch.2022.106168. URL: https://www.sciencedirect.com/science/article/pii/S1350417722002644 (visited on 10/29/2024).

[115] Matteo Erriu et al. “Microbial biofilm modulation by ultrasound: Current concepts and controversies”. In: *Ultrasonics Sonochemistry* 21.1 (Jan. 2014), pp. 15–22. ISSN: 1350-4177. DOI: 10.1016/j.ultsonch.2013.05.011. URL: https://www.sciencedirect.com/science/article/pii/S1350417713001193 (visited on 10/30/2024).

[116] N. Vyas et al. “The effect of standoff distance and surface roughness on biofilm disruption using cavitation”. en. In: *PLoS ONE* 15.7 (July 2020), e0236428. DOI: 10.1371/journal.pone.0236428. URL: https://pmc.ncbi.nlm.nih.gov/articles/PMC7392287/ (visited on 10/30/2024).

[117] R. G. Macedo et al. “Sonochemical and high-speed optical characterization of cavitation generated by an ultrasonically oscillating dental file in root canal models”. In: *Ultrasonics Sonochemistry* 21.1 (Jan. 2014), pp. 324–335. ISSN: 1350-4177. DOI: 10.1016/j.ultsonch.2013.03.001. URL: https://www.sciencedirect.com/science/article/pii/S1350417713000680 (visited on 01/30/2025).

[118] Do Yee Hoo et al. “Ultrasonic cavitation: An effective cleaner and greener intensification technology in the extraction and surface modification of nanocellulose”. In: *Ultrasonics Sonochemistry* 90 (Nov. 2022), p. 106176. ISSN: 1350-4177. DOI: 10.1016/j.ultsonch.2022.106176. URL: https://www.sciencedirect.com/science/article/pii/S1350417722002723 (visited on 09/12/2025).

[119] Mojca Zupanc et al. “Effects of cavitation on different microorganisms: The current understanding of the mechanisms taking place behind the phenomenon. A review and proposals for further research”. In: *Ultrasonics Sonochemistry* 57 (Oct. 2019), pp. 147–165. ISSN: 1350-4177. DOI: 10.1016/j.ultsonch.2019.05.009. URL: https://www.sciencedirect.com/science/article/pii/S1350417719302305 (visited on 09/12/2025).

[120] Yanzhen Zhang et al. “Ultrasonic vibration micro-jet ejection for metal additive manufacture”. In: *Journal of Materials Research and Technology* 28 (Jan. 2024), pp. 2149–2162. ISSN: 2238-7854. DOI: 10.1016/j.jmrt.2023.12.156. URL: https://www.sciencedirect.com/science/article/pii/S2238785423032209 (visited on 09/12/2025).

[121] W. L. Nyborg. “Ultrasonic microstreaming and related phenomena.” In: *The British Journal of Cancer. Supplement* 5 (Mar. 1982), pp. 156–160. ISSN: 0306-9443. URL: https://www.ncbi.nlm.nih.gov/pmc/articles/PMC2149335/ (visited on 09/12/2025).

[122] Joydip Mondal et al. “Bubble oscillations at low frequency ultrasound for biological applications”. In: *Ultrasonics Sonochemistry* 104 (Mar. 2024), p. 106816. ISSN: 1350-4177. DOI: 10.1016/j.ultsonch.2024.106816. URL: https://www.sciencedirect.com/science/article/pii/S1350417724000646 (visited on 09/12/2025).

[123] Nor Saadah Mohd Yusof et al. “Physical and chemical effects of acoustic cavitation in selected ultrasonic cleaning applications”. In: *Ultrasonics Sonochemistry* 29 (Mar. 2016), pp. 568–576. ISSN: 1350-4177. DOI: 10.1016/j.ultsonch.2015.06.013. URL: https://www.sciencedirect.com/science/article/pii/S1350417715001856 (visited on 09/12/2025).

[124] S. Arrojo, Y. Benito, and A. Martínez Tarifa. "A parametrical study of disinfection with hydrodynamic cavitation". In: *Ultrasonics Sonochemistry* 15.5 (July 2008), pp. 903–908. ISSN: 1350-4177. DOI: 10.1016/j.ultsonch.2007.11.001. URL: https://www.sciencedirect.com/science/article/pii/S1350417707001848 (visited on 09/12/2025).

[125] Masaki Kurokawa et al. "Effect of sonication frequency on the disruption of algae". In: *Ultrasonics Sonochemistry* 31 (July 2016), pp. 157–162. ISSN: 1350-4177. DOI: 10.1016/j.ultsonch.2015.12.011. URL: https://www.sciencedirect.com/science/article/pii/S1350417715301048 (visited on 09/12/2025).

[126] Gregory Loraine et al. "Disinfection of gram-negative and gram-positive bacteria using DynaJets® hydrodynamic cavitating jets". In: *Ultrasonics Sonochemistry* 19.3 (May 2012), pp. 710–717. ISSN: 1350-4177. DOI: 10.1016/j.ultsonch.2011.10.011. URL: https://www.sciencedirect.com/science/article/pii/S1350417711002148 (visited on 09/12/2025).

[127] P Piyasena, E Mohareb, and R. C McKellar. "Inactivation of microbes using ultrasound: a review". In: *International Journal of Food Microbiology* 87.3 (Nov. 2003), pp. 207–216. ISSN: 0168-1605. DOI: 10.1016/S0168-1605(03)00075-8. URL: https://www.sciencedirect.com/science/article/pii/S0168160503000758 (visited on 09/12/2025).

[128] Talal Yusaf and Raed A. Al-Juboori. "Alternative methods of microorganism disruption for agricultural applications". In: *Applied Energy* 114 (Feb. 2014), pp. 909–923. ISSN: 0306-2619. DOI: 10.1016/j.apenergy.2013.08.085. URL: https://www.sciencedirect.com/science/article/pii/S0306261913007290 (visited on 09/12/2025).

[129] Pedro A. Quinto-Su, Madoka Suzuki, and Claus-Dieter Ohl. "Fast temperature measurement following single laser-induced cavitation inside a microfluidic gap". en. In: *Scientific Reports* 4.1 (June 2014), p. 5445. ISSN: 2045-2322. DOI: 10.1038/srep05445. URL: https://www.nature.com/articles/srep05445 (visited on 02/20/2026).

[130] Nor Saadah M. Yusof et al. "A correlation between cavitation bubble temperature, sonoluminescence and interfacial chemistry – A minireview". In: *Ultrasonics Sonochemistry* 85 (Mar. 2022), p. 105988. ISSN: 1350-4177. DOI: 10.1016/j.ultsonch.2022.105988. URL: https://pmc.ncbi.nlm.nih.gov/articles/PMC8960979/ (visited on 02/20/2026).

[131] F. J. Fuchs. "19 - Ultrasonic cleaning and washing of surfaces". In: *Power Ultrasonics*. Ed. by Juan A. Gallego-Juárez and Karl F. Graff. Oxford: Woodhead Publishing, Jan. 2015, pp. 577–609. ISBN: 978-1-78242-028-6. DOI: 10.1016/B978-1-78242-028-6.00019-3. URL: https://www.sciencedirect.com/science/article/pii/B9781782420286000193 (visited on 09/09/2024).

[132] Ali Jangjou et al. "The promising shadow of microbubble over medical sciences: from fighting wide scope of prevalence disease to cancer eradication". In: *Journal of Biomedical Science* 28.1 (June 2021), p. 49. ISSN: 1423-0127. DOI: 10.1186/s12929-021-00744-4. URL: https://doi.org/10.1186/s12929-021-00744-4 (visited on 01/14/2025).

[133] Shinobu Koda et al. "Inactivation of *Escherichia coli* and *Streptococcus mutans* by ultrasound at 500 kHz". In: *Ultrasonics Sonochemistry* 16.5 (June 2009), pp. 655–659. ISSN: 1350-4177. DOI: 10.1016/j.ultsonch.2009.02.003. URL: https://www.sciencedirect.com/science/article/pii/S1350417709000133 (visited on 09/12/2025).

[134] Shengpu Gao et al. "Inactivation of microorganisms by low-frequency high-power ultrasound: 1. Effect of growth phase and capsule properties of the bacteria". en. In: *Ultrasonics Sonochemistry* 21.1 (Jan. 2014), pp. 446–453. ISSN: 13504177. DOI: 10.1016/j.ultsonch.2013.06.006. URL: https://linkinghub.elsevier.com/retrieve/pii/S1350417713001442 (visited on 09/12/2025).

[135] Elena S. Inguglia et al. "Effects of high intensity ultrasound on the inactivation profiles of *Escherichia coli* K12 and *Listeria innocua* with salt and salt replacers". In: *Ultrasonics Sonochemistry* 48 (Nov. 2018), pp. 492–498. ISSN: 1350-4177. DOI: 10.1016/j.ultsonch.2018.05.007. URL: https://www.sciencedirect.com/science/article/pii/S1350417718303821 (visited on 09/12/2025).

[136] Michelle Cameron, Lynn D. McMaster, and Trevor J. Britz. "Electron microscopic analysis of dairy microbes inactivated by ultrasound". In: *Ultrasonics Sonochemistry* 15.6 (Sept. 2008), pp. 960–964. ISSN: 1350-4177. DOI: 10.1016/j.ultsonch.2008.02.012. URL: https://www.sciencedirect.com/science/article/pii/S1350417708000382 (visited on 09/12/2025).

[137] Xinyu Liao et al. "Multiple action sites of ultrasound on *Escherichia coli* and *Staphylococcus aureus*". In: *Food Science and Human Wellness* 7.1 (Mar. 2018), pp. 102–109. ISSN: 2213-4530. DOI: 10.1016/j.fshw.2018.01.002. URL: https://www.sciencedirect.com/science/article/pii/S221345301730191X (visited on 05/29/2026).

[138] Jiao Li Tian Ding. "Evaluation of Ultrasound-Induced Damage to Escherichia coli and Staphylococcus aureus by Flow Cytometry and Transmission Electron Microscopy — Applied and Environmental Microbiology". In: *Applied and Environmental Microbiology - Vol. 82, No. 6* (). DOI: https://doi.org/10.1128/AEM.03080-15. URL: https://journals.asm.org/doi/10.1128/aem.03080-15 (visited on 09/12/2025).

[139] Naama Dror et al. "Advances in Microbial Biofilm Prevention on Indwelling Medical Devices with Emphasis on Usage of Acoustic Energy". en. In: *Sensors* 9.4 (Apr. 2009). Number: 4, pp. 2538–2554. ISSN: 1424-8220. DOI: 10.3390/s90402538. URL: https://www.mdpi.com/1424-8220/9/4/2538 (visited on 01/11/2025).

[140] Lasse Kvich et al. “The Combination of Low-Frequency Ultrasound and Antibiotics Improves the Killing of In Vitro Staphylococcus aureus and Pseudomonas aeruginosa Biofilms”. en. In: *Antibiotics* 11.11 (Nov. 2022). Number: 11, p. 1494. ISSN: 2079-6382. DOI: 10.3390/antibiotics11111494. URL: https://www.mdpi.com/2079-6382/11/11/1494 (visited on 01/11/2025).

[141] Danae Anastasia Apatzidou. “Modern Approaches to Non-Surgical Biofilm Management”. en. In: (Nov. 2011). DOI: 10.1159/000329674. URL: https://karger.com/books/book/2972/chapter/5841272/Modern-Approaches-to-Non-Surgical-Biofilm (visited on 09/09/2024).

[142] Wenhao Zhou, Frederick Sarpong, and Cunshan Zhou. “Use of Ultrasonic Cleaning Technology in the Whole Process of Fruit and Vegetable Processing”. In: *Foods* 11.18 (Sept. 2022), p. 2874. ISSN: 2304-8158. DOI: 10.3390/foods11182874. URL: https://www.ncbi.nlm.nih.gov/pmc/articles/PMC9498452/ (visited on 09/09/2024).

[143] Z. Qian, R. D. Sagers, and W. G. Pitt. “The effect of ultrasonic frequency upon enhanced killing of P. aeruginosa biofilms”. eng. In: *Annals of Biomedical Engineering* 25.1 (1997), pp. 69–76. ISSN: 0090-6964. DOI: 10.1007/BF02738539.

[144] Cassandra Rux et al. “Optimizing the use of low-frequency ultrasound for bacterial detachment of in vivo biofilms in dental research-a methodological study”. eng. In: *Clinical Oral Investigations* 28.1 (Dec. 2023), p. 19. ISSN: 1436-3771. DOI: 10.1007/s00784-023-05397-1.

[145] Mengqian Zhu et al. “Antimicrobial and cleaning effects of ultrasonic-mediated plasma-loaded microbubbles on Enterococcus faecalis biofilm: an in vitro study”. eng. In: *BMC oral health* 23.1 (Mar. 2023), p. 133. ISSN: 1472-6831. DOI: 10.1186/s12903-023-02813-6.

[146] Daiki Omata et al. “Effects of encapsulated gas on stability of lipid-based microbubbles and ultrasound-triggered drug delivery”. In: *Journal of Controlled Release* 311-312 (Oct. 2019), pp. 65–73. ISSN: 0168-3659. DOI: 10.1016/j.jconrel.2019.08.023. URL: https://www.sciencedirect.com/science/article/pii/S0168365919305073 (visited on 01/14/2025).

[147] Ying Deng et al. “Optimization of Staining with SYTO 9/Propidium Iodide: Interplay, Kinetics and Impact on Brevibacillus Brevis”. In: *BioTechniques* 69.2 (Aug. 2020). _eprint: https://doi.org/10.2144/btn-2020-0036, pp. 88–98. ISSN: 0736-6205. DOI: 10.2144/btn-2020-0036. URL: https://doi.org/10.2144/btn-2020-0036 (visited on 09/16/2024).

[148] Kathrin Becker et al. “Efficacy of 0.05% Chlorhexidine and 0.05% Cetylpyridinium Chloride Mouthwash to Eliminate Living Bacteria on In Situ Collected Biofilms: An In Vitro Study”. In: *Antibiotics* 10.6 (June 2021), p. 730. ISSN: 2079-6382. DOI: 10.3390/antibiotics10060730. URL: https://www.ncbi.nlm.nih.gov/pmc/articles/PMC8235160/ (visited on 01/14/2025).

[149] C. P. Ernst, K. Prockl, and B. Willershausen. “The effectiveness and side effects of 0.1% and 0.2% chlorhexidine mouthrinses: a clinical study”. eng. In: *Quintessence International (Berlin, Germany: 1985)* 29.7 (July 1998), pp. 443–448. ISSN: 0033-6572.

[150] Brigitte Kunze et al. “Damage of Streptococcus mutans biofilms by carolacton, a secondary metabolite from the myxobacterium Sorangium cellulosum”. en. In: *BMC Microbiology* 10.1 (July 2010), p. 199. ISSN: 1471-2180. DOI: 10.1186/1471-2180-10-199. URL: https://doi.org/10.1186/1471-2180-10-199 (visited on 04/17/2026).

[151] E.-M. Decker. “The ability of direct fluorescence-based, two-colour assays to detect different physiological states of oral streptococci”. In: *Letters in Applied Microbiology* 33.3 (Sept. 2001), pp. 188–192. ISSN: 0266-8254. DOI: 10.1046/j.1472-765x.2001.00971.x. URL: https://doi.org/10.1046/j.1472-765x.2001.00971.x (visited on 04/17/2026).

[152] Joelle Stilwell et al. “Effect of ultrasound-microbubble exposure on acute myeloid leukemia cancer cell proteome”. en. In: *Scientific Reports* 15.1 (Aug. 2025), p. 29817. ISSN: 2045-2322. DOI: 10.1038/s41598-025-14727-0. URL: https://www.nature.com/articles/s41598-025-14727-0 (visited on 12/09/2025).

[153] Linsey C. Phillips et al. “Ultrasound-microbubble-mediated drug delivery efficacy and cell viability depend on microbubble radius and ultrasound frequency”. In: *2010 IEEE International Ultrasonics Symposium*. Oct. 2010, pp. 1775–1778. DOI: 10.1109/ULTSYM.2010.5935988. URL: https://ieeexplore.ieee.org/document/5935988 (visited on 12/09/2025).

[154] Cameron A. B. Smith and Constantin C. Coussios. “Spatiotemporal Assessment of the Cellular Safety of Cavitation-Based Therapies by Passive Acoustic Mapping”. In: *Ultrasound in Medicine & Biology* 46.5 (May 2020), pp. 1235–1243. ISSN: 0301-5629. DOI: 10.1016/j.ultrasmedbio.2020.01.009. URL: https://www.sciencedirect.com/science/article/pii/S0301562920300119 (visited on 12/09/2025).

[155] Peter E. Murray, Jonathan A. Coffman, and Franklin Garcia-Godoy. “Oral Pathogens’ Substantial Burden on Cancer, Cardiovascular Diseases, Alzheimer’s, Diabetes, and Other Systemic Diseases: A Public Health Crisis—A Comprehensive Review”. In: *Pathogens* 13.12 (Dec. 2024), p. 1084. ISSN: 2076-0817. DOI: 10.3390/pathogens13121084. URL: https://pmc.ncbi.nlm.nih.gov/articles/PMC11677847/ (visited on 02/26/2026).

[156] Jing Yang et al. “The economic consequences of oral disorders at global, regional, and national levels”. In: *BMC Oral Health* 25 (Nov. 2025), p. 1802. ISSN: 1472-6831. DOI: 10.1186/s12903-025-07205-6. URL: https://pmc.ncbi.nlm.nih.gov/articles/PMC12628856/ (visited on 02/26/2026).

[157] A.J. Righolt et al. “Global-, Regional-, and Country-Level Economic Impacts of Dental Diseases in 2015”. EN. In: *Journal of Dental Research* 97.5 (May 2018), pp. 501–507. ISSN: 0022-0345. DOI: 10.1177/0022034517750572. URL: https://doi.org/10.1177/0022034517750572 (visited on 02/26/2026).

[158] H. Horsley et al. “Ultrasound-activated microbubbles as a novel intracellular drug delivery system for urinary tract infection”. In: *Journal of Controlled Release* 301 (May 2019), pp. 166–175. ISSN: 0168-3659. DOI: 10.1016/j.jconrel.2019.03.017. URL: https://www.sciencedirect.com/science/article/pii/S016836591930166X (visited on 08/23/2023).

[159] Juliana Sitta and Candace M. Howard. “Applications of Ultrasound-Mediated Drug Delivery and Gene Therapy”. en. In: *International Journal of Molecular Sciences* 22.21 (Oct. 2021), p. 11491. DOI: 10.3390/ijms222111491. URL: https://pmc.ncbi.nlm.nih.gov/articles/PMC8583720/ (visited on 11/05/2024).

[160] Shengpu Gao et al. “Inactivation of microorganisms by low-frequency high-power ultrasound: 1. Effect of growth phase and capsule properties of the bacteria”. In: *Ultrasonics Sonochemistry* 21.1 (Jan. 2014), pp. 446–453. ISSN: 1350-4177. DOI: 10.1016/j.ultsonch.2013.06.006. URL: https://www.sciencedirect.com/science/article/pii/S1350417713001442 (visited on 09/12/2025).

[161] S. Drakopoulou et al. “Ultrasound-induced inactivation of gram-negative and gram-positive bacteria in secondary treated municipal wastewater”. In: *Ultrasonics Sonochemistry* 16.5 (June 2009), pp. 629–634. ISSN: 1350-4177. DOI: 10.1016/j.ultsonch.2008.11.011. URL: https://www.sciencedirect.com/science/article/pii/S1350417708001946 (visited on 01/13/2026).

[162] P. A. Idowu and O. S. Idowu. “In-vitro Bactericidal Kinetics of Chlorhexidine Gluconate Disinfectant/ Antiseptic Formulations Containing Different Additives”. en. In: *African Journal of Biomedical Research* 17.1 (2014), pp. 37–42. ISSN: 1119-5096. URL: https://africanjournalofbiomedicalresearch.com/index.php/AJBR/article/view/576 (visited on 01/13/2026).

[163] Louisa V. Ashby et al. “Evaluating the bactericidal action of hypochlorous acid in culture media”. In: *Free Radical Biology and Medicine* 159 (Nov. 2020), pp. 119–124. ISSN: 0891-5849. DOI: 10.1016/j.freeradbiomed.2020.07.033. URL: https://www.sciencedirect.com/science/article/pii/S0891584920311801 (visited on 01/13/2026).

[164] *Hydro air washer – SOOVON KOREA*. URL: https://en.soovon.com/airwasher/ (visited on 01/28/2026).

[165] Julia L. Sharp, Albert E. Parker, and Martin A. Hamilton. “Calculating the limit of detection for a dilution series”. In: *Journal of Microbiological Methods* 208 (May 2023), p. 106723. ISSN: 0167-7012. DOI: 10.1016/j.mimet.2023.106723. URL: https://www.sciencedirect.com/science/article/pii/S016770122300057X (visited on 05/20/2026).

[166] Ahsan Mehran Hussain, G. A. (Fridus) van der Weijden, and Dagmar Else Slot. “Effect of a sodium hypochlorite mouthwash on plaque and clinical parameters of periodontal disease-a systematic review”. In: *International Journal of Dental Hygiene* 20.1 (Feb. 2022), pp. 40–52. ISSN: 1601-5029. DOI: 10.1111/idh.12510. URL: https://pmc.ncbi.nlm.nih.gov/articles/PMC9292655/ (visited on 01/30/2026).

[167] Zahed Mohammadi. “Sodium hypochlorite in endodontics: an update review”. In: *International Dental Journal* 58.6 (Dec. 2008), pp. 329–341. ISSN: 0020-6539. DOI: 10.1111/j.1875-595X.2008.tb00354.x. URL: https://www.sciencedirect.com/science/article/pii/S0020653920349960 (visited on 01/30/2026).

[168] Francisco Wilker Mustafa Gomes Muniz et al. “A Systematic Review of the Effect of Oral Rinsing with H2O2 on Clinical and Microbiological Parameters Related to Plaque, Gingivitis, and Microbes”. In: *International Journal of Dentistry* 2020 (Oct. 2020), p. 8841722. ISSN: 1687-8728. DOI: 10.1155/2020/8841722. URL: https://pmc.ncbi.nlm.nih.gov/articles/PMC7648695/ (visited on 01/30/2026).

[169] Monir Nobahar et al. “Effects of hydrogen peroxide mouthwash on preventing ventilator-associated pneumonia in patients admitted to the intensive care unit”. en. In: *The Brazilian Journal of Infectious Diseases* 20.5 (Sept. 2016), pp. 444–450. ISSN: 1413-8670. DOI: 10.1016/j.bjid.2016.06.005. URL: http://www.bjid.org.br/en-effects-hydrogen-peroxide-mouthwash-on-articulo-S1413867016301131 (visited on 01/30/2026).

[170] Zoë Brookes et al. “Mouthwash Effects on the Oral Microbiome: Are They Good, Bad, or Balanced?” In: *International Dental Journal* 73.Suppl 2 (Oct. 2023), S74–S81. ISSN: 0020-6539. DOI: 10.1016/j.identj.2023.08.010. URL: https://pmc.ncbi.nlm.nih.gov/articles/PMC10690560/ (visited on 03/03/2026).

[171] Saki Nishihama et al. “Bactericidal activity of slightly acidic electrolyzed water against the cariogenic bacterium Streptococcus mutans and other oral bacteria”. en. In: *Oral Science International* 21.3 (2024). _eprint: https://onlinelibrary.wiley.com/doi/pdf/10.1002/osi2.1224, pp. 344–351. ISSN: 1881-4204. DOI: 10.1002/osi2.1224. URL: https://onlinelibrary.wiley.com/doi/abs/10.1002/osi2.1224 (visited on 05/29/2026).

[172] T.E. Cloete et al. “The antimicrobial mechanism of electrochemically activated water against Pseudomonas aeruginosa and Escherichia coli as determined by SDS-PAGE analysis”. In: *Journal of Applied Microbiology* 107.2 (Aug. 2009), pp. 379–384. ISSN: 1364-5072. DOI: 10.1111/j.1365-2672.2009.04233.x. URL: https://doi.org/10.1111/j.1365-2672.2009.04233.x (visited on 05/29/2026).

[173] Filip Plazonic et al. “Bactericidal Effect of Ultrasound-Responsive Microbubbles and Sub-inhibitory Gentamicin against Pseudomonas aeruginosa Biofilms on Substrates With Differing Acoustic Impedance”. English. In: *Ultrasound in Medicine and Biology* 48.9 (Sept. 2022), pp. 1888–1898. ISSN: 0301-5629, 1879-291X. DOI: 10.1016/j.ultrasmedbio.2022.05.019. URL: https://www.umbjournal.org/article/S0301-5629(22)00407-0/fulltext (visited on 02/04/2026).

[174] Adam J. Singer et al. “The Effects of Low-Frequency Ultrasound on Staphylococcus epidermidis”. en. In: *Current Microbiology* 38.3 (Mar. 1999), pp. 194–196. ISSN: 1432-0991. DOI: 10.1007/PL00006786. URL: https://doi.org/10.1007/PL00006786 (visited on 02/04/2026).

[175] Andrew A. Brayman et al. “Inactivation of Planktonic *Escherichia coli* by Focused 1-MHz Ultrasound Pulses with Shocks: Efficacy and Kinetics Upon Volume Scale-Up”. In: *Ultrasound in Medicine & Biology* 44.9 (Sept. 2018), pp. 1996–2008. ISSN: 0301-5629. DOI: 10.1016/j.ultrasmedbio.2018.05.010. URL: https://www.sciencedirect.com/science/article/pii/S0301562918302138 (visited on 02/04/2026).

[176] *Medical Microbiology- The evaluation of ultrasonic effects on the pathogenesis of Gram negative and Gram positive bacteria*. en. URL: https://pureportal.coventry.ac.uk/en/studentTheses/medical-microbiology-the-evaluation-of-ultrasonic-effects-on-the-/ (visited on 02/06/2026).

[177] Zoran Herceg et al. “The Effect of High Intensity Ultrasound Treatment on the Amount of Staphylococcus aureus and Escherichia coli in Milk”. en. In: (2012).

[178] Mirat D. Gurol and Philip C. Singer. “Kinetics of ozone decomposition: a dynamic approach”. en. In: *Environmental Science & Technology* 16.7 (July 1982), pp. 377–383. ISSN: 0013-936X, 1520-5851. DOI: 10.1021/es00101a003. URL: https://pubs.acs.org/doi/abs/10.1021/es00101a003 (visited on 01/28/2026).

[179] Davide Gardoni, A Vailati, and Roberto Canziani. “Decay of Ozone in Water: A Review”. In: *Ozone Science and Engineering* 34 (July 2012), p. 233. DOI: 10.1080/01919512.2012.686354.

[180] C. Ganss et al. “Tooth brushing habits in uninstructed adults—frequency, technique, duration and force”. en. In: *Clinical Oral Investigations* 13.2 (June 2009), pp. 203–208. ISSN: 1436-3771. DOI: 10.1007/s00784-008-0230-8. URL: https://doi.org/10.1007/s00784-008-0230-8 (visited on 01/29/2026).

[181] U. P. Saxer, J. Barbakow, and S. L. Yankell. “New studies on estimated and actual toothbrushing times and dentifrice use”. eng. In: *The Journal of Clinical Dentistry* 9.2 (1998), pp. 49–51. ISSN: 0895-8831.

[182] Liana Dobler et al. “Abrasive Enamel and Dentin Wear Resulting from Brushing with Toothpastes with Highly Discrepant Relative Enamel Abrasivity (REA) and Relative Dentin Abrasivity (RDA) Values”. In: *Oral Health & Preventive Dentistry* 21 (), b3858625. ISSN: 1602-1622. DOI: 10.3290/j.ohpd.b3858625. URL: https://pmc.ncbi.nlm.nih.gov/articles/PMC11619904/ (visited on 02/13/2026).

[183] Philippe Marmottant et al. “Buckling resistance of solid shell bubbles under ultrasound”. In: *The Journal of the Acoustical Society of America* 129.3 (Mar. 2011), pp. 1231–1239. ISSN: 0001-4966. DOI: 10.1121/1.3543943. URL: https://doi.org/10.1121/1.3543943 (visited on 05/29/2026).

[184] Kenneth B. Bader, Eli Vlaisavljevich, and Adam D. Maxwell. “For Whom the Bubble Grows: Physical Principles of Bubble Nucleation and Dynamics in Histotripsy Ultrasound Therapy”. In: *Ultrasound in Medicine & Biology* 45.5 (May 2019), pp. 1056–1080. ISSN: 0301-5629. DOI: 10.1016/j.ultrasmedbio.2018.10.035. URL: https://www.sciencedirect.com/science/article/pii/S0301562919300821 (visited on 05/29/2026).

[185] Dario Carugo et al. “Scaleable production of microbubbles using an ultrasound-modulated microfluidic devicea)”. In: *The Journal of the Acoustical Society of America* 150.2 (Aug. 2021), pp. 1577–1589. ISSN: 0001-4966. DOI: 10.1121/10.0005911. URL: https://doi.org/10.1121/10.0005911 (visited on 03/24/2026).

[186] Daiki Omata et al. “Lipid-based microbubbles and ultrasound for therapeutic application”. In: *Advanced Drug Delivery Reviews*. Advanced Liposome Research 154-155 (Jan. 2020), pp. 236–244. ISSN: 0169-409X. DOI: 10.1016/j.addr.2020.07.005. URL: https://www.sciencedirect.com/science/article/pii/S0169409X20300818 (visited on 02/18/2026).

[187] Joshua Owen et al. “The Role of PEG-40-stearate in the Production, Morphology, and Stability of Microbubbles”. In: *Langmuir* 35.31 (Aug. 2019), pp. 10014–10024. ISSN: 0743-7463. DOI: 10.1021/acs.langmuir.8b02516. URL: https://doi.org/10.1021/acs.langmuir.8b02516 (visited on 09/03/2024).

[188] Simone A.G. Langeveld et al. “The Impact of Lipid Handling and Phase Distribution on the Acoustic Behavior of Microbubbles”. In: *Pharmaceutics* 13.1 (Jan. 2021), p. 119. ISSN: 1999-4923. DOI: 10.3390/pharmaceutics13010119. URL: https://pmc.ncbi.nlm.nih.gov/articles/PMC7832861/ (visited on 02/18/2026).

[189] Kenta Kakiuchi and Mark Andrew Borden. “Effect of lipid composition and stirring dynamics on oxygen microbubble stability and oxygen release”. In: *Langmuir : the ACS journal of surfaces and colloids* 41.3 (Jan. 2025), pp. 1745–1755. ISSN: 0743-7463. DOI: 10.1021/acs.langmuir.4c04104. URL: https://pmc.ncbi.nlm.nih.gov/articles/PMC12039959/ (visited on 05/29/2026).

[190] John R. Eisenbrey et al. “Development of an ultrasound sensitive oxygen carrier for oxygen delivery to hypoxic tissue”. In: *International Journal of Pharmaceutics* 478.1 (Jan. 2015), pp. 361–367. ISSN: 0378-5173. DOI: 10.1016/j.ijpharm.2014.11.023. URL: https://www.sciencedirect.com/science/article/pii/S0378517314008266 (visited on 05/05/2026).

[191] R. Sander. “Compilation of Henry’s law constants (version 4.0) for water as solvent”. English. In: *Atmospheric Chemistry and Physics* 15.8 (Apr. 2015), pp. 4399–4981. ISSN: 1680-7316. DOI: 10.5194/acp-15-4399-2015. URL: https://acp.copernicus.org/articles/15/4399/2015/acp-15-4399-2015.html (visited on 05/27/2026).

[192] Emmerich. Wilhelm, Rubin. Battino, and Robert J. Wilcock. “Low-pressure solubility of gases in liquid water”. en. In: *Chemical Reviews* 77.2 (Apr. 1977), pp. 219–262. ISSN: 0009-2665, 1520-6890. DOI: 10.1021/cr60306a003. URL: https://pubs.acs.org/doi/abs/10.1021/cr60306a003 (visited on 05/27/2026).

[193] *ISO 22412:2025*. en. URL: https://www.iso.org/standard/85505.html (visited on 05/29/2026).

[194] Qingyi Xu et al. “Biosurfactants for Microbubble Preparation and Application”. en. In: *International Journal of Molecular Sciences* 12.1 (Jan. 2011), pp. 462–475. ISSN: 1422-0067. DOI: 10.3390/ijms12010462. URL: https://www.mdpi.com/1422-0067/12/1/462 (visited on 06/01/2026).

[195] Hubert Chanson. “Summary : Air Bubble Diffusion in Shear Flows”. en. In: *Air Bubble Entrainment in Free-Surface Turbulent Shear Flows*. Elsevier, 1996, pp. 216–234. ISBN: 978-0-12-168110-4. DOI: 10.1016/B978-012168110-4/50022-9. URL: https://linkinghub.elsevier.com/retrieve/pii/B9780121681104500229 (visited on 05/26/2026).

[196] Shiyong Tan et al. “Dynamics of bubble collision and coalescence in three-dimensional turbulent flows”. en. In: *Journal of Fluid Mechanics* 1020 (Oct. 2025), A15. ISSN: 0022-1120, 1469-7645. DOI: 10.1017/jfm.2025.10603. URL: https://www.cambridge.org/core/journals/journal-of-fluid-mechanics/article/dynamics-of-bubble-collision-and-coalescence-in-threedimensional-turbulent-flows/970AF346260FE1B3F96B64BCBBD19734 (visited on 05/26/2026).

[197] Zhongqian Sun et al. “Bubble Manipulation Driven by Alternating Current Electrowetting: Oscillation Modes and Surface Detachment”. In: *Langmuir* 37.23 (June 2021), pp. 6898–6904. ISSN: 0743-7463. DOI: 10.1021/acs.langmuir.1c00096. URL: https://doi.org/10.1021/acs.langmuir.1c00096 (visited on 05/29/2026).

[198] Hongyi Zhang et al. “Characterization of stability and shell elasticity of monodisperse microbubbles with different pegylated-lipid content using pressure-dependent attenuation spectra”. In: *Acta Biomaterialia* 204 (Sept. 2025), pp. 596–609. ISSN: 1742-7061. DOI: 10.1016/j.actbio.2025.08.017. URL: https://www.sciencedirect.com/science/article/pii/S1742706125005999 (visited on 05/29/2026).

[199] Christopher M. Runyan et al. “Low-frequency ultrasound increases outer membrane permeability of Pseudomonas aeruginosa”. In: *The Journal of General and Applied Microbiology* 52.5 (2006), pp. 295–301. DOI: 10.2323/jgam.52.295.

[200] Jagannathan Sundaram, Berlyn R. Mellein, and Samir Mitragotri. “An Experimental and Theoretical Analysis of Ultrasound-Induced Permeabilization of Cell Membranes”. In: *Biophysical Journal* 84.5 (May 2003), pp. 3087–3101. ISSN: 0006-3495. DOI: 10.1016/S0006-3495(03)70034-4. URL: https://pmc.ncbi.nlm.nih.gov/articles/PMC1302870/ (visited on 05/29/2026).

[201] Qiao He et al. “Antibacterial mechanism of ultrasound against *Escherichia coli*: Alterations in membrane microstructures and properties”. In: *Ultrasonics Sonochemistry* 73 (May 2021), p. 105509. ISSN: 1350-4177. DOI: 10.1016/j.ultsonch.2021.105509. URL: https://www.sciencedirect.com/science/article/pii/S1350417721000511 (visited on 05/29/2026).

[202] Dawid Przystupski and Marek Ussowicz. “Landscape of Cellular Bioeffects Triggered by Ultrasound-Induced Sonoporation”. In: *International Journal of Molecular Sciences* 23.19 (Sept. 2022), p. 11222. ISSN: 1422-0067. DOI: 10.3390/ijms231911222. URL: https://pmc.ncbi.nlm.nih.gov/articles/PMC9569453/ (visited on 05/29/2026).

[203] Jing Li et al. “Animal models of oral infectious diseases”. English. In: *Frontiers in Oral Health* 6 (Apr. 2025). ISSN: 2673-4842. DOI: 10.3389/froh.2025.1571492. URL: https://www.frontiersin.org/journals/oral-health/articles/10.3389/froh.2025.1571492/full (visited on 06/01/2026).

[204] Qing Hong et al. “An in vitro and in vivo study of plasma treatment effects on oral biofilms”. In: *Journal of Oral Microbiology* 11.1 (Apr. 2019), p. 1603524. ISSN: 2000-2297. DOI: 10.1080/20002297.2019.1603524. URL: https://pmc.ncbi.nlm.nih.gov/articles/PMC6493255/ (visited on 06/01/2026).

[205] Hira Waqar et al. “Monodisperse magnetic lecithin-PFP submicron bubbles as dual imaging contrast agents for ultrasound (US) and MRI”. In: *RSC Advances* 12.17 (), pp. 10504–10513. ISSN: 2046-2069. DOI: 10.1039/d2ra01542k. URL: https://pmc.ncbi.nlm.nih.gov/articles/PMC8981111/ (visited on 06/01/2026).

Appendix to Chapter 2

Biofilm fluorescent microscopy image analysis script

```
"""
Davide De Grandi - davide.degrandi@eng.ox.ac.uk
November 2024

This script allows the user to upload microscopy fluorescence images (2 channels allowed in
↪  this version).
For each channel, the pictures get binarised using a moving average threshold algorithm
↪  (adaptive_threshold_mean())
Before the adaptive thresholding is computed, the image is cleaned from salt and pepper noise
↪  with a gaussian blur and the contrast is enhanced using CLAHE algorithm
Once the image is thresholded, the script evaluates the area of the disc coverd by biofilm
↪  (anything above threshold), and computes the mean fluorescence intensity for the area of
↪  the biofilm above the threshold.
Results are organised in a pandas df and saved in an excel file
"""

import cv2
import numpy as np
from aicsimageio import AICSImage
import os.path
import PIL
from datetime import date
import ctypes
import pandas as pd
from Plots_Biofilm import barplots_DavideBioflm, lineplots_DavideBioflm

PIL.Image.MAX_IMAGE_PIXELS = 999999999999999999999 #Needed to open big image, otherwise
↪  windows blocks the code because it seems like a decompression bomb DOS attack

"""functions"""
################################################################################
# This functions allow to click 3 points on an OpenCV image and save they're position in a
↪  np.array
def mousePoints(event, x, y, flags, params):
    global coord, counter
    if event == cv2.EVENT_LBUTTONDOWN:  # Left button click
        coord.append([x, y])
        counter += 1
        print(f"Point {counter}: ({x}, {y})")
    if counter >= 3:
        cv2.destroyAllWindows()

# Function to capture three points
def get_three_points(image):
    global coord, counter
    coord = []  # Reset coordinates
    counter = 0  # Reset counter
    # Display the image and set the mouse callback
    cv2.namedWindow('{}_{}'.format(t,j), cv2.WINDOW_NORMAL)
    cv2.resizeWindow('{}_{}'.format(t,j), round(width/16), round(height/16))
```

```
    cv2.imshow('{}_{}'.format(t,j), image)
    cv2.setMouseCallback('{}_{}'.format(t,j), mousePoints)
    # Wait until three points are clicked
    while counter < 3:
        cv2.waitKey(1)
    return np.array(coord)

# Adaptive threshold algorithm
def adaptive_threshold_mean(img, block_size, c_perc, min_perc_max):
    assert block_size % 2 == 1 and block_size > 1, "block_size must be an odd integer greater than 1"
    pad_size = block_size//2
    padded_img = np.pad(img, pad_size, mode='reflect')
    integral_img = padded_img.cumsum(axis=0).cumsum(axis=1)
    # Calculate the local sum for each pixel's neighborhood using the integral image
    total_sum = (integral_img[block_size:, block_size:]
                 - integral_img[:-block_size, block_size:]
                 - integral_img[block_size:, :-block_size]
                 + integral_img[:-block_size, :-block_size])
    # Compute the local count of pixels in each block
    block_area = block_size * block_size
    local_mean = total_sum / block_area
    local_mean = np.insert(local_mean,0, np.zeros(len(local_mean[0,:])), axis=0) # pad first column and row has they get lost in local_mean array
    local_mean = np.insert(local_mean,0, np.zeros(len(local_mean[:,0])), axis=1)
    # Apply the thresholding
    binary_img = (img >= (local_mean - (np.amax(img)*c_perc) )) * 255 # c_perc is an adjustment applied to the thresholding to fine tweak
    idx_zeropad = np.where(local_mean==0)
    binary_img[idx_zeropad]=0
    idx_manual_bg = np.where(img<np.amax(img)*min_perc_max)
    binary_img[idx_manual_bg]=0 # Manually set to zero all the pixels that are less than x% of the max intensity
    binary_img = binary_img.astype(np.uint8)
    return binary_img, local_mean

##########################################################################

datadir = r'D:\2022-2023-2024_UsefulData\BIOFILM-20240926-CFUvsFluorescence calibration -- PAPER'
dirs = [d for d in os.listdir(datadir) if os.path.isdir(os.path.join(datadir, d))] #get list of all directories in selected parent dir
today = str(date.today()) #just todays date used for naming files
pixel_size = 1.48e-6 #[m] from calibration of nikon 4x obj
# Area3dB = 22.28e-6 #[m^2] from US field calibration

PI_Int_mean = []; Syto9_Int_mean = []; Remov_area_Syto9 = []; Remov_area_PI = []; Bio_area_Syto9 = []; Bio_area_PI = []#empty lists for results

for t in dirs:
    coord = [];   counter=0 #needed for mousePoints fun

    path = datadir + '\\' + t
    onlyfiles = [f for f in os.listdir(path) if os.path.isfile(os.path.join(path, f))] #list of all the file in the selected directory
    img = AICSImage(path+'\\'+onlyfiles[0])  # selects the first file found (name appropriately, so that this is the tiled image)

    img_Syto9 = img.get_image_data("YX", T=0, Z=0, C=0, S=0) #Read first channel
    img_PI = img.get_image_data("YX", T=0, Z=0, C=0, S=1) #Read second channel

    height, width = img_Syto9.shape

    img_Syto9_8bit = cv2.normalize(img_Syto9, dst=None, alpha=0, beta=255, norm_type=cv2.NORM_MINMAX).astype(np.uint8) #Normalize to 8 bit so that OpenCV can show on screen
    img_PI_8bit = cv2.normalize(img_PI, dst=None, alpha=0, beta=255, norm_type=cv2.NORM_MINMAX).astype(np.uint8) #Normalize to 8 bit so that OpenCV can show on screen
    show_channels = np.concatenate((img_Syto9_8bit, img_PI_8bit), axis=1) # concatenate imgs to be shown
    cv2.namedWindow('Syto9_vs_PI_{}'.format(t), cv2.WINDOW_NORMAL)
```

```
    cv2.resizeWindow('Syto9_vs_PI_{}'.format(t), round(width/16)*2, round(height/16))
    cv2.imshow('Syto9_vs_PI_{}'.format(t), show_channels)
    cv2.waitKey(3000) #time in ms the img is shown (0) for infinite
    cv2.destroyAllWindows()

    imgs_list = [img_Syto9, img_PI] #list of channels, so that it's easy to loop through them
    for j in range(len(imgs_list)): #loop through the channels
        og_img = imgs_list[j] # 12bit
        og_img_8bit = cv2.normalize(og_img, dst=None, alpha=0, beta=255,
        ↪  norm_type=cv2.NORM_MINMAX).astype(np.uint8)
        clahe=cv2.createCLAHE(clipLimit=10) # contrast enhancement (the resulting image is in
        ↪  16bit intensity)
        img = clahe.apply(og_img)
        img = cv2.GaussianBlur(img, (31,31), 3) #small kernel blurring to remove a bit of
        ↪  noise
        img_8bit = cv2.normalize(img, dst=None, alpha=0, beta=255,
        ↪  norm_type=cv2.NORM_MINMAX).astype(np.uint8) #8bit img just to show

        if j==0:
            mask=np.zeros((height,width))
            ctypes.windll.user32.MessageBoxW(0, "Click 3 points on the circonference of the
            ↪  disc", "Instructions", 1)
            coord = get_three_points(img_8bit)
            (cx, cy), rad = cv2.minEnclosingCircle(coord) #Find minimun enclosing circle for
            ↪  3 points clicked on image using 3 points from previous function
            mask = cv2.circle(mask, (round(cx), round(cy)), round(rad), 1, -1) #Whitemask
            ↪  processing area

        img_adapt = np.multiply(img,mask)
        img_adapt, local_mean = adaptive_threshold_mean(img_adapt, 901, 0.15, 0.10)
        img_adapt = np.multiply(img_adapt,mask).astype(np.uint8)

        thrs_mask = np.where(img_adapt==255, 1, 0).astype(np.uint8) #mask of binarized img
        tot_area = np.sum(mask) # total area of disc
        thrs_area = np.sum(thrs_mask) #number of white pixels in white img
        Int_img = np.multiply(og_img,thrs_mask) #gray img masked with adapt mask
        Int_sum = np.sum(Int_img, dtype="float64") #sum of all pixel intensity adapt
        ↪  threshold
        Int_mean = Int_sum/thrs_area #mean of all pixel intensity above adapt threshold
        Area_of_removal = (tot_area-thrs_area)*pixel_size**2 #[m2]
        print(f"Area of removal is {Area_of_removal} [m^2]")
        Bio_area = (thrs_area)*pixel_size**2

        mask_8bit = mask.astype(np.uint8)
        mask_8bit[mask==1] = 255
        masked_img = np.multiply(img_8bit, thrs_mask)
        Image_check = np.concatenate((og_img_8bit, masked_img, mask_8bit, img_adapt), axis=1)
        cv2.namedWindow('Check images', cv2.WINDOW_NORMAL)
        cv2.resizeWindow('Check images', round(width/19)*4, round(height/19))
        cv2.imshow('Check images', Image_check)
        cv2.waitKey(3000)
        cv2.destroyAllWindows()

        if j==0:
            Syto9_Int_mean.append(Int_mean)
            Remov_area_Syto9.append(Area_of_removal)
            Bio_area_Syto9.append(Bio_area)

        elif j==1:
            PI_Int_mean.append(Int_mean)
            Remov_area_PI.append(Area_of_removal)
            Bio_area_PI.append(Bio_area)

PSratio_mean = np.array(PI_Int_mean)/np.array(Syto9_Int_mean) #ratio of mean intesities

data = np.array([Syto9_Int_mean, PI_Int_mean, PSratio_mean, Remov_area_Syto9,Bio_area_Syto9,
↪  Remov_area_PI, Bio_area_PI]).T #save data in np array
Sample_names = np.array([[i[:-2] for i in dirs],[i[-1] for i in dirs]]).T #save samplenames
↪  and repeat number in np array

Data_names = ["Syto9_Int_mean", "PI_Int_mean","PI-Syto9_ratio_mean", "Removal_Syto9[m2]",
↪  "Bio_area_Syto9", "Removal_PI[m2]", "Bio_area_PI"] #name for columns of pd df
```

```
df = pd.DataFrame(Sample_names[:,0], columns=["Sample"]) #df with only sample names
df2 = pd.DataFrame(data, columns=Data_names) #df with only numerical data
df = df.assign(**df2) # merging the two dfs

#########################################################################

Groups_means = df.groupby(["Sample"], sort=False).agg(["mean"]) #get df with means grouped by
↪  sample treatment
Groups_stds = df.groupby(["Sample"], sort=False).agg(["std"]) #get df with std grouped by
↪  sample treatment
df.to_excel(datadir+'\\data_{}.xlsx'.format(today)) #save df to excel file

filename = 'data_{}.xlsx'.format(today)

barplots_DavideBioflm(datadir, filename)
```

Listing 1: Python script for biofilm fluorescent image analysis

PCD computation script

```
%%%%%%%%%%%%%%%%%%%%%%%%%%%%%%%%%%%%%%%%%%%%%%%%%%%%%%%%%%%%%%%%%%%%%%%%%%%%%%%%%%%%%%%%
%
% davide.degrandi@eng.ox.ac.uk - 2023-10-10
%
%%%%%%%%%%%%%%%%%%%%%%%%%%%%%%%%%%%%%%%%%%%%%%%%%%%%%%%%%%%%%%%%%%%%%%%%%%%%%%%%%%%%%%%%

close all;
clear;

%% Input parameters
% Directories and load a temporary file
dataset_dir = 'D:\011-Data\2022-2023-2024_UsefulData\BIOFILM-20240718-US only and US+bbls --
↪  PAPER\DatausedforPCDimagesinpaper'; % Superdirectory of data directories
datadirs = Extract_dirlist(dataset_dir); % Get data folders
temp = dir([datadirs(1).folder, '\', datadirs(1).name]); % Get a random file to extract fs
tempdata = load([datadirs(1).folder, '\', datadirs(1).name, '\', temp(3).name]); % Load first
↪  data file
fs = double(tempdata.tpd.SampleFrequency); %[Hz] Sampling frequency (usually 50 MHz)
SamplingTime = 1/fs; %[s]

% Receiver amplification
PCDgain = 125; %[Multiplication, NOT dB]
% US Parameters
f0 = 0.5e6; %[Hz]
cycles = 1000; %number of cycles per burst
cwater = 1500; %[m/s] speed of sound in propagation media
HPFil = 2.0; % [MHz] HighPass filter (MHz) [USE ONLY HARMONICS VALUES HERE!!!!]
PRF = 5; % [Hz] Pulse repetition frequency of burst
PRT = 1/PRF; %[sec] Pulse repetition time of burst
Transducer = "H107-26"; % Name of transducer and focal distance
focal1 = 63.2e-3; % [m] focal distance of transducer
Receiver = "olympus 7.5MHz"; % Name of receiver
focal2 = 62e-3; % [m] % Focal distance of receiver (if unfocused, distance from focal spot)

%% Set Welch parameters
fmin = HPFil*1e6; % Analysis lower bound
fmax = min([12e6 0.9*(fs / 2)]); % Nyquist or lower as upper bound
f_harm =  fmin:f0:fmax; % List of harmonics
f_ultra = (fmin+0.5*f0):f0:fmax; % List of ultraharmonics
bin = 10e3; % Spectrum resolution (Hz)
Wel_win = round(fs/bin); % Samples needed for desired binsize
pwr_of2 = 2.^(1:1:35); % List of power of 2 up to 2^35
```

```
tempidx = pwr_of2-Wel_win>0;
Nfft = min(pwr_of2(tempidx)); % Define number of DFT points for PSD estimate. Default is 256
↪  or next power of 2 greater than segments length
Novr = 0.5*Wel_win; % Sample overlap Welch method
nbin = [21 17]; % [Harm, Ultra] Allow for finite tonalbandwidth, and since harmonics tend to
↪  be larger than ultraharmonics

%% set time domain signal windowing
toftw = (focal1+focal2)/cwater; %[s]
% win(1) = data.tpd.PreSampleCount+round((toftw/SamplingTime)); win(2) =
↪  win(1)+((cycles*(1/f0))/SamplingTime); %cut prefocal signal
win(1) = 1; win(2) = length(tempdata.tpd.Data); %keep all time domain signal
window = win(1):win(2);

%% Perform PSD estimate
%%%%%%%%%%%%%%%%%%%%%%%%%%%%%%%%%%%%%%%%%%%%%%%%%%%%%%%%%%%%%%%%%%%%%%%%%%%
[Tot_En, P] =
↪  SingleReceiver_PSDWelch(datadirs,window,fmin,fmax,f_harm,f_ultra,fs,Wel_win,Nfft,Novr,
↪  bin, nbin,PCDgain,HPFil);
%%%%%%%%%%%%%%%%%%%%%%%%%%%%%%%%%%%%%%%%%%%%%%%%%%%%%%%%%%%%%%%%%%%%%%%%%%%

%% Save resume figures/datatables
Tot_En_dB.total = db(Tot_En.total, "power"); %[dB re J]
Tot_En_dB.harm = db(Tot_En.harm, "power"); Tot_En_dB.harm(isinf(Tot_En_dB.harm)) = NaN;
Tot_En_dB.ultra = db(Tot_En.ultra, "power"); Tot_En_dB.ultra(isinf(Tot_En_dB.ultra)) = NaN;
Tot_En_dB.broad = db(Tot_En.broad, "power");

for i = 1:length(datadirs)
    labels{i} = datadirs(i).name; % Sample name, for plot labelling
end

figure(3)
nexttile()
hold on
scatter(1:length(datadirs),Tot_En_dB.total, 'r',"filled" )
scatter(1:length(datadirs),Tot_En_dB.broad, "b", "filled")
xticks(1:length(datadirs))
xticklabels(labels)
ylabel("Total Energy (dB re J)")
legend({"Total", "Broad"}, 'Location', 'northwest')
hold off
nexttile()
hold on
scatter(1:length(datadirs),Tot_En_dB.harm, "y", "filled")
scatter(1:length(datadirs),Tot_En_dB.ultra, "k", "filled")
xticks(1:length(datadirs))
xticklabels(labels)
ylabel("Total Energy (dB re J)")
legend({"Harm","Ultra"}, 'Location', 'northwest')
hold off

savefig(figure(3), strcat(datadirs(1).folder, '\', "Total_Energy.fig"))
save(strcat(datadirs(1).folder, '\', "PCD_Data.mat"))

FieldName = fieldnames(Tot_En_dB);
Value = cellfun( @(f) Tot_En_dB.(f),FieldName,'UniformOutput',false);
T = table( FieldName, Value );
writetable(T, "C:\Users\sedm7132\Desktop\ToTEnData.xlsx")
```

Listing 2: Main file for PCD computation

```
function [Tot_En, P] = SingleReceiver_PSDWelch(datadirs,window, fmin,fmax,f_harm,f_ultra,fs,
↪  Wel_win,Nfft,Novr, bin, nbin, PCDgain,HPFil)

%Get info on data directories
dataset_length = length(datadirs);
Data_folder = extractfield(datadirs, 'name');
Parent_folder = datadirs.folder;
```

```
for t = 1:dataset_length

    [file_list, n_files,Data_path] = List_matfiles(datadirs(t));

    % Run first spectrum to confirm data size
    data = load([Data_path,file_list(1).name]);
    remove_trend = detrend(double(data.tpd.Data(window)));
    [~,F] = pwelch(remove_trend/PCDgain,Wel_win,Novr,Nfft, fs);

    % % Preallocate for indices
    len_fh = min([length(f_harm) length(f_ultra)]); %to make harm and ultra of the same
    ↪  length
    bw{1} = -(nbin(1)-1)/2:(nbin(1)-1)/2;
    bw{2} = -(nbin(2)-1)/2:(nbin(2)-1)/2;
    index_f_harm = zeros(len_fh,nbin(1));
    index_f_ultra = zeros(len_fh,nbin(2));
    for i = 1:len_fh
        % Get index of harmonic tone
        [~, ind] = min(abs(F - f_harm(i)));
        % Store indices of the binned area around the harmonic
        index_f_harm(i,:) = ind + bw{1};
        % Get index of ultraharmonic tone
        [~, ind] = min(abs(F - f_ultra(i)));
        % Store indices of the binned area around the ultraharmonic
        index_f_ultra(i,:) = ind + bw{2};
    end

    f_MHz = F*1e-6;

    %% 2. LOOP over files
    time = zeros(n_files,1);

    wb = waitbar(0,'file loop');
    for i = 1:n_files
        % Load file
        data = load([Data_path,file_list(i).name]);
        %Get date/time
        tmp = datevec(data.tpd.DateTime);
        time(i) = tmp(4)*60^2 + tmp(5)*60 + tmp(6); %hour, min, sec
        % Power spectral density
        [P.total(:,i),~] =
        ↪  pwelch(detrend(double(data.tpd.Data(window)))/PCDgain,Wel_win,Novr,Nfft,fs);
        %Local std or local mean based bb_filter
        [harm_idx, ultra_idx] = bb_filt_PCD(P.total(:,i), index_f_ultra, index_f_harm);
        % Collect harmonics and ultraharmonics
        P.harm{:,i} = P.total(harm_idx,i);
        P.ultra{:,i} = P.total(ultra_idx,i);
        waitbar(i/n_files,wb)
    end
    close(wb)

    %% 3. Finish Processing

    % Sort by file acquisition time in case file names are ambiguous
    [file_times,ind] = sort(time);
    % Give time relative to the first aquisition
    file_times = file_times - file_times(1);
    % If you don't want to show the entire recording, you can choose where to start
    file_times_window = (file_times>3 & file_times<64); % time in seconds (total recording
    ↪  time, not time in a single signal)

    %     Find the indices of these times
    start_ind = find(file_times_window,1,'first');
    last_ind = find(file_times_window,1,'last');
    win_ind = start_ind:last_ind;
    file_times = file_times(win_ind); %Only contains elements between 10s and 120s
    file_times = file_times - file_times(1);

    % Signal power by type, units are Watts

    ze = 50; % (divide PSD by 50 Ohms for true electrical power from receiver)
```

```
ub = min([index_f_harm(1) index_f_ultra(1)]):max([index_f_harm(end) index_f_ultra(end)]);
↪  % freq range for power calcs, spanning Ph, Pu

[P.harm{1, 1:start_ind}] = deal([]);  %remove all values outside desired time window
[P.ultra{1, 1:start_ind}] = deal([]); %much easier to do it here, than to deal with
[P.harm{1, last_ind:end}] = deal([]); %summing only some of the cell arrays later

%%% Sum total power in the selected window (needed for total energy estimate)
SumP.total(win_ind,t) = sum(P.total(ub,win_ind),1)*bin/ze; % [W] total
for l=win_ind
    SumP.harm(l,t) = sum(P.harm{1,l})*bin/ze;  % [W] harmonic
    SumP.ultra(l,t) = sum(P.ultra{1,l})*bin/ze; % [W] ultraharmonic
end
SumP.broad(win_ind,t) = SumP.total(win_ind,t) - (SumP.harm(win_ind,t) +
↪  SumP.ultra(win_ind,t));   % [W] broadband

%%% Max power in each file, not sure if this is helpful, still checking if I see any
↪  trend in my results
MaxP.total(win_ind,t) = max(P.total(ub,win_ind),[],1)*bin/ze; % [W] total
tmpidx_harm = find(~cellfun(@isempty,P.harm)); %find index of all non empty cells in
↪  cells array

MaxP.harm = zeros(win_ind(end),dataset_length);
for l=tmpidx_harm
    MaxP.harm(l,t) = max(P.harm{1,l},[],1)*bin/ze;  % [W] harmonic
end

MaxP.ultra = zeros(win_ind(end),dataset_length);
tmpidx_ultra = find(~cellfun(@isempty,P.ultra)); %find index of all non empty cells in
↪  cells array
for l=tmpidx_ultra
    MaxP.ultra(l,t) = max(P.ultra{1,l},[],1)*bin/ze; % [W] ultraharmonic
end

%%% Total energy
t_window = length(data.tpd.Data)/fs; %[s] duration of each pulse
Energy.total = SumP.total(:,t)*t_window; % [J] Electrical energy
Tot_En.total(t) = nansum(Energy.total); % [J] Sum of electrical energy
Energy.harm = SumP.harm(:,t)*t_window;
Tot_En.harm(t) = nansum(Energy.harm);
Energy.ultra = SumP.ultra(:,t)*t_window;
Tot_En.ultra(t) = nansum(Energy.ultra);
Energy.broad = SumP.broad(:,t)*t_window;
Tot_En.broad(t) = nansum(Energy.broad);

% %%% extimate of cavitation time for each file
% %%% to be added

%% 4. DISPLAY
fig_folder = [Parent_folder '\']; %For figure save location
name = Data_folder(t); %For figure naming

Z= db(P.total./ze,'power'); % [dB re W(maybe??)]

figure(1), set(gcf,'name','PCD response', 'Position',[0 0 1900 1000])
ax=gca;
pcolor(file_times,f_MHz, Z(:,win_ind)), shading flat, colormap turbo
hold on;
plot(file_times([1 end]),HPFil,'--w', file_times([1 end]),fmax*[1 1]*1e-6,'--w')
xlabel(["Time (s)"]), ylabel(["Frequency (MHz)"])
ax.XAxis.FontSize=35;
ax.XAxis.FontWeight='bold';
ax.YAxis.FontSize=35;
ax.YAxis.FontWeight='bold';
title([name ' PSD'], 'FontSize',50, 'FontWeight','bold'), xlim([0 diff(file_times([1
↪  end]))])
hb=colorbar('vert'); hb.Label.String=strcat("PSD (dB re [V^2/R per", "
↪  ",string(bin*1e-3), " kHz])");
hb.Label.FontSize=35; hb.Label.FontWeight='bold'; hb.FontSize=35; hb.FontWeight='bold';
caxis([-175 -158])
ylim([ fmin*1e-6 fmax*1e-6 ]);
```

```
    %Figure 1
    % figure(1), set(gcf,'name','PCD response', 'Position', [0 0 980 980])
    % subplot(3,1,1),
    % pcolor(file_times,f_MHz, Z(:,win_ind)), shading flat, colormap jet
    % xlabel('Time (s)'), ylabel('Frequency (MHz)')
    % title([name ' PSD']), xlim([0 diff(file_times([1 end]))])
    % hb=colorbar('vert','FontSize',10); hb.Label.String=strcat('PSD (dB re [V^2/R per', '
    ↪  ',string(bin*1e-3),' kHz])');
    % caxis([-180 -155])
    % ylim([ fmin*1e-6 fmax*1e-6 ]);
    % hold on;
    % plot(file_times([1 end]),HPFil,'--w', file_times([1 end]),fmax*[1 1]*1e-6,'--w')
    %
    % subplot(3,1,2),
    % hold on
    % scatter(file_times, db(SumP.harm(win_ind,t),'power'),6)
    % scatter(file_times, db(SumP.ultra(win_ind,t),'power'),6)
    % plot(file_times, db(SumP.broad(win_ind,t),'power'))
    % plot(file_times, db(SumP.total(win_ind,t),'power'))
    % hold off
    % xlabel('Time (s)'), ylabel('Power (dB re W)')
    % legend({'Harmonic','Ultraharmonic','Broadband', 'Total'},'location','southeast')
    % title(['Power Sum, ',num2str(F(ub(1))*1e-6,'%1.2f'),' -
    ↪  ',num2str(F(ub(end))*1e-6,'%1.2f'),' MHz'])
    % xlim([0 diff(file_times([1 end]))])
    %
    % subplot(3,1,3),
    % hold on
    % scatter(file_times, db(MaxP.harm(win_ind,t),'power'),6)
    % scatter(file_times, db(MaxP.ultra(win_ind,t),'power'),6)
    % plot(file_times, db(MaxP.total(win_ind,t),'power'))
    % hold off
    % xlabel('Time (s)'), ylabel('Power (dB re W)')
    % legend({'Harmonic','Ultraharmonic', 'Total'},'location','southeast')
    % title(['Max power, ',num2str(F(ub(1))*1e-6,'%1.2f'),' -
    ↪  ',num2str(F(ub(end))*1e-6,'%1.2f'),' MHz'])
    % xlim([0 diff(file_times([1 end]))])

    % %%% extract one time domain and one freq domain signal as sanity check
    %
    % data = load([Data_path,file_list(round(length(file_list)/2,0)).name]);
    % remove_trend = detrend(double(data.tpd.Data(window)));
    % [pwr_check,F_check] = pwelch(remove_trend/PCDgain,Wel_win,Novr,Nfft, fs);

    % figure(2), set(gcf,'name','PCD response', 'Position', [0 0 980 980])
    % subplot(3,1,1),
    % plot(((1:length(remove_trend))*(1/data.tpd.SampleFrequency)),remove_trend)
    % xlabel('Time (s)'), ylabel('Volt (V)')
    % title([name 'time domain signal'])
    %
    % subplot(3,1,2),
    % plot(F_check*1e-6,pwr_check)
    % xlabel('Freq (MHz)'), ylabel('V^2')
    % title([name "Frequency domain signal"])
    %
    % subplot(3,1,3),
    % plot(F_check*1e-6,db(pwr_check, "Power"))
    % xlabel('Freq (MHz)'), ylabel('dB re V^2')
    % title([name "Frequency domain signal"])

    print(figure(1), '-dtiff', strcat(fig_folder, name,"_PSD.tiff"), '-r300');
    savefig(figure(1), strcat(fig_folder, name,"_PSD.fig"));
    % print(figure(2), '-dtiff', strcat(fig_folder, name,"_SignalCheck.tiff"), '-r300');
    % savefig(figure(2), strcat(fig_folder, name,"_SignalCheck.fig"));
    % uiwait(figure(1),3) %% for debugging
    % uiwait() %%for debugging
    close all
end
end
```

Listing 3: PSD and energy computation

```
%% bb_filter for PCD (adapted from Sara's code for PAM)

function [index_f_harm, index_f_ultra] = bb_filt_PCD(x, index_f_ultra, index_f_harm, bin)

SignLng = length(x); %Datalength
dBPower = db(x, 'power');
bandw = 350e3/bin;
remove_harm = [];
remove_ultra = [];

% %% dBversion
% %Evaluate if there's any significant HARMONIC peak
% for i=1:length(index_f_harm(:,1))
%     tmpIDX = index_f_harm(i,:);
%     meantrace = mean(dBPower(tmpIDX)); % evaluate mean value of signal in each "harmonic
↪  window"
%     if max(dBPower(tmpIDX))<(3+meantrace) % if signal is NOT great than mean+6dB, than is
↪  not a real harmonic
%         remove_harm(end+1) = i;
%     end
% end
% %Evaluate if there's any significant ULTRAharmonic peak
% for i=1:length(index_f_ultra(:,1))
%     tmpIDX = index_f_ultra(i,:);
%     meantrace = mean(dBPower(tmpIDX)); % evaluate mean value of signal in each "harmonic
↪  window"
%     if max(dBPower(tmpIDX))<(3+meantrace) % if signal is NOT great than mean+6dB, than is
↪  not a real ultrah
%         remove_ultra(end+1) = i;
%     end
% end

%% non-dB version
%Evaluate if there's any significant HARMONIC peak
for i=1:length(index_f_harm(:,1))
    tmpIDX = index_f_harm(i,:);
    harm_len=length(tmpIDX);
    tmpbwIDX = [index_f_harm(i,1)-floor((bandw-harm_len)/2):index_f_harm(i,1)-1,
        index_f_harm(i,end)+1:index_f_harm(i,end)+floor((bandw-harm_len)/2)];
    meanharm = mean(x(tmpIDX)); % evaluate mean value of signal in each "harmonic window"
    mean_around = mean(x(tmpbwIDX));
    if meanharm<(mean_around*2.5) % if signal is NOT great than mean*5, than is not a real
    ↪  harmonic
        remove_harm(end+1) = i;
    end
end
%Evaluate if there's any significant ULTRAharmonic peak
for i=1:length(index_f_ultra(:,1))
    tmpIDX = index_f_ultra(i,:);
    ultra_len=length(tmpIDX);
    tmpbwIDX = [index_f_ultra(i,1)-floor((bandw-ultra_len)/2):index_f_ultra(i,1)-1,
        index_f_ultra(i,end)+1:index_f_ultra(i,end)+floor((bandw-ultra_len)/2)];
    meanultra = mean(x(tmpIDX)); % evaluate mean value of signal in each "harmonic window"
    mean_around = mean(x(tmpbwIDX));
    if meanultra<(mean_around*2.5) % if signal is NOT great than mean*5, than is not a real
    ↪  harmonic
        remove_ultra(end+1) = i;
    end
end
    index_f_harm(remove_harm,:) = [];%harmonics to be kept
    index_f_ultra(remove_ultra,:) = []; %ultraharmonics to be kept
    index_f_harm = sort(reshape(index_f_harm,[],1)); %reshape in vector form
    index_f_harm = sort(reshape(index_f_harm,[],1)); %reshape in vector form

end
```

Listing 4: Filtering function to evaluate broadband component

GLM for data analysis

```
library(readxl)
library(dplyr)
library(tidyr)
library(ggplot2)
library(mgcv)
library(scam)
library(gratia)
library(nlme)
library(stringr)

# Custom theme for plots
theme_paper_pub = function(font_size = 7) {
  theme_minimal() +
    theme(
      panel.grid.major = element_blank(),
      panel.grid.minor = element_blank(),
      axis.ticks = element_line(size = 0.2),
      axis.line.x = element_line(colour = 'black', size = 0.25, linetype = 'solid'),
      axis.line.y = element_line(colour = 'black', size = 0.25, linetype = 'solid'),
      axis.title.y = element_text(size = font_size),
      axis.title.x = element_text(size = font_size),
      strip.text = element_text(size = font_size),
      axis.text.x = element_text(size = font_size),
      axis.text.y = element_text(size = font_size),
      legend.position = "right",
      legend.text = element_text(size = font_size),
      legend.title = element_text(size = font_size)
    )
}

# Function to get prediction dataframe
get_pred_df = function(fit, data = NULL, method = 'posterior', level = .834, finer_grid = F)
↪  {
  # Check if 'gls' is one of the classes of 'fit'
  if ("gls" %in% class(fit)) {
    df = as.data.frame(cbind(exp(coef(fit)), exp(confint(fit)))) %>%
      `rownames<-`(NULL) %>%
      `colnames<-`(c('PIsyto9ratio', 'lwr', 'upr')) %>%
      mutate(Pressure = unique(data$Pressure), CHX = data$CHX[1])
    return(df)
  }

  if (method == 'posterior') {
    gratia::fitted_samples(fit, n = 10000, method = 'mh', unconditional = F, seed = 2, thin =
    ↪  2) |>
      group_by(.row) |>
      ggdist::median_qi(.width = level, .exclude = c(".draw", ".parameter", ".row")) |>
      left_join(mutate(data, .row = 1:n()), by = join_by(.row == .row)) %>%
      dplyr::select(-PIsyto9ratio) %>%
      rename(PIsyto9ratio = .fitted, lwr = .lower, upr = .upper)
  } else if (method == 'se') {
    if (fit$family$family == 'gammals') {
      linkinv = exp
    } else {
      linkinv = identity
    }
    crit = qt((1 - level) / 2, nrow(data) - 1, lower.tail = F)
    if (finer_grid) {
      # Create a full grid of Pressure and CHX values
      pred_data = expand.grid(
        Pressure = seq(min(data$Pressure), max(data$Pressure), by = 0.05),
        CHX = unique(data$CHX)
      )
    } else {
      pred_data = data.frame(Pressure = unique(data$Pressure), CHX = unique(data$CHX))
    }
```

```
    pred = predict(fit, type = 'link', se.fit = T, newdata = pred_data)

    # Handle cases where pred$fit is a vector
    if (is.null(dim(pred$fit))) {
      pred_data$PIsyto9ratio = linkinv(pred$fit)
    } else {
      pred_data$PIsyto9ratio = linkinv(pred$fit[, 1])
    }

    pred_data$lwr = linkinv(pred$fit - crit * pred$se.fit)
    pred_data$upr = linkinv(pred$fit + crit * pred$se.fit)
    pred_data
  } else {
    fit %>%
      gratia::smooth_estimates() %>%
      gratia::add_confint() %>%
      rename(PIsyto9ratio = .estimate, lwr = .lower_ci, upr = .upper_ci)
  }
}

# Load and preprocess data
biofilm = readxl::read_excel('C:/Users/degra/OneDrive -
↪  Nexus365/00001-Writing/PAPER_BiofilmTreatment/Biofilm US Data/new processed
↪  data/Paper_plotsanddata/CHX&USubbls.xlsx') %>%
  dplyr::select(c(1, 2)) %>%
  rename(PIsyto9ratio = 'PI-syto9 ratio') %>%
  mutate(
    CHX = case_when(
      !endsWith(Sample, 'CHX') ~ 0,  # Set CHX to 0 if Sample does not end with 'CHX'
      TRUE ~ as.numeric(gsub('.*(\\d+\\.\\d+)% CHX', '\\1', Sample))  # Extract numeric value
      ↪  before '% CHX'
    ),
    Pressure = case_when(
      T ~ as.numeric(gsub('.*(\\d+\\.\\d+)MPa.*', '\\1', Sample)),  # Extract pressure value
      TRUE ~ 0  # Set Pressure to 0 for samples without a pressure value
    )
  ) %>%
  dplyr::select(-Sample)

# Filter out controls (no CHX) if needed
bf = biofilm %>%
  dplyr::mutate(
    Pressure = ifelse(is.na(Pressure), 0, Pressure),
    Pressure = factor(Pressure),
    # CHX = factor(CHX)
  )

# Fit separate GLM models for each Pressure group
fit_list = lapply(unique(bf$Pressure), function(pressure) {
  glm(PIsyto9ratio ~ CHX, data = bf %>% filter(Pressure == pressure), family = gaussian(link
  ↪  = "log"))
})

# Generate predictions for each Pressure group
biofilm_pred_list = lapply(seq_along(fit_list), function(i) {
  pressure = unique(bf$Pressure)[i]
  # Create a finer grid of CHX values for predictions
  pred_data = data.frame(
    CHX = seq(min(bf$CHX), max(bf$CHX), length.out = 100),
    Pressure = pressure
  )
  pred = predict(fit_list[[i]], newdata = pred_data, type = "response", se.fit = TRUE)
  pred_data$PIsyto9ratio = pred$fit
  pred_data$lwr = pred$fit - 1.96 * pred$se.fit
  pred_data$upr = pred$fit + 1.96 * pred$se.fit
  pred_data
})

# Combine predictions into a single dataframe
biofilm_pred = bind_rows(biofilm_pred_list)

# Plotting
```

```
font_size = 18

ggplot(bf, aes(x = CHX, y = PIsyto9ratio, group = Pressure, color = Pressure, fill =
↪  Pressure)) +
  geom_point(shape = 21, size = 5, alpha = .6) +
  geom_ribbon(data = biofilm_pred, aes(ymin = lwr, ymax = upr), alpha = .3, color =
  ↪  'transparent') +
  geom_line(data = biofilm_pred, aes(y = PIsyto9ratio), size = 2, alpha = .9) +
  xlab('CHX Concentration') +
  ylab('PI-syto9 Ratio') +
  scale_y_continuous() +
  scale_x_continuous(breaks = unique(bf$CHX)) +  # Ensure CHX values are displayed correctly
  coord_cartesian(ylim = c(0, 9))+#max(bf$PIsyto9ratio))) +
  geom_hline(yintercept = 0, linetype = 'dashed') +
  theme_paper_pub(font_size) +
  theme(legend.position = 'right')

# Save the plot
ggsave('C:/Users/degra/OneDrive - Nexus365/00001-Writing/PAPER_BiofilmTreatment/Biofilm US
↪  Data/new processed data/Paper_plotsanddata/GLM_plot_pisytoratio_CHX.pdf', width = 6,
↪  height = 6)
```

Listing 5: R script for GLM computation and data analysis

Appendix to Chapter 4

Microbubbles sizing, count, and concentration image analysis script

```
"""microbubbles dimensions and counter"""
""" Instructions:
    1- create a datadir folder
    2- create one folder for each experimental condition (this folders names are gonna be
    ↪  used as column names in the output df)
    3- place pictures in ach corresponding folder"""
import cv2
import numpy as np
from aicsimageio import AICSImage
import os.path
from datetime import date
import random
import plotly.graph_objects as go
import plotly.io as pio
import plotly.colors as pc
pio.renderers.default = "browser"

def filter_desired_chilren(cntrs,hierarchy):
    cntrs = list(cntrs)
    i = 0
    while i < len(cntrs):
        parent_idx = hierarchy[i][3]  # Get the index of the parent contour
        if parent_idx != -1:
            parent_cntr = cntrs[parent_idx]
            sibling_contour = cntrs[i]
            sphericity = cntr_sphericity(sibling_contour)
            if sphericity<0.8 and len(sibling_contour)>30: # Undesired children cntrs points
            ↪  get stacked at the end of the parent and then deleted
                parent_cntr = np.vstack((parent_cntr, sibling_contour))
                cntrs[parent_idx] = parent_cntr
                del cntrs[i]
                hierarchy = np.delete(hierarchy, i, axis=0)  # Update hierarchy
                hierarchy[:, 0:3][hierarchy[:, 0:3] > i] -= 1  # Adjust next, previous, and
                ↪  first child indices
                hierarchy[:, 3][hierarchy[:, 3] > i] -= 1  # Adjust parent indices
                i -= 1 # Decrement i to account for the removed contour
        i += 1  # Move to the next contour
    cntrs = tuple(cntrs)
    return cntrs,hierarchy

def random_color():
    return (random.randint(40, 255), random.randint(40, 255), random.randint(40, 255))

def contour_centroid(cntr):
    xc = round(sum(cntr[:,0,0])/len(cntr[:,0,0]))
```

```
    yc = round(sum(cntr[:,0,1])/len(cntr[:,0,1]))
    return(xc,yc)

def cntr_sphericity(cntr):
    xc,yc = contour_centroid(cntr)
    cntr_zerocentered =[cntr[:,0,0]-xc, cntr[:,0,1]-yc]
    d_list = []
    for x,y in zip(cntr_zerocentered[0],cntr_zerocentered[1]):
        d_list.append( (x**2+y**2) )
    sph_index = 1 - (abs(d_list-np.mean(d_list)))/np.mean(d_list) # 1 is perfect circle
    sph_index = np.mean(sph_index)
    return sph_index

def min_distance_and_points(child_cntr, parent_cntr):
    child_point = contour_centroid(child_cntr)
    distances=np.array(float('inf'))
    points = [(float('inf'),float('inf'))]
    for parent_point in parent_cntr:
        parent_point = tuple(parent_point[0])  # Convert to tuple (x, y)
        distances = np.append(distances, np.linalg.norm(np.array(child_point) -
        ↪  np.array(parent_point)) )
        points.append((child_point,parent_point))
    min_idx = np.argmin(distances)
    min_distance = distances[min_idx]
    min_child_point = points[min_idx][0]
    min_parent_point = points[min_idx][1]

    distances = np.sort(distances)
    ratios = distances[0:round(min_distance*1.2)]/min_distance
    if any(ratios>2):
        min_distance = float('inf') # Check if the first few minimum distances are similar to
        ↪  the minimum distance. If they are very different, discard this radius because
        ↪  it's probably a false positive
    return min_distance, min_child_point, min_parent_point

def process_contour_family(img, cntrs, hierarchy, cntr_idx, color, radii, pixel_len):
    # cv2.drawContours(img, cntrs, cntr_idx, color, 6) # Uncomment to draw every contour
    first_child_idx = hierarchy[cntr_idx][2]
    parent_idx = hierarchy[cntr_idx][3]
    if first_child_idx == -1 and parent_idx == -1: #no siblings and no parent -> compute
    ↪  diameter as max x or y span
        x_d = max(cntrs[cntr_idx][:,0,0])-min(cntrs[cntr_idx][:,0,0])
        y_d = max(cntrs[cntr_idx][:,0,1])-min(cntrs[cntr_idx][:,0,1])
        diam = max(x_d,y_d)
        if diam==x_d:
            high_point_idx = np.argmax(cntrs[cntr_idx][:,0,0])
            low_point_idx = np.argmin(cntrs[cntr_idx][:,0,0])
            x_h = cntrs[cntr_idx][high_point_idx,0,0]; y_h =
            ↪  cntrs[cntr_idx][high_point_idx,0,1]
            x_l = cntrs[cntr_idx][low_point_idx,0,0]; y_l =
            ↪  cntrs[cntr_idx][low_point_idx,0,1]
            cv2.line(img,(x_h,y_h),(x_l,y_l),(0,0,255),4)
        else:
            high_point_idx = np.argmax(cntrs[cntr_idx][:,0,1])
            low_point_idx = np.argmin(cntrs[cntr_idx][:,0,1])
            x_h = cntrs[cntr_idx][high_point_idx,0,0]; y_h =
            ↪  cntrs[cntr_idx][high_point_idx,0,1]
            x_l = cntrs[cntr_idx][low_point_idx,0,0]; y_l =
            ↪  cntrs[cntr_idx][low_point_idx,0,1]
            cv2.line(img,(x_h,y_h),(x_l,y_l),(0,0,255),4)

        radii.append(diam*pixel_len/2)

    child_idx = first_child_idx
    while child_idx !=-1 and child_idx <= len(hierarchy)-1: # Process all siblings || there
    ↪  is a edge case when if the last contour in the contour lists gets removed then the
    ↪  code throws a indexing error, that's why I added the second condition to the while
    ↪  loop
        if len(cntrs[child_idx])<500:
```

```
            cv2.drawContours(img, cntrs, child_idx, color, 6) # Draw only siblings with low
            ↪  count (added this condition because sometimes big parent contours are
            ↪  considered siblings because of the jumping connection added in
            ↪  filter_desired_children. It doesn't impact computation but it looks bad when
            ↪  showed on the image)
        parent_idx = hierarchy[child_idx][3]
        if parent_idx != -1:
            if len(cntrs[parent_idx])<4000:
                min_distance, min_child_point, min_parent_point =
                ↪  min_distance_and_points(cntrs[child_idx], cntrs[parent_idx])
            else:
                downsampled_parent = cntrs[parent_idx][::3] # downsample to speed up
                ↪  computing on long cntrs
                min_distance, min_child_point, min_parent_point =
                ↪  min_distance_and_points(cntrs[child_idx], downsampled_parent)
        else:
            min_distance = float('inf')

        if min_distance != float('inf'):
            cv2.line(img, min_child_point, min_parent_point, (255, 0, 0), 4)
            radii.append(min_distance*pixel_len)
        # Recursively process child's family
        process_contour_family(img, cntrs, hierarchy, child_idx,color,radii, pixel_len)
        child_idx = hierarchy[child_idx][0] # Move to the next sibling
    return radii

def size_and_conc_histogram(df_size,df_conc,datadir):
    palette = pc.qualitative.Dark24
    dirs = [d for d in os.listdir(datadir) if os.path.isdir(os.path.join(datadir, d))]
    fig = go.Figure()
    num_bins = 20
    for i in range(len(df_size[0])):
        counts, bin_edges = np.histogram(df_size[0,i], bins=num_bins)
        bin_centers = (bin_edges[:-1] + bin_edges[1:]) / 2

        fig.add_trace(go.Scatter(
            x=bin_centers,
            y=counts,
            mode='lines',
            name=dirs[i],
            line=dict(shape='hv', color=palette[i])
        ))
        # this second trace is a dummy used to add the concentration of bubbles for each
        ↪  histogram
        fig.add_trace(go.Scatter(
        x=[None],
        y=[None],
        mode='markers',
        marker=dict(size=0, color= palette[i]),
        name=f'concentration: {df_conc[0,i][1]:e} bubbles/ml'
        ))
    fig.update_layout(
        title='Bubbles diameter distribution',
        title_font=dict(
            family="Arial Black",
            size=18,
            color="Black"
                        ),
        legend_font=dict(
            family="Arial Black",
            size=15,
            color="Black"
                        )
    )
    fig.update_xaxes(
        title='um',
        title_font=dict(
            family="Arial Black",
            size=20,
            color="Black"
                    ),
        tickfont=dict(
```

```
            family="Arial Black",
            size=20,
            color="Black"
                )
    )
    fig.update_yaxes(
        title="Count",
        title_font=dict(
            family="Arial Black",
            size=20,
            color="Black"
                ),
        tickfont=dict(
            family="Arial Black",
            size=20,
            color="Black"
                )
    )
    fig.show()

from scipy.stats import gaussian_kde
def size_and_conc_smooth_curve(df_size, df_conc, datadir):
    palette = pc.qualitative.Dark24
    dirs = [d for d in os.listdir(datadir) if os.path.isdir(os.path.join(datadir, d))]
    fig = go.Figure()

    for i in range(len(df_size[0])):
        data = df_size[0,i]
        data = data[~np.isnan(data)]
        kde = gaussian_kde(data)
        x_smooth = np.linspace(min(data), max(data), 500)
        y_smooth = kde(x_smooth)
        y_smooth = (y_smooth - min(y_smooth)) / (max(y_smooth) - min(y_smooth))

        fig.add_trace(go.Scatter(
            x=x_smooth,
            y=y_smooth,
            mode='lines',
            name=dirs[i],
            line=dict(shape='spline', color=palette[i], smoothing=1.3)
        ))

        # Dummy trace for concentration
        fig.add_trace(go.Scatter(
            x=[None],
            y=[None],
            mode='markers',
            marker=dict(size=0, color=palette[i]),
            name=f'concentration: {df_conc[0,i][1]:e} bubbles/ml'
        ))

    fig.update_layout(
        title='Bubbles diameter distribution (Smoothed)',
        title_font=dict(
            family="Arial Black",
            size=18,
            color="Black"
        ),
        legend_font=dict(
            family="Arial Black",
            size=15,
            color="Black"
        )
    )
    fig.update_xaxes(
        title='um',
        title_font=dict(
            family="Arial Black",
            size=20,
            color="Black"
        ),
        tickfont=dict(
            family="Arial Black",
```

```
            size=20,
            color="Black"
        )
    )
    fig.update_yaxes(
        title="relative number",
        title_font=dict(
            family="Arial Black",
            size=20,
            color="Black"
        ),
        tickfont=dict(
            family="Arial Black",
            size=20,
            color="Black"
        )
    )
    fig.show()
########################################################################
datadir =
↪  r'C:\Users\degra\Desktop\Eindhoven_experimental_data\20251003_ImagingBubbles\Bubbles_images'
# get list of all directories in selected parent dir
dirs = [d for d in os.listdir(datadir) if os.path.isdir(os.path.join(datadir, d))]
today = str(date.today())  # just todays date used for naming files
df_diam = np.zeros((1,len(dirs)), dtype=object)
df_conc = np.zeros((1,len(dirs)), dtype=object)
channel_height = 400 #um
dirs_counter=0

for t in dirs:
    path = datadir + '\\' + t
    tif_files = [f for f in os.listdir(path) if f.endswith(".tif")]
    xml_files = [f for f in os.listdir(path) if f.endswith(".xml")]
    radii_list = []
    sample_volumes = []

    for tif,xml in zip(tif_files,xml_files):
        img = AICSImage(path+'\\'+tif)
        img = img.get_image_data()[0,0,0,:,:,:]
        img = cv2.cvtColor(img, cv2.COLOR_BGR2GRAY)
        with open(path+'\\'+xml, encoding="utf8") as f:
            metadata = f.read()

        ind = metadata.find("OnePixel")
        # pixel_len = np.float16(metadata[ind+10:ind+18]) #um
        pixel_len = 0.8333 #um
        height, width = img.shape
        img_volume = channel_height*((height*width)*pixel_len)*1e-12 #ml

        cv2.namedWindow('img_{}'.format(t), cv2.WINDOW_NORMAL)
        cv2.resizeWindow('img_{}'.format(t), round(width), round(height))
        cv2.imshow('img_{}'.format(t), img)
        cv2.waitKey(2000) #time in ms the img is shown (0) for infinite
        cv2.destroyAllWindows()

        og_img = img
        img = cv2.GaussianBlur(img, (3,3), 2) #small kernel blurring to remove a bit of noise
        _, img = cv2.threshold(img,0,255,cv2.THRESH_BINARY+cv2.THRESH_OTSU)
        img = img.astype(np.uint8)
        img = cv2.bitwise_not(img)
        img[0,:]=0; img[:,0]=0; img[-1,:]=0; img[:,-1]=0;#first and last columns/row set to
        ↪  zero to improve cntrs recognition
        img = np.pad(img, (20,20), constant_values=0)

        img[0,:] = 0 ; img[:,0] = 0 #remove first line and first row binarization artefact of
        ↪  white pixels
        cntrs, hierarchy= cv2.findContours(img, cv2.RETR_CCOMP, cv2.CHAIN_APPROX_NONE)
        img = cv2.cvtColor(img, cv2.COLOR_GRAY2RGB)

        #find false bubbles centres and concatenate those cntrs to the parent contour
        hierarchy = hierarchy[0]
        cntrs,hierarchy = filter_desired_chilren(cntrs, hierarchy)
        #process the img with the upadated siblings and parents
```

```
        for i in range(len(cntrs)):
            if hierarchy[i][3] == -1:  # Check if the contour has no parent
                color = random_color()  # Assign a random color to this family
                radii_list = process_contour_family(img, cntrs, hierarchy, i, color,
                ↪  radii_list, pixel_len)

        sample_volumes.append(img_volume)

        og_img_8bit = cv2.normalize(og_img, dst=None, alpha=0, beta=255,
        ↪  norm_type=cv2.NORM_MINMAX).astype(np.uint8) #8bit img just to show
        og_img_8bit = np.pad(og_img_8bit, (20,20), constant_values=0)
        og_img_8bit = cv2.cvtColor(og_img_8bit, cv2.COLOR_GRAY2BGR)
        show = np.concatenate((og_img_8bit,img), axis=1)
        cv2.namedWindow('img_{}'.format(t), cv2.WINDOW_NORMAL)
        cv2.resizeWindow('img_{}'.format(t), round(width)*2, round(height))
        cv2.imshow('img_{}'.format(t), show)
        cv2.waitKey(3000) #time in ms the img is shown (0) for infinite
        cv2.destroyAllWindows()

    diameters = np.array(radii_list)*2 #um
    diam_filter = diameters> 2 #um | remove possible artefacts too small to be accepted
    diameters = diameters[diam_filter]
    df_diam[0, dirs_counter] = diameters

    bubbles_num = len(diameters)
    conc = bubbles_num/(sum(sample_volumes)) #since the diameters data are pooled among
    ↪  pictures, divide by sum of images volumes
    df_conc[0, dirs_counter] = np.array([bubbles_num, conc])

    dirs_counter = dirs_counter+1

np.save(datadir+"\\"+"bubbles_size.npy", df_diam, allow_pickle=True)
np.save(datadir+"\\"+"bubbles_concentration.npy", df_conc, allow_pickle=True)
#######################################################################
datadir = datadir
df1 = np.load(datadir+"\\"+"bubbles_size.npy", allow_pickle=True)
df2 = np.load(datadir+"\\"+"bubbles_concentration.npy", allow_pickle=True)

# size_and_conc_histogram(df1, df2,datadir)
size_and_conc_smooth_curve(df1, df2,datadir)
```

Listing 6: Python script for evaluation of bubbles diameter and concentration